Physics-based modeling
for high-fidelity radar retrievals

by

Mariko Sofie Burgin

A dissertation submitted in partial fulfillment
of the requirements for the degree of
Doctor of Philosophy
(Electrical Engineering)
in The University of Michigan
2014

Doctoral Committee:

Professor Mahta Moghaddam, Co-Chair, University of Southern California
Professor Fawwaz T. Ulaby, Co-Chair
Professor Dara Entekhabi, Massachusetts Institute of Technology
Associate Professor Valeriy Y. Ivanov
Associate Research Scientist Leland E. Pierce

To my parents

ACKNOWLEDGEMENTS

This dissertation was made possible due to the support, guidance, and encouragement of many people. First of all, I would like to thank Prof. Mahta Moghaddam for her guidance, motivation, and support throughout this Ph.D. journey. I am also very grateful to Prof. Fawwaz Ulaby for his mentorship and support. I would also like to thank my committee members, Prof. Dara Entekhabi, Prof. Valeriy Ivanov, and Dr. Leland Pierce for their time and numerous helpful comments and suggestions at various stages of this dissertation.

I am lucky to be surrounded by many great people and they are all an imperative part to both my success and sanity. The encouragement, assistance, laughter, lunches, and friendship of my colleagues at the University of Michigan Radiation Laboratory have made my first three years enjoyable. Most notably, I'd like to thank Dr. Jackie Vitaz, Marc Sallin and Dr. Mauro Ettorre. My Ph.D. journey then brought me to the Microwave and Systems, Sensors and Imaging (MiXIL) Laboratory at the University of Southern California for the last two years. I would like to express my thanks to the entire MiXIL group for their friendship and companionship. Most notably, I'd like to thank Dr. Uday Khankhoje and Ruzbeh Akbar for their encouragement and friendship. Other friends, close and far, also have been an integral part to my life, my thanks go out to you. A special thanks goes to Dr. Rahul Ahlawat for his never-ending support and encouragement.

I would like to thank my peers and colleagues for the many interesting, motivating and inspiring discussions, as well as my many field work colleagues from universities

iii

and agencies all around the world for their friendship and hard work. I would also like to express my sincere thanks to Prof. Thomas Zurbuchen for his guidance and mentorship throughout my Ph.D.

Thanks also extend to Christine Eun, Alexis Frank, Anne Itsuno, Danese Joiner, and Jackie Vitaz for proof reading the dissertation on very short notice.

Finally, and most importantly, I would like to thank my parents Daniel and Shinobu for their love and support that makes it possible for me to achieve my goals.

TABLE OF CONTENTS

vi

LIST OF FIGURES

Figure

LIST OF TABLES

LIST OF APPENDICES

Appendix

LIST OF ABBREVIATIONS

AirMOSS   Airborne Microwave Observatory of Subcanopy and Subsurface

AIRSAR   Airborne SAR

ALOS   Advanced Land Observing Satellite

ASF   Alaska Satellite Facility

BBB   Brigalow Belt Bioregion

BERMS   Boreal Ecosystem Research and Monitoring Sites

BOREAS   Boreal Ecosystem-Atmosphere Study

BSA   Backscatter Alignment Convention

CanEx-SM2010   Canadian Experiment for Soil Moisture in 2010

DAAC   Distributed Active Archive Center

DBH   Diameter at Breast Height

DEM   Digital Elevation Model

DOY   Day Of Year

ESA   European Space Agency

EV-1   Earth Venture 1

G-III   Gulfstream III

GCRP   Global Change Research Program

GlobCover   Global land cover

GPS   Global Positioning System

GRD   Ground-projected gridded data

HDF5	Hierarchical Data Format
HECC	High-End Computing Capability
HPCC	High Performance Computing and Communications
HWSD	Harmonized World Soil Database
ICLP	Injune Collaborative Landscape Project
IGRF	International Geomagnetic Reference Field Model
IIASA	International Institute for Applied Systems Analysis
IPCC	Intergovernmental Panel on Climate Change
IRI	International Reference Ionosphere
JERS-1	Japanese Earth Resources Satellite 1
JPL	Jet Propulsion Laboratory
JSC	Johnson Space Center
LTER	Long Term Ecological Research
MBSDM	Mineralogy-Based Soil Dielectric Model
MOISST	Marena Oklahoma In Situ Sensor Testbed
NASA	National Aeronautics and Space Administration
nCGM	Non-linear Conjugate Gradient Method
NEE	Net Ecosystem Exchange
NED	National Elevation Database
NLCD	National Land Cover Database
OJP	Old Jack Pine
OBS	Old Black Spruce
ORNL	Oak Ridge National Laboratory
PALS	Passive/Active L-band Sensor
PALSAR	Phased Arrayed L-band SAR
PARC	Polarimetric Active Radar Calibrator
QNM	Quasi-Newton Method

RFI	Radio-Frequency Interference
RMS	Root Mean Square
RMSE	Root Mean Square Error
RZSM	Root Zone Soil Moisture
SAR	Synthetic Aperture Radar
SEBCM	Stabilized Extended Boundary Condition Method
simAnn	Simulated Annealing method
SIR-C	Shuttle Imaging Radar
SMAP	Soil Moisture Active Passive
SMAPVEX12	SMAP Validation Experiment 2012
SoilSCAPE	Soil moisture Sensing Controller And oPtimal Estimator
SSURGO	Soil Survey Geographic Database
SPM	Small Perturbation Model
SRTM	Shuttle Radar Topography Mission
STATSGO2	Digital General Soil Map of the United States
TA	Trembling Aspen
TEC	Total Electron Content
TLS	Terrestrial Laser Scanning
UAVSAR	Uninhabited Aerial Vehicle Synthetic Aperture Radar
UMBS	University of Michigan Biological Station
USC	University of Southern California
USGS	United States Geological Survey
VWC	Vegetation Water Content
WMM	World Magnetic Model
YJP	Young Jack Pine

ABSTRACT

Physics-based modeling for high-fidelity radar retrievals

by

Mariko Sofie Burgin

Co-Chair: Professor Mahta Moghaddam

Co-Chair: Professor Fawwaz T. Ulaby

Knowledge of soil moisture on a global scale is crucial for understanding the Earth's water, energy, and carbon cycles. This dissertation is motivated by the need for accurate soil moisture estimates and focuses on the improvement of the retrieval of soil moisture based on active remote sensing over vegetated and forested areas. It addresses three important, but often neglected, aspects in radar imaging: ionospheric effects, effects of multispecies vegetation (heterogeneity at pixel level), and heterogeneity at landscape level. The first contribution of this dissertation is the development of a generalized radar scattering model as an advancement of current radar modeling techniques for vegetated areas at a fine-scale pixel level. It consists of a realistic multispecies representation of vegetated areas, realistic subsurface soil layer modeling, and inclusion of terrain topography. This modeling improvement allows greater applicability to different land cover types and generally higher accuracy for retrieval of soil moisture. Most coarse-scale satellite pixels (km-scale or coarser) contain highly heterogeneous scenes with fine-scale (100 m or finer) variability of soil moisture, soil texture, topography, and vegetation cover types. The second con-

tribution is the development of spatial scaling techniques to investigate effects of landscape-level heterogeneity on radar scattering signatures. Using the above radar forward scattering model, which assumes homogeneity over fine scales, tailor-made models are derived for the contribution of fine-scale heterogeneity to the coarse-scale satellite pixel for effective soil moisture retrieval. Finally, the third contribution is the development of a self-contained calibration technique based on an end-to-end radar system model. The model includes the effects of the ionosphere allowing the use of spaceborne radar signals for accurate soil moisture retrieval from lower frequencies, such as L- and P-band.

These contributions in combination will greatly increase the usability of low-frequency spaceborne radar data for soil moisture retrieval: ionospheric effects are successfully mitigated, heterogeneity at landscape level is resolved, and fine-scale scenes are better modeled. All of these contributions ultimately allow improved fidelity in soil moisture retrieval. These contributions are immediately applicable in current missions such as the ongoing Airborne Microwave Observatory of Subcanopy and Subsurface (AirMOSS) mission that observes root-zone soil moisture with a P-band radar at fine-scale resolution (100 m), and National Aeronautics and Space Administration (NASA)'s upcoming Soil Moisture Active Passive (SMAP) spaceborne mission, which will assess surface soil moisture with an L-band radar and radiometer at km-scale resolution (3 km).

CHAPTER I

Introduction

Knowledge of soil moisture dynamics on a global scale is key in understanding the Earth's terrestrial water, energy, and carbon cycles. A visualization of the water cycle is shown in Fig. 1.1. Soil moisture impacts soil evaporation and plant transpiration at the air/land boundary, which in turn affects the energy balance and surface energy fluxes. Evaporation and transpiration provide a natural moisture supply to the atmosphere and evaporation acts as a cooling mechanism by transforming surface heat into moisture release instead of warming up the atmosphere [5]. Improved soil moisture estimates allow better modeling and prediction of these global water and energy fluxes on land surfaces, thereby improving weather and climate predictions. Besides impact on the processes of evaporation and transpiration, soil and plants are part of a complex system involving carbon fixation and release. The net carbon flux of boreal forests is a major source of uncertainty in the carbon budget [6]. With the availability of improved soil moisture estimates, this attributed and so-called "missing carbon" sink can be better quantified.

Scientists have hypothesized that the delicate balance in the water, energy, and carbon cycles has been unsettled due to the intensified natural greenhouse effect by human-induced emissions. In several regions of the world, increased extreme weather events such as heat waves, droughts, floods and hurricanes have been reported [5].
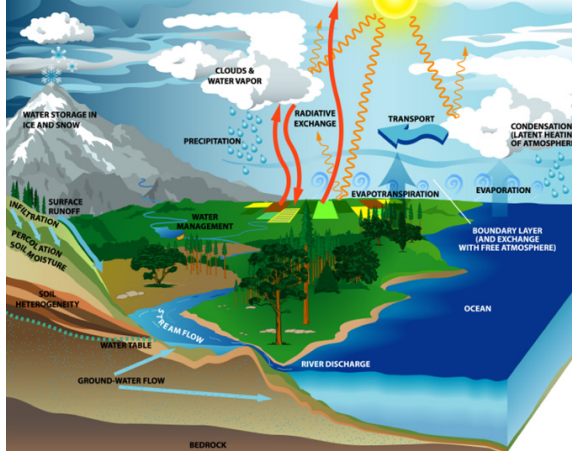
Figure 1.1: Earth's water cycle. Image courtesy of U.S. Global Change Research Program (GCRP) (Our Changing Planet (OCP) 2003).

Knowledge of soil moisture at a larger scale will allow more accurate modeling for flood prediction and drought monitoring. Studies analyzing the impact of greenhouse gases on the climate have shown that current model simulations agree in a global rise in temperature, but disagree on predicting a conclusive trend in surface soil moisture change and water resource availability as shown in Fig. 1.2. Better prediction of soil moisture is crucial to forecast future water supply and food production.

To accommodate this need for a global soil moisture estimate, several missions are underway to provide remote sensing observations for retrieval of soil moisture. For example, the Airborne Microwave Observatory of Subcanopy and Subsurface (AirMOSS) mission is part of the National Aeronautics and Space Administration (NASA) Earth Venture 1 (EV-1) program and observes root-zone soil moisture with a P-band Synthetic Aperture Radar (SAR) over nine different biomes of north America starting from September 2012 [7]. AirMOSS can be considered a stepping stone towards a spaceborne implementation of a low-frequency radar mission. For global observations of surface soil moisture, NASA is developing the Soil Moisture Active Passive (SMAP) spaceborne mission carrying an L-band radar and radiometer to be launched in November 2014 [8].

This dissertation is motivated by the requirements of these current and future
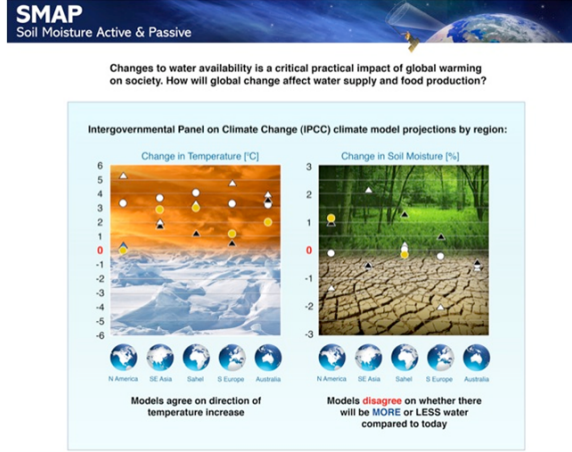
Figure 1.2: Intergovernmental Panel on Climate Change (IPCC) climate model projections by region. Image courtesy of SMAP.

missions for accurate soil moisture retrievals in the presence of several sources of uncertainty. It advances three important, but often neglected, aspects crucial for soil moisture retrieval based on spaceborne low-frequency radars: effects of multispecies vegetation (heterogeneity at pixel level), heterogeneity at landscape level, and ionospheric effects.

With SMAP, soil moisture will be retrieved globally at 9 km resolution, including vegetated areas of up to 5 kg/m^2 of Vegetation Water Content (VWC), which includes crops and many forested areas. This calls for an assessment and advancement of current radar modeling techniques for vegetated areas. The majority of existing radar models for high biomass areas, such as forests, address only single-species vegetation, which is typically an unrealistic representation. The use of lower frequencies such as P-band for AirMOSS furthermore shifts the focus to the subsurface layers, which have to be modeled more accurately due to the larger penetration depth of the radar signal. Terrain topography is generally overlooked in retrievals, even though it significantly alters the radar backscatter and must be considered for reliable soil moisture retrieval [9]. Ultimately, a generalized radar scattering model including all of these effects is envisioned. This defines the first contribution of this dissertation

and is discussed in chapter II. The availability of improved modeling techniques allows soil moisture retrieval with higher accuracy and more general applicability to different land cover types. The retrieval at fine scales is discussed in chapter III.

The SMAP mission will carry both a radar and a radiometer allowing synergistic use of the two data types for soil moisture retrieval. Radar data are delivered at higher resolution (3 km) than the radiometer data (36 km), and allow finer analysis of the connection between land cover type and soil moisture. But even this resolution involves challenges with respect to landscape heterogeneity. Most satellite resolution pixels contain highly heterogeneous scenes with small scale variability of soil moisture, soil texture, topography, and vegetation cover types. Traditional algorithms for radar soil moisture retrieval assume a homogeneous scene within each satellite resolution cell, which is not a reasonable assumption even for the 3 km resolution radar data from SMAP. This illuminates the need for the second contribution of this dissertation: the development of spatial scaling techniques using radar forward scattering models that assume homogeneity over finer scale sub-pixels and the derivation of tailor-made models for their contribution to the coarse-scale satellite pixel for effective soil moisture retrieval. This contribution is discussed in chapter IV.

Lower frequencies such as L-band for SMAP and P-band for AirMOSS allow a stronger penetration through vegetation and soil, and will hence enable the retrieval of the surface (with L-band) and root zone (with P-band) soil moisture. For frequencies below about 1.5 GHz, the ionosphere can no longer be assumed to be transparent. Therefore, for spaceborne missions such as SMAP, ionospheric effects such as the Faraday rotation could alter the radar signal significantly and introduce large uncertainties associated with radar backscattering coefficients; these in turn result in large errors in soil moisture retrievals if not mitigated. If a P-band mission were to fly on a spaceborne platform, the effects would be even more severe. There is a need to address mitigation of ionospheric effects such as Faraday rotation to allow the use

of radar signals for soil moisture retrieval. Developing a self-contained calibration technique based on an end-to-end radar system model, including the effects of the ionosphere, is the third contribution of this dissertation and is discussed in chapter V.

This dissertation is concluded with a summary of the contributed work and a discussion of future work in chapter VI.

CHAPTER II

Generalized radar scattering model at fine scales

2.1 Introduction

Many traditional radar scattering models make simplifying assumptions disregarding many natural features of the scene. With the prospect of soil moisture retrieval over high biomass areas as required by AirMOSS and SMAP, it is important to realistically model a wide variety of land cover types including forests. Single-species models cannot fulfill the demand for realistic modeling hence necessitating an extension to multispecies models. Traditional soil modeling has been mainly restricted to a single soil layer, which is inadequate for lower frequencies due to the longer penetration depth of signals at these frequency ranges. Therefore, the above-ground modeling has to be combined with a more realistic multilayered soil structure to account for soil moisture profiles and various soil horizons. Furthermore, to achieve a generalized and more accurate radar scattering model, the underlying terrain topography has to be considered. The fine-pixel modeling effort is divided into three parts: the above-ground (vegetation modeling), the below-ground (ground surface and subsurface modeling), and the terrain topography modeling aspects.

2.2 Vegetation modeling at fine-scale pixels

Vegetation, and specifically forest, exists in many structural forms. These vary with species, growth stage, and composition, along with environmental variables such as soil depth, wind exposure, and available soil moisture. Despite the increased availability of observations at scales ranging from individual plants to the entire terrestrial (vegetated) surface, characterizing and quantifying vegetation structure has remained a significant challenge to remote sensing scientists. The importance of obtaining such information on a routine basis is being increasingly realized due to the importance of vegetation structure in terms of quantifying biodiversity and understanding biogeochemical cycles of water and carbon.

Active remote sensing modalities of lidar and radar have shown the greatest promise for obtaining information on the three-dimensional structure of vegetation and particularly forests (e.g., [10–12]). Fine-scale radar retrieval is addressed in more detail in chapter III. The retrieval of structural attributes from these sources requires an understanding of the manner in which waves interact with plant elements (primarily leaves, branches, and trunks) as a function of their distribution and location within the volume. For radar measurements, such knowledge is best achieved by using models that simulate backscatter at different frequencies and polarizations. Two commonly used types of models are based on either wave theory or radiative transfer.

Models based on radiative transfer theory (e.g., [13–17]) solve energy transport equations in random media, however, ignore coherent effects. The majority of these models have been developed for relatively simple forests (single species and two layers (crown and trunk) or simple canonical shapes representing crown boundaries), with the exception of Liang *et al.* [18] who developed a radiative transfer model that considers forests with multiple layers and of mixed species composition.

Models based on wave theory (e.g., Durden *et al.* 1989, [19]) use a distorted Born approximation and an approximate solution of Maxwell's equations of the scattered

7

medium. These methods include coherent field effects. The majority of these models have focused on simple mono-species forests, although more complex forests have also been considered. For example, Sun *et al.* [20] simulated backscatter from woodlands with less than 60 percent crown cover with none interlocking and considering each tree as an individual scatterer. This model was improved by Wang *et al.* [21]. A coherent model for interferometric radar analysis was recently developed in [22] and tested for deciduous forests with simple species compositions. Another coherent model uses fractal-generated trees to model forest canopies [23]. In the model developed by Chauhan *et al.* [24], which has application to the multispecies case, woody components are associated with circular, lossy dielectric cylinders, which are variable in length and distributed randomly but homogeneously within a slab. Total, direct, direct-reflected, reflected and surface backscattering coefficients are then simulated. However, the assumption of the simplified slab results in the loss of the characteristic geometry of trees. Richards *et al.* [25] introduced an L-band HH radar backscatter model of a coniferous stand thus representing the forest as a discrete collection of finite dielectric cylinders. This model was further developed by Durden *et al.* [19] to model both softwood and hardwood trees.

The model in [19] has subsequently been used to better understand the use of SAR for retrieving soil moisture [26] and biomass [1]. The model allows any tree geometry to be approximately built from a defined set of input parameters. Knowledge of the major scattering mechanisms at the stand level can be obtained from the physically realistic trunk-crown structure. The model has been evaluated for mixed species forests [1], although each tree type (e.g., species and growth stage) was considered separately without regard to the presence of other species. To address the shortcomings of these existing forest scattering models, this dissertation aims to (1) develop a realistic multispecies and multilayer generalization of [19] and (2) evaluate the ability of the model to predict backscattering coefficients through comparisons with airborne
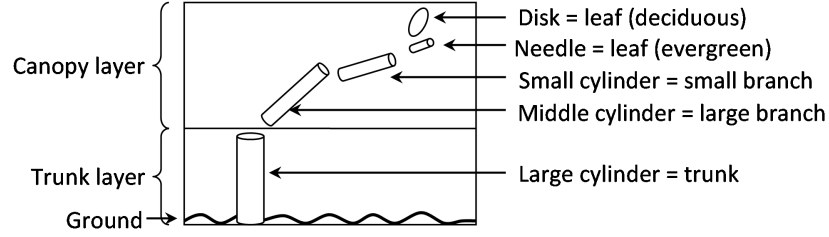
Figure 2.1: Discrete scatter building blocks used in single-species model.

and spaceborne SAR data.

Validation of the model focused specifically on two wooded savanna sites situated within the Brigalow Belt Bioregion (BBB) in central southeast Queensland, Australia. In the Tara Downs subregion, the considered structural formations included mature and older regrowth forests of mixed species composition dominated by Brigalow (or Acacia harpophylla). In the Injune Collaborative Landscape Project (ICLP) area, more complex forests of mixed species composition were considered. The availability of field data from both sites supported the parameterization of the model and ALOS PALSAR and NASA Jet Propulsion Laboratory (JPL) AIRSAR data had been acquired during periods of field data acquisition and are available for validating simulations of the backscattering coefficient.

2.2.1 The single species vegetation model

The following section highlights the key elements for the extension of Durden *et al.* [19] to the multilayered, multispecies case. In the model, trees are categorized into either hardwoods (deciduous) or softwoods (evergreen). Their major difference for modeling purposes is the extension of the trunk into the canopy layer for softwood trees and the use of either disks (deciduous species) or cylinders (evergreen species) to represent leaves or needles. Trees are assumed to consist of two layers, referred to as the trunk and canopy (or crown) layers as shown in Fig. 2.1.

The boundary between the trunk and canopy layer is not explicitly defined but,

9

for most trees, can be set at the first branching point, where the trunk divides into multiple large branches. Trunks populate the lower layer and are modeled as single vertically-oriented finite dielectric cylinders. The branch structure is divided into two categories, large and small, with each modeled as a collection of finite dielectric cylinders in the canopy layer. Depending on the tree type, either dielectric disks or needles are used to model the leaves. By defining densities of trunks, branches (large, small), and leaves, lateral homogeneity is implemented over a modeling unit (or radar pixel), while vertical heterogeneity is realized by allowing for multiple species. The type of scatterers of a specific species inside each vertical layer is considered homogeneous, with stationary statistics.

All scattering mechanisms within this model are based on scattering from discrete scatterers in the form of cylinders. These cylinders represent the trunks, branches, leaves, and needles or leaves. The first objective is to define the Stokes matrix for a layer of finite, randomly oriented cylinders.

The scattering matrix A for a single vertically infinite dielectric cylinder is defined by [19] in the traditional manner:

$$
\begin{bmatrix} E_H \\ E_V \end{bmatrix}^s = e^{\frac{i3\pi}{4}} \sqrt{\frac{2}{\pi k r \sin \theta_i}} e^{ik(r \sin \theta_i - z \cos \theta_i)} \begin{bmatrix} A_{HH} & A_{HV} \\ A_{VH} & A_{VV} \end{bmatrix} \begin{bmatrix} E_H \\ E_V \end{bmatrix}^i \tag{2.1}
$$

where θ_i is the incidence angle relative to the cylinder axis. The elements of the scattering matrix $A(\theta_i, \phi_s - \phi_i)$ are provided in [27]. The technique of [28] is used to determine the scattering matrix of a finite cylinder. This assumes the cylinder to be long compared to the electromagnetic wavelength. While this assumption is not necessarily valid considering the dimensions of needles and leaves, it is used nevertheless as their effect is minimal in the frequency of interest. This leads to the

scattering matrix S for a finite cylinder of length L [19]:

$$S_{pq}(\theta_i, \phi_i, \theta_s, \phi_s) = \frac{ikL\sin\theta_s}{\pi\sin\theta_i}\frac{\sin kL(\cos\theta_i + \cos\theta_s)/2}{kL(\cos\theta_i + \cos\theta_s)/2}A_{pq}(\theta_i, \phi_s - \phi_i) \qquad (2.2)$$

This is the general scattering matrix for a vertical cylinder and has to be further generalized to an arbitrarily oriented cylinder. This is achieved by introducing two tilting angles (ψ, δ), which represent the angle of tilting within the incidence plane, and in the direction normal to the incidence plane, respectively. This permits the transformation of the incident wave into the coordinate system of the cylinder. Equation (2.2) is then used to find the scattering matrix of a finite, vertical cylinder in the cylinder's coordinate system. Finally, the scattering matrix is transformed back to the coordinate system of the radar. Therefore, a scattering matrix for a tilted cylinder for incidence and scattering angles relative to the ground surface $S(\theta_i, \phi_i, \theta_s, \phi_s, \psi, \delta)$ is defined [19].

Four major scattering mechanisms are considered: direct backscattering from the branch layer volume (B), direct backscattering from ground (G), specular crown scattering followed by rough ground reflection (BG) and vice versa, and specular trunk scattering followed by rough ground reflection (TG) and vice versa, as presented in Fig. 2.2.

The BG and TG mechanisms are often referred to as "double bounce". The scattering matrix of double bounce backscatter for a tilted cylinder above a ground surface and in terms of the old scattering matrix elements is given as [19]:

$$S = \begin{bmatrix} 2\widetilde{r_H}S_{HH} & (\widetilde{r_H} + \widetilde{r_V})S_{HV} \\ (\widetilde{r_H} + \widetilde{r_V})S_{VH} & 2\widetilde{r_V}S_{VV} \end{bmatrix} \qquad (2.3)$$

where $\widetilde{r_H}, \widetilde{r_V}$ are the Fresnel reflection coefficients r_H, r_V modified by the presence
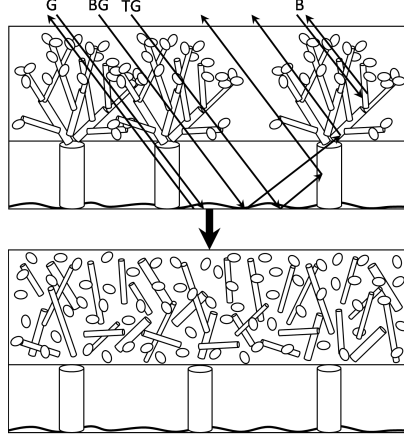
Figure 2.2: Realistic geometry of single species forest with four scattering mechanisms implemented in single-species model by Durden *et al.* (on top) and actual realization in model (on bottom).

of surface roughness according to [29]:

$$\widetilde{r_H} = r_H e^{-2H^2 k^2 \cos^2 \theta_i} \tag{2.4}$$

$$\widetilde{r_V} = r_V e^{-2H^2 k^2 \cos^2 \theta_i} \tag{2.5}$$

where H is the Root Mean Square (RMS) surface height.

For all scattering mechanisms, the scattering matrix is subsequently converted to a Stokes matrix, multiplied by the probability density function (pdf) for cylinder orientation, and averaged over all cylinder tilts. The mean and variance of the pdf for large and small branches of both soft- and hardwood trees can be selected according to species, but the trunks are assumed to be nearly vertical with a Gaussian tilt distribution of 5° standard deviation.

The attenuation due to a canopy layer of thickness z can be expressed as follows [19]:

$$S \quad = \quad \begin{bmatrix} e^{\frac{S_{HH} z}{\cos \theta_i}} & 0 \\ 0 & e^{\frac{S_{VV} z}{\cos \theta_i}} \end{bmatrix} \tag{2.6}$$

where the new scattering matrix S of the transmitted field can be expressed

through the incident field. To calculate the Stokes matrix for backscattering from a single layer, the attenuation within that layer has to be considered. The Stokes matrix M_b from a layer of thickness H can be found as in [19]:

$$M_b = \int_0^H T(z) M \, T(z) \mathrm{d}x \tag{2.7}$$

where T is the transmission matrix.

A two-way propagation takes place for the double bounce cases. This is accounted for by multiplying the double bounce Stokes matrix by the transmission matrices for transmission in both directions.

The ground is modeled as a random rough dielectric surface based on the first-order SPM. Using this method is justified as long as it can be assumed that the slopes and the RMS height of the random rough surface can be considered small [30]. It is noteworthy that, under this model, there is no depolarization (cross-polarized wave) for a linearly polarized incident wave in backscattering direction. The exact implementation can be found in [31].

The total Stokes matrix M_{Total} is therefore given by [19]:

$$M_{Total} = M_b + T_b T_t M_{bg} T_t T_b + T_b T_t M_{tg} T_t T_b + T_b T_t M_g T_t T_b \tag{2.8}$$

where b, t, and g represent the branch, trunk and ground layers, respectively.

The model of Durden *et al.* [19] uses a distorted Born approximation to account for wave propagation through the crown and trunk layers. This approximation assumes that the mean propagating field due to an incident plane wave is taken to be the field transmitted into the average medium. This can be assumed if there are only weak fluctuations of the dielectric constant around an average medium dielectric constant [29]. The distorted Born approximation further assumes the use of the unperturbed field

values in the background medium with the effective permittivity, which is valid if the permittivity of the medium is close to that of the background medium [30, 32]. Therefore, the mean field is assumed to propagate inside the heterogeneous medium without any loss of energy resulting from scattering by heterogeneities. This assumption is valid for the canopy and trunk layer in [19], as vegetation canopies are typically sparse random media.

The impact of multispecies modeling is illustrated in Fig. 2.3. Parameters of two tree species observed at CanEx-SM2010 are used: a mature OJP forest stand and a regrowth YJP forest. A visualization of the two forest stands is given in Fig. 2.4. The OJP forest is a sparse forest stand with a total height of 14 m, while the YJP forest is a stand with a total tree height of 2 m and an observed trunk density of 0.4 trees per square meter. The OJP forest stand is assumed to be always present while the YJP forest is grown as an understory by increasing the trunk, branch and needle densities. The radar backscatter for C-, L- and P-band is simulated. The scattering mechanisms contribute differently depending on frequency. At C-band when only the OJP forest is present, the radar perceives the ground due to the sparseness of the OJP forest (0.25 trees per square meter), but with increasing YJP understory, the canopy cover closes. Since C-band does not penetrate into the canopy, volume scattering starts to dominate and the total radar backscatter decreases and saturates. Lower frequencies, such as L- and P-band, penetrate into the canopy and the trunk-ground double bounce scattering mechanism dominates. With increasing understory, the number of trunks increases and therefore the trunk-ground double bounce scattering mechanism is reinforced, which strengthens the total scattering mechanism. This study shows the importance of multispecies vegetation modeling. A different aspect of multispecies modeling is the oversimplification of the forest structure, which can be a source of substantial error. An example is given in Fig. 2.5, where radar backscatter over soil moisture for three structurally different forests with equal VWC

14
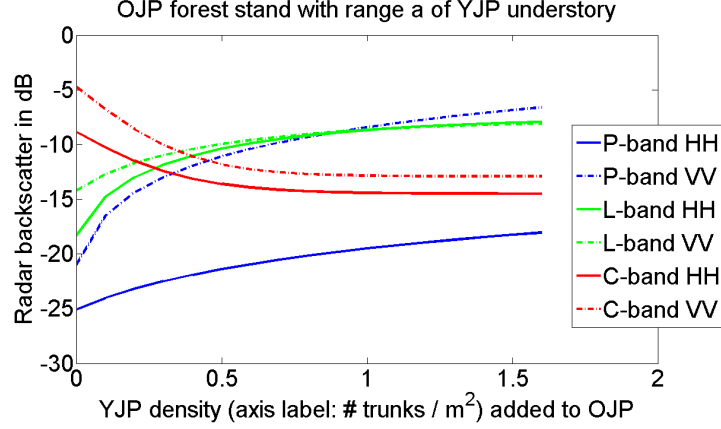
Figure 2.3: Impact of multispecies modeling: mature OJP forest stand with a range of regrowth YJP understory. The understory is grown by increasing the number of trunks, branches and needles of the YJP forest stand.

is shown. The VWC is a parameter that describes the water content in vegetation material, which is used to model the amount of volume scattering experienced by the radar signal due to leaves/needles, branches and trunks and to model the amount of attenuation of emission by and through vegetation in the tau-omega model [33]. The VWC parameter combines the quantification of water content and biomass. All forests in the study shown in Fig. 2.5 have a VWC of $6\frac{kg}{m^2}$, but their structure varies: A single-species mature OJP forest $(6\frac{kg}{m^2})$, an OJP forest $(4\frac{kg}{m^2})$ with a YJP understory $(2\frac{kg}{m^2})$, and a mixed forest with OJP $(3\frac{kg}{m^2})$ and deciduous forest $(3\frac{kg}{m^2})$ are compared. All other model parameters are identical save the structural parameters describing the forest. The frequency is L-band. A difference of about 4 dB can be observed in this particular example by simply assuming a different forest structure. This demonstrates the need to develop realistic forest models instead of assuming a single-species forest.

2.2.2 The development of a multilayered multispecies vegetation model

The mathematical machinery of the multilayered multispecies forest scattering model is built upon that of the single-species, two-layer model. Careful investigation

Figure 2.4: Visualization of mature OJP forest stand (left) and regrowth YJP understory (right) observed at CanEx-SM2010. The inherent trunk densities are 0.25 trees per square meter for OJP and 0.4 trees per square meter for YJP.
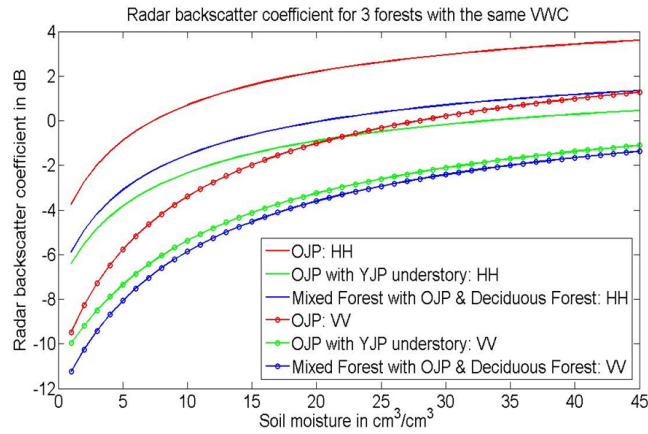
Figure 2.5: Radar backscatter over soil moisture for three structurally different forests with equal VWC.

of the four major scattering mechanisms considered in the single species model reveals the underlying structure of the calculations, which can be shaped into five separate functionalities. These functionalities for the multispecies generalization resemble the calculations for the previous four scattering mechanisms, but they have more capabilities and are able to handle scattering from and propagation through multiple species and multiple layers in the presence of each other.

All of the four scattering mechanisms in the single species model depend on incorporating the attenuation due to the canopy layer. Likewise, it is appropriate to establish and calculate this attenuation as the first functionality as subsequent calculations will depend on its results. As pointed out in 2.2.1, for example, the branch volume scattering of a canopy layer includes the effects of attenuation within that layer. In a multilayered forest, the scattering and propagation through overlying layers of vegetation volume will also require consideration. Therefore, the branch volume scattering is identified as the second functionality. The branch-ground and trunk-ground double bounces are also affected by canopy attenuation and constitute two further separate functionalities. The direct ground scatter follows suit as the last functionality. These five functionalities must be implemented carefully and systematically, regardless of the number of canopy layers and number of distinct species.

Combining multiple species with crown-trunk configuration yields a multilayer structure with overlapping layers as shown in Fig. 2.6. This permits a single layer to contain discrete scatterers of multiple species. A forest of N_S species has a maximum of $N = 2 N_S$ layers. In Fig. 2.6 an example for $N_S = 3$ is given. This calls for a separate module that is mainly concerned with ingesting the parameters of the different species and assembling the forest geometry prior to the calculations. This module requires flexibility regarding the order of species and the composition of discrete scatterers in each layer (combination of trunks, large or small branches, and
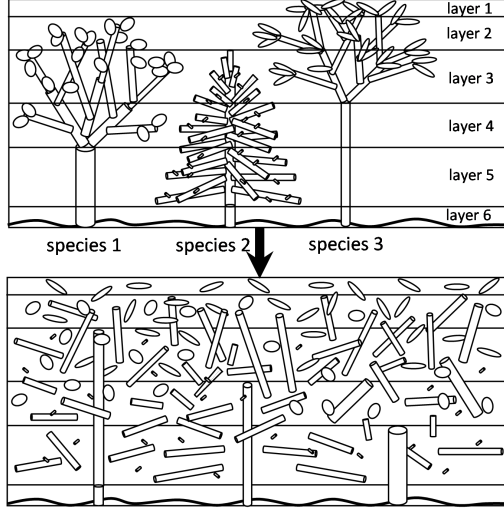
Figure 2.6: Realistic geometry of forest with three species $N_S = 3$ (on top) and actual realization in model (on bottom).

leaves) and has to be able to handle exceptions in forest geometries. This may occur, for example, when two species share an identical height, or if a species is considered a shrub and therefore does not have a trunk.

The following provides an example of such a module. It is not claimed to be an unique implementation, but rather suggests one working possibility. Four variables were created to contain all forest information: a geometry-height vector $(N \times 1)$ containing a sorted height profile that lists the heights of each layer from top-to-bottom and a geometry matrix $(N \times N_S)$ that maps the structure by noting if there is a trunk, canopy, or no scatterer present. A layer-height matrix $(2 \times N_S)$ keeps track of the trunk and canopy layer height. The trunk/branch-counter matrix $(N \times 2)$ tracks the branch or trunk count over one whole layer. These variables are completely dynamic and can be adapted to any number of species. All the geometry builder needs is the input parameters and the species count. With the knowledge of these four variable arrays, it can be assumed that the entire forest geometry is known and the different scattering functionalities can now be implemented. Figure 2.6 is useful for referencing the possible combinations of scatterers in layers.

In a top-to-bottom approach the attenuation associated with each layer is calcu-

lated, where each layer contains discrete scatterers of several species. These scatterers are a combination of large or small branches and leaves/needles, as well as trunks for softwood trees in branch layers (due to the extension of the stem into the canopy layer) or trunks in trunk layers. For attenuation due to large or small branches, leaves/needles, and trunks, the forward scattering matrix of each of these is calculated species-wise. These scattering matrices are then combined to obtain the scattering matrix of the total branch volume attenuation of one layer, which is converted to a Stokes matrix. This is the Stokes transmission matrix T of that particular layer and is stored for further use.

The branch volume scattering functionality is determined in a similar manner: in a top-to-bottom approach, the backscattering contributed from each layer is calculated, where each layer contains scatterers of several species. The scattering matrix for each of the scatterer types (large or small branches, leaves/needles and trunks) is calculated species-wise, converted to a Stokes matrix, multiplied by its species-specific pdf to account for cylinder orientation and averaged over all cylinder tilts. The resulting Stokes matrices are then summed. Then, the attenuation caused by scatterers within that layer is applied. This can be performed for each layer such that the branch volume scattering for all layers is known (M_{bL1} to M_{bLN}). The Stokes matrix of the total branch volume scattering of the forest M_b is the sum of the Stokes matrices of the total branch volume scattering of each layer (M_{bL1} to M_{bLN}) but for each layer the transmission through the overlaying layers has to be considered by multiplying with their respective Stokes transmission matrices T. This can be expressed as follows:

$$
\begin{aligned}
M_b &= M_{bL1} + T_{L1}M_{bL2}T_{L1} + \ldots \\
&\quad + T_{L1}T_{L2}\ldots T_{LN-1}M_{bLN}T_{LN-1}\ldots T_{L2}T_{L1}
\end{aligned} \tag{2.9}
$$

The double bounce functionalities are calculated separately for each species. For

each species, the double bounce Stokes matrices due to large or small branches and leaves/needles, as given in 2.2.1, are calculated and summed. This is the Stokes matrix for the branch double bounce of, for example, the first species M_{bg1}. Then, the transmission through all layers is considered by multiplying the Stokes transmission matrices T_{L1} to T_{LN}. The same procedure is followed for the remaining species. The total Stokes matrix due to branch-ground double bounce can be found as follows:

$$
\begin{aligned}
M_{bg} &= T_{L1}T_{L2}\dots T_{LN-1}T_{LN}M_{bg1}T_{LN}T_{LN-1}\dots T_{L2}T_{L1} \\
&+ T_{L1}T_{L2}\dots T_{LN-1}T_{LN}M_{bg2}T_{LN}T_{LN-1}\dots T_{L2}T_{L1} \\
&+ \dots \\
&+ T_{L1}T_{L2}\dots T_{LN-1}T_{LN}M_{bgN_S}T_{LN}T_{LN-1}\dots T_{L2}T_{L1}
\end{aligned}
\tag{2.10}
$$

Similarly, the Stokes matrix for the trunk-ground double bounce can be determined. The only difference for this calculation is that the double bounce Stokes matrices due to trunks for all species are calculated and summed up prior to multiplying the Stokes transmission matrices T_{L1} to T_{LN} of all layers. The total Stokes matrix due to trunk-ground double bounce can be found as follows:

$$
\begin{aligned}
M_{tg} &= T_{L1}T_{L2}\dots T_{LN-1}T_{LN}M_{tg1}T_{LN}T_{LN-1}\dots T_{L2}T_{L1} \\
&+ T_{L1}T_{L2}\dots T_{LN-1}T_{LN}M_{tg2}T_{LN}T_{LN-1}\dots T_{L2}T_{L1} \\
&+ \dots \\
&+ T_{L1}T_{L2}\dots T_{LN-1}T_{LN}M_{tgN_S}T_{LN}T_{LN-1}\dots T_{L2}T_{L1}
\end{aligned}
\tag{2.11}
$$

As a last functionality the ground scattering is realized by calculating the Stokes matrix for scattering from a rough surface M_g and accounting for the attenuation

caused by all layers:

$$M_g \quad = \quad T_{L1}T_{L2}\ldots T_{LN-1}T_{LN}M_g T_{LN}T_{LN-1}\ldots T_{L2}T_{L1} \qquad (2.12)$$

This procedure considers all scattering mechanisms contributing to the overall scattering. The Stokes matrix of the total backscatter M_{Total} can be found by summing the contributions of the four separate scattering mechanisms:

$$M_{Total} = M_b + M_{bg} + M_{tg} + M_g \qquad (2.13)$$

The four scattering mechanisms are assumed to be independent from each other, while the functionalities have a specified order of implementation and build on each other. Interspecies interaction is not included as scattering mechanisms of more than two scattering moments are considered to be small and can therefore be neglected [34]. Direct backscattering from trunks is also not included as it is expected to be extremely small. The multilayered multispecies model described above has been developed in a highly modular scheme to permit easy replacement of modeling mechanisms and application to any arbitrary combination of vegetation covers. The multispecies multilayer model is established in a modular manner such that it can read in any number of input parameters and build any forest with a number of N_S species. By setting the input parameters, the model can be adapted to other land cover types such as bare soil, grassland and shrubs. Examples of different land cover types and their representation with the discrete scatter model are given in Fig. 2.7. The color scheme is given in Fig. 2.8 where trunks are colored brown, small and large branches in green and leaves/needles in light green. More details on the leaves and needle parameters are provided in Fig. 2.9. The development of the above-ground vegetation model has been published [35–37].
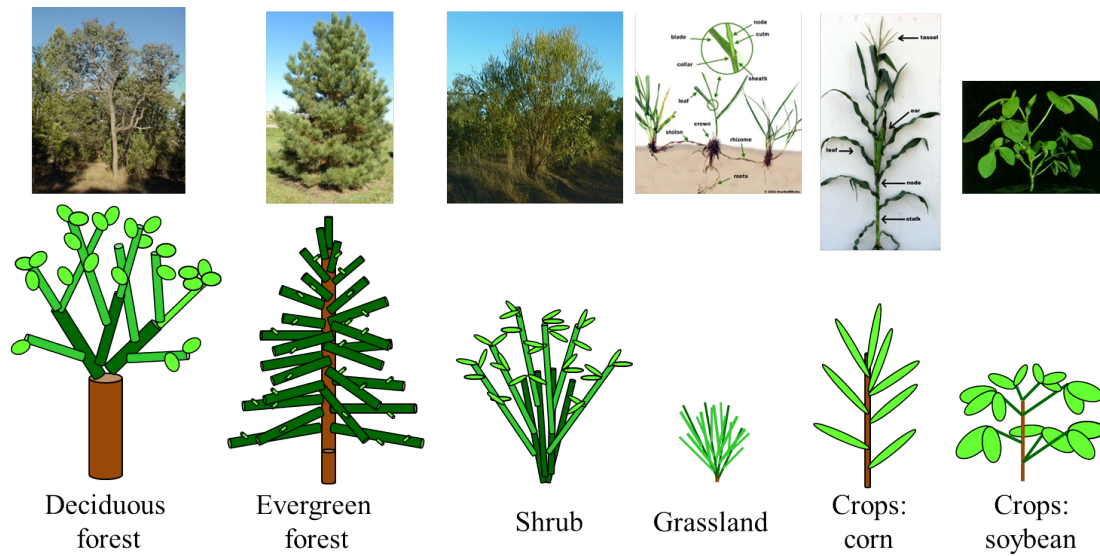
Figure 2.7: Overview over examples of land cover types represented by multispecies multilayered vegetation model by adapting parameters. Color scheme is given in Fig. 2.8.
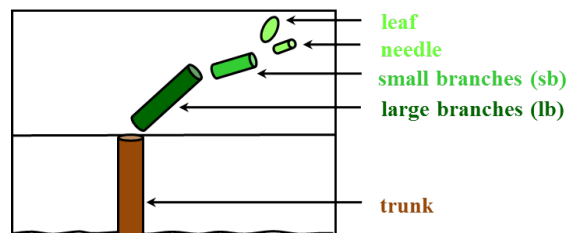
Figure 2.8: Color scheme for Fig. 2.7. Trunks are colored in brown, small and large branches in green and leaves/needles in light green.
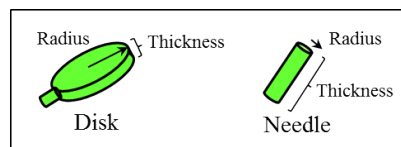
Figure 2.9: Parametrization convention for leaves and needles.

2.2.3 Model validation of multispecies vegetation over single half-space soil layer

Validation of the model is undertaken with reference to field data collected from the Tara Downs and the ICLP study area, both of which are located within the BBB of southeast Queensland, Australia. Within the BBB, a diversity of tree species exists; however, the forest is dominated by Brigalow (A. harpophylla). The extent of these forests has been reduced considerably due to heavy clearing following European settlement such that they now only occupy about 10 percent of their former range. While Brigalow dominates many forests, those that have remained undisturbed often contain other species such as Belah (Casuarina cristata), Eucalyptus species (e.g., E. melanophloia, E. cambageana), Bulloak (Allocasuarina luehmannii) and White Cypress Pine (Callitris glaucophylla).

Within the Tara Downs subregion in the western Darling Downs (27° 16' S, 149° 40' E to 27° 52' S, 150° 13' E), field data were available for 82 plots [38]. Many of the sampled forests were recovering from previous disturbance and a range of regrowth stages occurred, with several regarded as remnant (mature). Young regrowth is characterized as a single layer system supporting woody trees or shrubs of a similar size. However, as regrowth matures, the range of sizes increases and multilayered forests (e.g., with a canopy and shrub layer) become more common. Nine plots located within relatively homogeneous patches of brigalow-dominated forests and representing older regrowth and mature forests with two distinct layers were selected for this study. For each, simulations are based on appropriate parameterization (as described shortly) and conducted at L-band. The predicted backscattering coefficients are compared to fully polarimetric ALOS PALSAR data acquired in 2007 at a viewing angle of 21° (mid swath incidence angle of about 24°).

The ICLP is located within a 40 km x 60 km mixed forest/agricultural landscape west of the township of Injune (Latitude 25° 32' S, Longitude 147° 32' E). Within

Component	Parameter	Source	Component	Parameter	Source
Canopy	Depth [m]	Measurement	Vegetation	Dielectric constant	Destructive harvesting
Branches	Density [#/m^3]	Allometrics	Trunk	Density [#/m^2]	Allometrics
(small and	Length [m]	Measurement		Height [m]	Measurement
large)	Radius [m]	Measurement		Radius [m]	Measurement
	Orientation [deg]	Photographs	Soil	Dielectric Constant	Measurement
	(pdf) exponent	Photographs		RMS height [m]	Estimated
Leaves	Radius [m]	Measurement	Radar	Incidence angle ($^\circ$)	21.5/24°
					(AIRSAR/ALOS)
	Thickness [m]	Measurement		Wavelength [m]	C (0.056m), L (0.24m)
					or P (0.68m)
	Density [#/m^3]	Allometrics			

Figure 2.10: Parameters used as input to the multispecies multilayer model.

this area, the natural vegetation consists predominantly of low open woodland, open woodland, woodland, and open forest. Forests with Eucalyptus species dominate the more productive sandy and clay soils and White Cypress Pine (C. glaucophylla) occurs on the poorer sandy soils. On the clay soils, Brigalow is common and within the open forests of the plateau, Iron barks (e.g., Silver-leaved ironbark or E. melanophloia) are frequent. Details of the study site are found in [1] and [39]. In 2000, in-situ measurements of trees were undertaken within 34 50 m x 50 m plots located within forests common to the study area, as determined through reference to large scale (1:4000) stereo aerial photography acquired prior to field data acquisition. A wide range of measurements were undertaken to support the parameterization of SAR simulation models, details of which can be found in [1]. Fourteen of these plots representing multilayered forests typical to the area were considered for simulation, with backscattering coefficients then compared to JPL AIRSAR fully polarimetric C, L and P-band SAR data acquired in 2000 at the same time as field data collection.

For both sites, the model is parameterized using field measurements from a range of studies [1, 38, 40]. Allometric equations for estimating the biomass of plant components (trunk, branches and leaves) are also used. The input parameters for the multispecies multilayer model are listed in Fig. 2.10.

Parameters describing species geometry were obtained from digital photographs of individual trees and, for brigalow species, from TLS data. Parameters related to

dielectric properties of soils were obtained through direct measurement (e.g., of soil moisture) or from knowledge of soils within the study area.

For the ICLP, more details on the parameterization can be found in [1]. The soil RMS roughness is assumed to be 2.5 cm for all plots, obtained through referencing digital photographs. The dielectric constant for vegetation (large and small branches, leaves/needles and trunks) is assumed to be (12, 2) for C-band, (15, 2) for L-band and (25, 2) for P-band, based on values in previous publications [1]. The soil dielectric constant is assumed to be (2, 1) for both C- and L-band and (3, 1) for P-band as soils in the area are generally quite dry. The notation for the complex number for the dielectric constant is as follows: Re + j Im = (Re, Im). All of the plots supported at least one species, with the maximum number being five. The composition is provided by collaborators [1] and is given in Fig. 2.11. In some plots, the same species occurred in the overstory and understory, but the parameterization differed for each. In Fig. 2.11, the notation in the first column is as follows: PSU stands for "primary sampling unit" and SSU stands for "secondary sampling unit". Each PSU contained 30 SSUs, each of size 50 m x 50 m, arranged in a 10 x 3 rectangular grid. A visualization of three Australian tree species is shown in Fig. 2.12.

For the Tara Downs, five primary plots are selected that are considered to represent forests that were relatively expansive, homogeneous and supporting two distinct layers. The distribution of trees is described as over-dispersed (uniform; [41]). A second group of four secondary plots is also selected with these located on the boundary to cleared areas, and supporting less than 60 percent brigalow (in terms of the number of stems) and a more random distribution of trees. As the primary aim of the study [38] was not model parameterization, only a limited number of measurements had been collected. These measurements are typical of those measured in standard surveys such as tree height, stem DBH and number of trees in a plot. Through the use of data from separate surveys and published allometric equations [42], rela-

PSU_SSU	Total # of species	SLI	CP-	PBX	SBA	ANE	BRH	Other
23_15	5	2	2		1			
58_29	3	2		1				
81_8	4	1	1		1		1	
83_20	3	1	1		1			
111_12	3	1	2					
114_4	4		2		2			
114_12	4		1		2	1		
124_19	5	1	2		1			1
138_16	3	2	1					
142_2	1			1				
142_18	1	1						
142_20	1	1						
144_19	3	1	2					
148_16	3	1	2					

Figure 2.11: Overview of the species occurring within the plots studied, provided by collaborators [1]. These were Silver-leaved Ironbark (E. melanophloia; SLI), White Cypress Pine (C. glaucophylla; CP-), Poplar Pox (E. populnea; PBX), Smooth-barked Apple (Angophora leiocarpa; SBA), Mulga (Acacia aneura; ANE) and Brown Hazelwood (Lysicarpus angustifolius; BRH)

Figure 2.12: Visualization of Australian tree species: White Cypress Pine (left), Smooth-barked Apple (middle), and Silver-leaved Ironbark (right).

Plot	Total height (m)	Trunk height (m)	Total height (m)	Trunk height (m)	% Brigalow
	Species 1		Species 2		
3[1]	7.00	4.16	1.55	0.64	
31[1]	9.70	6.05	2.00	0.89	
47[1]	6.70	3.91	1.60	0.66	
51[1]	10.10	6.31	1.90	0.83	
52[1]	6.20	3.57	2.20	1.00	
44	10.32	6.47	2.55	1.21	79
48	8.95	5.49	2.05	0.92	89 thin[2]
61	8.70	5.31	2.29	1.06	70
63	13.6	8.87	2.89	1.41	65

Figure 2.13: Characteristics of Brigalow and other species within the 9 plots selected for simulation. ((1) Primary plots, all other plots are secondary; (2) Plot located within a narrow strip of forest).

Frequency [GHz]	1.25
Water temperature [C]	20
Salinity of water [4-35] (grams salt per kg water)	4
Specific density of the solid soil particles[g/cm3]	2.66
Empirically defined constant alpha	0.65
Bulk density[g/cm3]	1.55
Mass fraction of sand	0.40
Mass fraction of clay	0.50
Water volume fraction	0.05

Figure 2.14: Input parameters for Peplinski's model in [2, 3] for sites in the Tara Downs.

tionships were established allowing most model parameters to be estimated from the measurements taken.

The height characteristics of the forests for the Tara Downs are given in Fig. 2.13. Simulations for the Tara Downs are undertaken at an incidence angle of 24°, the same as that of ALOS PALSAR data acquired over this site. The ground is assumed to have a RMS surface height of 2.5 cm and its dielectric constant is calculated using the Peplinski *et al.* model in [2], [3]. All plots were located on Vertisol soils. The surface soil moisture was not measured, but provided by collaborators. Based on consultation with meteorological data, a volumetric soil moisture content of 5 percent is assumed. Additional parameters relating to the soil modeling are given in Fig. 2.14.

The correspondence between actual and simulated SAR data at HH, VV, and HV polarizations for all Brigalow sites is shown in Fig. 2.15. Each simulated case

corresponds to one physical stand in the field. To reduce speckle, which is inherently present in the radar image, an average over all pixels within and overlapping the plot was taken (about 50 pixels, dependent on plot size and orientation). In Fig. 2.15, the average, the minimum, and maximum of all pixels are recorded. For both primary and secondary sites, a close correspondence is observed at HH and VV polarizations. Such results suggest successful parameterization for a relatively homogeneous and dense forest structure with two species (i.e., the primary plots). At HV polarization, the simulations underestimated the backscattering coefficients. This is attributed to the current ground modeling, as it is based on the first-order SPM. This model does not produce any HV-polarized backscattering coefficient for the rough ground surface, meaning that the ground contribution to HV measurements are absent from the simulated values. The model predictions are therefore expected to be underestimated for this polarization.

Compared to the Tara Downs, the geometry and structure of forests within ICLP was more heterogeneous and ranged from sparse (managed) woodlands to relatively closed (up to 60 percent foliage projected cover or FPC; [43]) forest. For each site, the mean, minimum and maximum values of backscattering coefficients were extracted from a 5 x 5 pixel box centered on the location of the sampled plots. Even though the small size of the box may have biased the mean value, this strategy was chosen to balance heterogeneity in the forest structure against high speckle noise and to allow for more targeted comparison between simulated and actual SAR data.

The correspondence between simulated and actual SAR data is shown in Fig. 2.16 and 2.17. For C, L and P frequencies and at HH and VV polarizations, about 67 percent of simulations were within 3 dB of the actual AIRSAR data and about 80 percent within 4 dB (see Fig. 2.17). In the majority of cases, the simulated backscatter was within the range observed for the SSUs considered, with the best agreement noted for channels C-VV, L-HH, L-VV and P-HH. However, at HV polarizations,
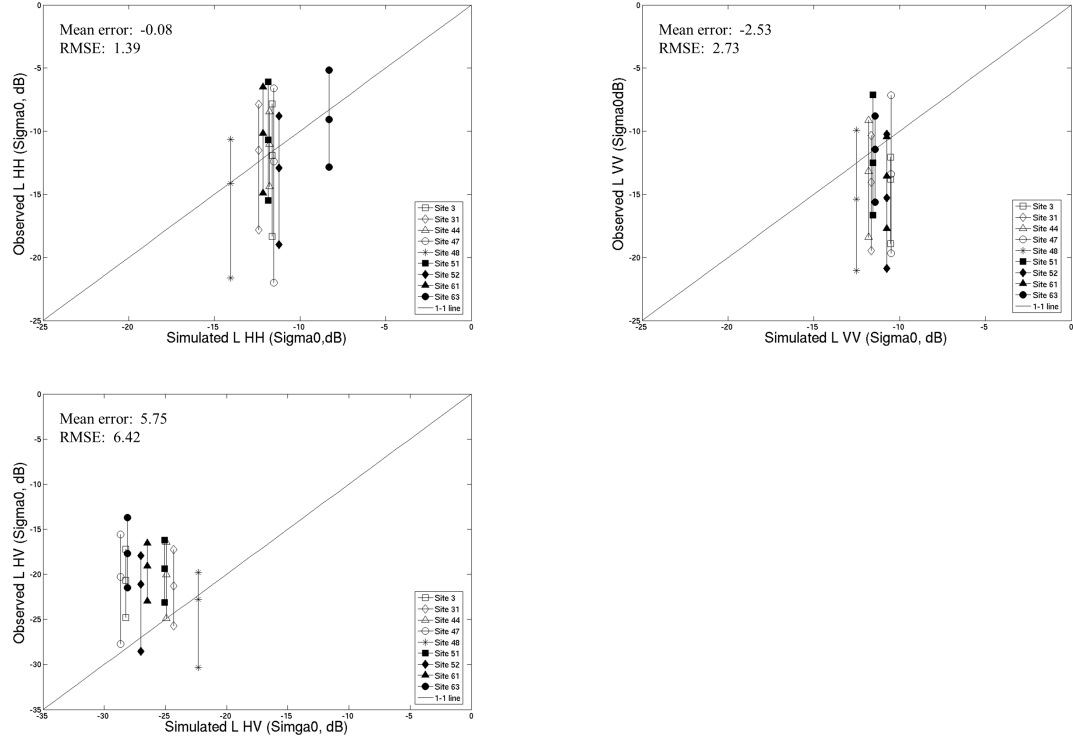
Figure 2.15: Comparison of ALOS PALSAR L-band HH (top left), VV (top right) and HV (bottom left) versus simulated backscattering coefficients for nine sites in the Tara Downs region. The average, minimum, and maximum of all pixels within and overlapping the plot are recorded. Good agreement is observed at HH and VV. The HV channel is underestimated by the model because of the lack of contribution to this channel from the rough ground surface first-order SPM.
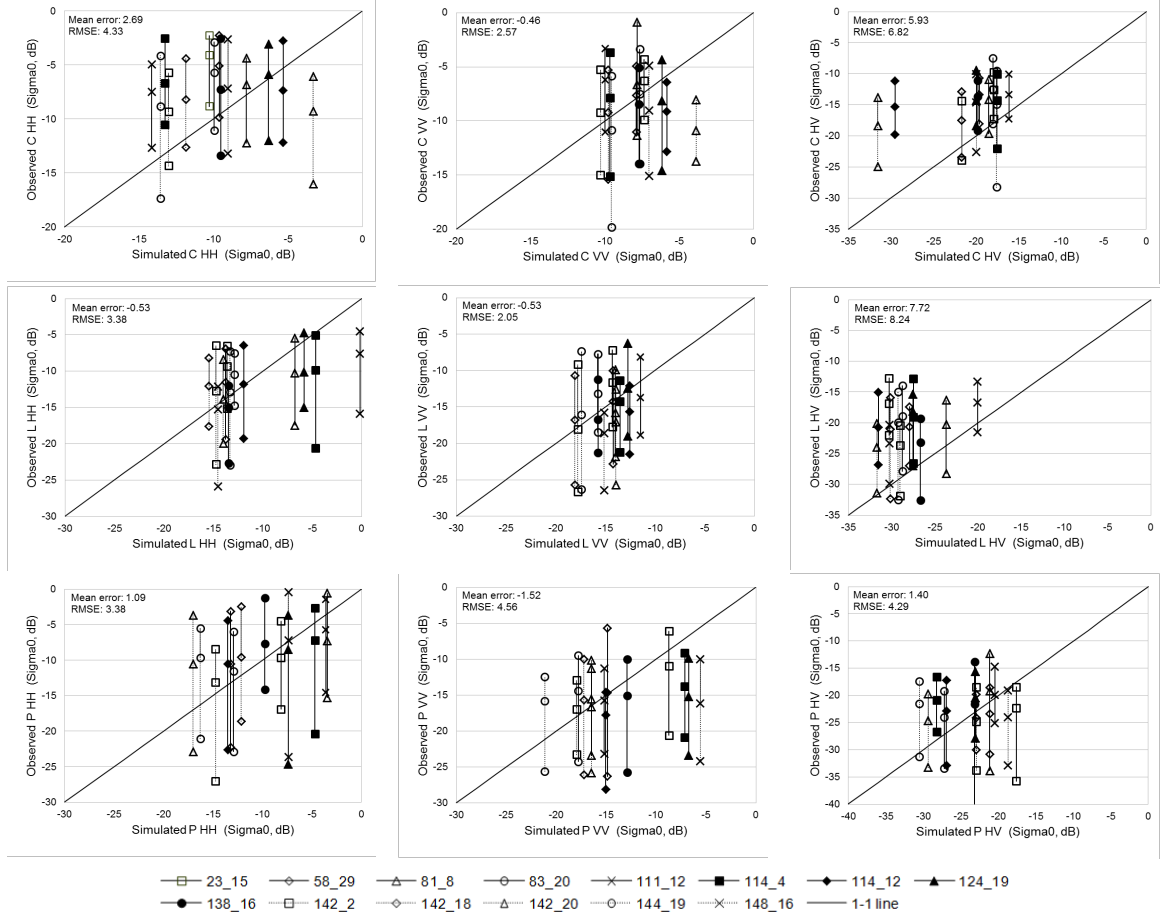
Figure 2.16: Correspondence between simulated and observed AIRSAR backscattering coefficient at C, L and P-band for fourteen sites with estimates of mean error (indicative of bias) and RMSE (indicative of correspondence). The RMSE assessment includes a small number of extreme outliers.

and particularly at C-band and L-band, a lower correspondence is observed. This can be explained by the current implementation of the rough surface model using the first-order SPM, which does not provide contributions at HV polarizations and under-represents ground surface scattering. This surface model also introduces inaccuracies at the HH and VV channels, and could also be partially responsible for errors in those channels at all frequencies.

The outliers observed for some channels, namely C-HH and HV, L-HH and P-VV, could be explained, in part, by uncertainties in the parameterization, variations within the terrain surface and changes in forest structure occurring between the times of field

PSU_SSU	C-HH	C-VV	C-HV	L-HH	L-VV	L-HV	P-HH	P-VV	P-HV
23_15	6.16	**1.06**	5.37	4.32	**2.69**	13.45	**-1.56**	**-2.22**	-4.74
58_29	4.53	**0.23**	6.26	**2.26**	**-0.01**	7.33	**2.69**	**0.18**	-2.29
81_08	**0.96**	**1.19**	4.39	**-3.47**	**-1.79**	3.45	**-3.84**	**0.94**	1.99
83_20	4.26	**0.14**	5.50	**2.42**	**2.61**	9.87	**1.33**	**3.37**	**3.16**
111_12	6.65	**3.80**	**2.78**	-7.40	**-2.21**	3.32	**-2.14**	**-0.56**	**0.59**
114_04	6.56	**1.82**	**3.24**	-5.19	**-0.74**	8.38	**-2.52**	-6.67	7.31
114_12	**-2.06**	**-3.30**	14.22	**0.13**	-3.09	10.82	**2.99**	**-2.76**	4.05
124_19	**0.40**	**-1.95**	5.63	-4.25	**0.31**	9.39	**-1.13**	-8.50	**2.60**
138_16	**2.23**	**-0.75**	6.10	**-1.52**	**-0.99**	**3.52**	2.10	-2.20	1.57
142_02	**3.70**	**1.07**	4.15	**2.01**	**-0.26**	5.35	**1.61**	**1.01**	-1.92
142_18	**3.64**	**0.58**	4.17	**3.42**	**1.28**	9.15	**2.52**	**1.55**	-1.16
142_20	-5.98	-7.03	13.14	**0.17**	-3.10	7.70	6.48	**-0.15**	4.69
144_19	4.72	**-1.27**	**2.70**	**0.44**	**1.38**	9.33	6.60	5.34	9.02
148_16	**1.84**	**-2.02**	5.39	**-0.70**	**-3.49**	6.96	**0.15**	-10.60	-5.30

Figure 2.17: Difference (in dB) between simulated and measured mean backscattering coefficients separated by frequency, polarization, and site. Largest discrepancies are observed for HV channels.

and SAR data acquisitions. For example, within several SSUs, large individuals of the species *A. leiocarpa* (SBA) occurred. This species typically supports a large, expansive crown but the number and dimensions of large branches contained are variable. Therefore, the use of allometric relations may not provide realistic parameterization in all cases and could explain discrepancies between actual and simulated SAR in some channels and for some SSUs (e.g., 114_4, 114_12, 23_15, 124_19). A dry river bed with steep banks was contained within SSU 144_19, which would explain the higher returns at lower frequencies in particular. Differences between actual and simulated backscattering coefficients within SSU 142_20 may be attributable to loss of trees due to harvesting immediately adjacent to the SSU between the time of field data collection and the AIRSAR overpass. Sites 81_8 and 138_16 were modeled best, with these supporting larger trees, and three and four species, respectively.

To provide insight into the main scattering mechanisms occurring, a subset of three sites (142_18, 58_29 and 23_15) was selected. The sites selected differ in their species composition, varying from one species (142_18; SLI), three species (58_29; SLI and PBX, with SLI also present in the understory) and five species (23_15; SLI, CP-(overstory and understory) and SBA). TLS of forests located in proximity to 142_18
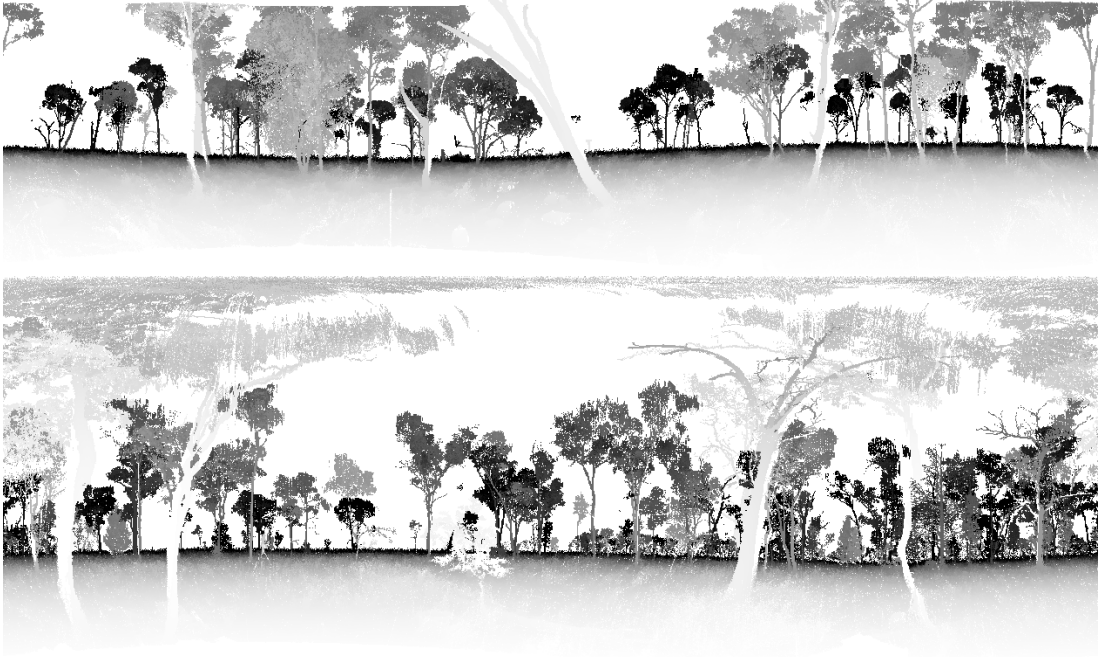
Figure 2.18: TLS of forests located at PSUs 142 (top) and 58 (bottom).

and in 58_29 are provided in Fig. 2.18. The contribution of the main scattering mechanisms (B, BG, TG and G) to the total for each forest is depicted in Fig. 2.19. The branch layer contribution is given as the summation of the total branch scattering coefficient of all branch layers.

At C-band, and at all polarizations, the radar backscatter is almost entirely attributable to branch layer (volume) scattering for all three sites, with some contribution of the ground at HH and VV polarizations. These observations agree with the findings of [18] and [1]. At C-band, the incident wave can not penetrate into the canopy beyond the branch layer, especially in forests with a high canopy cover and/or thick branch layer. Modeling of C-band backscatter is therefore sensitive to appropriate parameterization of the canopy layer as there is little influence from plant elements in the lower layers. Branch-ground and trunk-ground double bounces are very small and negligible.

At L-band, waves penetrate deeper into the forest resulting in greater interaction with the woody components (branches and trunks). At L-band HH, the primary
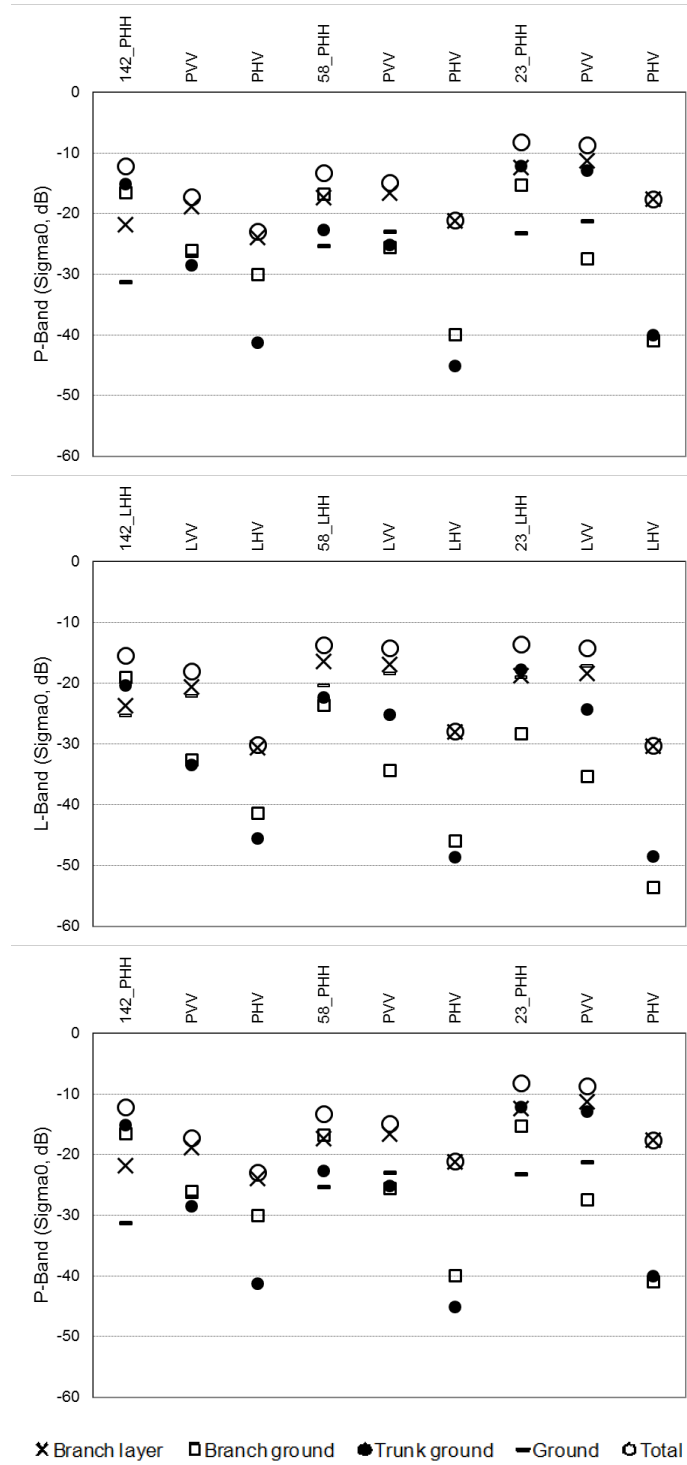
Figure 2.19: Contributions of four scattering mechanisms to the total backscatter at C, L and P-band for a subset of three sites (142_18, 58_29 and 23_15).

contribution for SSU 23_15 is from trunk ground, but also crown volume scattering. However, for 58_29 and to a lesser extent 142_18, interactions between the branch and ground and with the ground and trunk layer are more apparent, reflecting the more open nature of the canopy. The forest at 58_29 supports an increased density of scattering elements as well as a greater diversity of species compared to 142_18, and branch volume scattering therefore dominates compared to branch-ground and trunk-ground scattering.

At P-band, differences in the contribution of the four scattering mechanisms are more evident. At HH polarizations, trunk-ground scattering is more dominant due to the greater penetration of waves through the canopy and subsequent interaction with the ground layer, although some branch-ground interactions can be observed within 58_29. At VV and HV polarizations, scattering from the branch layer dominates, with minimal interaction with the trunks. At 23_15, branch-ground and branch scattering are also relatively strong, with this attributed to greater complexity of the forest volume (five different species and a dense forest structure).

The same parameters are used here as with the study of [1], although the AIRSAR data for the present study are extracted from a more confined area associated with each SSU to maximize the spatial correspondence between the ground measurements and the simulation domain. The present study also considers several more plots, which were too complex to be simulated with the simpler model used in [1]. Compared to [1], a greater correspondence between actual and simulated data is observed at HH and VV polarizations in the current model. It is also possible to simulate stands with an arbitrary number of species (five species was the maximum number present in the study area), as opposed to only 3 species in [1] beyond which the simple approach of that paper was deemed unsuitable. The contribution of the different scattering mechanisms is similar to those observed by [1], with HV polarized returns largely dependent on volume scattering from the leaves and branches within the canopy

layer at C, L and P-band respectively. Double bounce scattering between the trunk and branch layer is most evident at HH polarizations (at L- and P-band) while the VV polarization response is primarily the result of branch layer but also ground scattering (particularly at C-band, but progressively reducing at lower frequencies).

Simulations of SAR backscatter are difficult to validate due to the errors associated with the model inputs, the model itself, and additionally SAR calibration and post-processing. The increased number of species and/or growth stages, up to five species within the considered forest stands, leads to a more complex geometry and size class distribution of plant elements, which are difficult to describe. Therefore, only an abstraction of the structural complexity can be provided. Nevertheless, greater opportunities now exist for model parameterization with the advent of TLS, an example of which is provided in Fig. 2.18. TLS has been successfully used by collaborators to automate the process of measuring forest structure and geometry parameters. Future studies should therefore focus on establishing the trade-off between simplifying descriptions of forest structures and providing a full inventory using, for example, TLS. Other errors are introduced through approximation of the dielectric constants for soil and vegetation. The conducted sensitivity analyses indicated that the moisture content of the soils could have a disproportionate impact on the overall backscatter, which has also been observed in actual field observations, including those in Australia [44]. Obtaining measurements of dielectrics at the same time as the overpass of the SAR is difficult and hence rarely undertaken. Nevertheless, such information needs to be collected more routinely to better understand the impacts of changes in moisture content on the overall SAR backscatter and the relative contribution of the different scattering mechanisms. When comparing simulated and actual SAR data, the area from which values are extracted must be considered and misregistration and georectification errors reduced as these compound problems associated with pixel type and location. A further source of error is the calibration of the SAR instrument. For

example, AIRSAR is quoted as having typically an absolute calibration accuracy of $\pm$ 1.5 dB. The use of the 3 dB and 4 dB difference criteria to assess the robustness of the modeling is therefore considered a realistic measure. The close correspondence between actual (both ALOS PALSAR and AIRSAR) and simulated backscatter at HH and VV polarizations for the sites studied is encouraging, although further attention needs to be given to the ground surface model and hence the simulation of the HV backscattering coefficient.

2.2.4 Further improvements on the multilayered multispecies vegetation model

To round off the generalization of the vegetation model, trunk averaging and trunk tapering capabilities are implemented. The trunk averaging capability ensures that the chosen trunk diameter does not lead to a resonance behavior. Instead, the scattering mechanisms are averaged over a range of trunk radii. The implementation of the trunk tapering utilizes the geometrical structure of the generalized multispecies multilayer model. For N_S species there are $2 N_S$ vegetation layers, and by defining the DBH of each vegetation layer from bottom to top with a slightly smaller value, a simple trunk tapering can be implemented. This approach is more accurate with an increasing number of species. Currently trunk averaging is enabled, however tapering is not used for model validation.
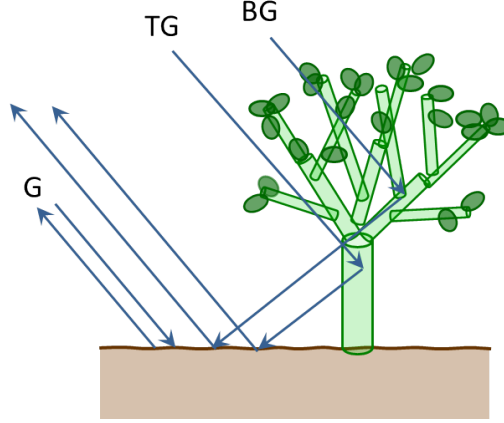
Figure 2.20: Visualization of two scattering mechanisms containing ground contribution: direct ground (G), trunk-ground double bounce (TG) and branch-ground double bounce (BG).

2.3 Ground surface and subsurface scattering model at fine-scale pixels

2.3.1 The modeling improvements to the ground surface and subsurface modeling

An integral part of a forest scattering model is the model for the underlying ground. As shown in Fig. 2.20, there are two scattering mechanisms that contain ground contribution: direct ground scattering (G) and double bounce scattering for trunk-ground (TG) and branch-ground (BG). The model in [19] and the aforementioned generalized radar backscattering model based on wave theory for multilayer multispecies vegetation [37] realize the direct ground backscattering with a first-order SPM assuming a single half-space soil layer. For the double bounce cases, the ground surface reflection coefficients or Fresnel reflection coefficients are modified by the presence of surface roughness, as derived in [29]. These are used to form the scattering matrix of double bounce backscatter for a tilted cylinder above a ground surface in terms of the old scattering matrix elements as given in Eq. (2.3).

The first improvement to the below-ground modeling is the inclusion of the second-

order terms of the SPM for the direct backscattering term as given by Tsang and Kong [30]. This allows a more accurate modeling of the HV contribution from the ground. The implementation of the second-order terms of the SPM has been validated with published results. Since the second-order SPM is only an intermediate step in the improvement of the below-ground modeling, the validation results are not shown here. The second improvement is related to the subsurface representation. The assumption of a single soil layer is unrealistic since soil may have many horizons, texture interfaces, and a depth-varying moisture profile. The increased penetration depth of lower frequencies further weakens the homogeneous half-space assumption. Therefore, a more accurate modeling of the sub-surface domain is required. The multilayer soil model based on first-order SPM [45] has the capability to model an arbitrary number of soil layers with different soil texture, soil moisture profiles, and layer thickness. The coefficient for the direct ground scattering is defined as:

$$
\begin{aligned}
\sigma_{pq}^o &= 4\pi k_o^2 \cos\theta_s \xi^2 (\left|\alpha_{pq}^{f_1}(k_\perp^s)\right|^2 W_{f_1}(k_\perp^s - k_\perp^i), \\
&\quad + \left|\alpha_{pq}^{f_2}(k_\perp^s)\right|^2 W_{f_2}(k_\perp^s - k_\perp^i))
\end{aligned}
\tag{2.14}
$$

where $\alpha_{pq}^{f_i}(k_\perp^s) = \alpha_p^{f_i}(k_\perp^s)$ with the incidence field being $\hat{q}(-k_{0z}^i)$. $W_{f_1}(k_\perp)$ and $W_{f_2}(k_\perp)$ are the power spectral densities of the rough boundaries. More details are given in [45]. To represent the soil moisture profile as a layered structure for the double bounce cases, the closed-form expression of the Fresnel reflection coefficient of an equivalent stratified medium is derived. This Fresnel reflection coefficient is then modified by the presence of the surface roughness of the top soil layer. This approach disregards possible roughness at the soil layer interfaces, which could have a significant impact, but also allows the definition of a depth-varying moisture profile. This is visualized in Fig. 2.21 on the left.

With the development of a coherent scattering model, the double bounce mecha-
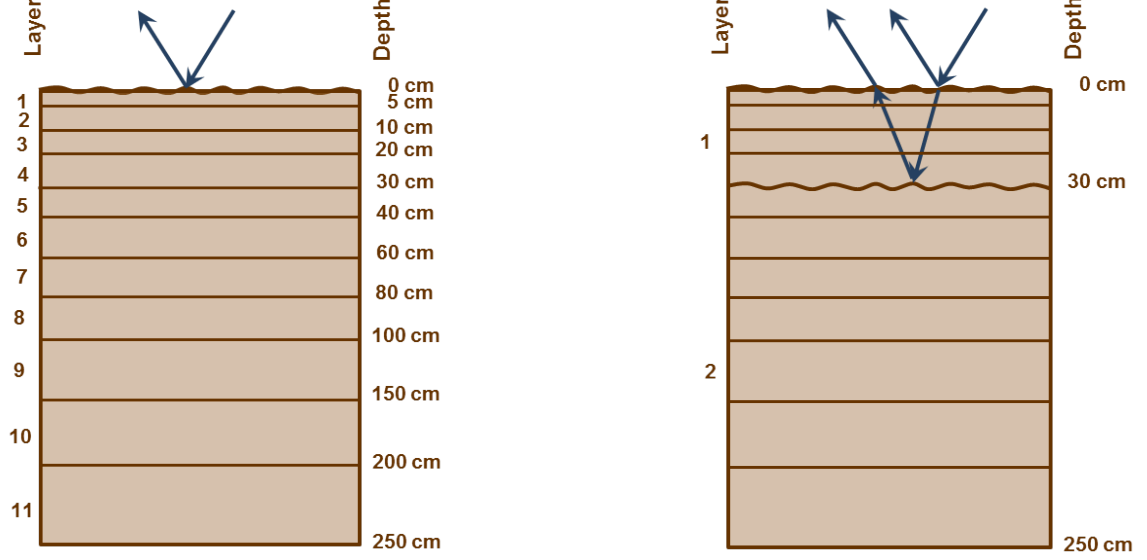
Figure 2.21: Two structural representations of subsurface soil layers: N-layered soil with surface roughness (left) and N-layered soil with two-layered roughness interface (right).

nism of a two-layered rough structure can be modeled in presence of a multilayered soil structure [46]. The reflection coefficient of the multilayered ground can be defined as:

$$
\begin{aligned}
\tilde{R}_p &= \tilde{R}_{p01} + \frac{\tilde{T}_{p01}\tilde{R}_{p12}\tilde{T}_{p10}exp(i2k^i_{1z}d)}{1 + \tilde{R}_{p12}\tilde{R}_{p01}exp(i2k^i_{1z}d)}, \\
\tilde{R}_{p01} &= R_{p01}\,exp(-2k^{i}_{0z}{}^2 h_1^2), \\
\tilde{R}_{p12} &= R_{p12}\,exp(-2k^{i}_{1z}{}^2 h_2^2), \\
\tilde{T}_{p01} &= T_{p01}\,exp(-\frac{1}{2}(k^i_{0z}-k^i_{1z})^2 h_1^2), \\
\tilde{T}_{p10} &= T_{p10}\,exp(-\frac{1}{2}(k^i_{0z}-k^i_{1z})^2 h_1^2)
\end{aligned}
\tag{2.15}
$$

The reflection coefficient resembles that of a dielectric slab modified with an exponential term. More details are given in [46]. A visualization of the two-layer rough subsurface structure combined with the N-layered soil is shown in Fig. 2.21 on the right.

39

2.3.2 Model validation of single species vegetation on multilayered soil

Validation of the model is conducted with field data from the Boreal Ecosystem-Atmosphere Study (BOREAS) collected in the Canadian Boreal forest north of Prince Albert in Saskatchewan, Canada. Vegetation measurements of homogeneous forests, such as OJP and YJP, were collected in 1994 [26] and are used in this study. Missing vegetation parameters are assumed based on parameters collected during field work at the same site during the Canadian Experiment for Soil Moisture in 2010 (CanEx-SM2010) [47]. For OJP small branch length is set to 0.5 m and for YJP it is set to 0.25 m. A surface soil roughness of 2.5 cm is assumed. The OJP and YJP forest stands in 1994 are shown in Fig. 2.22. The available radar data is L-band AIRSAR data from 29 June 1994 for HH, VV and HV (CM5283) as shown in Fig. 2.23. Soil moisture profiles are available at locations around the flux tower site: five profiles at OJP and six profiles at YJP. These soil moisture profiles are available from the Oak Ridge National Laboratory (ORNL) Distributed Active Archive Center (DAAC) [48]. An example soil moisture profile is shown in Fig. 2.24. Soil texture profiles are available at locations around the flux tower: four profiles at OJP and three profiles at YJP. The soil texture profiles are also available from the ORNL DAAC [49]. The soil texture profiles show vertical homogeneity with a soil composition of 40% sand, 50% clay and a bulk density of 1.55 $\frac{g}{cm^3}$ for both sites. The other parameters necessary for the Peplinski *et al.* model [2, 3] are chosen as soil temperature of 10 degrees and soil salinity of 4 grams per kg water.

The vegetation and soil information collected during BOREAS is used to parameterize the multispecies multilayered soil model. The multispecies multilayered soil model is set to model a single-species forest in this case. Groups of five by five pixels around the two sites are averaged and compared to the forward simulated model. The comparison can be seen in Fig. 2.25. The root mean square errors ($RMSE_{HH}$, $RMSE_{VV}$, $RMSE_{HV}$) are relatively small with (0.89, 0.69, 5.46) for OJP and (2.18,
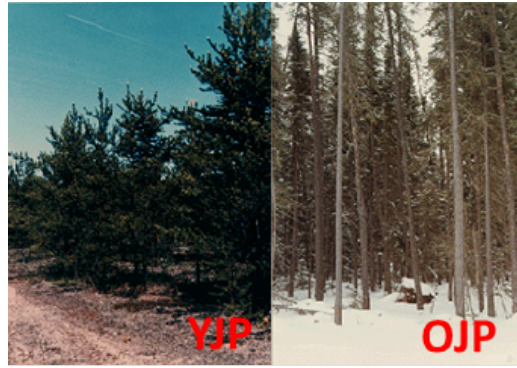
Figure 2.22: Visualization of OJP and YJP site in BOREAS.
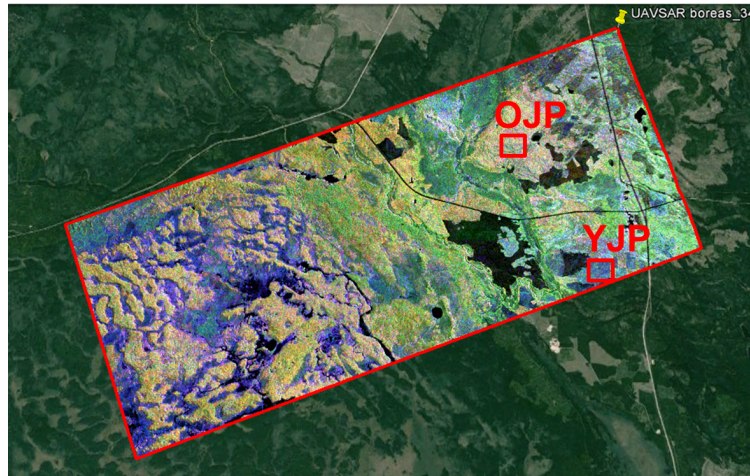
Figure 2.23: L-band AIRSAR data from 29 June 1994.
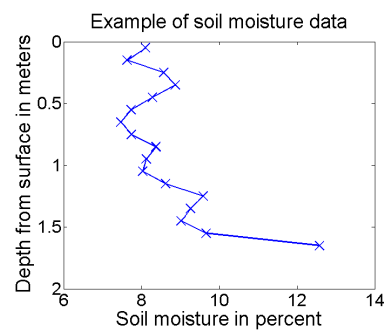
Figure 2.24: Example soil moisture profile at OJP for 29 June 1994.
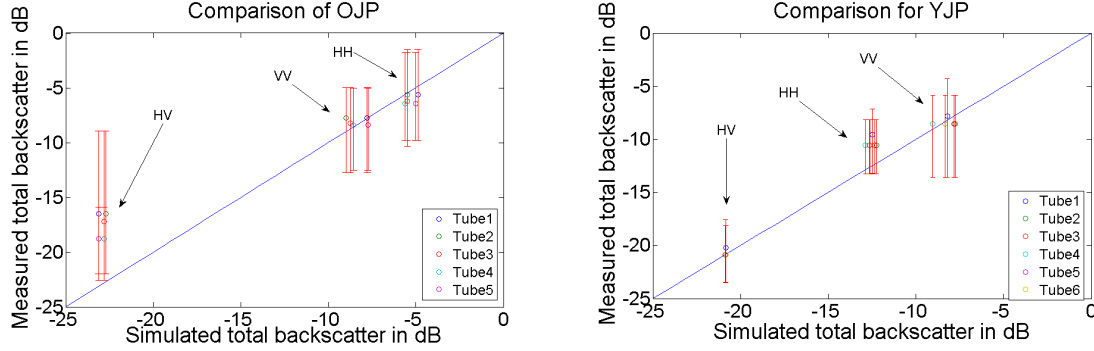
Figure 2.25: Comparison of simulated and measured AIRSAR radar backscatter in HH, VV, HV for OJP (left) and YJP (right) for 29 June 1994.

0.53, 0.27) for YJP.

2.3.3 Model validation of multispecies vegetation on single-layered soil with tower radar data

Validation of the model for a multispecies vegetation on single-layered soil is conducted with seasonal forest measurements at the University of Michigan Biological Station (UMBS) in Pellston, MI. An overview of the site can be seen in Fig. 2.26. Beginning in 2011, radar measurements were collected in October, November, April (2012) and July (2012) with a tower based radar [4]. Measurements were collected at frequencies of 1 GHz (L-band) and 435 MHz (P-band) at an incidence angle of 45°. The tower radar illuminated an area of approximately 25 m x 25 m with a tower height of 26.3 m. Soil moisture sampling using a Trase TDR 40 cm probe has been conducted along transects of the radar footprint during the radar measurements. The soil moisture averaged over the transects increased from 8.07% in October 2011 to 13.51% in November 2011, and then decreased to 10.54% in April 2012 and 6.17% in July 2012 [50]. A visualization of the seasonal vegetation at the radar footprint can be seen in Fig. 2.27. More details of the radar measurements, field work in 2011/2012 and the soil moisture sampling technique are given in [4].

In May 2013, the site was revisited to conduct measurements of the vegetation

Figure 2.26: Google Earth image of the UMBS site with radar tower, two transects of May 2013 field work and flux tower location.

Figure 2.27: Seasonal variations in canopy at UMBS (top left: October 2011; top right: November 2011; bottom left: April 2012; bottom right: July 2012).

within the footprint of the radar, shown in Fig 2.28. Two transects with a length of 60 m were overlaid on the soil moisture transects from 2011/2012 and all trees within $\pm$ 1 m of the transect line and with a DBH of more than 1 inch were recorded. For each tree, the DBH, total height, trunk height, number of primary and secondary branches as well as minimum and maximum primary branch angles were recorded. Five major tree species were observed in the radar footprint, namely Populus grandidentata (Aspen), Betula papyrifera (Birch), Pinus strobes/resinous (Pine), Quercus rubra (Oak) and Acer rubrum/saccharum (Maple). Examples of the collected data are shown in Fig. 2.29. The distribution of total tree height and trunk height over DBH is shown at the top of the figure. It can be seen that the site consists of a mature and a young cluster of trees, which again can be divided into evergreen (pine) and deciduous (aspen, birch, oak, maple) clusters. Due to the difference in geometrical structure between evergreen and deciduous trees, this mixed forest site is modeled as a combination of mature evergreen and mature deciduous forest with a young evergreen and young deciduous forest. The measured values for the four different types are averaged and are shown with black markers in Fig. 2.29. The number of primary and secondary branches are included in the middle of the figure. It is worth noting that the evergreen clusters show higher numbers of branches. The minimum and maximum branch range for the primary branches are shown at the bottom of the figure. The dielectric constant of the vegetation are taken from the SMAP Validation Experiment 2012 (SMAPVEX12) campaign, discussed in more detail in Appendix A. The soil consists of well-drained spodosols with a composition of 92% sand, 1% clay, 7% silt and a bulk density of 1.28 $\frac{g}{cm^3}$. A surface soil roughness of 2 cm is assumed. Other vegetation parameters not measured during field wok in May 2013 were deduced from photographs.

The uncalibrated measured P-band tower radar data is shown on the left in Fig. 2.30. The calibration of the radar data proved to be challenging due to the

Figure 2.28: Field work in May 2013 at UMBS. Figure on left: folded tower radar with view on radar footprint (behind radar). Figure on right: measurement in the radar footprint.
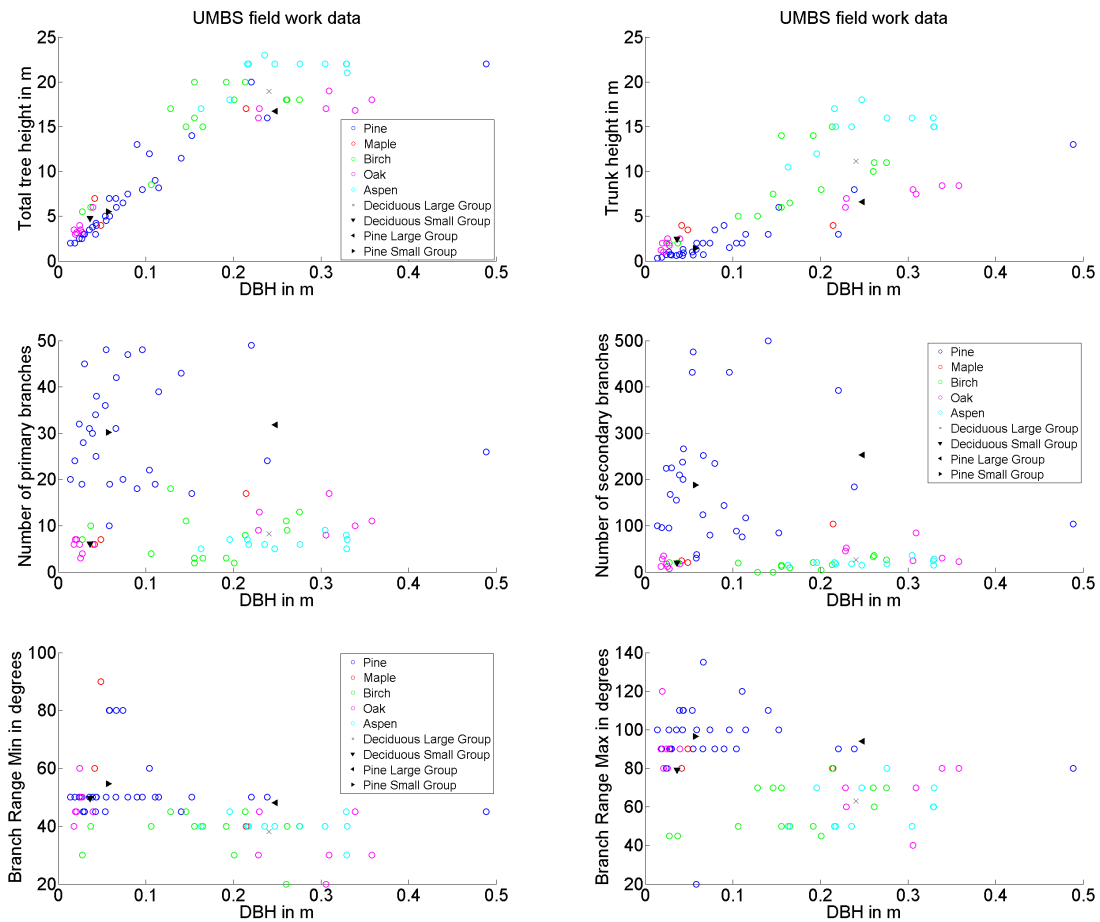
Figure 2.29: Collected field data from May 2013 at UMBS: Total tree height and trunk height in meters over DBH (top), number of primary and secondary branches over DBH (middle), minimum and maximum mean orientation angle for primary branches in degrees over DBH (bottom). Legends apply to all figures.
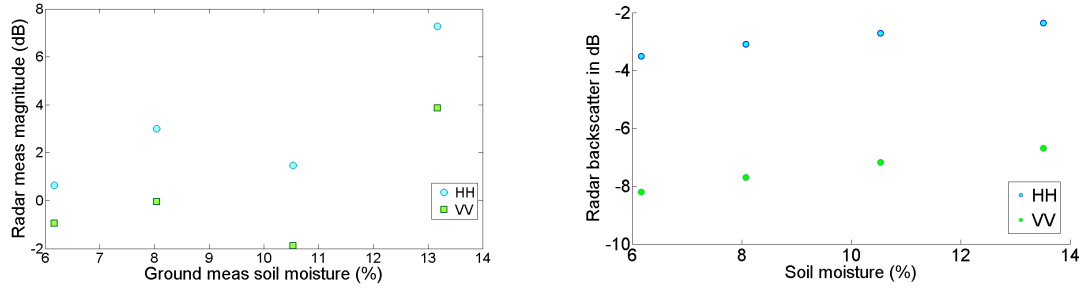
Figure 2.30: Radar backscatter coefficient in dB over measured soil moisture for P-band at UMBS. Figure on left extracted from Duan and Moghaddam [4] showing uncalibrated measured backscatter over measured soil moisture. Figure on right: simulated radar backscatter coefficient over measured soil moisture.

lack of adequately sized corner reflectors and the short measurement distance for P-band [4]. Therefore, it is not possible at the present time to directly compare the simulated radar backscatter coefficients with the measured radar backscatter coefficients. The measured vegetation parameters are used to parameterize the multispecies radar model with multilayered soil with the respective soil moisture values as observed during the field work in 2011/2012. The simulated radar backscatter coefficients are shown on the right in Fig. 2.30. The overall trend is similar, although the April 2012 measurement seems to be an outlier, as observed in [4]. The bias between the measured and simulated radar backscatter coefficient due to the uncalibrated measured radar backscatter is shown in Fig. 2.31. The uncalibrated radar data is expected to show higher values than the calibrated data, but the difference is not a linear bias due to the calibration. The radar instrument team is planning to address the calibration of the radar data in the future permitting absolute validation of the forward modeling work.
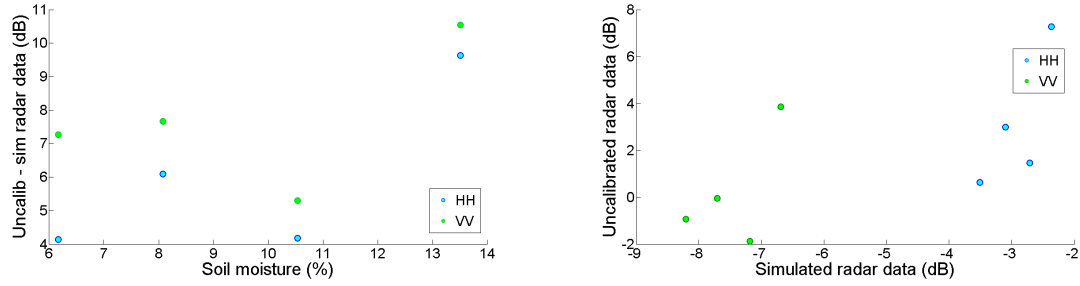
Figure 2.31: Bias between the measured and simulated radar backscatter coefficient at UMBS. On left: bias between measured uncalibrated and simulated radar data in dB over soil moisture in percent at P-band. On right: comparison of measured uncalibrated and simulated radar data in dB.

2.3.4 Model validation of multispecies vegetation on single-layered soil with airborne data

Validation of the multispecies vegetation model on multilayered soil is undertaken with the collected data from SMAPVEX12. Details to the ground sampling methodology, collected ground data over the forested sites and the used UAVSAR data are included in Appendix A.

The UAVSAR data is linearly averaged over a 200 m by 200 m area covering the orthogonal transects for each site. Figure 2.32 shows the comparison of UAVSAR data for all four sites (HH in dB) with hand-held soil moisture. At the beginning of the campaign, the conditions were very wet, followed by a steady dry down and rainfall events near the end of the campaign, as shown in Fig. A.8. The precipitation trend is clearly visible, especially for site F1. The radar data of 27 June seems to be an outlier for all flight lines and sites, although no problems have been reported with this flight date. It will be excluded in the following analysis.

The initial comparison of UAVSAR data and forward simulation of site F1 shows a potential problem with channel imbalance. The VV radar data channel also shows a dampened incidence angle effect as can be observed in Fig. 2.33. The figure shows the simulated and measured HH and VV channels over a simulation number (all dates from beginning to end of campaign with their incidence angles strung to-
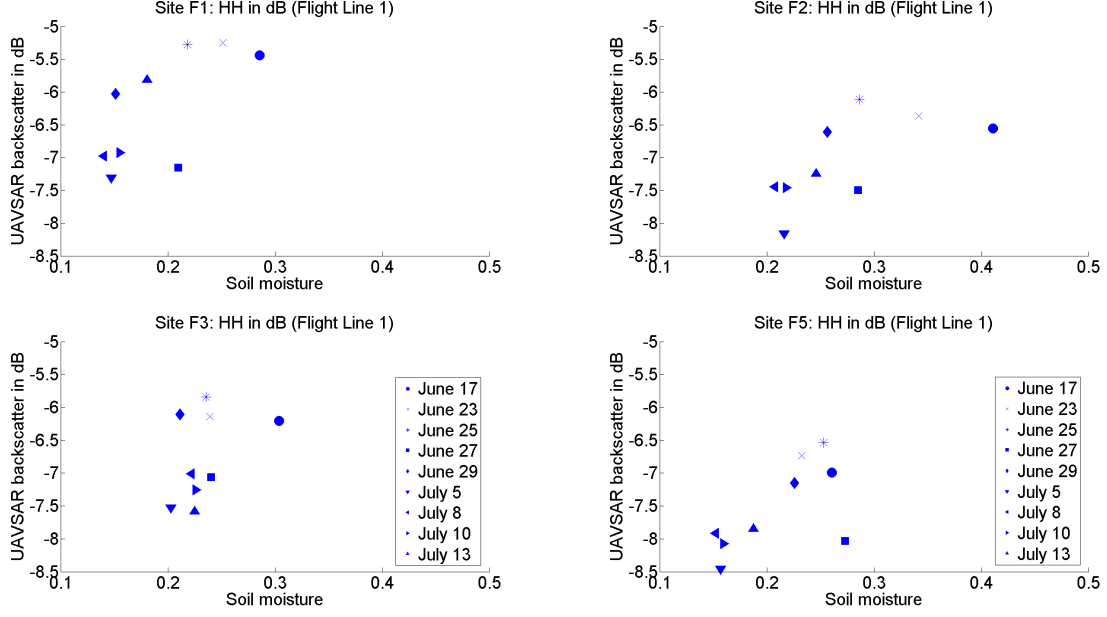
Figure 2.32: Comparison of UAVSAR data collected during SMAPVEX12 for all four sites (HH in dB) with hand-held soil moisture.

gether). The jagged pattern is due to a change in incidence angle between the four flight lines $(30°, 40°, 48°, 54°)$. The comparison between simulated HH and measured HH UAVSAR data is very good and the incidence angle behavior is well reflected in the modeling. The measured VV backscatter shows a decreased incidence angle dependence, especially during the middle of the campaign. The modeled VV backscatter does not reflect this behavior. This issue has been addressed to the JPL UAVSAR group, and for the current analysis the VV channel is excluded. Only the UAVSAR HH channel is compared to forward simulations.

Figure 2.34 shows the vegetation at the four forested sites F1, F2, F3 and F5 and Fig. 2.35 shows the comparison of height over DBH for each species for each site. Figure 2.36 shows the comparison of simulated radar data over measured UAVSAR data for each site. Hand-held soil moisture measurements collected during overflight days are used to define a uniform soil moisture profile for this comparison. In the following each site is discussed separately starting from the most simple forest F1 to the most complex forest F5.

48
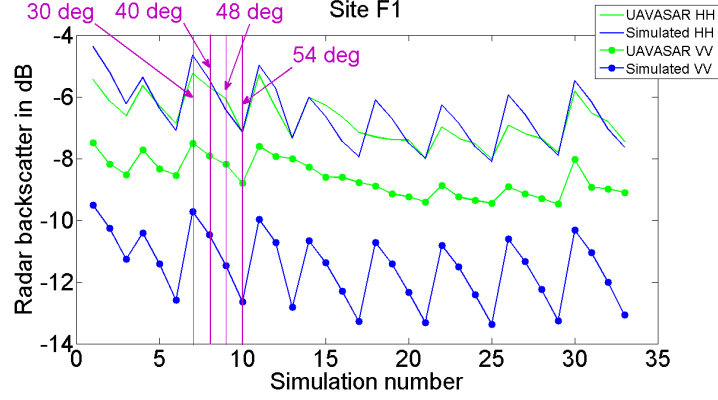
Figure 2.33: Comparison of UAVSAR radar backscatter in dB with simulation number for site F1 (each date consists of four incidence angles).

Site F1 is a sparsely forested, homogeneous, single-species forest with minimal understory on a dry and sandy soil. The forest consists only of trembling aspen trees, which can also be observed in the height over DBH figure. This permits modeling this site as a single-species forest over a single soil layer as indicated by the intersection of the black lines in the height over DBH figure. The forward model compares very well with the UAVSAR data with a mean difference of 0.2 dB and an RMSE of 0.53 dB.

Site F2 is more varied with a complex and multispecies forest with significant understory. This can clearly be observed in the height over DBH figure, which shows a first cluster of trembling aspens and a second cluster of understory. Therefore, this site is modeled as a two-species forest over a single-layered soil. The soil is sandy, yet contains more water than site F1. The comparison of the forward model with the UAVSAR data is reasonable with 0.25 dB mean difference and 0.44 dB RMSE.

Site F3 is again a complex and dense single-species forest with varying growth stages and significant understory. The height over DBH figure shows mainly trembling aspen. Modeling this site as a single-species forest is not realistic due to the significant age spread within the trembling aspen. Therefore, the site is modeled as a two-species forest where the two "species" are two growth stages. The comparison of forward

49

model with UAVSAR data shows some bias. The mean difference is 0.84 dB with an RMSE of 0.92 dB.

Site F5 is the most diverse site with a complex, multispecies forest and sparser drier areas with various degrees of understory. The height over DBH figure shows a large cluster of trembling aspen as well as a secondary understory group. Therefore, this site is modeled as a forest with two species, one of them with two age groups over a single layered soil. The soils are sandy, yet with increased water content under denser canopy and drier under sparser canopy. The simulated data compares well with the UAVSAR data with a mean difference of 0.06 dB and an RMSE of 0.49 dB.

The comparison of simulated radar backscatter with the measured UAVSAR data for all sites is shown in Fig. 2.37. Hand-held soil moisture measurements collected during overflight days are used to define a uniform soil moisture profile for this comparison. The simulated data agree well to the measured with a mean difference of 0.34 dB and an RMSE of 0.63 dB. This comparison shows the full capability of the multispecies vegetation model on top of a multilayered soil.

The study of modeling complex multispecies forests with multilayered soil reveals the necessity for modeling complex dense forests as multispecies vegetation. Multispecies vegetation can consist of different species or a single species with different growth stages. The measurements of the volumetric water content of the organic layers (litter and organic soil) have yet to be processed. Including this information into forward modeling in the future might improve results. Future work also includes clarification of the discrepancy previously noted with the UAVSAR VV channel.

2.3.5 Further improvements on surface and subsurface modeling

All modeling validations use the dielectric soil model by Peplinski *et al.* [2, 3]. The alternative model by Mironov *et al.* [51, 52], formally known as the Mineralogy-Based Soil Dielectric Model (MBSDM), is used by the SMAP algorithms group and is imple-

Figure 2.34: Four forested sites F1, F2, F3, F5 (from top left to bottom right).
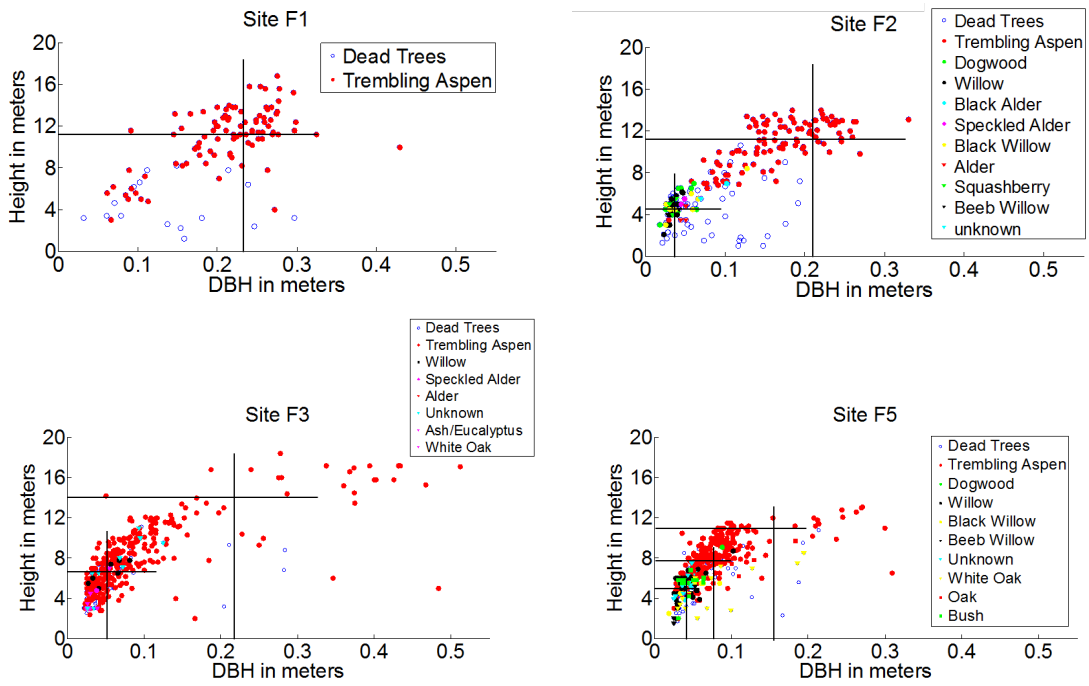
Figure 2.35: Comparison of height in meters with DBH in meters for four sites F1, F2, F3, F5 (from top left to bottom right).
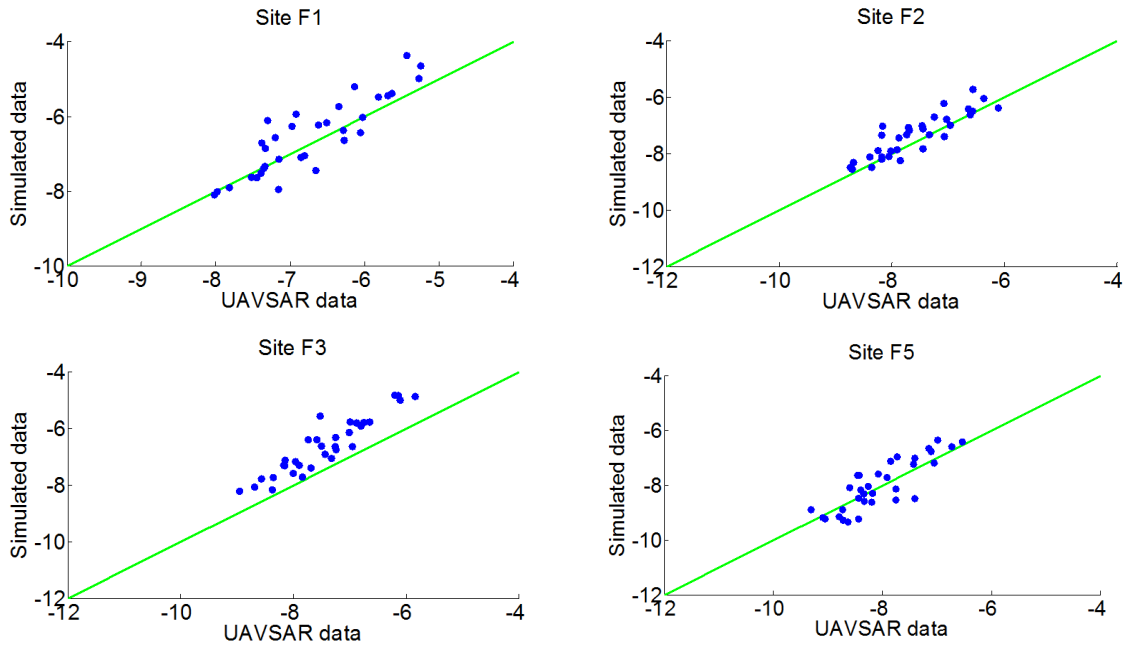
Figure 2.36: Comparison of forward simulated HH with UAVSAR HH data (in dB) for four sites F1, F2, F3, F5 (from top left to bottom right).
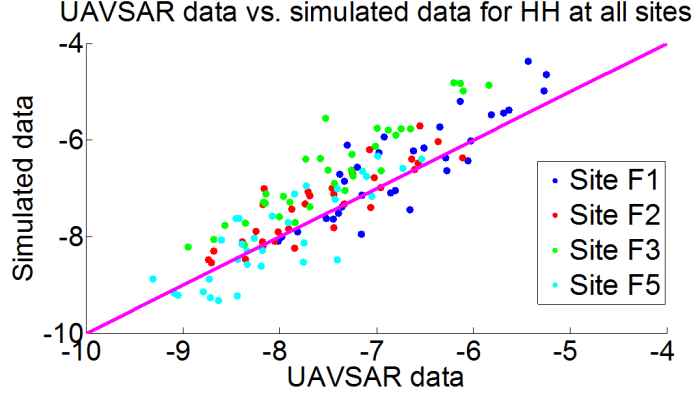
Figure 2.37: Comparison of simulated radar data with measured UAVSAR data (in dB) for all forested sites.

mented for future modeling attempts. Mironov obtained a set of regression equations to derive many of the spectroscopic parameters needed by a previously developed model. The resulting model applies to a wider range of soil types, but also requires fewer input parameters, with clay percentage as the only soil input parameter [53]. The model by Peplinski *et al.* further requires the sand percentage, the bulk density, the water temperature and the salinity of water, besides the frequency and and the water volume fraction required by both models.

2.3.6   Expression of soil moisture as a profile

Consideration of ground surface and subsurface scattering terms can be shown to be the dominant scattering mechanism at low frequencies in many cases, especially in the presence of tall trees. Introducing a multilayered soil structure and the subsequent retrieval of a soil moisture profile complicates the inversion due to the requisite N soil moisture values to be retrieved for an N-layered soil structure. A solution to this has recently been found by representing a moisture profile (of a forested area) with a second-order polynomial [54, 55] as shown in Fig. 2.38. Soil moisture at depth z can be represented as a second-order polynomial with coefficients (a, b, c) as follows:

$$SM(z) = az^2 + bz + c \tag{2.16}$$
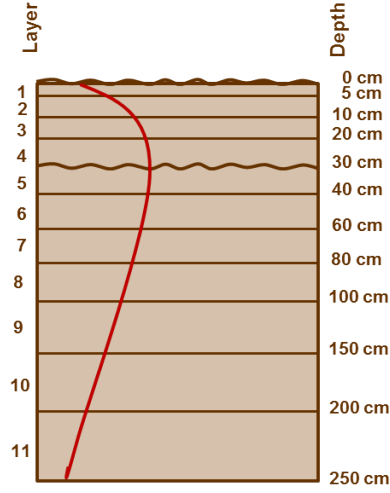
Figure 2.38: Visualization of soil moisture profile N-layered soil with two roughness interfaces.

A second-order polynomial is found to adequately represent the soil profile, while reducing the number of unknowns necessary for retrieving a soil moisture profile to three; this would otherwise restrict the number of layers included in the inversion. Three examples of measured soil moisture profiles and second-order polynomial fit are shown in Fig. 2.39. Assuming information about layered soil texture and soil layers is known, soil moisture can be described by three coefficients, therefore successfully reducing the number of variables to be retrieved. The link between soil permittivity and soil moisture is made by utilizing the model by Peplinski *et al.* [2, 3]. Retrieval of soil moisture at fine scales with a soil moisture profile expressed as a second-order polynomial is discussed further in chapter III as part of the AirMOSS retrieval effort.

The importance of soil moisture profile modeling is shown with the following study: Three measured soil moisture profiles and two fundamental assumptions are modeled for C-, L- and P-band assuming no vegetation. The measured soil moisture profiles are taken from measurements at Tonzi Ranch from 2012 and Arizona Lucky Hills from 2003 (wet and dry profile) as shown in Fig. 2.40 in green. Two fundamental assumptions are made: 1) only the surface soil moisture is measured and a
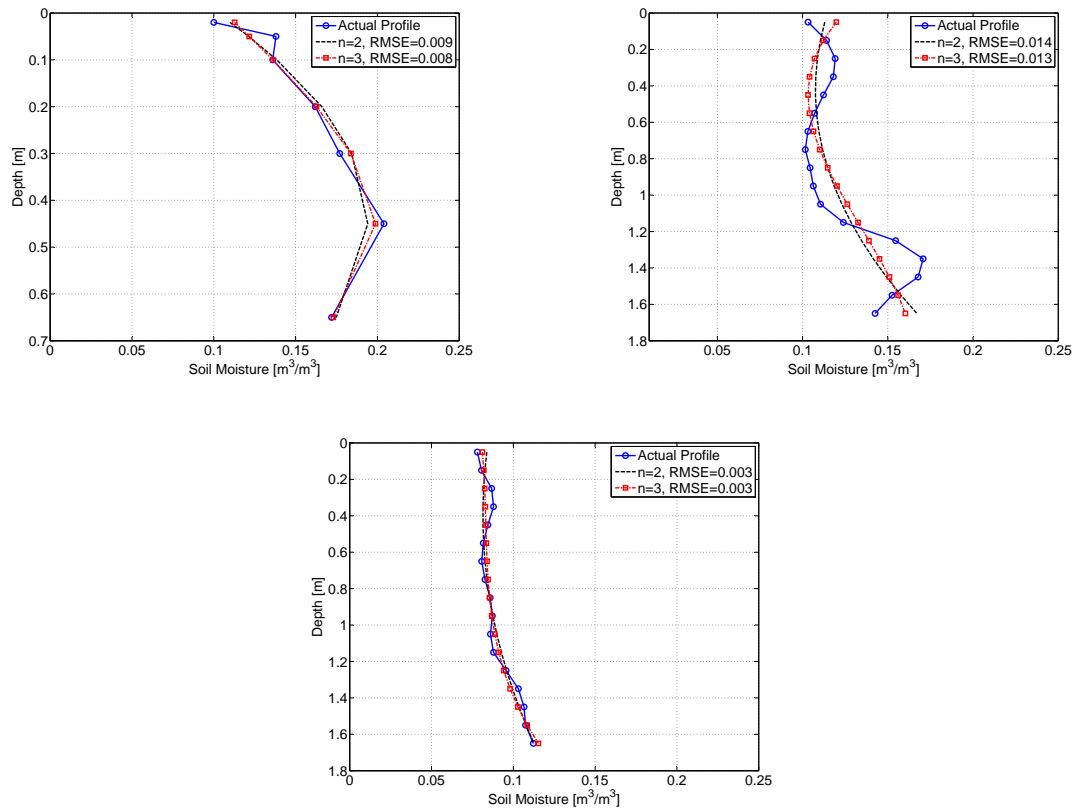
Figure 2.39: Three examples of measured soil moisture profiles and second-order polynomial fit: Tonzi Ranch from 8 January 2012 (left) and BOREAS OJP from 25 May 1994 (middle) and 2 July 1994 (right).

uniform profile in depth is assumed (blue) and 2) the average of the soil moisture profile is calculated and assumed to be uniform in depth (red). All other soil texture information is assumed to be uniform in depth. The radar backscatter for the three soil moisture profiles assuming no vegetation is shown in Fig. 2.41. At C-band, the sensed moisture corresponds to the surface soil moisture as the difference between the in-situ soil moisture profile and the uniform profile assuming surface soil moisture is very small. But lower frequencies, such as L- and P-band, penetrate deeper into the soil and the difference between the in-situ soil moisture profile and the uniform profile assuming surface soil moisture becomes significant. For the case of Profile 5, the difference at P-band is 5.5 dB in HH and 2.5 dB in VV. This study shows the importance of soil moisture profiles, especially for low-frequency radars.

2.4 Terrain topography at fine-scale pixels

Terrain topography is of great importance for vegetated areas both for active [56] and passive remote sensing [9]. Topography impacts the spatial distribution of geophysical parameters such as vegetation, soil moisture and surface/canopy temperature, as well as the incidence angle observed at the sensor. It further impacts the radar wave interactions between the ground and overlying vegetation. Previous work on effects of terrain topography on radar scattering includes a high-frequency electromagnetic radar scattering model for a tree trunk above a tilted ground plane by Lin and Sarabandi [57]. This model treats the trunk as a finite-length stratified dielectric cylinder with a corrugated bark while the ground is considered a smooth homogeneous dielectric with an arbitrary slope. The effect of the ground is implemented based on the ground surface reflection coefficients or Fresnel reflection coefficients of a smooth, tilted surface. The validity of the model is investigated and discussed by simulating several cases for a tilted ground plane. The model by Lopez-Sanchez *et al.* [58] extends the previous model by introducing multiple vertical dielectric cylinders representing
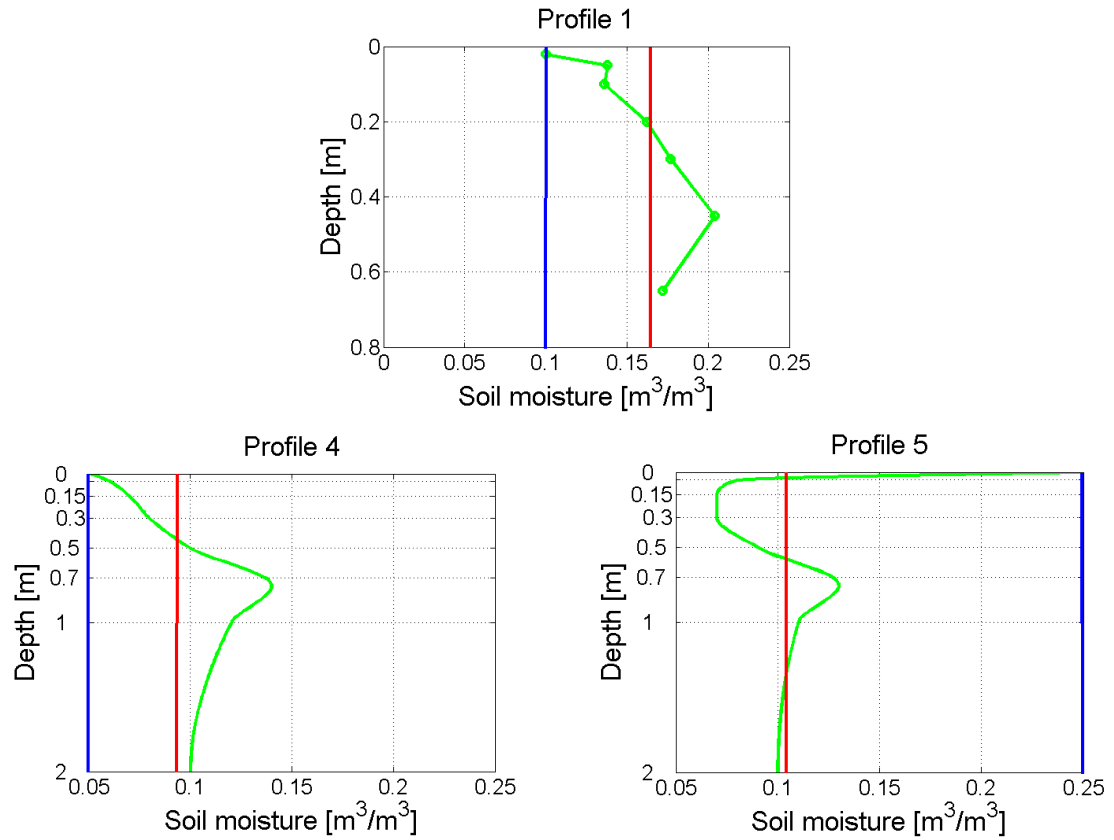
Figure 2.40: Three soil moisture profile locations: Tonzi Ranch from 2012 (Profile 1) and Arizona Lucky Hills from 2003 (Profile 4 and 5). Three profiles are considered: the in-situ soil moisture profile (green), the measured surface soil moisture assuming a uniform profile in depth (blue), and the average of the respective soil moisture profile assuming a uniform profile in depth (red).

57
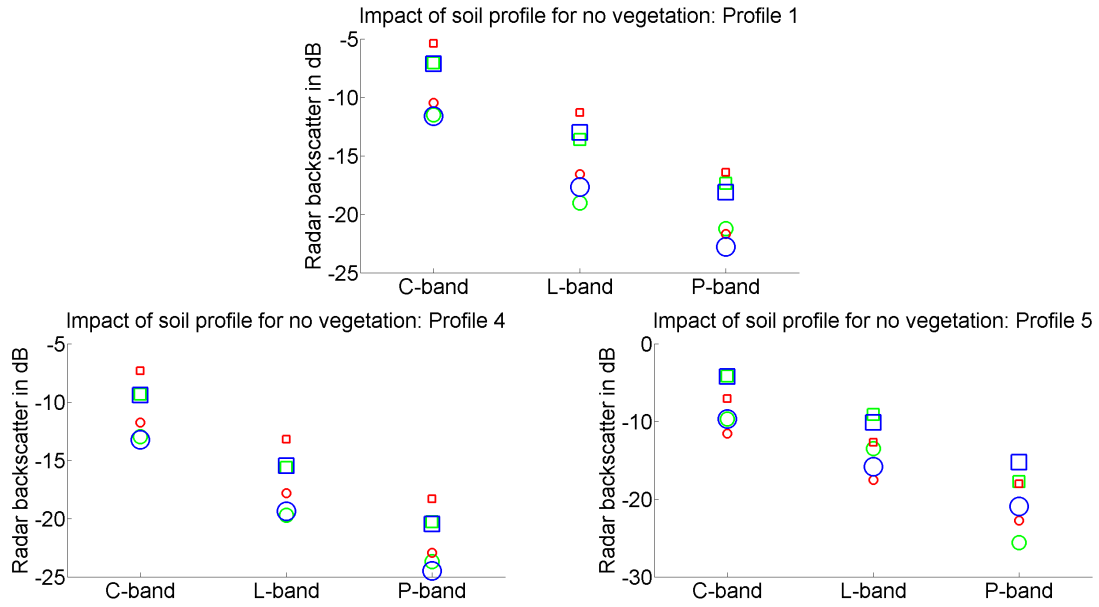
Figure 2.41: Radar backscatter at C-, L- and P-band for three soil moisture profiles at three locations assuming no vegetation: in-situ soil moisture profile (green), measured surface soil moisture assuming a uniform profile in depth (blue), and the average of the respective soil moisture profile assuming a uniform profile in depth (red). Radar backscatter in dB for HH with circle markers and VV with square markers. Profile 1 from Tonzi Ranch in 2012 and Profile 4 and 5 from Arizona Lucky Hills in 2003.

58

trunks above a dielectric half space according to Tsang *et al.* [59], but no validation with measured radar data is presented. Smith-Jonforsen *et al.* introduce a model for backscatter from forests for the VHF frequency range [60]. It models the trunks as dielectric cylinders, the ground as a homogeneous, smooth, dielectric half-space and addresses the slope by calculating the reflectivity matrix based on the Fresnel reflection coefficients and the scalar products between the local and global coordinate systems. It appears to agree reasonably well with measurements. Our approach is motivated by and substantially expands on the work of van Zyl [61]. Topography for bare surfaces can be easily implemented by varying the local incidence angle. For vegetated areas, and especially forested areas, the trunk-ground and branch-ground double bounce can contribute significantly to the total radar backscatter, and are strong functions of the underlying topography. For a flat scene, both scattering moments at the trunk and the ground are specular, resulting in a potentially strong scattering mechanism. In [61] a methodology was introduced to define topography in two dimensions by an angle α in the plane of incidence and an angle β perpendicular to the plane of incidence. This method considers the trunk to stay perpendicular to the slope, which is an unrealistic assumption. It also assumes a Gaussian pattern for the double-bounce scattering, which is arbitrarily assumed and may or may not hold in general. In our consideration, we assume the trees to grow vertically. The definition of the slope with two angles (α, β) is maintained, although with a different definition. The notation used to describe the coordinate system is shown in Fig. 2.42 and corresponds to the notation used in [19]. Introducing a topography, as an example in one dimension $(\beta = 0)$, will alter the scattering moments at the trunk and the ground. There will be two possible paths: (1) specular scattering at the trunk followed by non-specular scattering at the ground as shown in Fig. 2.43 on the left, and (2) non-specular scattering at the trunk followed by specular scattering at the ground as shown in Fig. 2.43 on the right. Adding another dimension of topography

will render the setup more complex, but the two main scattering moments remain the same. The adjustment to take into account non-specular scattering from the trunk can be implemented by sweeping the scattering angle at the trunk, while the non-specular scattering on the ground can be implemented by using the Stabilized Extended Boundary Condition Method (SEBCM) [62]. The use of the SEBCM model allows the treatment of an N-layered soil with rough interfaces. The scattering pattern of a cylinder shows a strong specular direction in $\theta_s = \pi - \theta_i$ while being nearly independent of ϕ. Therefore, the scattering pattern of a trunk cylinder will hereby be called a *skirt*. This is in contrast to the scattering pattern of a rough layered ground, which shows a strong specular scattering in $\theta_s = \theta_i$ and $\phi_i = \phi_s$ that diminishes quickly if the scattering angles depart from the true specular direction. Therefore the specular scattering from the ground will be called a *cone*. A visualization of the *skirt* and *cone* scattering pattern is given in Fig. 2.44. In the case of double bounce scattering, there is always a two-way propagation. This is taken into account by multiplying the double bounce Stokes matrix by the transmission matrices for transmission in both directions. This theoretical development assumes for consistency that the first scattering event is at the trunk or branches, followed by the second scattering event at the ground. The novelty of this work rests on the general ground orientation producing non-trivial backscatter, and in describing an integration scheme over the available degrees of freedom to derive the total radar backscatter coefficient.

2.4.1 Theoretical development for terrain topography

The following interactions are modeled in the presence of non-planar topography:

- Backscatter from canopy structure adjusted for sloped terrain (TT-B)
- Backscatter from a rough surface underneath vegetation layers (TT-G)
- Double bounce scattering interactions between trunks and the ground (TT-TG)
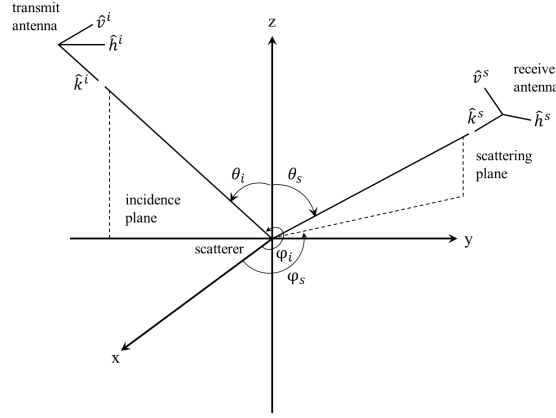
Figure 2.42: Coordinate system for terrain topography calculations. The xy plane is parallel to the ground surface.
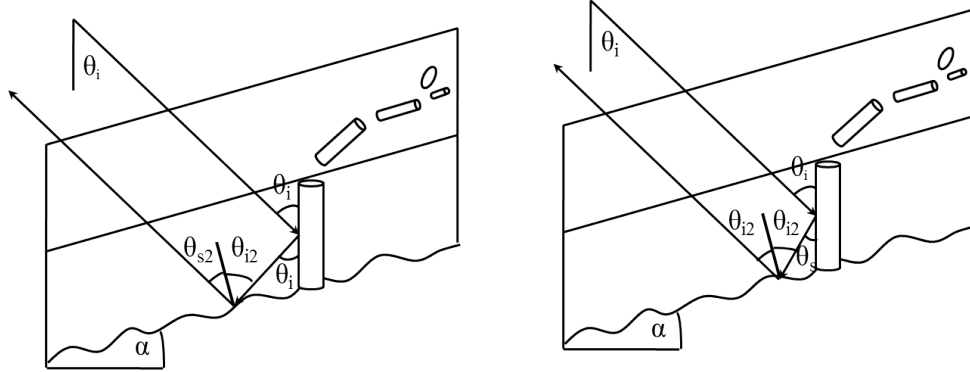
Figure 2.43: Two possible paths for double bounce scattering mechanism on a random slope described with (α, β): specular scattering at the trunk followed by non-specular scattering at the ground (left), and non-specular scattering at the trunk followed by specular scattering at the ground (right). For clarity, $\beta = 0$ assumed in figure.

61
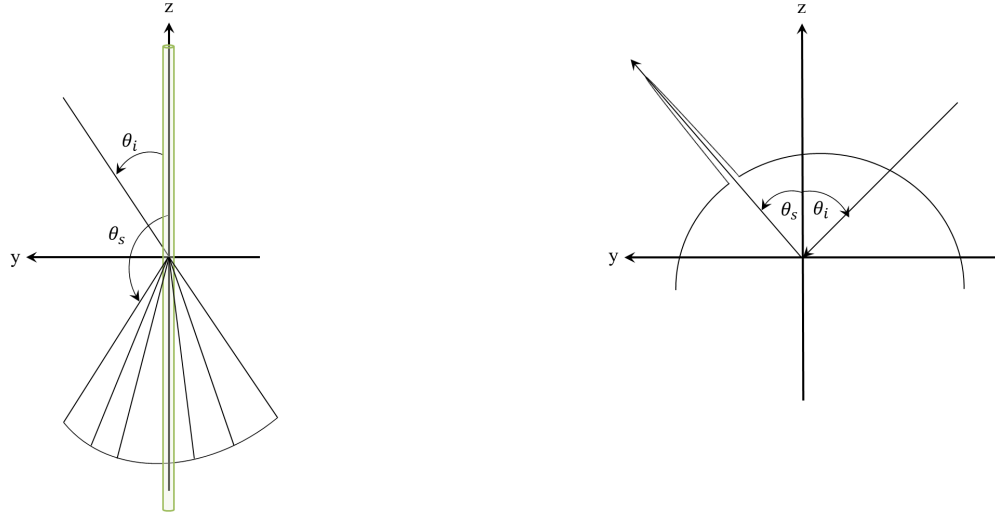
Figure 2.44: Symbolical visualization of the scattering pattern from a cylinder (left) showing the skirt pattern and from a rough layered ground (right) showing the cone pattern.

- Double bounce scattering interactions between canopy (large/small branches and leaves/needles) and ground (TT-BG)

2.4.1.1 Methodology

A two-dimensional slope can be expressed with two parameters: angle α for a tilt in the plane of incidence (angle α in x-z plane with $\alpha = 90°$ rotating the x- into the z-axis) and angle β for a tilt perpendicular to the plane of incidence (angle β in y-z plane with $\beta = 90°$ rotating the y- into the z-axis) as shown in Fig. 2.45. Associated with these angles is a rotation matrix R, that rotates the standard orientation (x, y, z) to the new respective orientation (x', y', z'). The rotation matrix in (x, y, z) basis can therefore be expressed as:

$$R(\alpha, \beta) = \begin{bmatrix} \cos\alpha & 0 & \sin\alpha\cos\beta \\ 0 & \cos\beta & -\cos\alpha\sin\beta \\ -\sin\alpha & \sin\beta & \cos\alpha\cos\beta \end{bmatrix} \tag{2.17}$$
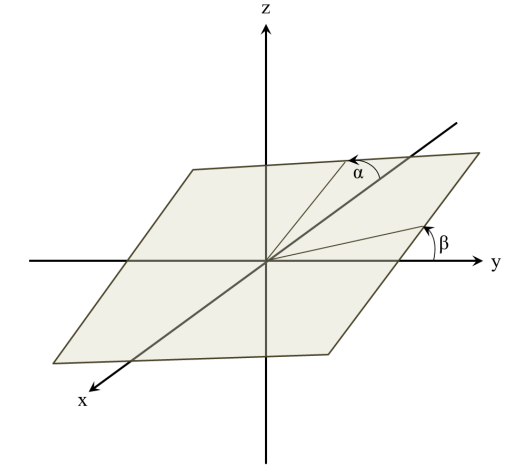
Figure 2.45: Definition of slope angles (α, β) in standard coordinate system. The xy plane is parallel to the ground surface.

The inverse of the rotation matrix R^{-1} rotates the new respective orientation (x', y', z') back to the standard rotation (x, y, z), and is defined as:

$$R^{-1}(\alpha, \beta) \;=\; \frac{1}{\cos^2\alpha - \cos^2\alpha\cos^2\beta + \cos^2\beta} \cdot$$

$$\begin{bmatrix} \cos\alpha & \sin\alpha\sin\beta\cos\beta & -\sin\alpha\cos^2\beta \\ \sin\alpha\sin\beta\cos\alpha & \cos\beta & \sin\beta\cos^2\alpha \\ \sin\alpha\cos\beta & -\cos\alpha\sin\beta & \cos\alpha\cos\beta \end{bmatrix} \quad (2.18)$$

It is notable that (α, β) are the slope angles in range (in plane of incidence) and azimuth (out of plane of incidence) direction, respectively, as seen from the radar. Therefore, when using radar data, such as those from AirMOSS, for validation, the regular (North, East) slope pixel definition provided with the radar data must be converted to the (Range, Azimuth) slope definition as shown in Fig. 2.46.

A vector can be expressed in the spatial (x, y, z) basis, or in the (right-handed, orthonormal) wave vector basis (h, v, k). For a given orientation of a wave vector in
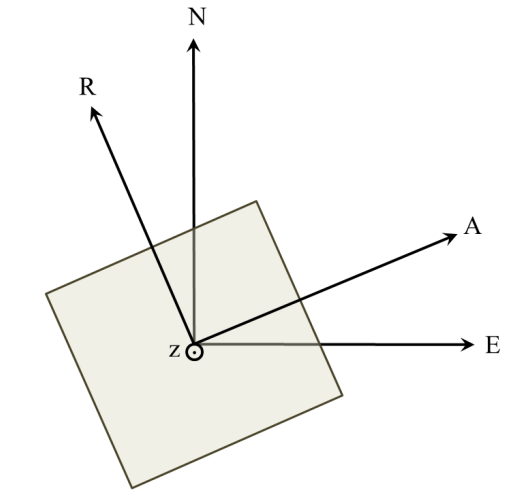
Figure 2.46: Visualization of slope angles (α, β) in (**R**ange, **A**zimuth) slope definition with respect to (**N**orth, **E**ast) slope definition as provided by AirMOSS.

polar coordinates (θ, ϕ), the vectors $\hat{h}$, $\hat{v}$, $\hat{k}$ can be expressed in the spatial basis as:

$$\hat{h} = (\sin\phi, -\cos\phi, 0)$$

$$\hat{v} = (-\cos\theta\cos\phi, -\cos\theta\sin\phi, \sin\theta)$$

$$\hat{k} = (-\cos\phi\sin\theta, -\sin\phi\sin\theta, -\cos\theta) \tag{2.19}$$

The standard wavevector basis is referred to when $\hat{h} \cdot \hat{z} = 0$. We define a matrix $P(\theta, \phi)$ that expresses a vector from the (h, v) basis as a vector in the (x, y, z) basis:

$$P(\theta, \phi) \quad = \quad \begin{bmatrix} \sin\phi & -\cos\theta\cos\phi \\ -\cos\phi & -\cos\theta\sin\phi \\ 0 & \sin\theta \end{bmatrix} \tag{2.20}$$

The columns of $P(\theta, \phi)$ are the spatial components of $(\hat{h}, \hat{v})$, respectively. Similarly, the $P^{-1}(\theta, \phi)$ matrix performs the reverse operation going from (x, y, z) basis

to the (h, v) basis, and is defined as follows:

$$P^{-1}(\theta, \phi) = \begin{bmatrix} \sin\phi & -\cos\phi & 0 \\ -\cos\theta\cos\phi & -\cos\theta\sin\phi & \sin\theta \end{bmatrix} \tag{2.21}$$

All scattering events can now be formally expressed.

2.4.1.2 Backscatter from canopy structure adjusted for sloped terrain (TT-B)

The change for the backscatter from the canopy structure in presence of topography is mainly an adjustment of all layer heights to reflect the altered path length through each layer. This can be expressed by $h' = h\cos\alpha\cos\beta$, where h' is the new layer height. The adjustment of the vegetation layer heights also adjusts the attenuation accordingly.

2.4.1.3 Backscatter from a rough surface underneath vegetation layers (TT-G)

In the case of the direct ground scattering, there are no degrees of freedom to be chosen. All angles are defined by the respective slope given through (α, β). The incident wave vector is $\hat{k}_i(\theta_i, \phi_i)$ and the electric field in the (h, v, k) basis is $\vec{e}_i = (e_h^i, e_v^i, 0)$.

(i). Bring $\vec{e}$ into the (x, y, z) basis, i.e. apply $P(\theta_i, \phi_i)$.

(ii). Rotate the coordinate axis such that the ground is upright, i.e. apply $R(\alpha, \beta)$. Also apply the rotation to $\hat{k}_i$, which gives $\hat{k}_i^g(\theta_i^g, \phi_i^g) = R(\alpha, \beta)\hat{k}_i(\theta_i, \phi_i)$, and thus the new (θ_i^g, ϕ_i^g).

(iii). Bring the electric field back into the (h, v, k) basis, i.e. apply $P^{-1}(\theta_i^g, \phi_i^g)$.

(iv). Scatter the wave in the direction of choice (θ_s, ϕ_s) from the ground, i.e. apply $S_g(\theta_s^g, \phi_s^g; \theta_i^g, \phi_i^g)$, which is the scattering matrix for an upright ground. Since

65

this setup is a backscatter case in the local coordinate system of the ground, the following applies: $\theta_s^g = \theta_i^g$ and $\phi_s^g = \phi_i^g$.

(v). Bring the electric field to the (x, y, z) basis, i.e. apply $P(\theta_s^g, \phi_s^g)$.

(vi). Undo the rotation of step (ii), i.e. apply $R^{-1}(\alpha, \beta)$. This implies that the wavevector has been brought back to the backscattered direction with $\hat{k}_s(\theta_s, \phi_s) = R^{-1}(\alpha, \beta)\hat{k}_s^g(\theta_s^g, \phi_s^g)$, and therefore (θ_s, ϕ_s).

(vii). Finally, bring the electric field back to the (h, v, k) basis, i.e. apply $P^{-1}(\theta_s, \phi_s)$.

Thus, the scattered electric field $\vec{e}_s = (e_h^s, e_v^s, 0)$ is given by the following sequence of matrix multiplications:

$$\vec{e}_s = P^{-1}(\theta_s, \phi_s)\, R^{-1}(\alpha, \beta)\, P(\theta_s^g, \phi_s^g)\, S_g(\theta_s^g, \phi_s^g; \theta_i^g, \phi_i^g)\, P^{-1}(\theta_i^g, \phi_i^g)\, R(\alpha, \beta)\, P(\theta_i, \phi_i)$$

$$(2.22)$$

Generally, the new, rotated angles can be found by the following technique. As an example the incident angles are (θ, ϕ) and the new, rotated angles are (θ', ϕ') :

$$\hat{k}'(\theta', \phi') = R(\alpha, \beta)\hat{k}(\theta, \phi) \qquad (2.23)$$

The new, rotated angles can be found by the following equations:

$$\tan \phi' = \frac{k_y}{k_x}$$

$$\cos \theta' = k_z \qquad (2.24)$$

2.4.1.4 Double bounce scattering interactions between cylinder and the ground (TT-TG and TT-BG)

The same technique is applicable to the trunk-ground (TT-TG) and branch-ground (TT-BG) double bounce. In the case of the double bounce, there are four degrees of freedom: The angles (θ_s^c, ϕ_s^c) determine the scattering angles from the cylinder and specify the intermediate wavevector $\hat{k}_s^c(\theta_s^c, \phi_s^c)$ between the cylinder and

ground, and the angles (θ^g_s, ϕ^g_s) determine the scattering angles from the ground and specify the intermediate wavevector $\hat{k}^g_s(\theta^g_s, \phi^g_s)$ between the ground and the radar. Again, the incident wave vector is $\hat{k}_i(\theta_i, \phi_i)$ and the electric field in the (h, v, k) basis is $\vec{e}_i = (e^i_h, e^i_v, 0)$.

(i). Scatter the wave in the direction of choice with angles (θ^c_s, ϕ^c_s) from the cylinder, i.e. apply $S_c(\theta^c_s, \phi^c_s; \theta_i, \phi_i)$, which is the scattering matrix for a cylinder.

(ii). Bring the electric field to the (x, y, z) basis, i.e. apply $P(\theta^c_s, \phi^c_s)$.

(iii). Rotate the coordinate axis such that the ground is upright, i.e. apply $R(\alpha, \beta)$. Also apply the rotation to $\hat{k}^c_s$, which gives $\hat{k}^g_i(\theta^g_i, \phi^g_i) = R(\alpha, \beta)\hat{k}^c_s(\theta^c_s, \phi^c_s)$, and thus the new (θ^g_i, ϕ^g_i).

(iv). Bring the electric field back to the (h, v, k) basis, i.e. apply $P^{-1}(\theta^g_i, \phi^g_i)$.

(v). Scatter the wave in the direction of choice with angles (θ^g_s, ϕ^g_s) from the ground, i.e. apply $S_g(\theta^g_s, \phi^g_s; \theta^g_i, \phi^g_i)$, which is the scattering matrix for an upright ground.

(vi). Bring the electric field to the (x, y, z) basis, i.e. apply $P(\theta^g_s, \phi^g_s)$.

(vii). Undo the rotation of step (iii), i.e. apply $R^{-1}(\alpha, \beta)$. This implies that the wavevector has been brought back to the backscattered direction with $\hat{k}_s(\theta_s, \phi_s) = R^{-1}(\alpha, \beta)\hat{k}^g_s(\theta^g_s, \phi^g_s)$, and therefore (θ_s, ϕ_s).

(viii). Finally, bring the electric field back to the (h, v, k) basis, i.e. apply $P^{-1}(\theta_s, \phi_s)$.

Thus, the scattered electric field, $\vec{e}_s = (e^s_h, e^s_v, 0)$ is given by the following sequence of matrix multiplications:

$$\vec{e}_s = \qquad P^{-1}(\theta_s, \phi_s)\, R^{-1}(\alpha, \beta)\, P(\theta^g_s, \phi^g_s)\, S_g(\theta^g_s, \phi^g_s; \theta^g_i, \phi^g_i)\cdot$$
$$P^{-1}(\theta^g_i, \phi^g_i)\, R(\alpha, \beta)\, P(\theta^c_s, \phi^c_s)\, S_c(\theta^c_s, \phi^c_s; \theta_i, \phi_i) \qquad (2.25)$$

2.4.2 Implementation of terrain topography

The implementation of the adjustment for terrain topography for the canopy (TT-B) and for the direct rough surface (TT-G) contribution is straightforward. The

implementation for the double bounce interactions (TT-TG and TT-BG) is more involved since there are four degrees of freedom to be considered. The simplest implementation is to find the exact two scattering paths of specular scattering at the trunk followed by non-specular scattering at the ground and the non-specular scattering at the trunk followed by specular scattering at the ground. As both scattering events, both at the cylinder and the ground, are not simply delta functions, it is advisable to integrate over a range of angles around the two scattering paths. The two scattering moments are treated as two separate integrals, since the difference in θ and ϕ between the two scattering moments can be high for a large slope. This permits a flexible and modular implementation. After loading the input parameter that determine the vegetation, soil and slope into the model, a module calculates the lower and upper limits of the two integrals, which are then fed into the respective trunk-ground and branch-ground double bounce calculations. The integral itself is implemented with the Simpson's rule in 2D.

The scattering matrix of the ground is provided using the SEBCM method [62]. Prior to executing the multispecies vegetation multilayered soil model, the case to be modeled is established. The SEBCM is executed with the respective soil conditions (soil layers, soil texture, soil roughness) and the general scattering matrix of the ground is generated. This can be very time intensive and simulations may take weeks. The SEBCM provides a scattering matrix, which is a look-up table for any incidence and scattering angle. Since the SEBCM is based on discrete Floquet modes, the final scattering matrix has been interpolated such that incidence and scattering angles at every 1° or 5° are available. To setup a sample simulation, the radar incidence angle is assumed to be $\theta_i = 40°$. Therefore, the incidence and scattering angles are interpolated to be at 1° within $\pm$ 10° of $\theta_i = 40°$ and $\theta_s = 140°$. All other angles are spaced at 5°. The scattering matrix of the ground is read into the multispecies vegetation multilayered soil model and depending on the slope of each

68

pixel, the correct scattering matrix for the different scattering moments is selected. Two scattering mechanisms involve the ground: direct ground (TT-G) and double bounce (TT-TG, TT-BG) scattering. For both scattering mechanisms, the scattering matrix provided by SEBCM is used.

2.4.3 Proof of concept of terrain topography

To illustrate the importance of modeling terrain topography, a sample simulation is set up. It is inspired by the AirMOSS Metolius site in Oregon and considers P-band at an incidence angle of 40 degrees. The above-ground vegetation falls under the land cover type of evergreen forest and, for the purpose of this forward simulation, measured parameters of OJP forest collected during CanEx-SM2010 are used. The vegetation parameters are given in Table 2.1. It is noted that trunk averaging is enabled for this simulation, and the range of trunk radii is set to $\pm 22\%$ of the initial trunk radius. The soil is defined as 20 homogeneous soil layers representative of the evergreen forest land cover type found in Metolius. The soil information is based on STATSGO2 gap-filled SSURGO data and the necessary information to utilize the soil model by Peplinski *et al.* [2, 3] is summarized in Table 2.2. A volumetric soil moisture of 5 percent is assumed for all 20 soil layers.

The simulation results showing the effect of a ground surface tilt described with (α, β) in degrees are presented in Fig. 2.47. The predicted P-band radar backscatter coefficients for HH, VV and HV in dB are broken down to show the volume (TT-B), ground (TT-G) and trunk-ground double bounce (TT-TG) scattering mechanisms, as well as the total radar backscatter coefficient (TT-Total) in dB. The branch-ground double bounce (TT-BG) contribution is consistently smaller than -40 dB and is therefore not shown. For each scattering mechanism, the case with $\alpha = \beta = 0°$ describes a scene with no slope. Simulation results show the impact of a two-dimensional slope for a range of tilt angles: $\alpha \pm 3°$ and $\beta \pm 3°$.

The volume scattering can be seen to decrease on the order of 0.1 dB for a tilted scene due to the adjusted vegetation layer height. The ground contribution varies when tilting in the plane of incidence for HH and VV and varies when tilting out of plane of incidence for HV. This is consistent with the backscatter behavior of SEBCM in backscatter direction. A tilt of 3 degrees in the plane of incidence results in 1-2 dB difference for HH and VV and a tilt of 3 degrees out of the plane of incidence relates to a 10 dB difference in HV.

The trunk-ground double bounce is strongest for $\alpha = 0$. In this situation, the skirt scattering pattern of the cylinder perfectly coincides with the cone scattering pattern of the ground, creating a very strong specular backscatter. If α is kept zero and β is varied, the double bounce mechanism stays strong since the skirt scattering pattern still picks up the cone scattering pattern of the ground. When α is slightly increased, the cone scattering pattern from the ground no longer intersects with the skirt pattern from the cylinder, therefore greatly reducing the strength of the trunk-ground double bounce scattering mechanism. For a 3 degrees tilt in the plane of incidence a decrease of up to 15 dB is observed in HH, VV and HV. The total backscatter shows a pattern that is highly influenced by the trunk-ground double bounce mechanism as it is the strongest scattering mechanism for forested scenes. A 3 degree tilt in the plane of incidence translates to a change of up to 6 dB in HH, 2 dB in VV and 1 dB in HV for the total radar backscatter. These observations are consistent with the analysis of van Zyl [61] for a forest over a sloped ground tilted only in the plane of incidence ($\beta = 0$). It shows a similar breakdown of the scattering mechanisms.

The ground contribution in van Zyl [61] increases for an increasing α, which differs from the trend seen in Fig. 2.47. This can be traced back to the difference in the ground model. It can be safely assumed that the SEBCM model is more representative of the ground contribution than the approximation used in van Zyl [61]. The presented simulations demonstrate the need for accurate topography modeling since even a small

Table 2.1: Parameters for an OJP forest based on measurements collected during CanEx-SM2010.

Parameter	Measured Value	Parameter	Measured Value
Canopy Height	11.4 m	SB Orientation	70°
LB Dielectric	32-j4	Needle Dielectric	32-j4
LB Length	1.2 m	Needle Length	3 cm
LB Radius	0.66 cm	Needle Radius	0.15 cm
LB Density	$7/\text{m}^3$	Needle Density	$1728/\text{m}^3$
LB Orientation	80°	Trunk Dielectric	36-j2
SB Dielectric	32-j4	Trunk Length	2.0 m
SB Length	0.8 m	Trunk Radius	6.8 cm ($\pm$ 1.5 cm)
SB Radius	0.46 cm	Trunk Density	$0.25/\text{m}^2$
SB Density	$70/\text{m}^3$		

slope greatly alters the radar backscatter strength.

Table 2.2: Soil parameter from STATSGO2 gap-filled SSURGO data over Metolius.

Parameter	Value
Soil moisture	0.05
Percentage sand	0.68
Percentage clay	0.10
Bulk density	$1.0\,\frac{g}{cm^3}$
Soil temperature	10°
Soil salinity	$4\,\frac{g}{cm^3}$
Soil surface roughness	$0.02\,m$

2.5   Summary of modeling developments

Models presented in chapter II describe multispecies vegetation, multilayered soil and terrain topography on a fine-scale level as visualized in Fig. 2.48. A summary of the models and their origin, either a new contribution to the field or a reference, are given in Table 2.3.

To investigate the modeling contributions, Model D.2 (Model D with trunk averaging enabled), as described in Table 2.3, is used. Three simulation sets are presented at C-, L- and P-band: 1) a single species vegetation on a uniform soil moisture profile (Table 2.4 for C-band, Table 2.7 for L-band, and Table 2.10 for P-band), 2)
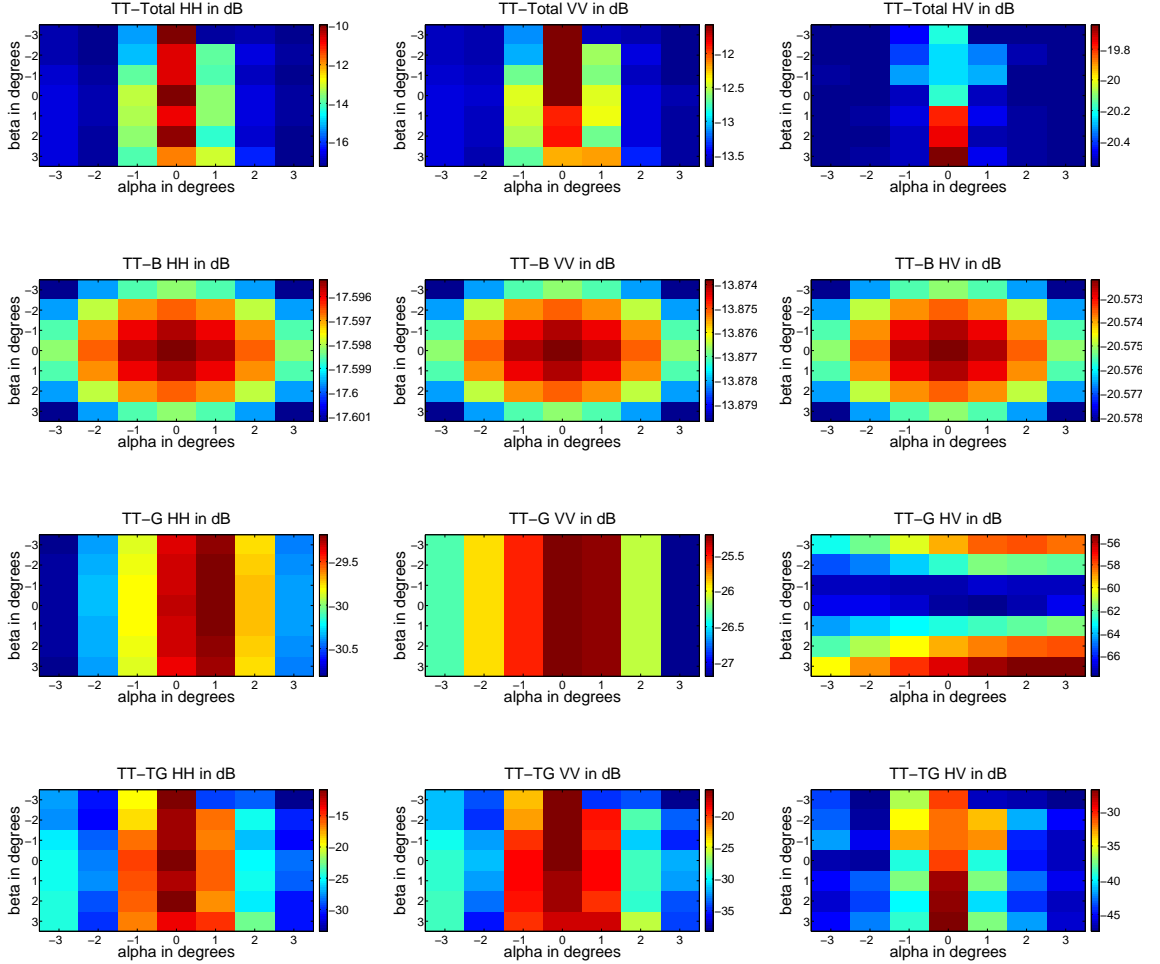
Figure 2.47: Effect of ground surface tilt described with (α, β) in degrees. Predicted P-band radar backscatter coefficients for HH (left), VV (middle), HV (right) in dB for total (TT-Total), volume (TT-B), ground (TT-G) and trunk-ground double bounce (TT-TG) contributions. The branch-ground double bounce (TT-BG) contribution is less than -40 dB and is therefore neglected.

Table 2.3: List and origin of models presented in chapter II.

Model version	Description
Model A	Single-species vegetation model on homogeneous dielectric half-space with soil modeled as first-order SPM. Vegetation and soil modeling technique are based on Durden *et al.* [19].
Model B	Multispecies vegetation model on homogeneous dielectric half-space with soil modeled as first-order SPM. The multispecies vegetation model is a new contribution.
Model B.2	Multispecies vegetation model on homogeneous dielectric half-space with soil modeled as first-order SPM with trunk averaging. The trunk averaging technique is a new conribution.
Model C	Multispecies vegetation model with soil modeled as a single layer with second-order SPM. The second-order SPM is based on Tsang and Kong [30].
Model D	Multispecies vegetation model with N-layered soil model based on first-order SPM and a coherent scattering model for a two-layered rough interface. The N-layered first-order SPM and the two-layered coherent model are based on Tabatabaeenejad and Moghaddam [45] and Tabatabaeenejad, Duan and Moghaddam [46].
Model E	Multispecies vegetation model with N-layered soil model based on first-order SPM and a coherent scattering model for a two-layered rough interface. The soil moisture is expressed as a second-order polynomial, a technique developed by Tabatabaeenejad, Burgin, Duan and Moghaddam [55].
Model F	Multispecies vegetation model with N-layered soil modeled with SEBCM considering terrain topography. The SEBCM model is based on Duan and Moghaddam [62]. The terrain topography modeling technique is a new contribution.

Figure 2.48: Visualization of fine-scale level complexity presented in chapter II: multispecies vegetation, multilayered soil and terrain topography.

a multispecies vegetation on a uniform soil moisture profile (Table 2.5 for C-band, Table 2.8 for L-band, and Table 2.11 for P-band), and 3) a multispecies vegetation on a measured in-situ soil moisture profile (Table 2.6 for C-band, Table 2.9 for L-band, and Table 2.12 for P-band). The soil texture is kept the same for all simulations with a percentage sand of 68 %, percentage clay of 10 %, bulk density of $1 \frac{g}{cm^3}$, soil temperature of $10°$ and soil salinity of 4 gram salt per kg water. The surface soil roughness is assumed to be 2 cm for all simulations, the incidence angle is $40°$ and no terrain topography is assumed. The two single species vegetation cases are an OJP forest as observed during CanEx-SM2010 and a TA forest as observed during SMAPVEX12. The OJP forest is sparse with 0.25 trees per square meter and a total height of 11.4 m. The TA forest is very sparse with 0.08 trees per square meter and a total height of 11.7 m. The multispecies vegetation is modeled by a adding understory to the single species forests: a YJP understory with a total height of 2 m is added to the OJP forest ("OJP & YJP"), and a young regrowth TA forest with understory is added to the mature TA forest ("SMAPVEX12"). The YJP forest was observed during CanEx-SM2010 and is a sparse forest with 0.4 trees per square meter. The multispecies TA forest was observed during SMAPVEX12 and reflects the parametrization of site F5 with two TA growth stages and an understory. The used

soil moisture profiles are shown in Fig. 2.40 and consist of two measured in-situ soil moisture profiles (Profile 4 and Profile 5), two profiles assuming the measured surface soil moisture with a uniform profile in depth (Profile 4.A and Profile 5.A), and two profiles assuming the average over the soil moisture profile with a uniform profile in depth (Profile 4.B and Profile 5.B). The two-way attenuation for all of these profiles up to a depth of 1 meter is calculated to be approximately +3 dB.

The simulations show that the difference between the single species OJP forest and the multispecies OJP & YJP forest is minimal at C-band since the volume scattering is found to be the major scattering mechanism. The double bounce contribution, and therefore the soil moisture profile impact, is not perceivable in the total radar backscatter. The single-species TA forest is very sparse and at C-band the trunk ground double bounce scattering mechanism is the major contribution. For the single-species TA forest, a difference of about 1.5 dB in HH and 3.5 dB in VV is perceived in the total radar backscatter due to the different soil moisture profiles. When adding the young regrowth TA forest with understory, volume scattering becomes more important due to the canopy density and the added canopy attenuates the trunk ground double bounce contribution. A difference of about 6-7 dB in HH and 2-4.5 dB in VV is observed in the total radar backscatter when modeling the forest as a single or multi-species forest stand while maintaining the soil moisture profiles. The impact of the soil profiles for the multispecies SMAPVEX12 forest is about 1.5 dB in HH and about 1 dB in VV. At C-band, the sensed soil moisture can be considered to be the surface soil moisture. A difference of up to 0.5 dB in HH and up to 0.3 dB in VV is observed when comparing the in-situ soil moisture profile against the uniform profile with the surface soil moisture assumption.

At L-band, the single species OJP and the multispecies OJP & YJP forest are opaque due to the dense canopy for this particular sample forest. At L-band, a similar trend as at C-band is observed for the SMAPVEX12 forest. For a single species TA

forest, the impact of the soil moisture profiles on the total radar backscatter is about 3.5 dB in HH and 5 dB in VV. When adding the young regrowth TA forest with understory while maintaining the soil moisture profiles, a difference of 7-8 dB in HH and 5-7 dB in VV is observed. The impact of the soil moisture profiles on the total radar backscatter for the multispecies SMAPVEX12 forest is about 3 dB in HH and 3 dB in VV. A difference up to 1 dB in HH and up to 1.2 dB in VV is observed when comparing the in-situ soil moisture profiles against the uniform profile with the surface soil moisture assumption. Compared to C-band, the sensed soil moisture difference between the uniform and in-situ soil moisture profiles has become noticeable in the total radar backscatter of the SMAPVEX12 forest. This is due to a decrease in volume scattering contribution and an increase in the double bounce contribution.

At P-band both single and multispecies forests show a considerable dependency on the trunk-ground double bounce scattering mechanisms, thereby picking up soil moisture information from the ground. The impact of the soil moisture profiles on the total radar backscatter at P-band for both single species forests ranges around 3 dB in HH and 4-5 dB in VV. When adding understory while maintaining the soil moisture profiles, a difference of about 1.2 dB in HH and 2.8 dB in VV is observed for the OJP & YJP forest, while a difference of about 3.3 dB in HH and 2.2 dB in VV is observed for the SMAPVEX12 forest. The impact of the soil moisture profiles for both multispecies forests is about 3 dB in HH and 5 dB in VV. The impact of the different soil moisture profiles is clearly visible in the total radar backscatter coefficient when comparing the difference between in-situ and uniform soil moisture profiles for both multispecies forests. The sensed soil moisture cannot be identified to be the surface soil moisture and is instead a sensed soil moisture column as the radar signal penetrates deeper into the soil. A difference up to 2.8 dB in HH and 4.4 dB in VV is observed when comparing the in-situ with the uniform soil moisture profiles for both multispecies forests.

These simulations show the importance of the modeling contributions (single to multispecies and inclusion of a soil moisture and texture profile) as the frequency is decreased. It can therefore be concluded that this chapter has addressed the original objective of improving the model for lower frequencies, especially for P-band but also for L-band.

2.6   Conclusions

This chapter presented a generalized radar scattering model at fine scales. First, the vegetation modeling is generalized to multispecies multilayered vegetation and validated with data from Injune and Tara Downs in Australia. The comparison is good, but the first-order SPM is determined to be the main source of errors. Second, the below-ground modeling is generalized with an N-layered soil model. The resulting multispecies model with multilayered soil is validated with three data sets: (1) a single-species vegetation on multilayered soil at BOREAS, (2) a multispecies vegetation on a single-layered soil at UMBS, and (3) a multispecies vegetation on a single-layered soil from SMAPVEX12 in Canada. The comparison of all three data sets is very promising, but the VV channel discrepancy for the SMAPVEX12 data set has to be resolved. Future work for the SMAPVEX12 data set also includes improvement of the forward modeling by including the organic soil layer. The tower-based radar measurements at UMBS are currently still uncalibrated which prevented an absolute validation of the forward model results. The full calibration will be addressed by the radar instrument developers in the future. Finally, the model is generalized to permit terrain topography. A methodology is developed and the implementation is outlined. A first set of simulations for a two-dimensional slope with $\alpha \pm 3°$ and $\beta \pm 3°$ is presented and terrain topography is shown to be crucial to for accurate forward modeling, especially over forested areas. Future work will include the validation of the terrain topography methodology by forward simulating moderately hilly areas

Table 2.4: Single species vegetation on a uniform soil moisture profile at C-band for three different channels (HH, VV and HV). The total radar backscatter (TOT) is split into its scattering contributions by volume scattering (VOL), branch-ground double bounce (BG), trunk-ground double bounce (TG) and ground scattering (G). For the single species OJP forest, the impact of soil moisture is minimal since the volume scattering is the major contribution. For the single species TA forest, a difference of about 1.5 dB in HH and 3.5 dB in VV is perceived in the total radar backscatter due to the different soil moisture profiles.

Description	Channel	*TOT*	*VOL*	*BG*	*TG*	*G*
OJP Profile 4.A	HH	-8.85	-8.85	-121.57	-116.80	-92.04
	VV	-9.96	-9.96	-151.74	-144.86	-109.16
	HV	-15.70	-15.70	-149.25	-170.31	N/A
OJP Profile 4.B	HH	-8.85	-8.85	-120.05	-115.08	-90.66
	VV	-9.96	-9.96	-150.39	-143.51	-107.17
	HV	-15.70	-15.70	-147.51	-168.57	N/A
OJP Profile 5.A	HH	-8.85	-8.85	-106.81	-101.83	-88.61
	VV	-9.96	-9.96	-137.95	-130.91	-104.07
	HV	-15.70	-15.70	-123.48	-144.53	N/A
OJP Profile 5.B	HH	-8.85	-8.85	-120.41	-115.43	-90.49
	VV	-9.96	-9.96	-151.72	-144.84	-106.92
	HV	-15.70	-15.70	-146.75	-167.84	N/A
TA Profile 4.A	HH	-1.42	-9.00	-14.18	-2.59	-21.58
	VV	-6.95	-9.39	-23.28	-11.59	-19.03
	HV	-22.61	-22.70	-39.65	-54.07	N/A
TA Profile 4.B	HH	-0.25	-9.00	-12.80	-1.22	-20.20
	VV	-5.84	-9.39	-20.98	-9.30	-17.04
	HV	-22.61	-22.70	-39.65	-54.21	N/A
TA Profile 5.A	HH	1.59	-9.00	-10.74	0.85	-18.15
	VV	-3.62	-9.39	-17.50	-5.83	-13.93
	HV	-22.64	-22.70	-41.02	-55.48	N/A
TA Profile 5.B	HH	-0.10	-9.00	-12.62	-1.04	-20.03
	VV	-5.68	-9.39	-20.68	-9.01	-16.78
	HV	-22.61	-22.70	-39.76	-54.14	N/A

Table 2.5: Multispecies vegetation on a uniform soil moisture profile at C-band for three different channels (HH, VV and HV). The total radar backscatter (TOT) is split into its scattering contributions by volume scattering (VOL), branch-ground double bounce (BG), trunk-ground double bounce (TG) and ground scattering (G). For the multispecies OJP & YJP forest, the impact of soil moisture is minimal since the volume scattering is the major contribution. For the SMAPVEX12 forest, a difference of about 6-7 dB in HH and 2-4.5 dB in VV is observed in the total radar backscatter when modeling the forest as a single or a multi-species forest stand while maintaining the soil moisture profiles. The impact of the soil profiles for the multispecies SMAPVEX12 forest is about 1.5 dB in HH and about 1 dB in VV.

Description	Channel	*TOT*	*VOL*	*BG*	*TG*	*G*
	HH	-8.85	-8.85	-74.94	-70.03	-96.25
OJP & YJP Profile 4.A	VV	-9.96	-9.96	-106.09	-99.36	-114.60
	HV	-15.70	-15.70	-103.56	-124.64	N/A
	HH	-8.85	-8.85	-73.56	-68.65	-94.87
OJP & YJP Profile 4.B	VV	-9.96	-9.96	-103.80	-97.07	-112.61
	HV	-15.70	-15.70	-103.63	-124.71	N/A
	HH	-8.85	-8.85	-63.82	-58.91	-92.82
OJP & YJP Profile 5.A	VV	-9.96	-9.96	-88.65	-81.93	-109.51
	HV	-15.70	-15.70	-97.57	-118.65	N/A
	HH	-8.85	-8.85	-73.34	-68.48	-94.70
OJP & YJP Profile 5.B	VV	-9.96	-9.96	-103.51	-96.77	-112.35
	HV	-15.70	-15.70	-103.67	-124.71	N/A
	HH	-6.44	-8.46	-18.76	-11.53	-31.31
SMAPVEX12 Profile 4.A	VV	-8.66	-8.96	-28.52	-21.76	-30.24
	HV	-22.25	-22.27	-45.36	-60.21	N/A
	HH	-5.88	-8.46	-17.38	-10.15	-29.93
SMAPVEX12 Profile 4.B	VV	-8.47	-8.96	-26.22	-19.47	-28.25
	HV	-22.45	-22.27	-45.43	-60.28	N/A
	HH	-4.83	-8.46	-15.32	-8.09	-27.88
SMAPVEX12 Profile 5.A	VV	-7.95	-8.96	-22.75	-16.00	-25.14
	HV	-22.26	-22.27	-46.74	-61.57	N/A
	HH	-5.80	-8.46	-17.21	-9.98	-29.75
SMAPVEX12 Profile 5.B	VV	-8.44	-8.96	-25.93	-19.18	-27.99
	HV	-22.25	-22.27	-45.48	-60.30	N/A

Table 2.6: Multispecies vegetation on a soil moisture profile at C-band for three different channels (HH, VV and HV). The total radar backscatter (TOT) is split into its scattering contributions by volume scattering (VOL), branch-ground double bounce (BG), trunk-ground double bounce (TG) and ground scattering (G). For the SMAPVEX12 forest, a difference of up to 0.5 dB in HH and up to 0.3 dB in VV is observed when comparing the in-situ soil moisture profile against the uniform profile with the surface soil moisture assumption. At C-band, the sensed soil moisture can be considered to be the surface soil moisture.

Description	Channel	TOT	VOL	BG	TG	G
OJP & YJP Profile 4	HH	-8.85	-8.85	-75.27	-70.36	-96.09
	VV	-9.96	-9.96	-106.61	-99.87	-114.64
	HV	-15.70	-15.70	-103.52	-124.58	N/A
OJP & YJP Profile 4	HH	-8.85	-8.85	-70.53	-65.62	-92.80
	VV	-9.96	-9.96	-98.81	-92.08	-109.50
	HV	-15.70	-15.70	-105.72	-126.92	N/A
SMAPVEX12 Profile 5	HH	-6.56	-8.46	-19.08	-11.86	-31.15
	VV	-8.69	-8.96	-29.03	-22.27	-30.28
	HV	-22.25	-22.27	-45.32	-60.17	N/A
SMAPVEX12 Profile 5	HH	-4.26	-8.46	-14.35	-7.12	-27.86
	VV	-7.61	-8.96	-21.23	-14.48	-25.13
	HV	-22.26	-22.27	-47.53	-62.43	N/A

Table 2.7: Single species vegetation on a uniform soil moisture profile at L-band for three different channels (HH, VV and HV). The total radar backscatter (TOT) is split into its scattering contributions by volume scattering (VOL), branch-ground double bounce (BG), trunk-ground double bounce (TG) and ground scattering (G). The single species OJP forest is opaque for L-band frequencies due to the dense canopy for this particular sample forest. For a single species TA forest, the impact of the soil moisture profiles on the total radar backscatter is about 3.5 dB in HH and 5 dB in VV.

Description	Channel	*TOT*	*VOL*	*BG*	*TG*	*G*
OJP Profile 4.A	HH	-11.86	-11.86	-76.18	-74.11	-97.48
	VV	-9.07	-9.07	-124.23	-121.52	-135.42
	HV	-14.99	-14.99	-115.61	-127.57	N/A
OJP Profile 4.B	HH	-11.86	-11.86	-74.71	-72.64	-96.01
	VV	-9.07	-9.07	-121.97	-119.09	-133.28
	HV	-14.99	-14.99	-115.82	-127.78	N/A
OJP Profile 5.A	HH	-11.86	-11.86	-72.72	-70.65	-94.02
	VV	-9.07	-9.07	-118.73	-115.75	-130.24
	HV	-14.99	-14.99	-117.42	-129.49	N/A
OJP Profile 5.B	HH	-11.86	-11.86	-61.00	-58.92	-95.83
	VV	-9.07	-9.07	-95.61	-92.92	-133.02
	HV	-14.99	-14.99	-86.64	-98.59	N/A
TA Profile 4.A	HH	-1.79	-20.48	-13.01	-2.24	-22.19
	VV	-8.34	-17.81	-21.45	-9.55	-19.17
	HV	-21.86	-22.22	-33.32	-42.89	N/A
TA Profile 4.B	HH	-0.34	-20.48	-11.55	-0.77	-20.73
	VV	-6.14	-17.81	-19.01	-7.11	-17.04
	HV	-21.88	-22.22	-33.53	-43.09	N/A
TA Profile 5.A	HH	1.63	-20.48	-9.56	1.21	-18.74
	VV	-2.98	-17.81	-15.66	-3.76	-14.00
	HV	-21.98	-22.22	-35.13	-44.71	N/A
TA Profile 5.B	HH	-0.17	-20.48	-11.37	-0.60	-20.55
	VV	-5.86	-17.81	-18.71	-6.81	-16.77
	HV	-21.88	-22.22	-33.59	-43.17	N/A

Table 2.8: Multispecies vegetation on a uniform soil moisture profile at L-band for three different channels (HH, VV and HV). The total radar backscatter (TOT) is split into its scattering contributions by volume scattering (VOL), branch-ground double bounce (BG), trunk-ground double bounce (TG) and ground scattering (G). The multispecies OJP & YJP forest is opaque for L-band frequencies due to the dense canopy for this particular sample forest. A difference of 7-8 dB in HH and 5-7 dB in VV is observed when adding a young regrowth TA forest with understory to the mature TA forest while maintaining the soil moisture profiles. The impact of the soil moisture profiles on the total radar backscatter for the multispecies SMAPVEX12 forest is about 3 dB in HH and 3 dB in VV.

Description	Channel	*TOT*	*VOL*	*BG*	*TG*	*G*
	HH	-11.86	-11.86	-74.29	-72.14	-98.06
OJP & YJP Profile 4.A	VV	-9.07	-9.07	-122.50	-119.73	-136.12
	HV	-14.99	-14.99	-113.79	-125.41	N/A
	HH	-11.86	-11.86	-72.83	-70.68	-96.59
OJP & YJP Profile 4.B	VV	-9.07	-9.07	-120.18	-117.31	-133.98
	HV	-14.99	-14.99	-113.99	-125.60	N/A
	HH	-11.86	-11.86	-70.84	-68.69	-94.61
OJP & YJP Profile 5.A	VV	-9.07	-9.07	-116.97	-113.96	-130.94
	HV	-14.99	-14.99	-115.60	-127.22	N/A
	HH	-11.86	-11.86	-72.65	-70.50	-96.42
OJP & YJP Profile 5.B	VV	-9.07	-9.07	-119.91	-117.01	-133.72
	HV	-14.99	-14.99	-114.06	-125.70	N/A
	HH	-9.30	-17.72	-15.45	-11.48	-30.99
SMAPVEX12 Profile 4.A	VV	-13.09	-15.22	-24.12	-18.61	-28.31
	HV	-19.19	-19.29	-35.83	-46.86	N/A
	HH	-8.02	-17.72	-13.98	-10.01	-29.53
SMAPVEX12 Profile 4.B	VV	-11.98	-15.22	-21.67	-16.17	-26.17
	HV	-19.20	-19.29	-36.04	-47.07	N/A
	HH	-6.21	-17.72	-11.99	-8.02	-27.54
SMAPVEX12 Profile 5.A	VV	-9.92	-15.22	-18.33	-12.82	-23.13
	HV	-19.23	-19.29	-37.65	-48.67	N/A
	HH	-7.86	-17.72	-13.80	-9.83	-29.35
SMAPVEX12 Profile 5.B	VV	-11.82	-15.22	-21.38	-15.87	-25.90
	HV	-19.20	-19.29	-36.11	-47.13	N/A

Table 2.9: Multispecies vegetation on a soil moisture profile at L-band for three different channels (HH, VV and HV). The total radar backscatter (TOT) is split into its scattering contributions by volume scattering (VOL), branch-ground double bounce (BG), trunk-ground double bounce (TG) and ground scattering (G). The multispecies OJP & YJP forest is opaque for L-band frequencies due to the dense canopy for this particular sample forest. A difference up to 1 dB in HH and up to 1.2 dB in VV is observed when comparing the in-situ soil moisture profiles with the uniform profile with the surface soil moisture assumption. The sensed soil moisture difference between the uniform and in-situ profiles is noticeable in the total radar backscatter of the SMAPVEX12 forest.

Description	Channel	*TOT*	*VOL*	*BG*	*TG*	*G*
OJP & YJP Profile 4	HH	-11.86	-11.86	-74.63	-72.48	-98.52
	VV	-9.07	-9.07	-122.97	-120.28	-136.41
	HV	-14.99	-14.99	-113.74	-125.38	N/A
OJP & YJP Profile 4	HH	-11.86	-11.86	-69.75	-67.60	-92.27
	VV	-9.07	-9.07	-115.29	-112.25	-129.87
	HV	-14.99	-14.99	-116.59	-128.12	N/A
SMAPVEX12 Profile 5	HH	-9.59	-17.72	-15.79	-11.82	-31.45
	VV	-13.28	-15.22	-24.65	-19.14	-28.59
	HV	-19.19	-19.29	-35.79	-46.82	N/A
SMAPVEX12 Profile 5	HH	-5.18	-17.72	-10.91	-6.94	-25.21
	VV	-8.69	-15.22	-16.62	-11.12	-22.06
	HV	-19.24	-19.29	-38.64	-49.67	N/A

Table 2.10: Single species vegetation on a uniform soil moisture profile at P-band for three different channels (HH, VV and HV). The total radar backscatter (TOT) is split into its scattering contributions by volume scattering (VOL), branch-ground double bounce (BG), trunk-ground double bounce (TG) and ground scattering (G). The impact of the soil moisture profiles on the total radar backscatter at P-band for both single species forests ranges around 3 dB in HH and 4-5 dB in VV.

Description	Channel	*TOT*	*VOL*	*BG*	*TG*	*G*
	HH	-7.11	-18.44	-17.77	-7.80	-30.75
OJP Profile 4.A	VV	-9.26	-13.80	-30.78	-11.30	-26.66
	HV	-20.21	-20.45	-39.94	-33.86	N/A
	HH	-5.77	-17.44	-17.31	-6.44	-29.30
OJP Profile 4.B	VV	-7.55	-13.80	-28.42	-8.88	-24.54
	HV	-20.22	-20.45	-40.16	-34.08	N/A
	HH	-3.91	-17.44	-15.34	-4.47	-27.32
OJP Profile 5.A	VV	-4.81	-13.80	-25.14	-5.55	-21.52
	HV	-20.29	-20.45	-41.78	-35.70	N/A
	HH	-5.61	-17.44	-17.14	-6.27	-29.12
OJP Profile 5.B	VV	-7.32	-13.80	-28.13	-8.59	-24.28
	HV	-20.23	-20.45	-40.23	-34.15	N/A
	HH	-5.17	-18.38	-17.12	-5.72	-26.35
TA Profile 4.A	VV	-8.71	-16.15	-27.02	-9.91	-22.03
	HV	-21.67	-22.03	-37.57	-34.30	N/A
	HH	-3.77	-18.38	-15.67	-4.26	-24.90
TA Profile 4.B	VV	-6.65	-16.15	-24.60	-7.48	-19.91
	HV	-21.68	-22.03	-37.79	-34.52	N/A
	HH	-1.85	-18.38	-13.69	-2.29	-22.93
TA Profile 5.A	VV	-3.60	-16.15	-21.28	-4.16	-16.89
	HV	-21.79	-22.03	-39.41	-36.14	N/A
	HH	-3.60	-18.38	-15.49	-4.09	-24.73
TA Profile 5.B	VV	-6.39	-16.15	-24.31	-7.19	-19.65
	HV	-21.69	-22.03	-37.86	-34.59	N/A

Table 2.11: Multispecies vegetation on a uniform soil moisture profile at P-band for three different channels (HH, VV and HV). The total radar backscatter (TOT) is split into its scattering contributions by volume scattering (VOL), branch-ground double bounce (BG), trunk-ground double bounce (TG) and ground scattering (G). When adding understory while maintaining the soil moisture profiles, a difference of about 1.2 dB in HH and 2.8 dB in VV is observed for the OJP & YJP forest, while a difference of about 3.3 dB in HH and 2.2 dB in VV is observed for the SMAPVEX12 forest. The impact of the soil moisture profiles for the multispecies forests is about 3 dB in HH and 5 dB in VV.

Description	Channel	*TOT*	*VOL*	*BG*	*TG*	*G*
	HH	-5.99	-17.43	-18.86	-6.58	-30.86
OJP & YJP Profile 4.A	VV	-6.75	-13.79	-30.35	-7.79	-26.27
	HV	-20.11	-20.44	-39.76	-32.12	N/A
	HH	-4.63	-17.43	-17.41	-5.13	-29.41
OJP & YJP Profile 4.B	VV	-4.72	-13.79	-27.98	-5.37	-24.14
	HV	-20.13	-20.44	-39.98	-32.34	N/A
	HH	-2.74	-17.43	-15.43	-3.15	-27.44
OJP & YJP Profile 5.A	VV	-1.69	-13.79	-24.70	-2.05	-21.12
	HV	-20.22	-20.44	-41.60	-33.95	N/A
	HH	-4.46	-17.43	-17.23	-4.95	-29.23
OJP & YJP Profile 5.B	VV	-4.46	-13.79	-27.69	-5.08	-23.88
	HV	-20.13	-20.44	-40.05	-32.40	N/A
	HH	-8.23	-13.88	-15.34	-11.00	-31.06
SMAPVEX12 Profile 4.A	VV	-6.31	-11.94	-25.17	-7.83	-26.56
	HV	-17.54	-17.68	-35.76	-35.27	N/A
	HH	-7.12	-13.88	-13.88	-9.55	-29.61
SMAPVEX12 Profile 4.B	VV	-4.43	-11.94	-22.75	-5.41	-24.43
	HV	-17.54	-17.68	-35.97	-35.49	N/A
	HH	-5.50	-13.88	-11.91	-7.57	-27.63
SMAPVEX12 Profile 5.A	VV	-1.54	-11.94	-19.42	-2.08	-21.41
	HV	-17.58	-17.68	-37.59	-37.11	N/A
	HH	-6.98	-13.88	-13.71	-9.37	-29.43
SMAPVEX12 Profile 5.B	VV	-4.19	-11.94	-22.45	-5.11	-24.17
	HV	-17.54	-17.68	-36.04	-35.56	N/A

Table 2.12: Multispecies vegetation on a soil moisture profile at P-band for three different channels (HH, VV and HV). The total radar backscatter (TOT) is split into its scattering contributions by volume scattering (VOL), branch-ground double bounce (BG), trunk-ground double bounce (TG) and ground scattering (G). A difference up to 2.8 dB in HH and 4.4 dB in VV is observed when comparing the in-situ with the uniform soil moisture profiles for both multispecies forests. The sensed soil moisture is a soil moisture column as the radar signal penetrates deeper into the soil.

Description	Channel	*TOT*	*VOL*	*BG*	*TG*	*G*
	HH	-6.24	-17.43	-19.16	-6.85	-30.18
OJP & YJP Profile 4	VV	-7.08	-13.79	-30.76	-8.22	-26.12
	HV	-20.11	-20.44	-39.69	-32.05	N/A
	HH	-1.67	-17.43	-14.31	-2.04	-32.10
OJP & YJP Profile 4	VV	-0.07	-13.79	-22.97	-0.30	-23.60
	HV	-20.27	-20.44	-42.66	-35.01	N/A
	HH	-8.42	-13.88	-15.61	-11.27	-30.37
SMAPVEX12 Profile 5	VV	-6.60	-11.94	-25.59	-8.25	-26.41
	HV	-17.53	-17.68	-35.69	-35.21	N/A
	HH	-4.55	-13.88	-10.80	-6.46	-32.30
SMAPVEX12 Profile 5	VV	0.04	-11.94	-17.68	-0.34	-32.89
	HV	-17.60	-17.68	-38.65	-38.89	N/A

and investigating the impact of slope.

CHAPTER III

Retrieval of soil moisture at fine scales

3.1 Introduction

For several decades active and passive microwave remote sensing have been used to observe vegetation and soil due to their sensitivity to vegetation and soil dielectric constants. Extensive studies have been conducted to investigate the dielectric properties of vegetation [63–65] and soil [66] at microwave frequencies, and subsequently dielectric models have been developed for both vegetation [67, 68] and soils [2, 3, 51, 52, 69]. These create the link between bio- and geophysical parameters and the sensed dielectric constants, and therefore allow the retrieval of bio-and geophysical parameters based on microwave remote sensing observations. Passive remote sensing has a long standing tradition of both instrument development and soil moisture retrieval. In recent years, active remote sensing has come into the spotlight due to its higher resolution and greater sensitivity to vegetation, surface roughness, and topography. This sensitivity was initially discarded as an interference to the soil moisture retrieval process, but it also holds the key to retrieve soil moisture on a finer scale while the availability of increasingly detailed ancillary data layers allows improved modeling of vegetation, surface roughness and topography. Coarse-scale heterogeneous scenes can be broken down into fine-scale pixels that can be assumed homogeneous and for which ancillary data is available. At this resolution and with

the homogeneous pixel assumption, the parametrization of radar forward models can be closely related to the physical structure of the soil and vegetation, allowing for a high-fidelity retrieval of soil moisture at fine-scales. These fine-scale pixels then allow the analysis of heterogeneous scenes and the retrieval of coarse-scale soil moisture.

Radar retrieval techniques can be divided into two major groups: classification and estimation/inversion. Classification algorithms utilize the radar observations to identify into which category an observation belongs and thereby classify bio- and geophysical parameters. There are two subcategories: supervised and unsupervised classification. An example for a supervised classification is a threshold-based classification to map wetland extend based on radar [70, 71]. Generally, supervised classification does not utilize the physical properties of the scene and only depends on the radar data itself. Unsupervised classification on the other hand more closely depends on the physical properties of the scene as it utilizes radar scattering models to classify radar observations [72–76]. Estimation/inversion depends on direct retrieval of geophysical parameters from radar observations using either empirical or theoretical scattering models. Empirical regression models are commonly utilized to retrieve biomass [77–79] or other biophysical characteristics such as basal area, height and dry crown biomass [80] or crown and stem water content [81]. Scattering models can also be used to train neural networks to estimate forest parameters [82, 83] or to obtain statistics of the retrieval parameters that are then used in a Bayesian estimation [84]. Another approach uses scattering models to generate lookup tables or data cubes to retrieve soil moisture under vegetation [85]. This approach is the the baseline retrieval approach for the SMAP L2/L3 radar soil moisture (active) data products. Finally, parameter retrieval can be achieved by directly inverting forest variables from radar scattering data with the use of theoretical scattering models (i.e., the biophysical parameters such as tree moisture [86] or subcanopy soil moisture [87]). A more extensive discussion on the different retrieval techniques is given in [88].

The research work discussed in this chapter is based on the heritage of direct retrieval based on theoretical scattering models and focuses on fine-scale soil moisture retrieval under densely vegetated scenes. The SMAP mission combined active/passive soil moisture requirement is an RMSE of less than 0.04 $\frac{cm^3}{cm^3}$ for a 9 km pixel resolution, and for radar-only an RMSE of less than 0.06 $\frac{cm^3}{cm^3}$ with a 3 km resolution. The AirMOSS project requirement is an RMSE of less than 0.05 $\frac{cm^3}{cm^3}$ over all sites, dates and years, for both 0.5 ($\sim$ 15 m) and 3 ($\sim$ 90 m) arc second resolution pixels. Motivated by these requirements, fine-scale soil moisture retrieval is shown for a surface soil moisture in chapter 3.3 and a soil moisture profile in chapter 3.4.

3.2   General retrieval procedure

The inversion problem sets out to determine a vector of unknown parameters $\mathbf{X}$ given a set of measured radar data d_{pq} and a forward scattering model $\sigma_{pq}^o(\mathbf{X}, p) = f(\mathbf{X}, p)$ where the function f represents the forward scattering model and the vector p represents the known measurement parameters (i.e. frequency and incidence angle). The goal is to locate the most probable set of model parameters $\mathbf{X}$ given the measured radar data d_{pq}.

The simulated annealing method is used to minimize a cost function that is based on the difference between measured and forward simulated backscattering coefficients. The used simulated annealing scheme is based on the algorithm by Corana *et al.* [89, 90]. The cost function used here is defined as follows:

$$L(\mathbf{X}) = \sum_{pq} \left(\frac{10 \log \sigma_{pq}^o(\mathbf{X}, p) - 10 \log d_{pq}}{10 \log d_{pq}} \right)^2 \tag{3.1}$$

where $\sigma_{pq}^o(\mathbf{X}, p)$ and d_{pq} are the forward simulated and measured backscattering coefficient of the forested area with $(p, q) \in \{H, V\}$. The quantities $\sigma_{pq}^o(\mathbf{X}, p)$ and d_{pq} are expressed in decibels to make L more sensitive to changes in the model parame-

ters during inversion. The simulated annealing method is inspired by the annealing process of metals. After starting at an initial guess at an initial temperature T, this hypothetical temperature is slowly lowered to find the global minimum. At each temperature level, a small perturbation is applied to the current model parameters and the cost function is evaluated. If the cost function value is decreased (i.e. $\Delta L \leq 0$), the new state is accepted. Otherwise the new state is accepted with a probability $e^{-\Delta/T}$, which is called the Metropolis criterion [91]. This step is iterated until the maximum number of iterations at this state is reached, then the best point of this set is selected and the temperature is further reduced. The iteration then continues at the lower temperature starting from the current new point. The inversion stops when the cost function value becomes smaller than a defined limit (i.e. a global minimum is found) or when the total number of function evaluations are exhausted. More details of the simulated annealing implementation are given in [89, 90, 92].

3.3 Retrieval of fine-scale soil moisture with CanEx-SM2010 data

In this section, the radar based retrieval of soil moisture for a range of boreal forests is shown [93]. The retrieval is formulated as an optimization problem as defined in chapter 3.2. The inversion algorithm is validated using L-band data from NASA/ JPL UAVSAR from June 2010 over boreal forests in central Canada in support of pre-launch calibration and validation activities for NASA's SMAP mission. Field work was conducted during overflight days in 2010.

During CanEx-SM2010, the NASA/ JPL UAVSAR acquired fully polarimetric L-band radar measurements. Three sample sites are used for this retrieval validation: an OJP, YJP and Old Black Spruce (OBS) forest, all located within the BERMS super site north of Prince Albert National Park in Saskatchewan, Canada. All three

Figure 3.1: Sample sites consisting of OJP, YJP and OBS forests (from top left over top right to bottom).

Figure 3.2: The ground measurement locations for the OJP, YJP, and OBS sites. The 15 x 6 pixel area, over which HH, VV, and HV backscattering coefficients of each pixel are available, is illustrated in each figure. The pixels for which ground measurements of soil moisture are available are indicated with 'OJP', 'YJP', and 'OBS', respectively. Each 18 m x 36 m pixel is formed by averaging the measured radar backscattering coefficients over the corresponding 3 x 3 pixel block.

sites are typical boreal forest biomes. A visualization of the three forest stands can be seen in Fig. 3.1. The OJP site is a sparse forest with columnar trees on a dry sandy loam ground that is densely covered with dry lichen. The YJP site contains the same tree species, although at a younger growth stage. The young trees are pyramidally shaped on a very dry sandy ground with short and sparse ground cover. The OBS site contains coniferous trees on a wet loam ground, which is complicated by moss and a thick organic layer, as well as water puddles and bushy understory. Ground measurements at each site consisted of a 100 m long transect as shown in Fig. 3.2. Soil moisture was recorded with a Steven's Portable Hydra Probe at each 10 m point within the transect. Vegetation measurements, such as total tree height, canopy and trunk height, trunk radius and tree count were taken along the entire transect line. At each site, one average tree was destructively sampled to record sample radii and lengths of large/small branches and sample leaf dimensions. The mean orientation angle and distribution around the mean angle of the branches were deduced from photographs and visualization in the field. The RMS height of the soil roughness was noted from inspection in the field. The soil type is based on a previous soil type assessment during BOREAS and was found to be 70 percent sand, 10 percent clay and $1.57 \frac{g}{cm^3}$ bulk density for OJP; 90 percent sand, 4 percent clay and $1.57 \frac{g}{cm^3}$ bulk density for YJP; and 51.5 percent sand, 13.5 percent clay and $1.49 \frac{g}{cm^3}$ bulk density for OBS. The remaining parameters necessary to define the relationship of soil moisture with dielectric constant with the model by Peplinski *et al.* [2, 3] are chosen based on typical boreal forest environment: soil temperature of $10° C$ and water salinity of 4 gram salt per kg water for all sites. The dielectric constants of tree trunks and branches were measured in the field with a dielectric probe provided by JPL, but the measurements were found unreliable due to calibration problems. Therefore, the dielectric constant of the vegetation was calculated with the dual dispersion model by Ulaby and El-Rayes [67]. The field work measurement data

Table 3.1: Parameters of the OJP forest based on measurements collected during CanEx-SM2010.

Parameter	Measured Value	Parameter	Measured Value
Canopy Height	11.4 m	SB Orientation	70°
LB Dielectric	32-j4	Needle Dielectric	32-j4
LB Length	1.2 m	Needle Length	3 cm
LB Radius	0.66 cm	Needle Radius	0.15 cm
LB Density	$0.54/m^3$	Needle Density	$1728/m^3$
LB Orientation	80°	Trunk Dielectric	36-j2
SB Dielectric	32-j4	Trunk Length	2.0 m
SB Length	0.8 m	Trunk Radius	6.8 cm
SB Radius	0.46 cm	Trunk Density	$0.25/m^2$
SB Density	$0.54/m^3$		

Table 3.2: Parameters of the YJP forest based on measurements collected during CanEx-SM2010.

Parameter	Measured Value	Parameter	Measured Value
Canopy Height	1.8 m	SB Orientation	40°
LB Dielectric	32-j4	Needle Dielectric	32-j4
LB Length	0.5 m	Needle Length	2 cm
LB Radius	0.35 cm	Needle Radius	0.1 cm
LB Density	$17/m^3$	Needle Density	$2000/m^3$
LB Orientation	80°	Trunk Dielectric	32-j4
SB Dielectric	32-j4	Trunk Length	5.0 cm
SB Length	0.2 m	Trunk Radius	2 cm
SB Radius	0.15 cm	Trunk Density	$0.4/m^2$
SB Density	$60/m^3$		

was extrapolated to represent the entire 15 x 6 pixel area. This is a reasonable assumption since the three sample sites are highly homogeneous in vegetation. The single-species vegetation model with a single soil layer by Durden *et al.* [19] is chosen as the scattering model for this retrieval and the used vegetation parameters are given in Tables 3.1, 3.2, and 3.3. The source of the input parameters for the multispecies multilayer model (measurement, allometrics, photographs or estimation) is given in Fig. 2.10.

The UAVSAR radar data were post-processed by georeferencing and mosaicking multiple flight swaths into one image. Figure 3.3 shows the L-band UAVSAR data

Table 3.3: Parameters of the OBS forest based on measurements collected during CanEx-SM2010.

Parameter	Measured Value	Parameter	Measured Value
Canopy Height	5.1 m	SB Orientation	80°
LB Dielectric	32-j8	Needle Dielectric	32-j8
LB Length	0.55 m	Needle Length	1 cm
LB Radius	0.5 cm	Needle Radius	0.05 cm
LB Density	$2.83/m^3$	Needle Density	$7545/m^3$
LB Orientation	100°	Trunk Dielectric	12-j3
SB Dielectric	32-j8	Trunk Length	2.0 m
SB Length	0.55 m	Trunk Radius	3.7 cm
SB Radius	0.5 cm	Trunk Density	$0.72/m^2$
SB Density	$14.2/m^3$		

over the BERMS super site including the OJP, YJP, and OBS sample sites. An area of 15 x 6 pixels centered on the 100 m transect is extracted for each site. Each pixel provides HH, VV and HV radar backscattering coefficients at a 6 m x 12 m resolution. Figure 3.2 shows the overlay of the transects with the extracted radar data. Larger pixels are then formed by averaging the backscattering coefficients of a 3 x 3 block, creating a 18 m x 36 m pixel. The local incidence angle for each site is extracted from the radar data and used in the simulation.

The inversion algorithm is applied for two data sets for each site. The first data set is the measured radar backscattering coefficients for the original 6 m x 12 m pixels that contain in-situ surface soil moisture measurements. The 6 m x 12 m pixels marked with 'OJP', 'YJP', and 'OBS' are shown in Fig. 3.2. The second data set are the radar backscattering coefficients over the 18 m x 36 m pixels, which is the linear average of the 6 m x 12 m pixels. The soil moisture for each 18 m x 36 m pixel is the average of the available in-situ soil moisture of the 6 m x 12 m pixels within that block. The frequency used is 1.25 GHz, and the observation angles for the OJP, YJP, and OBS sites are 22.7°, 38.1°, and 42.2°.

A major challenge in a direct inversion of forest variables from radar scattering data with the use of a scattering model is the large number of unknowns compared to
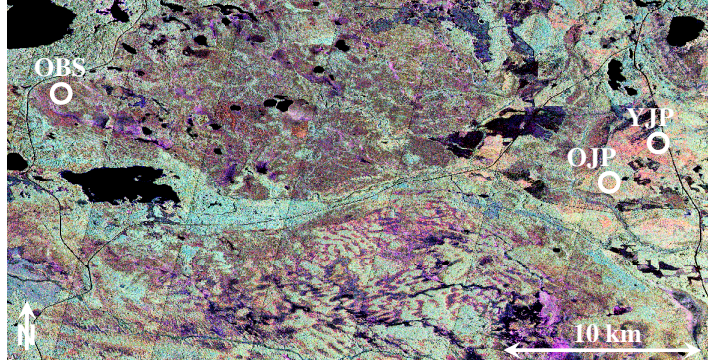
Figure 3.3: L-band UAVSAR radar data over OJP, YJP and OBS given as an RGB (HH, VV, HV) image. Locations of the OJP, YJP and OBS sites are marked with white circles. The sites are located at (53.916, -104.692) for OJP, (53.945, -104.650) for YJP, and (53.987, -105.118) for OBS.

the number of radar measurements. This can potentially lead to an under-determined problem with multiple solutions. Ideally, multiple frequencies and incidence angles would be utilized to increase the number of unknowns that can be retrieved. In this case, the vegetation parameters are assumed known and only the soil moisture and the RMS soil roughness height are retrieved. Therefore, only the the L-band co-pol backscattering coefficients are used for inversion.

Figure 3.4 shows the retrieved soil moisture error for the 6 m x 12 m and 18 m x 36 m pixels at the OJP site. The RMSE is 0.043 and 0.03, respectively. Errors are expressed in $\frac{cm^3}{cm^3}$. Figure 3.5 shows the retrieved soil moisture error for the 6 m x 12 m and 18 m x 36 m pixels at the YJP site. Expressed in $\frac{cm^3}{cm^3}$, the RMSE is 0.02 and 0.022, respectively. Figure 3.6 shows the retrieved soil moisture error for the 6 m x 12 m pixels at the OBS site. The RMSE is 0.243 $\frac{cm^3}{cm^3}$. The retrieved soil moisture over the 18 m x 36 m pixels is shown in Fig. 3.7 with square markers, with
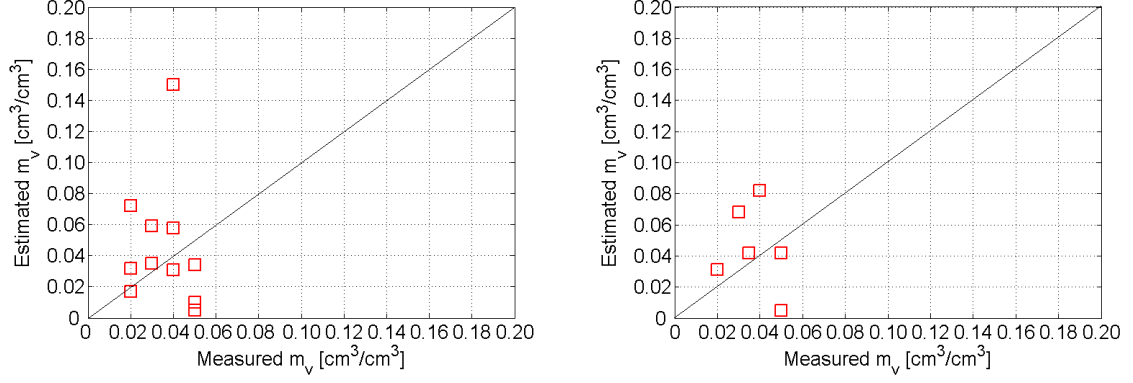
Figure 3.4: The retrieved soil moisture at the OJP site for the 6 m x 12 m (left) and 18 m x 36 m (right) pixels with an RMSE of 0.043 and 0.03 $\frac{cm^3}{cm^3}$, respectively.

an RMSE of $0.159\frac{cm^3}{cm^3}$. The dense vegetation canopy, the complexity of the understory and possible georeferencing errors are most likely cause for the inaccurate inversion at the OBS site. For the OBS site, the inversion algorithm is also applied to the radar backscattering coefficients of the 18 m x 36 m pixels, which is compared with the average of the retrieved soil moisture values for the corresponding 3 x 3 blocks. The retrieval is shown as an RMSE of 0.105 in Fig. 3.7 with the starred markers. The error bars show the minimum and maximum values of the retrieved soil moisture within the 3 x 3 block.

Retrievals for OJP and YJP show good accuracy and meet the 0.06 $\frac{cm^3}{cm^3}$ radar-only soil moisture retrieval requirement of SMAP. The retrieval for OBS are insufficient mostly due to the oversimplified modeling and complexity of the scene. In the future, improvements can be made by modeling the OBS site as a multispecies vegetation and taking into account the complex understory.
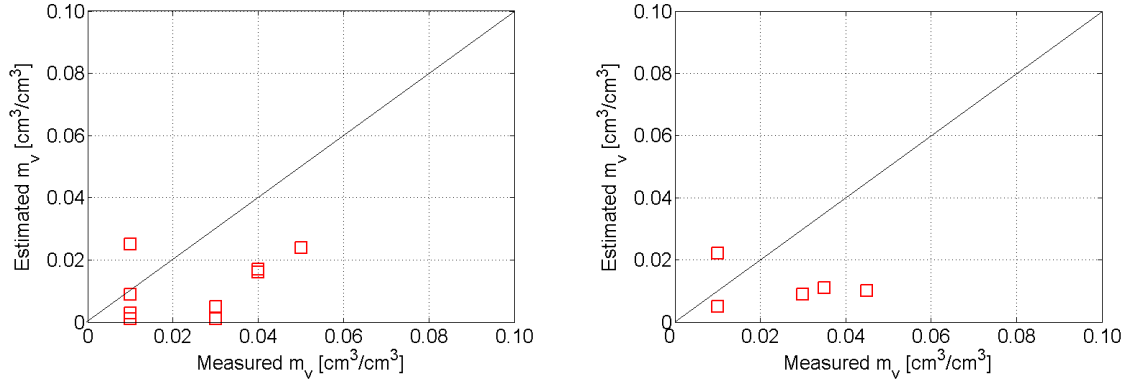
Figure 3.5: The retrieved soil moisture in the YJP site for the 6 m x 12 m (left) and 18 m x 36 m (right) pixels, over which the RMSE is 0.02 and 0.022 $\frac{cm^3}{cm^3}$, respectively.
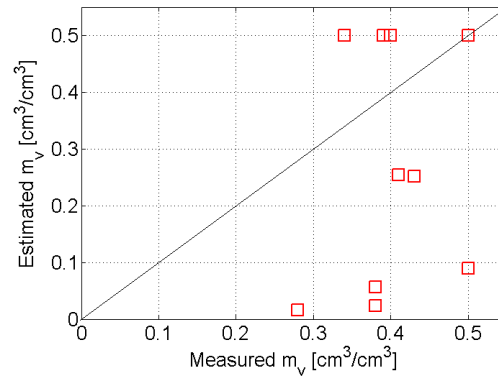
Figure 3.6: The retrieved soil moisture in the OBS site for the transect 6 m x 12 m pixels over which the RMSE is 0.243 $\frac{cm^3}{cm^3}$.
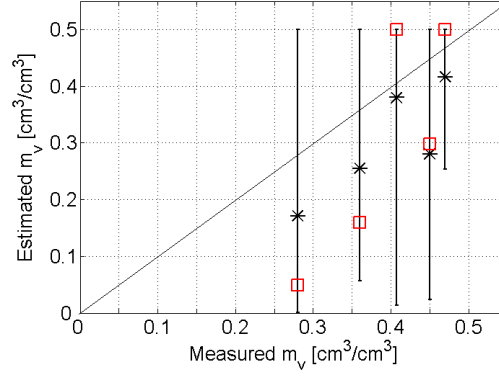
Figure 3.7: The square markers show the retrieved soil moisture in the OBS site for the 18 m x 36 m pixels over which the RMSE is 0.159 $\frac{cm^3}{cm^3}$. The starred markers shows the retrieved soil moisture over the 18 m x 36 m pixels calculated by averaging the retrieved soil moisture values of the 6 m x 12 m pixels contained in the corresponding 18 m x 36 m block. The RMSE is 0.105 $\frac{cm^3}{cm^3}$. The error bars over the starred markers show the minimum and maximum values of the retrieved soil moisture of the 6 m x 12 m pixels. The upper bound for soil moisture values is set to 0.50 $\frac{cm^3}{cm^3}$ in the inversion.

3.4 Retrieval of fine-scale soil moisture profile with AirMOSS data

In this section, the radar based retrieval of soil moisture profiles with AirMOSS data is shown [55]. First, a summary of the observed data, ancillary data and an overview of the data and work flow for the AirMOSS project is given. For complete details on the AirMOSS mission and its general data handling and processing, please refer to Appendix B. AirMOSS covers nine regions representative of the major North American biomes ranging from the boreal forests in Saskatchewan, Canada, to the tropical forests in La Selva, Costa Rica. AirMOSS seeks to improve the estimate of the North American Net Ecosystem Exchange (NEE) by providing high-resolution observations of Root Zone Soil Moisture (RZSM). An extensive radar data set has been accumulated since the start of the campaign in August 2012. This is achieved by flying a P-band SAR instrument to capture the gradients of soil, topography,

and vegetation heterogeneity over an area of 100 km x 25 km at each of the nine biomes. The high-resolution radar data are acquired by conducting three campaigns over the temperate sites (BERMS in Canada, Howland/Harvard in Massachusetts, Duke forest in North Carolina, Metolius in Oregon and Marena Oklahoma In Situ Sensor Testbed (MOISST) in Oklahoma), two campaigns over the savanna/grassland sites (Tonzi Ranch in California and Walnut Gulch in Arizona) and one campaign over the tropical sites (Chamela in Mexico and La Selva in Costa Rica) per year over a three year period. The nine biomes are described in more detail in Table B.1. The AirMOSS study sites cover a wide variety of vegetation covers, such that the retrieval algorithms may vary for different sites. In general, the sites are categorized into monospecies forested sites (including bare surfaces and grasslands) and mixed species forested sites. The following strategy applies to those biomes that have a predominance of monospecies vegetation at most of their image pixels (even if the pixels contain different types of monospecies vegetation): BERMS, Metolius, MOISST, Tonzi Ranch and Walnut Gulch. For the monospecies sites, the well-defined vegetation structure allows the use of the widely accepted discrete scatterer radar vegetation models [19, 37]. Along with scattering models of layered soil [45, 46], it is possible to calculate the radar measurement corresponding to a given land cover type and arbitrary soil moisture profile. The multichannel radar data set can then be used in snapshot mode to estimate the RZSM in an iterative scheme based on the full scattering model. The RZSM retrievals are performed such that for each pixel in the radar image, a smooth profile represented by a second-order polynomial is retrieved, as detailed in chapter 2.3.6. The retrieval is formulated as an optimization problem as defined in chapter 3.2. Extensive field campaigns are ongoing to collect ground truth data for vegetation structure throughout the AirMOSS radar swaths. These data are being used to parameterize the scattering models and hence making it possible to solve the retrieval problem for profiles of RZSM only. The accuracy requirement

for RZSM retrieval is 0.05 m^3/m^3 root-mean squared, when averaged over all campaigns, all years and all sites. For sites that have a predominance of mixed species vegetation, the retrievals are performed in a slightly different fashion by the team at JPL.

AirMOSS delivers polarimetric P-band radar backscattering coefficients at resolutions of 0.5 and 3 arc seconds over the nine mentioned biomes. On overflight days, each study site is covered by flying an area approximately 25 km wide and 100 km long with four to six flight swaths. Ancillary to the radar data, same-resolution files for incidence angle and slope are delivered. The above-ground vegetation is parameterized based solely on land cover type maps such as the NLCD map from 2006 at 1 arc second resolution [94] for sites inside the United States, and the GlobCover data product provided by European Space Agency (ESA) at 1 arc second resolution [95] for sites outside the United States. Extensive vegetation sampling is performed at the nine sites concurrent with the campaign to determine a standardized above-ground vegetation parametrization for each land cover type. The vegetation parameterization is validated by comparing the output of the forward model against radar data within the same scene. The below-ground information is based on soil texture data from SSURGO at 1 arc second resolution gap-filled with STATSGO2 data [96] for sites within the United States, and the Harmonized World Soil Database (HWSD) produced by the International Institute for Applied Systems Analysis (IIASA) at 1 arc second resolution [97] for sites outside the United States. The soil roughness of each soil interface and the soil temperature at each layer are determined based on field measurements.

The data volume of the observed and ancillary data layers is in general large, demanding special handling to reduce the data in the computer memory at all times. The data handling is divided into pre-flight and post-flight tasks. The pre-flight tasks consist of ingesting, pixel-to-pixel crosschecking, mosaicking, and performing general

quality control for the soils and land cover type information, as well as laying out the grid on which all data layers are oriented. This grid is about roughly the size of a 1-degree box centered around the flight lines. With the delivery of the radar data, the post-flight data handling is initiated. It includes the processing of the radar and their ancillary data layers, such as incidence angle and slope, to the base grid at 3 arc second resolution. The overlap areas of the flight swaths are selected based on their incidence angle and the prominent land cover type for each site: the radar data with the smaller incidence angle are chosen for Walnut Gulch and MOISST where mostly grassland or bare soil is expected. For Metolius, BERMS, and Tonzi Ranch, the pixel with the larger incidence angle is chosen. Next, the soil and land cover type information are scaled up to 3 arc second resolution, which are then used to identify pixels enabled for inversion. The 3 arc second pixels that are disabled (or masked out) are the pixels that 1) are classified by the NLCD as water, ice/snow, developed space (open space, low/medium/high intensity) or any of the wetland classes or 2) have a slope of more than 10 degrees. In a final step, all data layers are stacked and the vegetation parametrization according to land cover type is associated with each pixel. Each pixel is described with two general parameters (local incidence angle and wavelength), 31 parameters for the above-ground vegetation, 1 parameter specifying the number of soil layers (which can vary from site to site) and 8 parameters characterizing each soil layer. Additionally, each pixel will carry four flags consisting of one flag enabling the pixel inversion and three quality control flags for the land cover, slope, and soil, as well as the four observed radar channels for inversion. To speed up inversion, the total number of pixels is divided into segments for more efficient parallel processing on high-performance computing clusters. Currently, the High Performance Computing and Communications (HPCC) supercomputer cluster at University of Southern California (USC) and the High-End Computing Capability (HECC) cluster at the NASA Ames Research Center are used. Each utilized HPCC node has two Dodecacore AMD

102

Opteron 2.3 GHz processors with 48 GB of memory, and each utilized HECC node has two Quadcore Intel Xeon 3 GHz processors with 8 GB of memory. After successful inversion over all segments, the segmentation mask is used to assemble all segments into one data layer containing the three coefficients of the second-order polynomial (a, b, c) for each pixel from which the soil moisture at any depth within the validity range can be calculated. More details on the AirMOSS mission, the radar data, the ancillary data and the general data handling and processing of the AirMOSS campaign are given in Appendix B.

Ideally, multiple frequencies and observation angles would be available for soil moisture retrieval to increase the total number of unknowns to be retrieved. For the AirMOSS project, there is only 1 frequency (435 MHz) and 1 look angle within the range of 25°-65° available. Therefore, a method to estimate the surface and subsurface moisture without introducing a large number of unknowns has to be found. The proposed solution assumes a specific functional form for the soil moisture profile and estimates the parameters of that function, as introduced in chapter 2.3.6. A quadratic function is used as the AirMOSS baseline approach. The soil moisture profile has the form $SM(z) = a\,z^2 + b\,z + c$ where z is the depth and (a, b, c) are the coefficients to be retrieved from radar measurements. A preliminary version of this concept has been previously reported [54]. Results shown in this section use P-band radar data from three different dates in October 2012 acquired over the BERMS site in Canada. Field work at BERMS was conducted during CanEx-SM2010.

Figure 3.8 shows sample ancillary data layers over the AirMOSS BERMS site in Canada. The slope over the entire area is very small, less than 3 degrees in most areas. The incidence angle is provided along with the radar data and the mosaicked pattern of several flight lines can be clearly seen. The land cover type map is based on GlobCover and contains predominantly evergreen forest. The soil texture information is based on the HWSD and an example layer is given in Fig. 3.8 with the
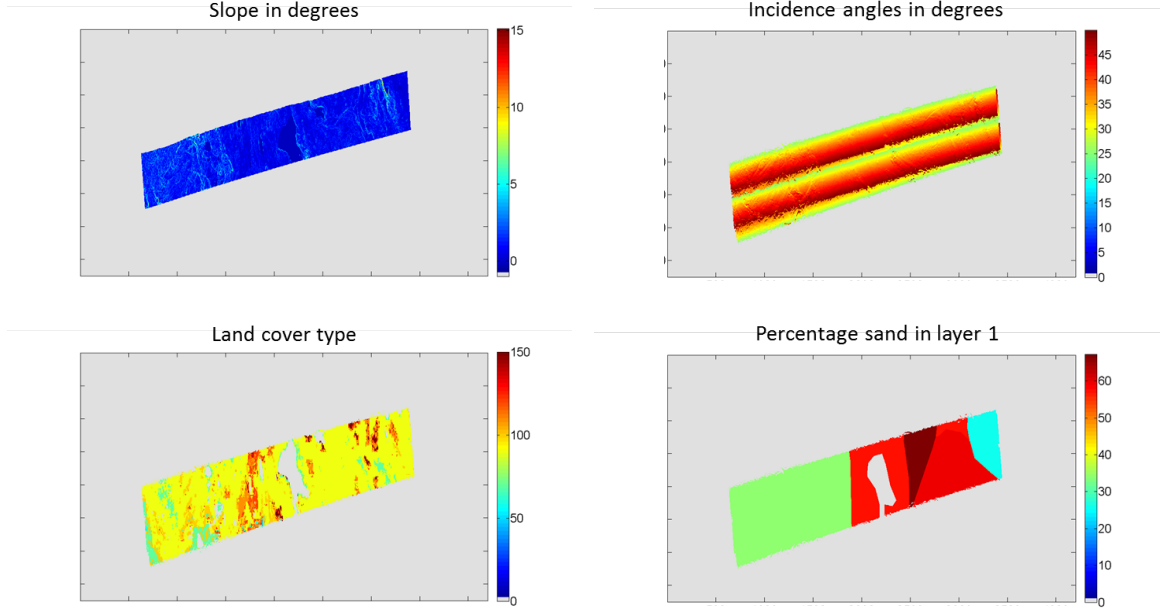
Figure 3.8: Sample ancillary data layers of the AirMOSS site in BERMS: slope in degrees (top left), incidence angle in degrees (top right), land cover type mask (bottom left), and percentage sand in layer 1 (bottom right).

percentage sand in the first layer. The soil texture information outside the United States is generally much coarser than inside the United States where SSURGO data gap-filled with STATSGO2 data is available.

Figures 3.9–3.11 show the retrieved soil moisture maps of the AirMOSS BERMS site in Canada at four sample depths of 0, 10, 30, and 75 cm for 4 October, 7 October, and 11 October 2012. For this set of inversions, twenty subsurface soil layers with a thickness of 5 cm for each have been used to discretize the unknown profile. The retrieval result is valid up to 95 cm [55].

The validation of the RZSM retrieval is conducted over land cover types of evergreen forest at BERMS in Saskatchewan, Canada. In-situ soil moisture probes installed near the flux tower site are used for validation. The in-situ soil moisture installations are supervised by AirMOSS collaborators at Oregon State University. Multiple soil moisture profiles are installed at each location with probes at various depths. The retrieved soil moisture profiles are compared against the available soil
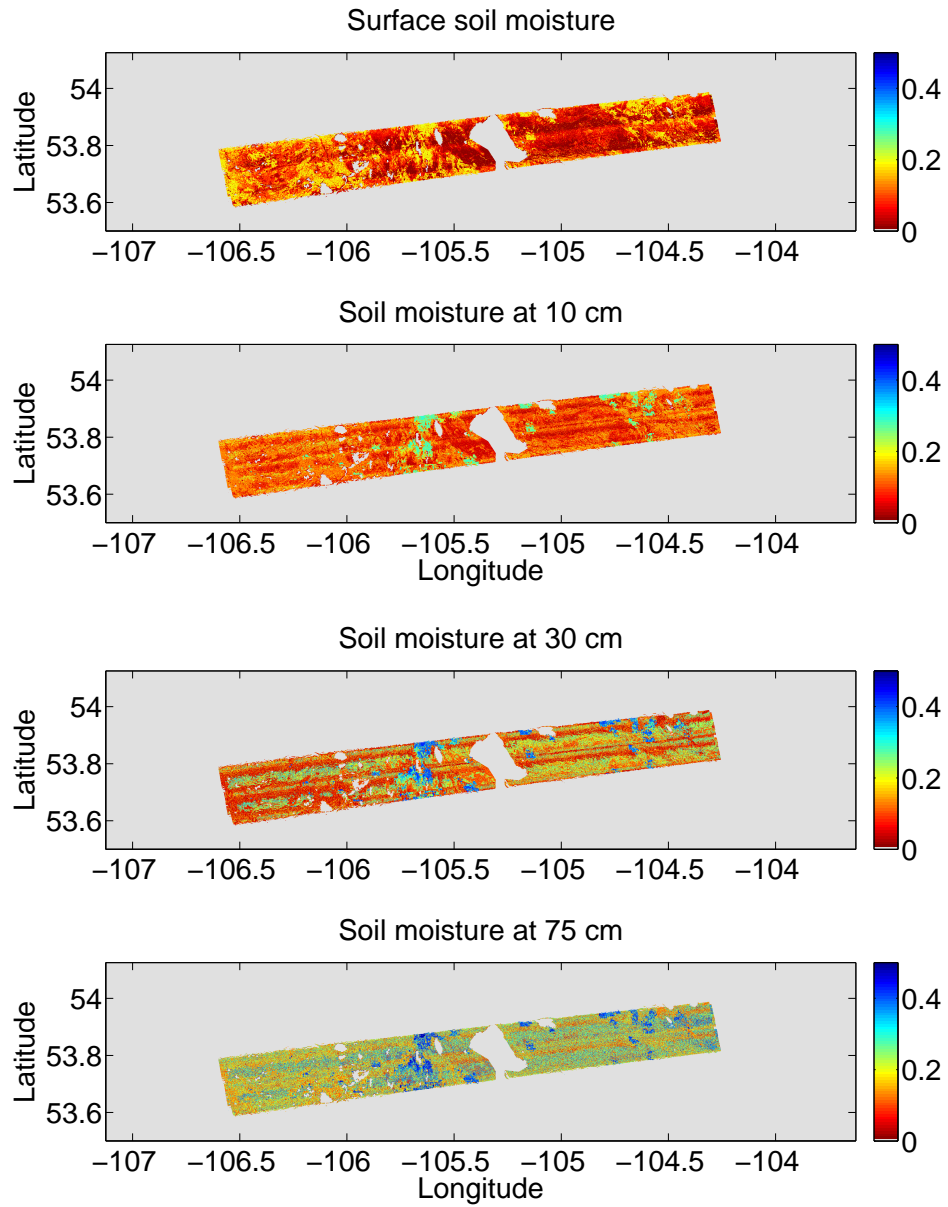
Figure 3.9: Map of soil moisture of the AirMOSS site in BERMS at four sample depths of 0, 10, 30, and 75 cm estimated by the inversion algorithm for 4 October 2012.
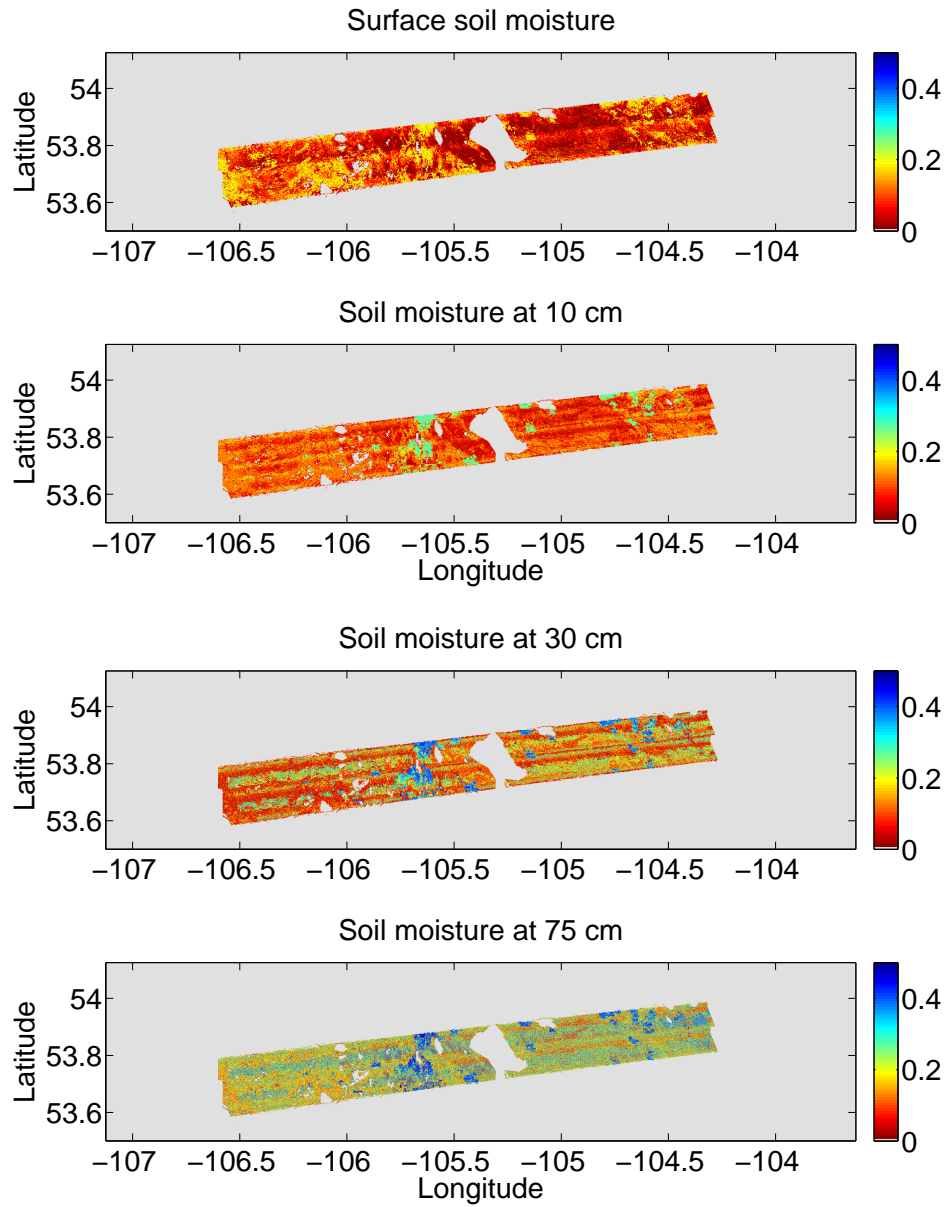
Figure 3.10: Map of soil moisture of the AirMOSS site in BERMS at four sample depths of 0, 10, 30, and 75 cm estimated by the inversion algorithm for 7 October 2012.
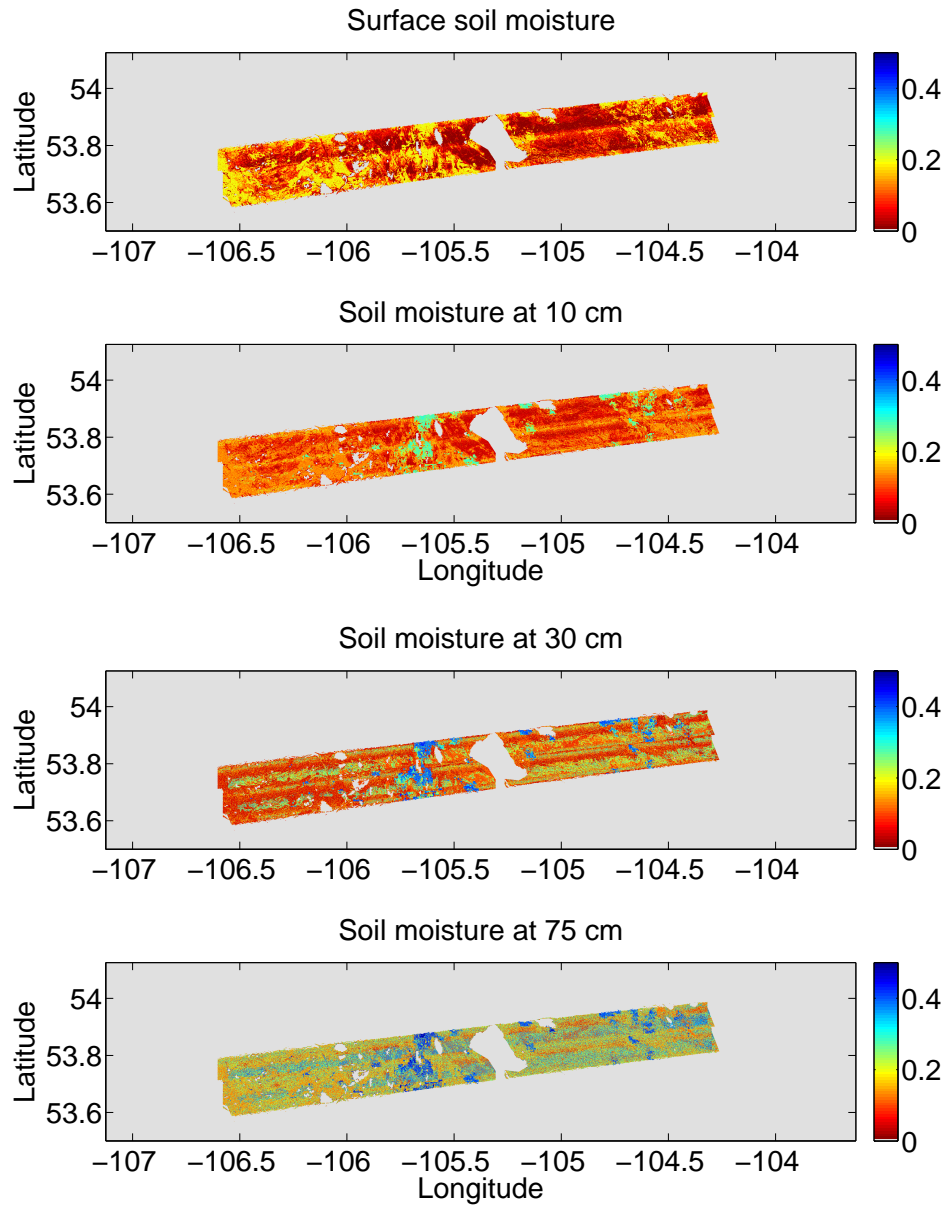
Figure 3.11: Map of soil moisture of the AirMOSS site in BERMS at four sample depths of 0, 10, 30, and 75 cm estimated by the inversion algorithm for 11 October 2012.
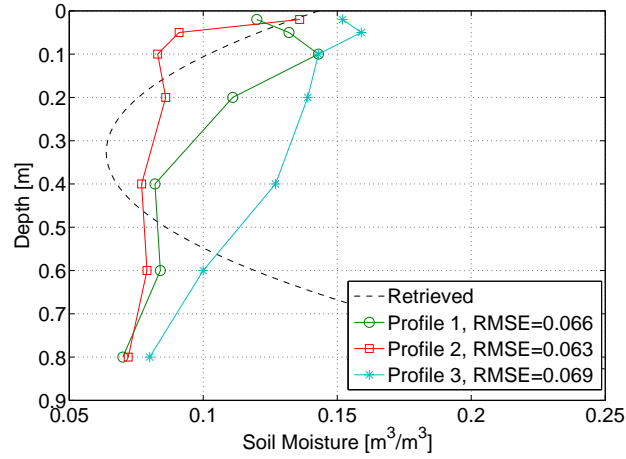
Figure 3.12: Comparison between the retrieved and measured profiles on 4 October 2012 at BERMS with RMSE over all profiles of 0.059. The RMSE is calculated based on depths less than 95 cm.

moisture data for three dates at BERMS.

Figure 3.12 shows an example comparison for 4 October 2012 with an average RMSE over all probes of 0.059 cm^3/cm^3. This validation shows promising results for soil moisture profile retrieval over forested sites but at deeper depths, the second-order polynomial function overshoots the in-situ soil moisture profile measurement significantly. Investigation of the level on confidence in the retrieval results for different depth thresholds show that the RMSE shows better accuracy if the retrieval is restricted to points closer to the surface, for example to a depth of 30 cm. Current and future work includes setting constraints on the quadratic function to restrict the soil moisture profile to hydrologically sound profiles. Additionally, possible radar calibration errors, inaccuracies in vegetation parameterization and modeling, surface roughness assumptions, and inaccuracies in the scattering and inversion models can contribute to the retrieval errors. The prospect of longer term data sets over the course of the AirMOSS mission will allow a time-series analysis to study dry down and wetting behaviors, which will help to understand and improve soil moisture retrieval results further.

3.5 Conclusion

In this chapter, the fine-scale retrieval capability has been presented with two different data sets. L-band UAVSAR data has been used to retrieve surface soil moisture under a single-species boreal forest. The OJP and YJP sites showed good retrieval results (within the SMAP mission requirement), while the OBS site contained too much heterogeneity and vegetation complexity to be modeled with a single-species vegetation model. The second data set is P-band radar data from the AirMOSS campaign. Retrieval of soil moisture profiles under evergreen forest has been discussed and shown to be successful. The AirMOSS validation is continuously expanding and validation for different land cover types are underway. Furthermore, for some specific sites, namely Tonzi Ranch in California and Canton in Oklahoma, there is more in-situ soil moisture data available from the Soil moisture Sensing Controller And oPtimal Estimator (SoilSCAPE) wireless sensor network [98]. The data is freely available and can be downloaded from USC's SoilSCAPE website [99].

CHAPTER IV

Analysis of heterogeneity at landscape level

4.1   Introduction

In chapter II the development of a generalized radar forward model for a fine-scale homogeneous area has been discussed. In chapter III the inversion for soil moisture over a fine-scale homogeneous area has been shown. All the pieces are hereby in place to address the analysis of heterogeneity at landscape level. The ultimate goal is the retrieval of a radar based coarse-scale soil moisture product. A spaceborne radar such as that in the SMAP instrument suite will measure a single radar backscatter value over a large coarse-resolution image; in the case of SMAP this is a pixel on the order of 1 to 3 km. At this scale, the scene will contain a wide variety of land cover types, soils, and incidence angles. Therefore, it is not reasonable to apply a single forward model to the entire coarse-scale scene since an area at km-scale cannot be considered homogeneous. The heterogeneous scene can instead be divided into smaller homogeneous scenes to which the forward model can be applied. The forward model then allows us to relate radar backscatter and soil moisture on the fine-scale. A novel method to retrieve coarse-scale soil moisture based on a coarse-scale radar image with the help of ancillary data is developed in this chapter. The problem setup is shown symbolically in Fig. 4.1.

There are multiple layers of heterogeneity to be considered at a 1 to 3 km coarse-
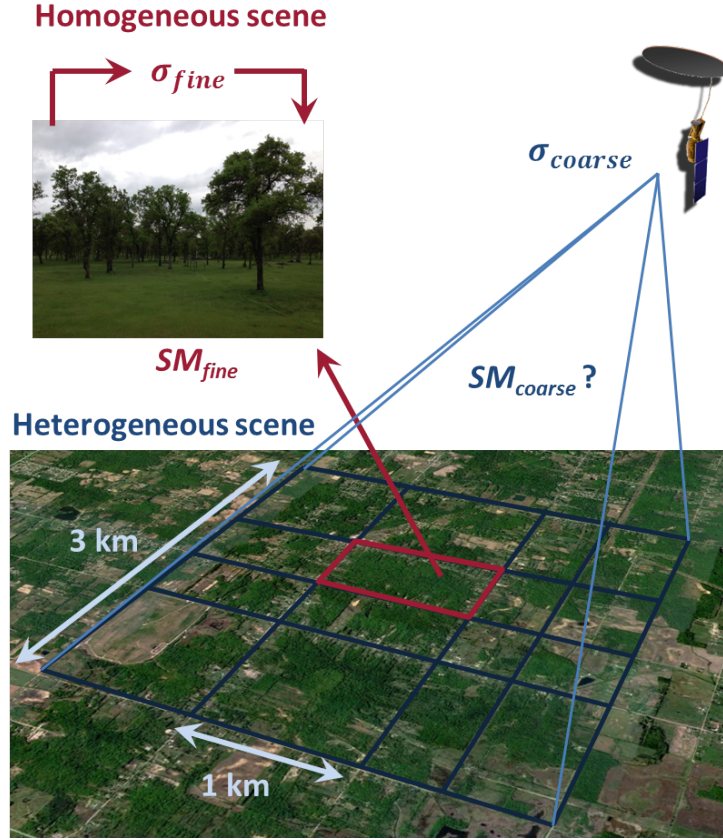
Figure 4.1: Problem setup of heterogeneity at landscape level: A spaceborne instrument, such as SMAP, observes a coarse (km-scale) resolution pixel containing heterogeneity. Spatially homogeneous scenes within the coarse-scale image can be defined and modeled as fine-scale pixels as discussed in chapter II. Soil moisture retrieval at fine-scale level is described in chapter III. The retrieval of coarse-scale soil moisture retrieval within the heterogeneous pixel is discussed in this chapter.

resolution scale: the in-situ soil moisture measurements to be used as validation, as well as the soil, vegetation and topography information. These layers have various levels of resolution, but are generally posted at a higher resolution than the coarse-scale radar pixel. This can be used to our advantage to define fine-scale homogeneous scenes. The in-situ soil moisture measurements are usually point measurements sparse in space and time, and there is ongoing research on how to appropriately use such soil moisture measurements for validation [100]. In this analysis, in-situ soil moisture measurements combined with precipitation data from weather stations and rain gauges are used to validate the retrieved overall soil moisture trend within the coarse-scale image. The soil, vegetation, and topography information is assumed to be known as ancillary information. More information on the used ancillary data products will be given with the description of the selected sample site.

Traditionally, soil moisture has been retrieved based on passive microwave sensing. Inherently, the resolution of radiometers is coarser than radars, and therefore scene heterogeneity has been a concern for radiometer based soil moisture retrieval. Drusch *et al.* [101] investigated spatial upscaling effects in passive microwave remote sensing over sparsely vegetated surfaces in the Southern Great Plains study area. They investigated differences between mean soil moisture derived from high resolution ($800\,m^2$) 1.4 GHz brightness temperatures and soil moisture calculated from mean brightness temperatures at larger scales. They concluded that for spatial resolutions of $31.4\,km^2$, the difference in estimated volumetric surface soil moisture does not exceed $0.02\,\frac{cm^3}{cm^3}$, and is less than $0.03\,\frac{cm^3}{cm^3}$ for spatial scales larger than $18.4\,km^2$, which is equivalent to the error of the retrieval itself. Galantowicz *et al.* [102] state that soil type heterogeneity effects within the coarse-scale radiometer pixel contribute less than $0.007\,\frac{m^3}{m^3}$ volumetric soil moisture error for an L-band bare soil scenario. Zhan *et al.* [103] investigate how soil moisture retrievals can be improved in highly heterogeneous vegetated areas by aggregation of ancillary parameters. Essentially, effective, potentially non-

physical, parameters are found to allow the radiometer based retrieval of coarse-scale soil moisture.

Crosson *et al.* [104] identify at least three nonlinear relationships as sources of scaling errors for radiometer based soil moisture retrieval:

  (i). Heterogeneity in volumetric soil moisture
 (ii). Heterogeneity in vegetation water content
(iii). Heterogeneity in surface roughness

Similar sources of scaling errors exist for radars, and for a quick investigation an example with one pixel consisting of two subpixels is presented. The nonlinear relationship between radar backscatter and soil moisture is shown in Fig. 4.2. The left figure shows simulated HH and VV for an OJP forest on sandy loam. Assuming subpixels with soil moisture of 2% and 36%, the true soil moisture SM_{true} is the linear average of 19%. Taking a linear average of the radar backscatter of the two subpixels and retrieving a single soil moisture for the whole pixel (SM_{ret}) results in a soil moisture that is smaller than the true soil moisture. An underestimation of the areal mean soil moisture is found and the bias increases with increasing soil moisture difference between the two subpixels. The right figure shows the retrieved soil moisture with respect to the soil moisture of the wetter pixel that is swept from 0% to 50%. In comparison, the true mean soil moisture is shown. Figure 4.3 shows radar backscatter over VWC for an OJP forest on sandy loam with a soil moisture of 3.55%. The same VWC value can relate to two different forest geometries therefore resulting in a non-unique relationship and rendering this parameter unsuitable for describing vegetation for radar purposes. Finally, heterogeneity in surface roughness can introduce a substantial difference in radar backscatter as can be seen in Fig. 4.4. The lack of variability in roughness in existing simulations is mostly due to lack of reliable data and inconsistent relationships between landcover type and surface roughness.

113
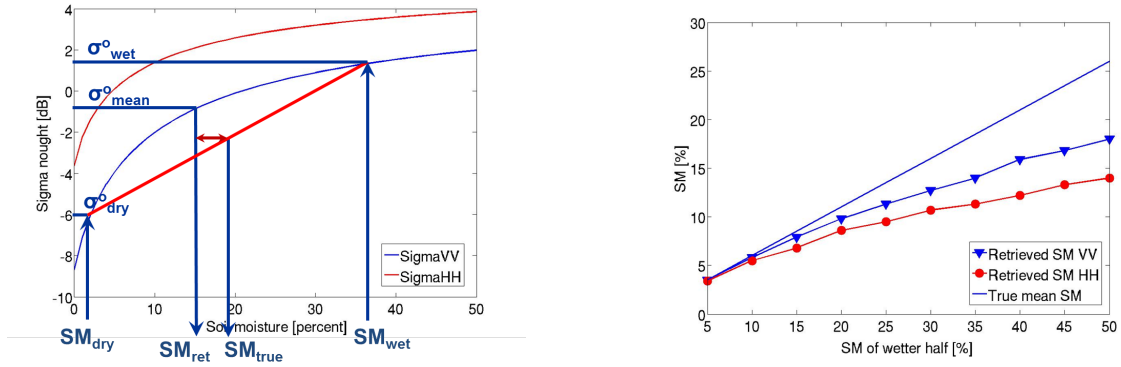
Figure 4.2: Left figure: One pixel with OJP forest on sandy loam soil with soil moisture $SM = 2\%$ and 36%. True mean SM of the pixel is SM_{true}, while SM_{ret} is the retrieved SM. Right figure: First sub-pixel with $SM = 2\%$ and second (wetter) sub-pixel with SM ranging from 0% to 50%.
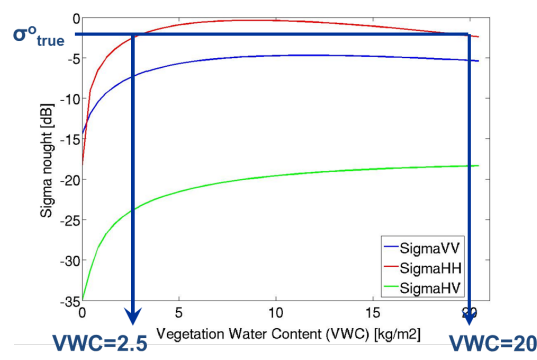
Figure 4.3: OJP on sandy loam with $SM = 3.55\%$ for a range of VWC.
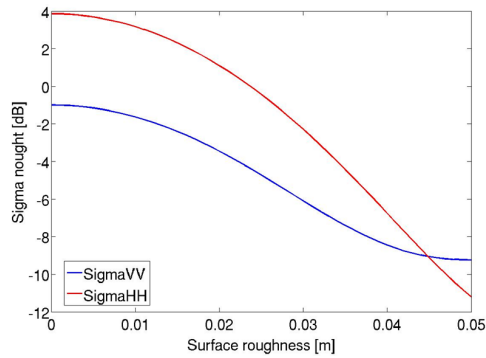
Figure 4.4: OJP on sandy loam with $SM = 3.55\%$ for a range of surface roughness.
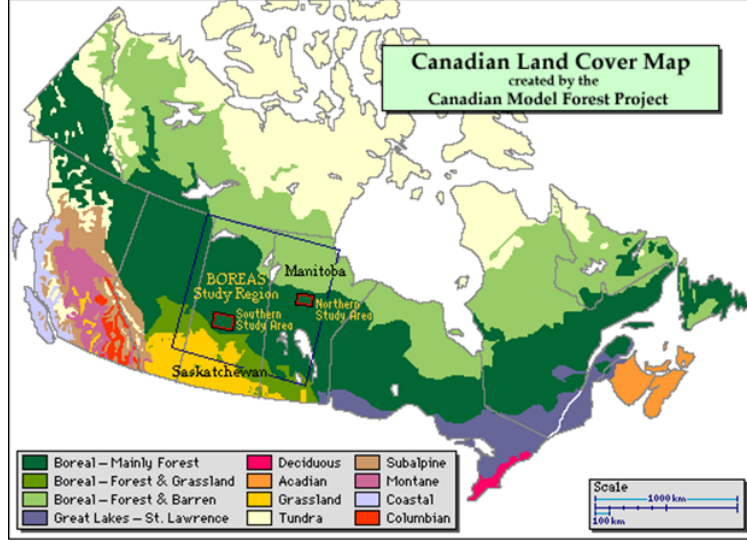
Image courtesy of: BOREAS ORNL DAAC

Figure 4.5: Location of BOREAS Southern Study Area.

4.2 Sample area: BERMS/ BOREAS super site

A suitable high resolution radar data set is provided by the AirMOSS mission, posted at 0.5 and 3 arc seconds for nine biomes over North America. Additional to the radar data set, ancillary data layers, in-situ soil moisture and vegetation ground measurements are available as part of the AirMOSS project as discussed in Appendix B. The BERMS/ BOREAS super site is selected as a sample site due to its long standing heritage, diversity in vegetation types and density in ancillary data layers. The BOREAS campaign took place in 1994 and the BERMS CanEx-SM2010 campaign took place in 2010. AirMOSS flights have been collecting radar data since September 2012. The site is located north of Prince Albert in Saskatchewan, Canada, as can be seen in Fig. 4.5. The Southern Study Area is shown in more detail in Fig. 4.6. A sampling area of 1 km x 9 km is centered around the OJP site. The sampling area is chosen to be large enough such that it captures the heterogeneity of land cover types, while at the same time covering radar incidence angles around 40 degrees, which corresponds to the SMAP incidence angle.

115
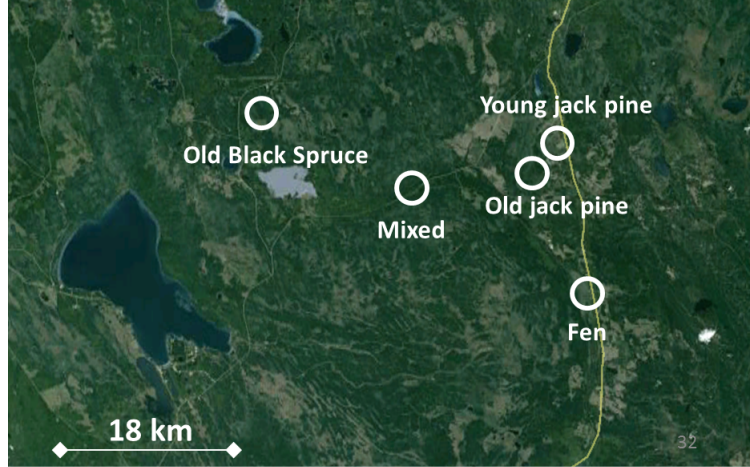
Figure 4.6: Detail of BERMS/ BOREAS study area.

4.2.1 Radar data

Radar backscattering coefficients for heterogeneous pixels are traditionally assumed to be the average of the coefficients for the constitutive homogeneous pixels. This assumption is only correct in specific conditions [105]. With the advent of the AirMOSS radar data, separately processed radar data are available at two resolutions (0.5 and 3 arc seconds), it is possible to investigate the applicability of averaging by comparing the original 3 arc second data with the 0.5 arc second radar data linearly averaged up to 3 arc seconds. In Figs. 4.7 and 4.8, the radar backscatter for HH and VV over the sample area is shown for 11 October 2012. It can be seen that averaging radar backscatter coefficients is applicable to homogeneous scenes, but is more problematic for complex, heterogeneous scenes or transitions between homogeneous areas. The complete used radar data set available over the sample area as part of the AirMOSS project is shown in Figs. 4.9, 4.10 and 4.11. The first data set from October 2012 is shown in Fig. 4.9. The radar data appears stable over the three dates and in-situ soil moisture measurements at OJP indicate a slight dry down over the first two dates with a small rain event on the third date. This is reflected in the radar data signal strength. The second data set from April and May 2013 shows frozen/thawing conditions in Fig. 4.10, which corresponds to the ground conditions.

116
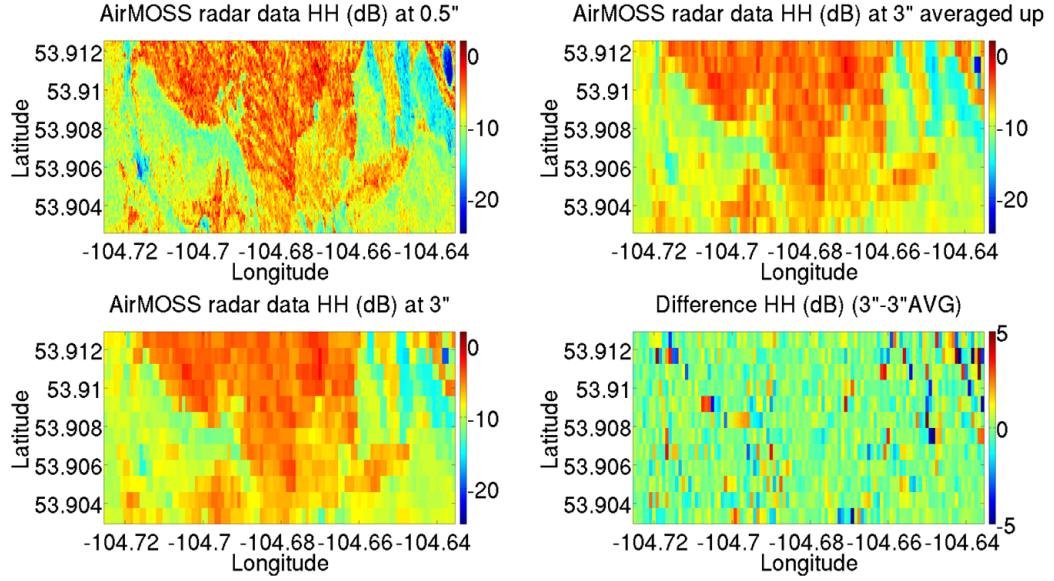
Figure 4.7: Averaging of HH radar backscatter over sample area for 11 October 2012.

The third data set from July and August 2013 is shown in Fig. 4.11. Figure 4.12 shows histograms of the radar backscatter of the third data set in HH, VV and HV, as well as the incidence angle for the three dates. These data sets show a signal that intensifies steadily over the three dates while in-situ soil moisture measurements at OJP indicate a dry down over the three dates. Based on modeling with radar scattering models assuming that there are no further changes in the scene besides soil moisture (which is a reasonable assumption for a time span of five days), this radar data is non-intuitive. Therefore, this third data set is flagged and cannot be used reliably for soil moisture retrieval. The JPL radar group is currently investigating the validity of this radar data set.

117
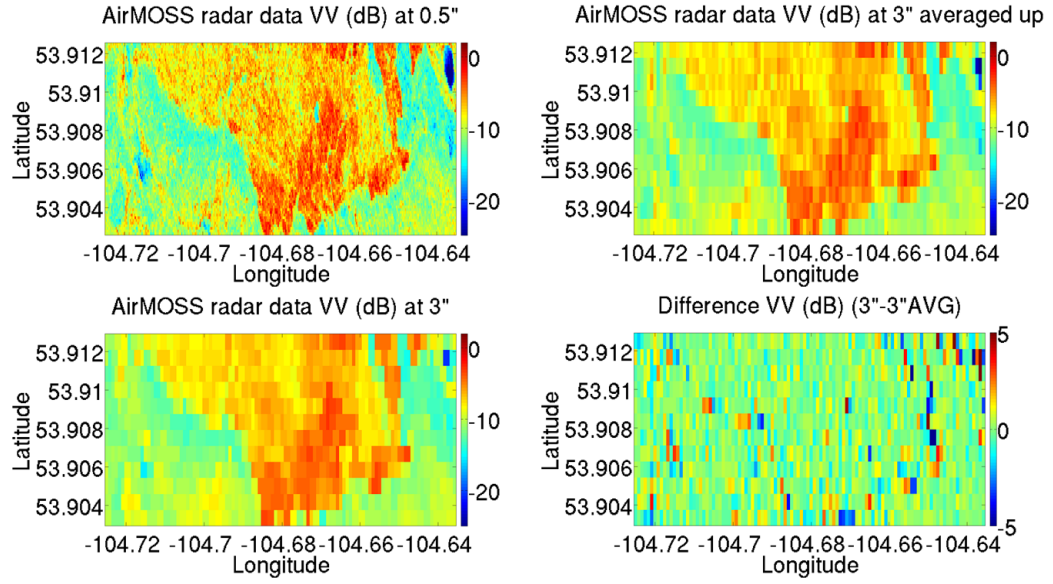
Figure 4.8: Averaging of VV radar backscatter over sample area for 11 October 2012.
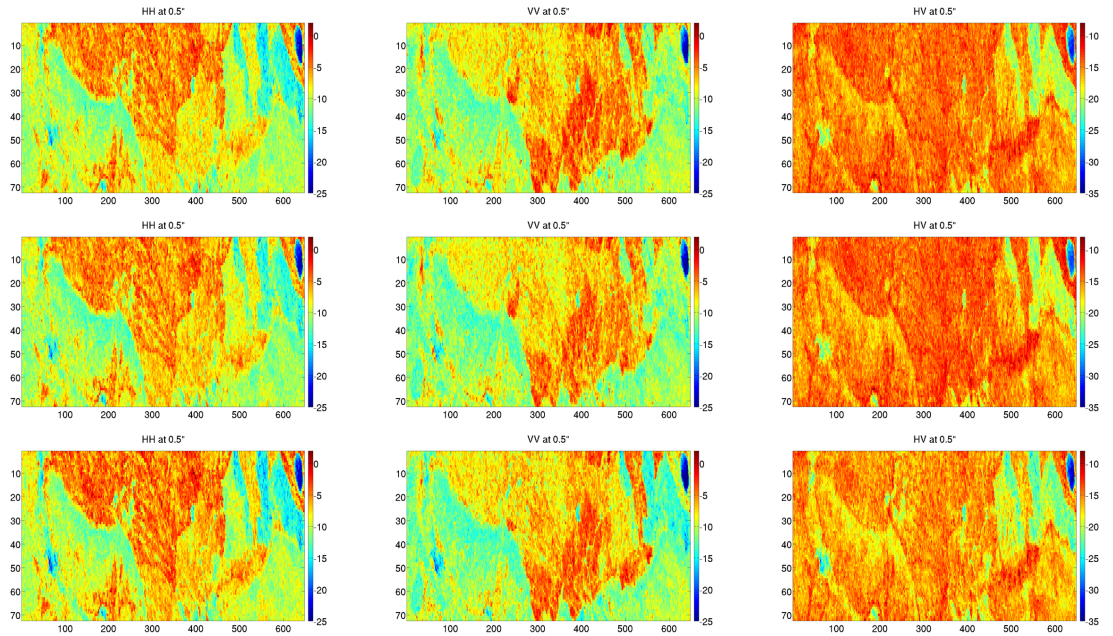
Figure 4.9: First radar data set from AirMOSS BERMS: 4 October 2012 (top), 7 October 2012 (middle), and 11 October 2012 (bottom).
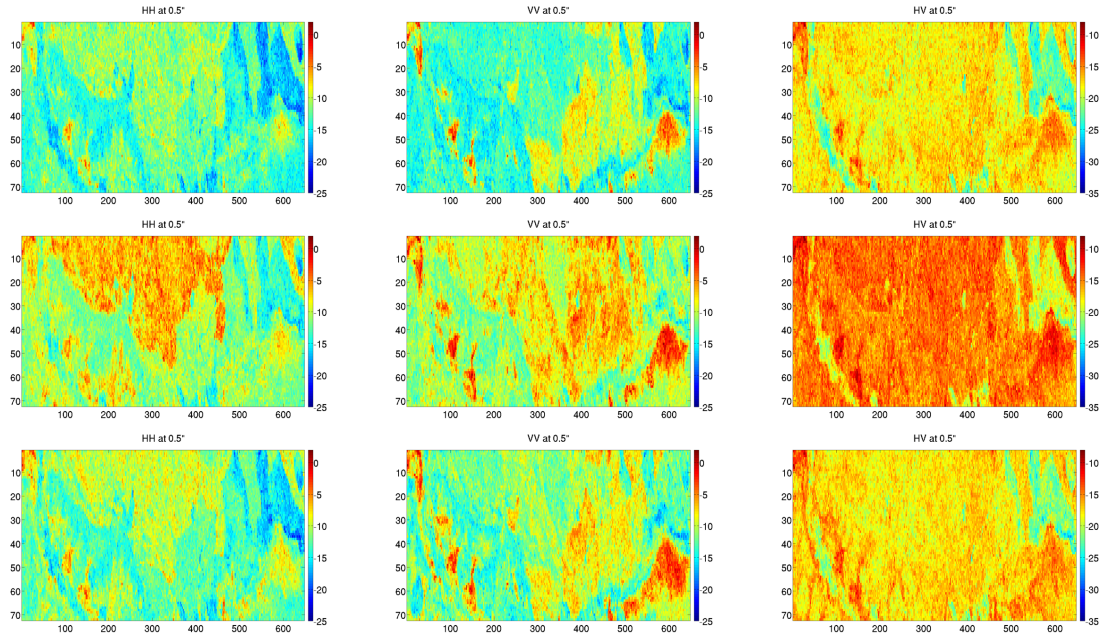
Figure 4.10: Second radar data set from AirMOSS BERMS: 22 April 2013 (top), 26 April 2013 (middle), and 1 May 2013 (bottom).
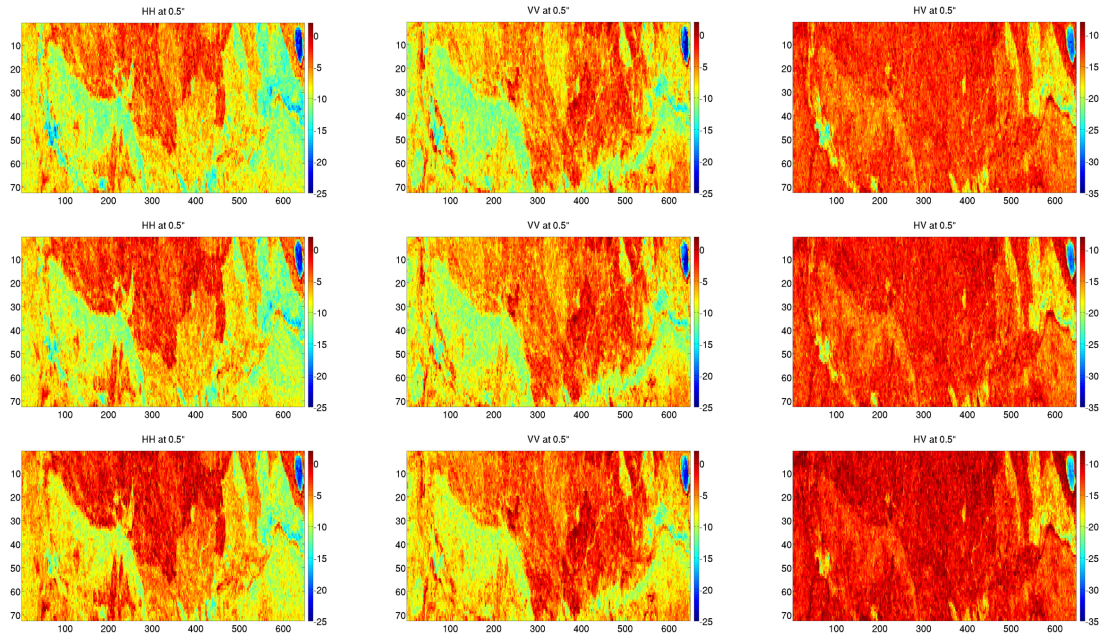
Figure 4.11: Third radar data set from AirMOSS BERMS: 27 July 2013 (top), 29 July 2013 (middle), and 1 August 2013 (bottom).
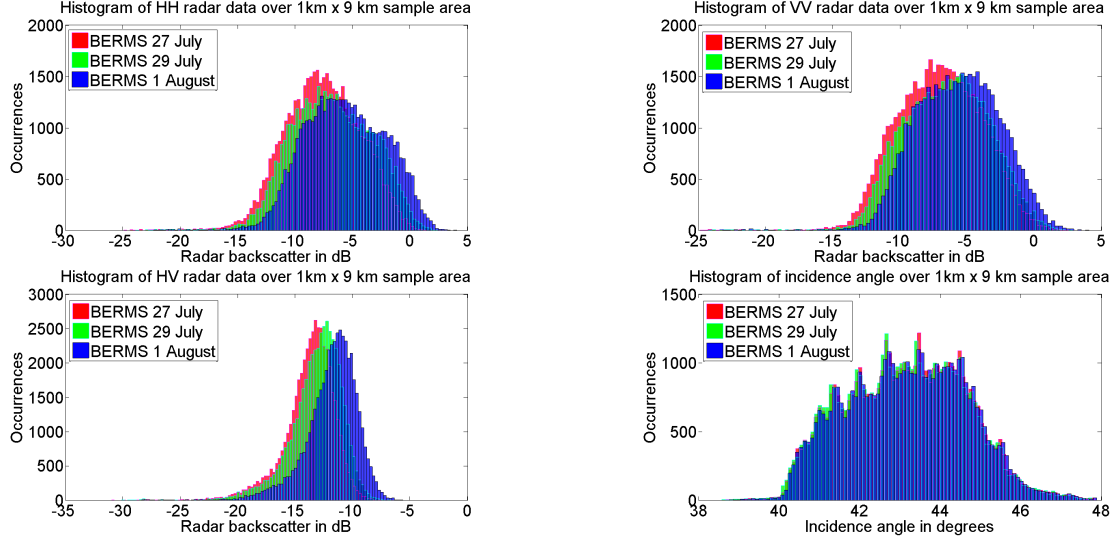
Figure 4.12: Histograms for HH, VV, HV and incidence angle of AirMOSS radar data from BERMS: 27 July 2013, 29 July 2013 and 1 August 2013.

4.2.2 Ancillary data

Many ancillary data layers are available over the sample area. These can be divided into four categories: (1) radar based, (2) above-ground, (3) below-ground and (4) in-situ measurements such as soil moisture, precipitation and rain gauge measurements. The radar based ancillary data consist of incidence angle and slope data that is coregistered with the radar data. An example set for incidence angle and slope data for a sample date is shown in Fig. 4.13. The incidence angle information is used at 0.5 arc second resolution as provided with the radar data. The slope is less than 3 degrees over the sample area. To simplify modeling, the slope is neglected for the following analysis.

The above-ground data consist of land cover type maps. Available land cover type maps for the sample area are the GlobCover map at 3 arc second and the BOREAS land cover type map at 3 arc second resolution [106] as shown in Fig. 4.14. These two land cover type maps are not sufficient in describing the heterogeneity of the sample area. The GlobCover land cover map is too coarse, while the used BOREAS land cover type map is too coarse and outdated. Therefore, a new threshold-based land

120

cover classification is developed by utilizing the HH, VV and HV radar data. The resulting threshold-based land cover classification can be seen in Fig. 4.14. The new threshold-based land cover type map consists of seven land cover types, most of which are similar to the BOREAS land cover types. The new land cover type classification technique improves forward modeling significantly as it better reflects the landscape heterogeneity and has the same posting as the radar data itself.

The below-ground data consist of STATSGO2 gap-filled SSURGO data as used by the AirMOSS mission. The soil texture information at OJP is given in Table 4.1.

Table 4.1: Soil parameter from STATSGO2 gap-filled SSURGO data at OJP site.

Parameter	Value
Percentage sand	0.597
Percentage clay	0.162
Percentage silt	0.241
Bulk density	$1.533 \frac{g}{cm^3}$
Soil temperature	$10°$
Soil salinity	$4 \frac{g}{cm^3}$
Soil surface RMS height	$0.02 - 0.05\, m$

The in-situ measurements consist of soil moisture, precipitation and rain gauge data, which has been available since the start of the AirMOSS project in September 2012. The in-situ soil moisture data for the specific overflight dates are given in Fig. 4.15. The average soil moisture profiles for all three data sets are shown in Fig. 4.16. The first data set is given in blue and shows a dry down over the first two dates and an increased soil moisture for the last date. The second data set is given in red. The first two dates show nearly frozen conditions with small soil moisture values while the last date indicates thawed conditions. The third data set is given in green and shows a gradual dry down over the three dates.

The used ancillary data layers over the sample area include the following:

(i). Radar based: incidence angle and slope

(ii). Above ground: threshold-based land cover type map
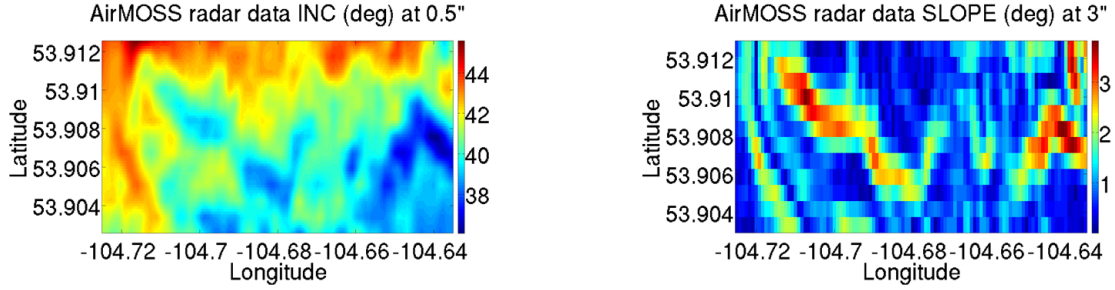
Figure 4.13: Example ancillary data layers at BERMS/ BOREAS sample area for 11 October 2012: incidence angle at 0.5 arc seconds resolution (left) and slope at 3 arc seconds (right).

(iii). Below ground: STATSGO2 gap-filled SSURGO soil texture

(iv). In-situ: Soil moisture measurements, precipitation and rain gauge information

4.2.3   Model setup

The land cover type is critical as it determines the above-ground vegetation parameterization. The land cover types range from forested sites such as pine, spruce and aspen over less-vegetated types such as shrubland and clearing to water-based types such as fen and water as shown in Fig. 4.17. Field work has been conducted over similar sites and the sampled vegetation is used to parameterize each land cover type. The percentage land cover types over the sample area for the threshold-based land cover type map is given in Fig. 4.18. The soil texture information is extracted for the OJP site and is applied to all non-water land cover types. The soil texture information for the OJP site is given in Table 4.1. Forested land cover types are assigned a soil roughness of 2 cm while the shrub and clearing land cover classes are assigned a surface soil roughness of 5 cm. For the water based land cover types the ground is modeled as water with a surface roughness of 1 cm. A single soil layer structure for all land cover types is assumed to simplify forward modeling. The sample area can be considered flat as can be seen from Fig. 4.13. In the future, a multilayered soil structure and topography can be considered in the analysis.

To restrict the modeling space, discrete modeling points are chosen:
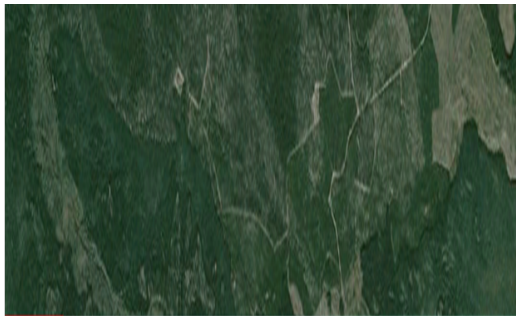
Google Earth Image
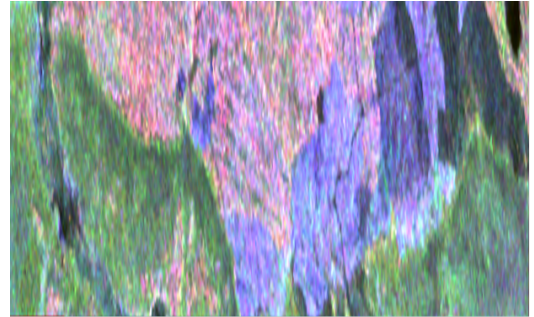
AirMOSS RGB at 0.5″
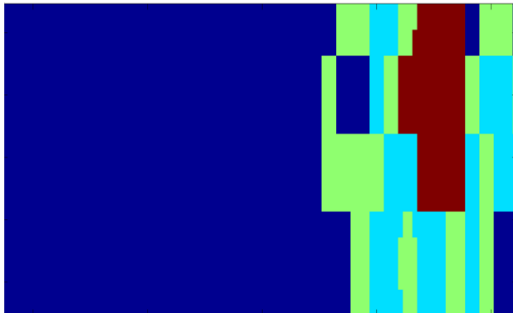
GLOBCOVER at 3″
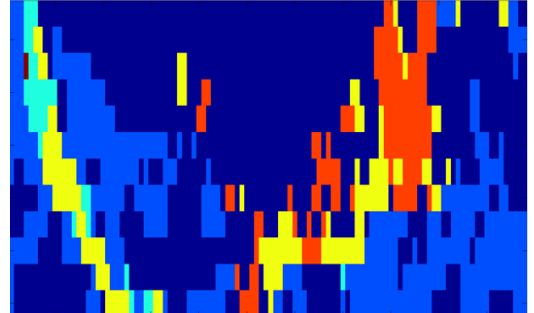
BOREAS LC at 3″
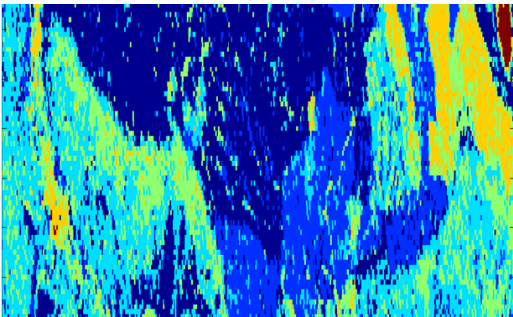
Threshold-based land cover map at 0.5″

Figure 4.14: Above-ground ancillary data layers at BERMS / BOREAS sample area: GlobCover land cover map at 3 arc seconds (middle left), BOREAS land cover map at 3 arc seconds (middle right) and threshold-based land cover map at 0.5 arc seconds (bottom left). The BOREAS and threshold-based land cover maps contain seven land cover types, while GlobCover contains only three. For comparison of sample area features: Google Earth image (top left) and AirMOSS RGB image (top right).
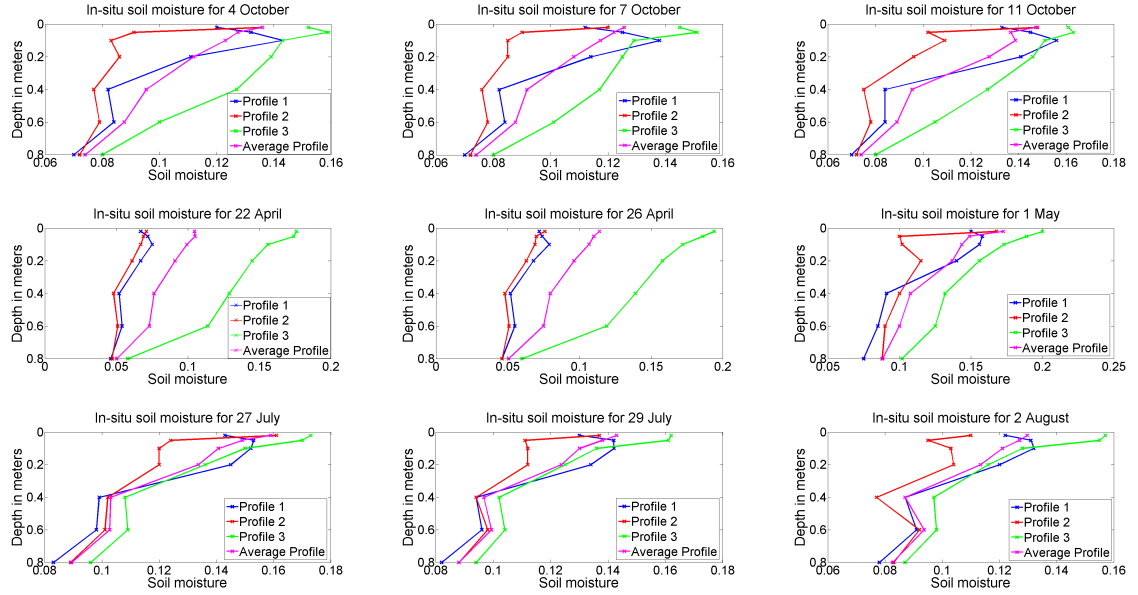
Figure 4.15: In-situ soil moisture for overflight days at OJP. Each figure shows three soil moisture profiles and the average profile.
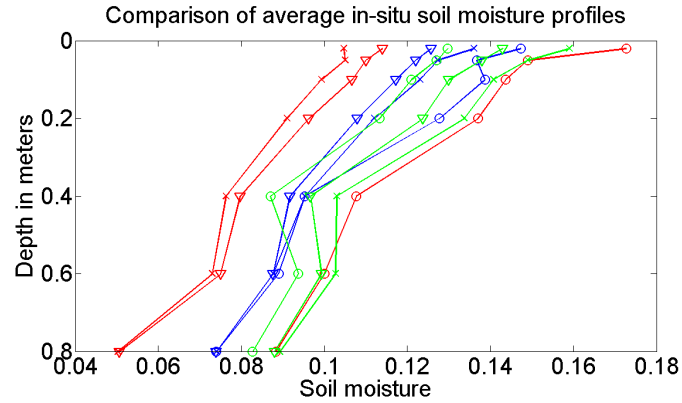
Figure 4.16: Average soil moisture profiles at OJP in BERMS. Legend: 4 October / 7 October / 11 October (blue), 22 April / 26 April / 1 May (red), 27 July / 29 July / 1 August (green) with first date (cross), second date (diamond) and third date (circle).

Figure 4.17: Seven land cover types used for forward modeling of BERMS / BOREAS sample site.
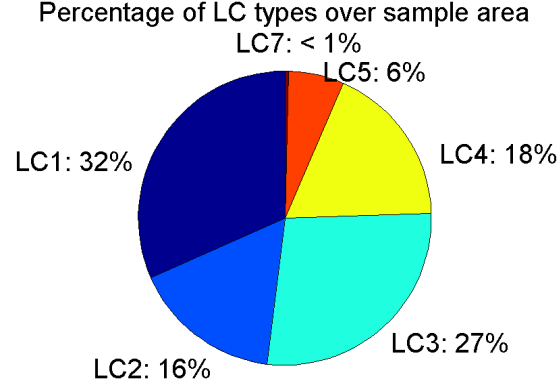
Figure 4.18: Percentage land cover (LC) types over sample area with threshold-based land cover type map.

(i). Land cover: 7 types

(ii). Soil moisture: 0.03, 0.07, 0.10, 0.15, 0.20 $\left[\frac{cm^3}{cm^3}\right]$

(iii). Radar incidence angle: 38, 40, 42 [degrees]

The resulting relationships of radar backscatter over discrete soil moisture values are shown in Fig. 4.19. Radar backscatter over soil moisture is not shown for land cover types fen and water since these are based on standing water and would show no sensitivity.

To validate the forward modeling, the radar backscatter is modeled according to the threshold-based land cover type map. The surface soil moisture at the OJP site for 11 October 2012 is found to be approximately 15 %, therefore this soil moisture is assumed for the entire sample area. After comparing the forward model with the radar data and investigating the vegetation of land cover type 4 (shrubland), it was found that the vegetation classified as land cover type 4 is better modeled as an aspen forest (land cover type 3). The final comparison between forward model and radar data for 11 October 2012 is shown in Fig. 4.20. The comparison is very promising even for a simplified setup with equal soil moisture over the whole sample area.
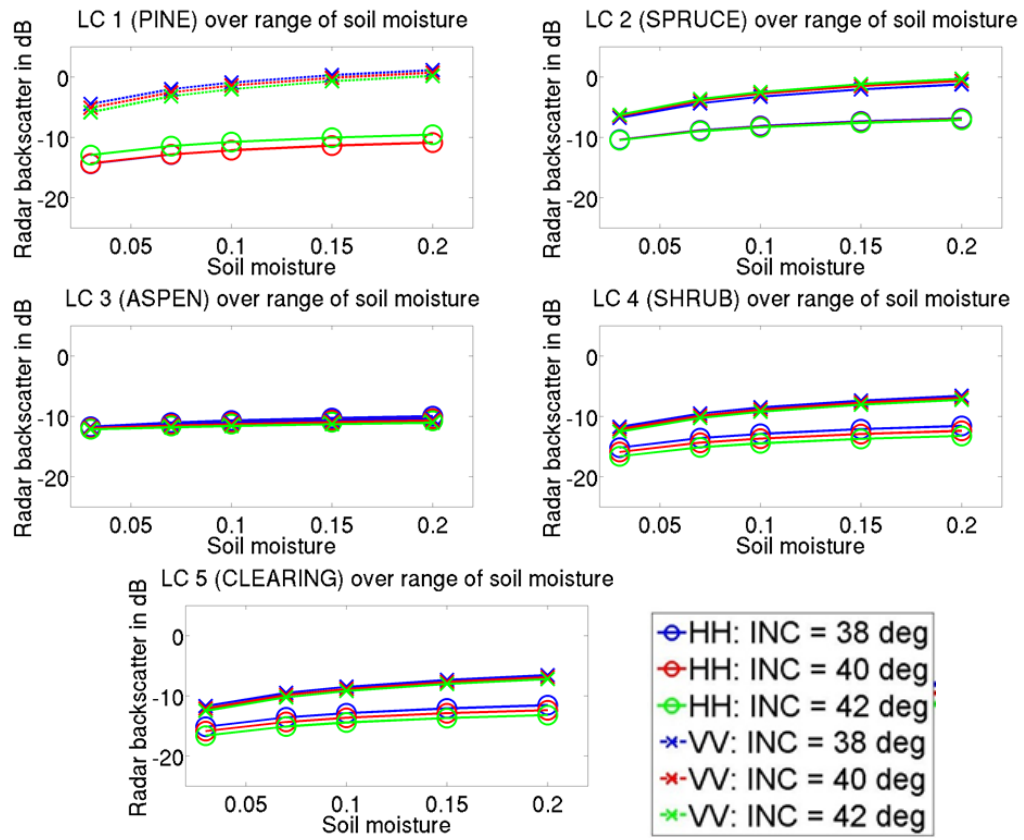
Figure 4.19: Radar backscatter over discrete soil moisture for five of the seven land cover types.
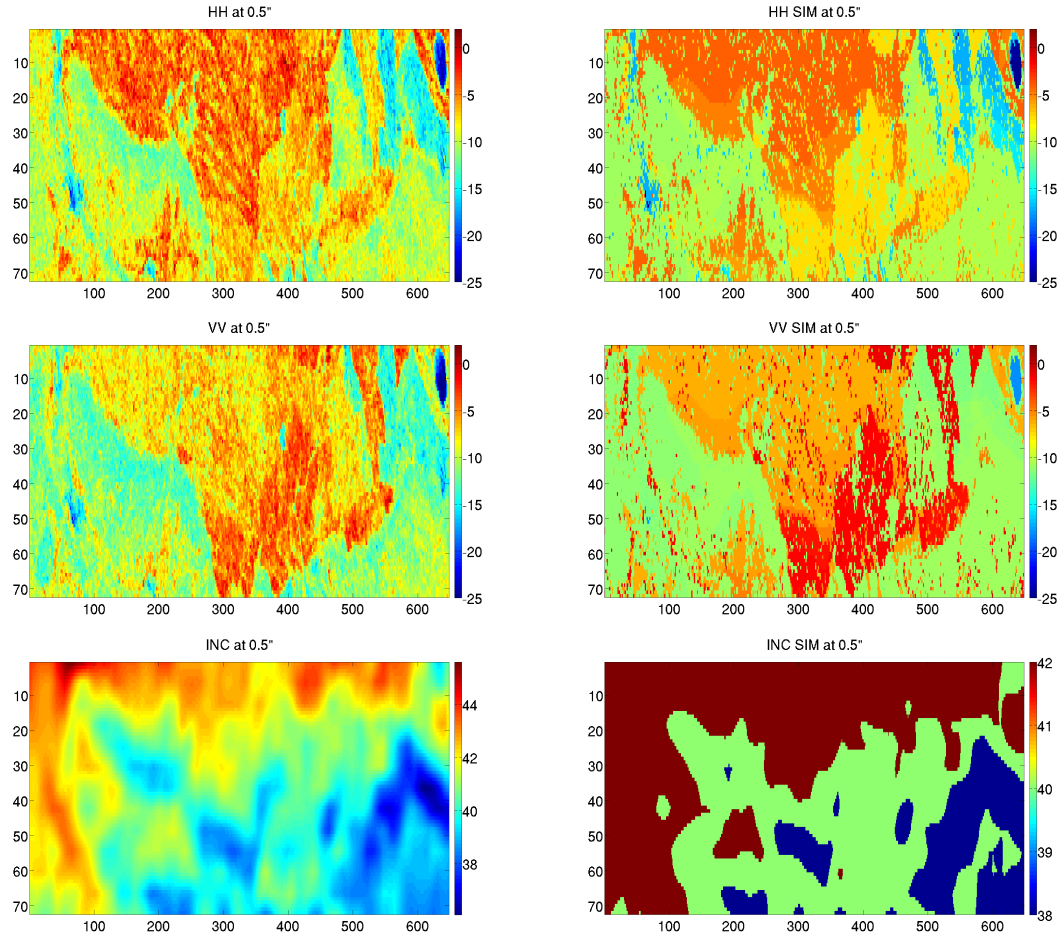
Figure 4.20: Comparison of measured (left) and simulated (right) radar data in dB for HH (top), VV (middle) and incidence angle in degrees (bottom) assuming soil moisture of 15 % for all land cover types over BERMS sample area.

4.3 Analysis of fine- to coarse-scale transformation

As previously shown, linear averaging is applicable for homogeneous scenes, but introduces considerable error in heterogeneous scenes. To define the radar backscatter representative of a heterogeneous scene, a weighted average of the pixel contributions is defined. The concept of scaling analysis transforms fine-scale pixel contribution to representative coarse-scale pixel values in forward simulation mode and allows to link the measured coarse-scale radar backscatter value with the fine-scale heterogeneity of the scene. The problem can be defined by the following variables, acknowledging that in reality there may be several more variables but that those considered here have been chosen due to their first-order impact on radar scattering measurements:

$S_p^j =$ Soil moisture with discrete value S_p of pixel j

$L_m^j =$ Land cover with discrete value L_m of pixel j

$I_k^j =$ Incidence angle with discrete value I_k of pixel j

with

$N : \#$ pixels

$M : \#$ land cover (LC) types

$K : \#$ incidence angles

$P : \#$ soil moisture values

$Q : \#$ scenarios

where the discrete values are described as:

$S_p^j \in \{0.03, 0.07, 0.10, 0.15, 0.20\}$

$L_m^j \in \{LC1, LC2, LC3, LC4, LC5, LC6, LC7\}$

$K_k^j \in \{38°, 40°, 42°\}$

The problem can be defined as finding the weights w_j to be multiplied to the fine-scale radar backscatter coefficients to express radar backscatter of the entire coarse-scale image:

$$\sigma = \frac{1}{N} \sum_{j=1}^{N} w_j \sigma^j_{S_p L_m I_k} \tag{4.1}$$

The total soil moisture is an average over all pixels within the image:

$$S = \frac{1}{N} \sum_{j=1}^{N} S^j \tag{4.2}$$

The soil moisture of pixel j is given as (4.3), where for example $w_p = [0, 1, 0, 0, 0]$:

$$S^j = \sum_{p=1}^{P} w_p \sigma^j_{S_p} \tag{4.3}$$

Radar backscatter is a function of soil moisture, land cover and incidence angle:

$$\sigma^j_{S_p L_m I_k} = \text{radar backscatter of pixel } j \text{ with } S_p, L_m, I_k \tag{4.4}$$

The radar backscatter of the entire coarse-scale image can then be found as follows:

$$
\begin{aligned}
\sigma_{L_m I_k} &= \sum_{p=1}^{P} w_p \sigma_{S_p L_m I_k} \\
\sigma_{I_k} &= \sum_{m=1}^{M} w_m \sigma_{L_m I_k} \\
\sigma &= \sum_{k=1}^{K} w_k \sigma_{I_k} \\
\sigma &= \frac{1}{Q} \sum_{q=1}^{Q} \sigma^q
\end{aligned} \tag{4.5}
$$
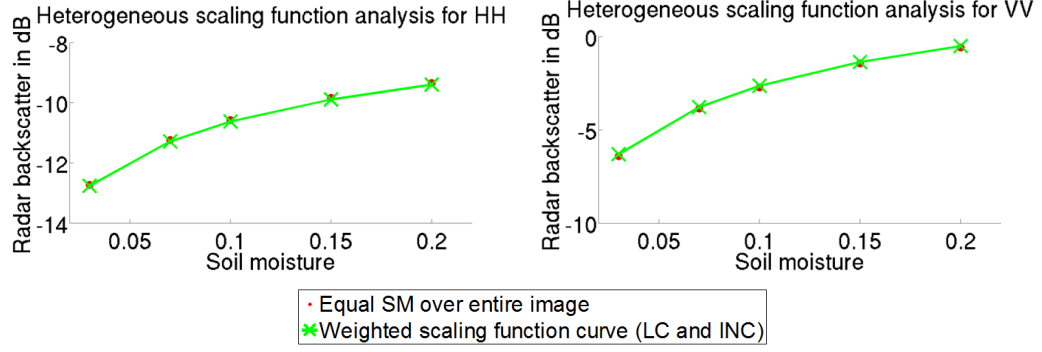
Figure 4.21: Functions for HH and VV assuming equal soil moisture for all land cover types over BERMS sample area.

where w_m are the respective percentage land cover for the coarse-scale image and w_k are the percentage cover of incidence angle for the coarse-scale image.

4.4 Closed-loop validation

The first step to validate the theory is to conduct a closed-loop validation, i.e. no radar data involved. Assuming all land cover types have equal soil moisture, the technique outlined in Eq. (4.5) has to be applied separately to HH and VV. The resulting functions relating coarse-scale radar backscatter to coarse-scale soil moisture can be seen in Fig. 4.21. Coarse-scale soil moisture can be looked up in the figures from the respective coarse-scale radar backscatter.

However, it is not realistic to assume equal soil moisture over all land cover types. Therefore, the most generalized case with all possible soil moisture combinations should be assumed. There are a total of 5^7 combinations of soil moistures, with seven land cover types and five discrete values for soil moistures. Each measured coarse-scale radar backscatter value corresponds to a range of potential coarse-scale soil moistures, as can be seen in Fig. 4.22. Not all of these combinations are necessarily physically realistic, therefore constraints such as the following scenarios can be imposed: dry (soil moisture of $3\%, 7\%, 10\%$), moderate (soil moisture of $7\%, 10\%, 15\%$) and wet (soil moisture of $10\%, 15\%, 20\%$).
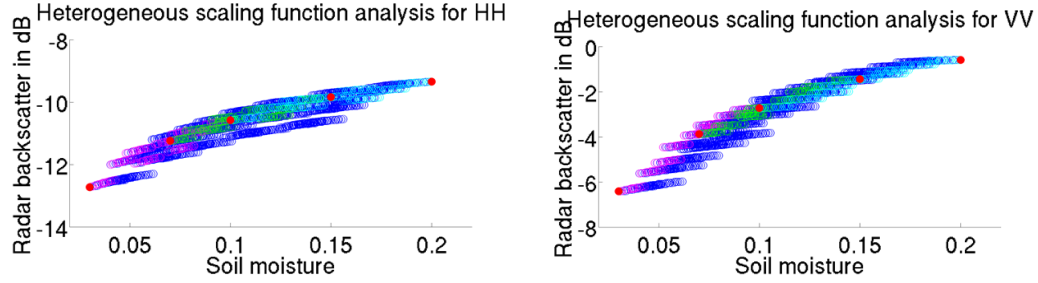
Figure 4.22: Function for HH and VV assuming all possible soil moisture combinations over BERMS sample area.

The closed-loop validation shows that the procedure works correctly and is the first step in understanding the heterogeneity problem. The next step is the validation of the theory with AirMOSS data where the coarse-scale soil moisture can be found.

4.5   Validation with AirMOSS data

Ultimately, SMAP (or any other spaceborne radar) will observe one radar backscatter value over a km-scaled area. In this validation setup, the sampling area is 1 km x 9 km. To emulate what SMAP would observe, AirMOSS radar data is linearly averaged up to one single radar backscattering coefficient in HH and VV for the entire sampling area. A Monte Carlo simulation is set up to populate the relationship between coarse-scale radar backscatter and coarse-scale soil moisture. For each execution, the fine-scale soil moisture values are assigned according to land cover type and incidence angle of the fine-scale pixel. The linear average of fine-scale radar backscatter values over the entire sample area is considered the coarse-scale radar backscatter value. The fine-scale soil moisture values are averaged to determine the coarse-scale soil moisture value. Ten thousand executions are considered to heuristically determine sufficient probabilities. The resulting relationship between coarse-scale radar backscatter and coarse-scale soil moisture is shown in Fig. 4.23 for 11 October 2012.

From the relationship of coarse-scale radar backscatter and coarse-scale soil moisture, the coarse-scale soil moisture can be looked up by using the measured radar
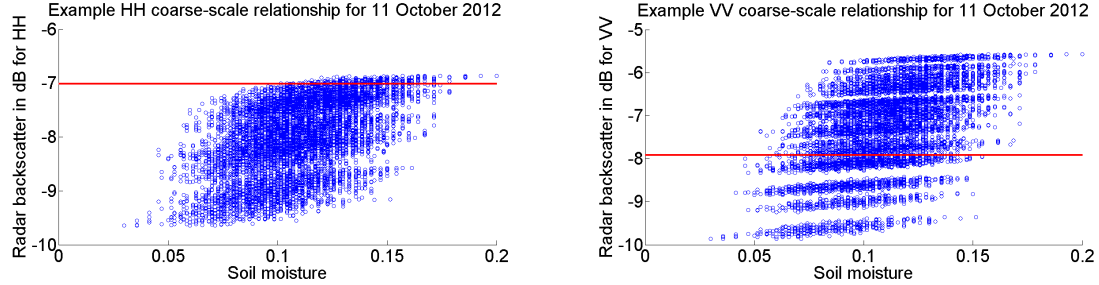
Figure 4.23: Relationship of coarse-scale radar backscatter coefficient with coarse-scale soil moisture for HH and VV from Monte Carlo simulation for BERMS on 11 October 2012. Red line indicates linear average of measured AirMOSS radar backscatter over the sample area.
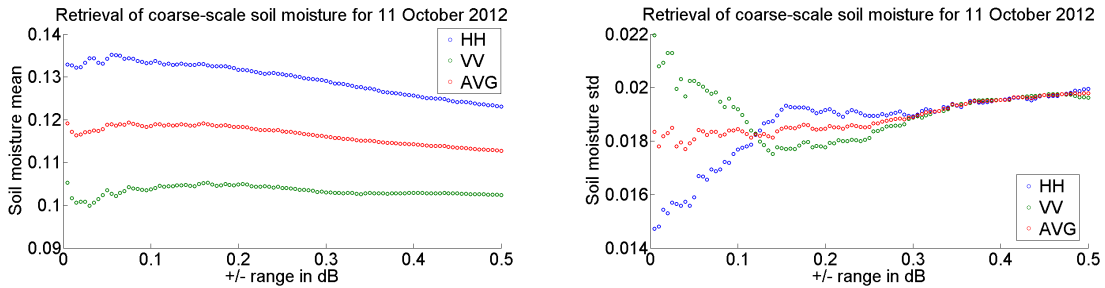
Figure 4.24: Retrieval of coarse-scale mean and standard deviation of soil moisture for BERMS on 11 October 2012 for a range of backscatter values around the linear average of measured AirMOSS radar backscatter over sample area.

backscatter coefficient from a spaceborne instrument. In this case, the measured radar backscatter coefficient is the linear average of the radar backscatter coefficients within the 1 km by 9 km sample area. To lookup the coarse-scale soil moisture, the mean and standard deviation of a range of radar backscatter values is investigated. The corresponding relationship is shown in Fig. 4.24. The HH and VV channels retrieve soil moisture values that show a 3 percent difference. This could be traced back to potential differences in the modeling accuracy of the HH and VV channels. The retrieved mean and standard deviation of the soil moisture value for HH and VV is averaged. The retrieved mean standard deviation is determined to coincide where the standard deviation of the HH and VV channels correspond. For the example of BERMS on 11 October 2012, the mean soil moisture is 11.6 percent with a standard deviation of 0.0189 for a range of $\pm$ 0.3 dB. The complete set of retrieval results for the first data set is given in Table 4.2. We observe a dry down over the first two dates and an increased soil moisture for the last date. The retrieved mean soil moisture trend corresponds well with the in-situ soil moisture profile as given in Fig. 4.16.

Table 4.2: Retrieved coarse-scale soil moisture mean and standard deviation for first data set.

	4 October 2012	7 October 2012	11 October 2012
Soil moisture mean	11.12 %	10.86 %	11.6 %
Soil moisture std	0.01935	0.01937	0.0189
$\pm$ range in dB	0.335	0.34	0.3

The second radar data set for April and May 2013 shows frozen/thawing conditions and therefore the discrete soil moisture range for forward modeling has to be adjusted. Since soil moisture for frozen soil is zero percent, the discrete soil moisture set has to be adjusted to {0.1, 0.01, 0.03, 0.07, 0.10}. With this discrete soil moisture set and the above described procedure, the relationship between coarse-scale radar backscatter and coarse-scale soil moisture is simulated. An example relationship for 26 April
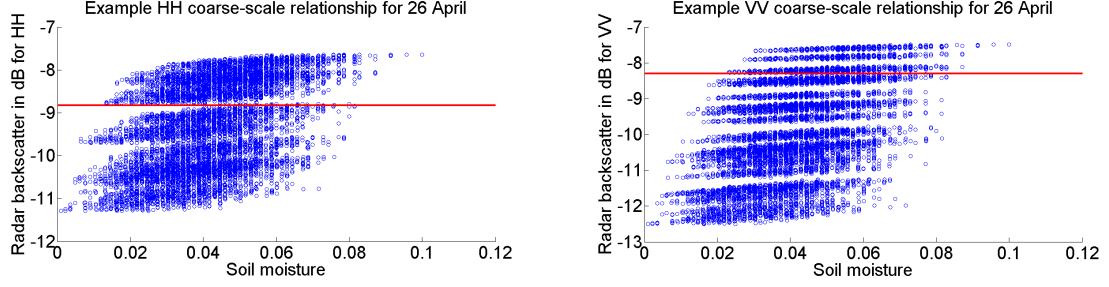
Figure 4.25: Relationship of coarse-scale radar backscatter coefficient with coarse-scale soil moisture for HH and VV from Monte Carlo simulation for BERMS on 26 April 2013. Red line indicates linear average of measured AirMOSS radar backscatter over sample area.
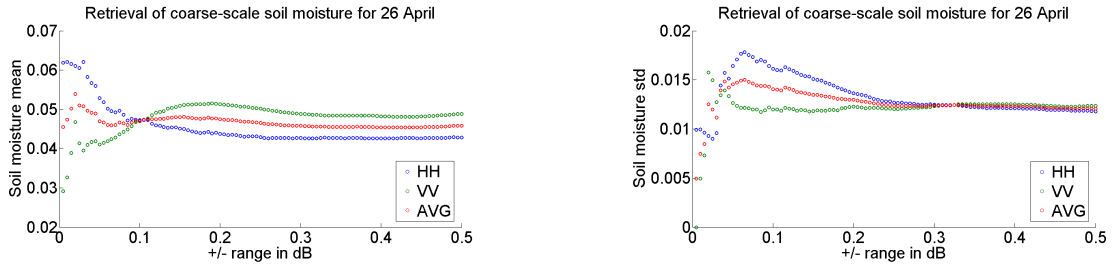
Figure 4.26: Retrieval of coarse-scale mean and standard deviation of soil moisture for BERMS on 26 April 2013 for a range of backscatter values around the linear average of measured AirMOSS radar backscatter over sample area.

2013 is shown in Fig. 4.25. The retrieved mean and standard deviation of the soil moisture for BERMS on 26 April 2013 is shown in Fig. 4.26. The retrieved mean soil moisture values compare well with the in-situ soil moisture values in Fig. 4.16, but the validation with this radar data set should be used with caution as the forward model is not specifically designed for frozen soil conditions. The retrieved values for the complete second data set are given in Table 4.3. The discrepancy in retrieved and in-situ soil moisture values can be explained by the frozen/thawing conditions.

Table 4.3: Retrieved coarse-scale soil moisture mean and standard deviation for second data set.

	22 April 2013	26 April 2013	1 May 2013
Soil moisture mean	3.4%	4.5%	3.6%
Soil moisture std	0.012	0.0125	0.012
$\pm$ range in dB	0.35	0.3	0.415

The third data set cannot be used for validation. Detailed analysis of the radar data in comparison with in-situ soil moisture, precipitation and rain gauge data showed that there is a strong increasing trend of the radar backscatter signal over the three dates while there is a dry down in soil moisture over the three dates. Assuming that the ground conditions did not change during these days, this is not an intuitive behavior. JPL is currently investigating this data set.

4.6   Conclusion

In this chapter a new radar based technique to retrieve the coarse-scale soil moisture based on a coarse-scale radar backscatter image (where homogeneity within the radar pixel cannot be assumed anymore) is presented. The link between fine- and coarse-scale pixels is analyzed and weights are identified, which have to be multiplied with the fine-scale radar backscatter coefficients to model the radar backscatter of the entire coarse-scale image. This allows the simulation of the representative coarse-scale radar backscatter for all possible soil moisture scenarios. The coarse-scale soil moisture can then be found based on the measured coarse-scale radar backscatter by analyzing statistics of a Monte-Carlo simulation. The methodology is presented and validated with data from the BERMS/ BOREAS super site. A closed-loop validation is setup and the general behavior of the coarse-scale radar backscatter with respect to coarse-scale soil moisture is shown. Two retrieval sets over the sample area are shown with promising results. The frame work is setup to allow for more validation in the future, especially for different land cover types, multilayered soil, different coarse-scale extents, and topography.

CHAPTER V

Mitigation of Faraday rotation effects from long-wavelength spaceborne radar data

5.1   Introduction

With the upcoming SMAP mission and the prospect of a spaceborne P-band radar mission following the example of the AirMOSS airborne mission (such as the ESA BIOMASS mission), there is a need to address mitigation of ionospheric effects to allow the use of radar signals for soil moisture retrieval. Ionospheric effects include group delay, attenuation, absorption, refraction, pulse dispersion, defocusing of the synthetic aperture in case of SAR systems, and Faraday rotation [7, 107]. These ionospheric effects are significant to varying degrees [107, 108]. The group delay effect causes a geolocation error in the radar image as well as a reduction of the range resolution. Due to the km-level ground resolution requirement for spaceborne missions, this effect can be neglected after ionospheric corrections are applied. The ionospheric attenuation varies significantly depending on frequency, for example at 100 MHz it varies from 0.1 to 0.01 dB [108], but can be corrected with ionospheric modeling. Pulse dispersion can lead to range compression errors if the ratio of bandwidth to center frequency is large enough. Due to the generally small bandwidth of the present spaceborne radar designs, this ratio is less than 1% causing only small

compression errors. Fluctuation of phase from a scatterer due to fluctuations in the ionospheric Total Electron Content (TEC) in the along-track direction could result in defocusing of the synthesized image and therefore reduce azimuth resolution. But due to the km-level resolution requirement for spaceborne mission, this effect can be neglected. The remaining dominant effect of the ionosphere is the Faraday rotation effect. In the presence of a steady magnetic field such as the Earth's magnetic field, the ionized medium in the ionosphere becomes anisotropic. Radio waves propagating through this medium will experience a rotation of the polarization vector known as Faraday rotation. Calculation of the Faraday rotation depends on the electron density profile along the propagation path (Ne), the Earth's magnetic field (H), the radio frequency (f) and the path direction of the signal, all of which can vary in space and time. Since the Faraday rotation effect correlates with the solar cycle, the effect can be stronger in years of high solar activity [109, 110]. Furthermore, the Faraday rotation effect is nonreciprocal since a clockwise rotation by an angle Ω is added to the electric field polarization vectors during transmission of a radar signal through the ionosphere both when transmitting to the Earth and back to the satellite. This mixing of the HH, VV and HV channels with each other will cause scattering properties to appear different if the Faraday rotation effect is present, leading to misinterpretation of the signal and introducing a source of error. The Faraday rotation effect is proportional to the inverse square of frequency. It therefore becomes stronger with decreasing frequency leading to more significant alterations of the radar signal. Under peak ionospheric TEC conditions, the Faraday rotation angle ranges from 2.5° (C-band) to more than 320° (P-band) [107], which results in altering the values of the radar backscattering coefficients by several dB.

The Faraday rotation effect does not impact circularly polarized signals [110]. Unfortunately, the circular polarization is not ideal for radar based retrieval of geophysical parameters like vegetation biomass or soil moisture because the full scattering

matrix has to be used for a sensitive analysis. The orbiting altitude is also an important factor due to the electron density peaking at around 400 km [111]. The Shuttle Imaging Radar (SIR-C), for example, had an orbit of around 200 km. An example for a higher orbit is the Japanese Earth Resources Satellite 1 (JERS-1), which had an orbit of around 575 km [110]. SMAP will have an orbit of 685 km, therefore falling into the category of the higher orbits where Faraday rotation mitigation will be essential. Furthermore, the orbit can be carefully designed to avoid any additional ionospheric irregularities; only the background ionospheric effects then have be mitigated [112]. So far, mainly C- and L-band frequencies have been used for satellite design. Recently, interest has grown to launch a P-band radar satellite to observe Earth with lower frequencies. In May 2013, ESA selected the BIOMASS mission concept to become the next in the series of Earth observing satellites [113]. BIOMASS will monitor forest biomass to assess terrestrial carbon stocks and fluxes.

The upcoming SMAP mission will carry both an active and passive L-band instrument allowing Faraday rotation mitigation via either the passive and/or the active measurement channel. There are two basic Faraday rotation removal approaches considered for SMAP [114]: (1) apply the Faraday correction produced by the radiometer, which uses its third Stokes channel to estimate the amount of Faraday rotation, or (2) use estimates of Faraday rotation derived from externally supplied measurements of the ionosphere TEC. Approach (1) is expected to be accurate and meet the radar error budget for Faraday correction, but it will require radar processing to wait for the radiometer processing, therefore introducing more latency. A variation of this approach is to incorporate the radiometer Faraday correction algorithm in the radar processor and to compute the correction from the radiometer data. This would mitigate latency, but would require copying major parts of the radiometer calibration and Radio-Frequency Interference (RFI) processing algorithms. Approach (2) will utilize externally supplied daily Global Positioning System (GPS)

based L-band TEC measurements. Since the GPS constellation is located at much higher altitude than SMAP, it will sense a more completely integrated TEC. Based on Aquarius experience, a correction factor of 0.75 is applied to the GPS based TEC values to account for the shorter atmospheric column seen by SMAP. The GPS based measurements provide an estimation of the Faraday rotation angle with an uncertainty of about 2°. If a Faraday rotation correction is applied using the GPS based measurements of TEC, then all radar measurements are expected to meet the Faraday correction residual error budget. The drawback of the GPS based measurement of TEC is its spatial sparsity and its potential for interruptions. TEC measurements are taken at specific points on the globe, which are then extrapolated and applied to other regions of the Earth. Applying a Faraday rotation correction to an area where the Faraday rotation effect is small can increase the errors instead of mitigating the effect. Therefore, the Faraday rotation is only planned to be applied when the estimated rotation angle exceed its own uncertainty.

Realizing the impact of the Faraday rotation effect and considering its importance in the light of SMAP and future potential P-band missions on spaceborne platforms, mitigation of the Faraday rotation effect has to be addressed in more detail. In this dissertation, a radar-only method to predict and mitigate the Faraday rotation effect is presented. First, a method for predicting the Faraday rotation angle for any instrument altitude, location, and time on the globe is introduced. With this predicted Faraday rotation angle, synthetic spaceborne data based on AIRSAR data is generated. This synthetic spaceborne data can be used to develop and validate algorithms to retrieve the Faraday rotation angle both assuming no other disturbances and in the presence of other system distortion terms. In this work, an existing method to retrieve Faraday rotation angles assuming no other system disturbances is validated, and then a novel method to retrieve the Faraday rotation angle by using optimization techniques in the presence of other system distortion terms with no external targets

140

is presented.

5.2 Polarimetric radar system model

The fundamental problem in polarimetric radar calibration is to find the true scattering matrix S based on the measured scattering matrix M [115]. The polarimetric radar system model is defined in Eq. (5.1):

$$
\begin{bmatrix} M_{HH} & M_{VH} \\ M_{HV} & M_{VV} \end{bmatrix} = A(r,\theta)e^{j\phi} \begin{bmatrix} 1 & \delta_2 \\ \delta_1 & f_1 \end{bmatrix} \begin{bmatrix} \cos\Omega & \sin\Omega \\ -\sin\Omega & \cos\Omega \end{bmatrix} \begin{bmatrix} S_{HH} & S_{VH} \\ S_{HV} & S_{VV} \end{bmatrix}
$$
$$
\begin{bmatrix} \cos\Omega & \sin\Omega \\ -\sin\Omega & \cos\Omega \end{bmatrix} \begin{bmatrix} 1 & \delta_3 \\ \delta_4 & f_2 \end{bmatrix} + \begin{bmatrix} \mathcal{N}_{HH} & \mathcal{N}_{VH} \\ \mathcal{N}_{HV} & \mathcal{N}_{VV} \end{bmatrix}
$$
(5.1)

The system model can be written in a compact notation as follows (5.2):

$$
M = Ae^{j\phi}R^T R_F S R_F T + \mathcal{N}
$$
(5.2)

In Eq. (5.2), S is the scattering matrix, R_F is the one-way Faraday rotation matrix, R is the receive distortion matrix (of the radar system) and T is the transmit distortion matrix (of the radar system). The matrices R and T contain the cross talk values δ_i (i = 1, 2, 3, 4) and the channel amplitude and phase imbalance terms f_1 and f_2. $A(r,\theta)$ is a real factor representing the overall gain of the radar system and $e^{j\phi}$ is a complex factor, which represents the round-trip phase delay and system dependent phase effects on the signal. $\mathcal{N}$ represents additive noise terms present in each measurement due to Earth radiation, thermal fluctuation in the receiver and digitization noise. The terms $A(r,\theta)$, $e^{j\phi}$ and the matrix $\mathcal{N}$ can be neglected as they can be easily mitigated or neutralized.

There exist many methods to calibrate the system model in Eq. (5.1). These meth-

ods can be divided into two major types: calibration of the system model (1) with or (2) without Faraday rotation present. Freeman [116] provides a useful overview over the different methods. Assuming no Faraday rotation, the system model can be calibrated by either using external targets and/or by making assumptions about the scene or the system parameter. Solutions using only external targets and no assumptions for the scene or system parameter generally use several external targets. Whitt *et al.* [117] showed that calibration is possible with at most three known external targets. Freeman *et al.* [118] showed that three Polarimetric Active Radar Calibrator (PARC) signatures are sufficient to solve the problem whereas Klein [119] shows that an exact general solution can be obtained for two passive known targets and an extended target. Unfortunately, these approaches requiring external targets are sensitive to small errors in the rotation angles of the targets [120, 121]. Making assumptions about the system and the scene backscatter helps reduce the number of external targets needed. Van Zyl [122] assumes symmetries in the polarimetric system model ($\delta_1 = \delta_3$, $\delta_2 = \delta_4$, $f_1 = f_2$), and that the magnitudes of channel amplitude and phase imbalance terms are small compared to 1. Based on the reciprocity principle, it can be defined that $S_{HV} = S_{VH}$. Furthermore, it can be assumed that for most natural backscatter scenes the like- and cross-polarized backscatter terms are uncorrelated, i.e. $\langle S_{HH}S_{HV}^* \rangle = 0$ and $\langle S_{HV}S_{VV}^* \rangle = 0$. With the additional help of at least one external trihedral reflector, the system can be successfully calibrated. Klein [123] relies on similar assumptions such as backscatter reciprocity and the lack of correlation between co- and cross-pol backscatter found in natural targets. Quegan [124] assumes that the crosstalk values ($\delta_1, \delta_2, \delta_3, \delta_4$) are small compared to the diagonal terms and also utilizes the reciprocity principle with $S_{HV} = S_{VH}$. Furthermore, it is also assumed that for most natural backscatter scenes the like- and cross-polarized backscatter terms are uncorrelated, i.e. $\langle S_{HH}S_{HV}^* \rangle = 0$ and $\langle S_{HV}S_{VV}^* \rangle = 0$. This method depends on the covariance matrix of unsymmetrized data to be available and is described to be

successful as long as the scattering matrix data has not been symmetrized. Sarabandi *et al.* showed calibration with the assumption of $\delta_1 = \delta_2 = \delta_3 = \delta_4$ using point targets [125] and by using a single calibration target to calibrate the radar system including the cross-polarization channels [121].

The second type of methods assumes a system model with Faraday rotation. Freeman [115] assumes that a SAR system can be built with small levels of crosstalk ($\delta_i < $ -30 dB) and that the crosstalk amplitude and phase are stable and measurable and can therefore be removed. This assumption can be expressed as $\delta_i = 0$ ($i = $ 1, 2, 3, 4). The next step is the estimation, correction and removal of the channel amplitude and phase imbalance terms f_1 and f_2 while assuming reciprocity $S_{HV} = S_{VH}$ [115, 126]. The successful removal of δ_1, δ_2, δ_3, δ_4, f_1 and f_2 reduces the system model to the following system model:

$$
\begin{bmatrix} M_{HH} & M_{VH} \\ M_{HV} & M_{VV} \end{bmatrix} = \begin{bmatrix} \cos \Omega & \sin \Omega \\ -\sin \Omega & \cos \Omega \end{bmatrix} \begin{bmatrix} S_{HH} & S_{VH} \\ S_{HV} & S_{VV} \end{bmatrix} \begin{bmatrix} \cos \Omega & \sin \Omega \\ -\sin \Omega & \cos \Omega \end{bmatrix} \tag{5.3}
$$

The only remaining step is then to correct for the Faraday rotation. Bickel and Bates [127] found that the Faraday rotation angle can be retrieved if a transformation of M to a circular basis is applied; this is called the Z matrix:

$$
\begin{bmatrix} Z_{11} & Z_{12} \\ Z_{21} & Z_{22} \end{bmatrix} = \begin{bmatrix} 1 & j \\ j & 1 \end{bmatrix} \begin{bmatrix} M_{HH} & M_{VH} \\ M_{HV} & M_{VV} \end{bmatrix} \begin{bmatrix} 1 & j \\ j & 1 \end{bmatrix} \tag{5.4}
$$

Bickel and Bates [127] state that if $S_{HV} = S_{VH}$ holds, the Faraday rotation angle can be retrieved from Z as follows:

$$
\Omega = \frac{1}{4} \arg \left(Z_{12} Z_{21}^* \right) \tag{5.5}
$$

Another approach to retrieve the Faraday rotation angle when all other system

distortion terms have been successfully removed is given by Freeman [115]. Furthermore, it is a common technique to apply the aforementioned type of methods to remove all other system distortion terms first assuming no Faraday rotation, and then remove the Faraday rotation in a second separate step.

The proposed approach in this dissertation opts for a simultaneous system calibration and estimation of Faraday rotation using the full system model as given in Eq. (5.1), but neglecting the additive noise term $\mathcal{N}$ and the terms $A(r,\theta)$ and $e^{j\phi}$. Therefore, the polarimetric radar system model used is the following:

$$
\begin{bmatrix} M_{HH} & M_{VH} \\ M_{HV} & M_{VV} \end{bmatrix} = \begin{bmatrix} 1 & \delta_2 \\ \delta_1 & f_1 \end{bmatrix} \begin{bmatrix} \cos\Omega & \sin\Omega \\ -\sin\Omega & \cos\Omega \end{bmatrix} \begin{bmatrix} S_{HH} & S_{VH} \\ S_{HV} & S_{VV} \end{bmatrix}.
$$
$$
\begin{bmatrix} \cos\Omega & \sin\Omega \\ -\sin\Omega & \cos\Omega \end{bmatrix} \begin{bmatrix} 1 & \delta_3 \\ \delta_4 & f_2 \end{bmatrix}
\tag{5.6}
$$

The proposed novel method will define a procedure to relate the observed polarimetric signals to the desired (true) calibrated signals and estimate the model parameters by utilizing the observed data. This will be discussed in chapters 5.5 and 5.6.

5.3 Prediction of Faraday rotation angle

The Faraday rotation angle can be calculated for a given date, latitude, longitude and instrument altitude according to [32]:

$$
\Omega = \frac{K}{f^2} \int_0^h NH \cos\theta \sec\chi \, \mathrm{d}h
\tag{5.7}
$$

where K is a constant given as $2.97 \cdot 10^{-2}$, f is the frequency [Hertz], N stands for the electron concentration per cubic meter $[m^{-3}]$, H is the intensity of Earth's magnetic

field $[\frac{A}{m}]$, θ is the angle between the nadir track and the Earth magnetic field vector and χ is the angle of the ray with respect to nadir. The angle θ is also known as the azimuth angle and χ as the look angle.

Some of the parameters such as the electron concentration per cubic meter N and the magnetic field B cannot be easily defined. Methods to find the electron content in the ionosphere consist of either retrieving real-time GPS data and calculating the actual electron content or modeling and thereby predicting the actual values. Due to the sparsity of GPS data in time and space, the prediction of the TEC based on models is favored. Once the TEC is found, there exist various simplified formulas to estimate the Faraday rotation angle. Nicoll *et al.* [128] utilize the TEC and the magnetic field as follows:

$$ \Omega = \frac{K}{f^2} \cdot B \cdot \cos\theta \cdot \sec\phi \cdot TEC \tag{5.8} $$

where K is a composite constant, f is the frequency, θ is the angle between the magnetic field and the satellite pointing vector (azimuth angle), ϕ is the off-nadir angle of the satellite (look angle) and TEC is the total electron content.

The most popular model for electron content prediction is the International Reference Ionosphere (IRI) model [129], which predicts the electron density, electron temperature, ion temperature and ion composition for any given location, time and date. The model is based on a worldwide network of ionosondes, incoherent scatter radars (Jicamarca, Arecibo, Millstone Hill, Malvern and St. Santin), ISIS and Alouette topside sounders, and other in-situ instruments on several satellites and rockets. The ionosondes only measure the lower part of the ionosphere and there are only about ten incoherent scatter radars in the world, with only one in the US (Massachusetts), but the combination of all these sources provides a stable model. The IRI version from 2007 is used for this work. More information about the IRI model as well as
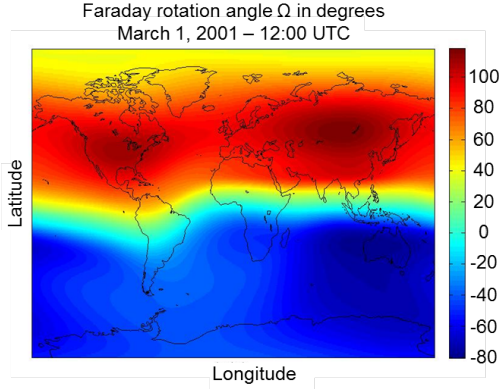
Figure 5.1: Worldwide Faraday rotation angle (in degrees) for 1 March 2001, 12:00 UTC.

an online computation and plotting tool can be found at [129]. For the magnetic field, there exist two models: the World Magnetic Model (WMM) updated every 5 years and the International Geomagnetic Reference Field Model (IGRF) [130] updated yearly. The international research reference model IGRF is chosen since it is more widely used. More information about this model can be found at [130] and an online modeling tool is provided at [131]. Based on the IRI and IGRF models the Faraday rotation angle can be calculated for any scenario. An example world map is shown in Fig. 5.1.

The Fortran source code for all models can be retrieved from the National Space Science Data Center [132]. The IRI and IGRF models need the following input parameter to predict the Faraday rotation angle:

- Instrument altitude
- Frequency
- Year and Day Of Year (DOY)
- Look angle
- Azimuth angle
- Time
- Latitude and Longitude

With the help of the assembled program structure it is possible to predict the Faraday rotation angle, and the algorithms have been validated and studied by several comparisons with published literature. The paper by Le Vine and Kao [109] contains two figures of interest. The first figure compares the Faraday rotation during summer versus winter, and during a solar maximum (1990) versus during a solar minimum (1995), over the course of a day. Most input parameters have been adopted from the paper, although some parameters were not defined; these have been chosen as best as possible. The two comparisons in Fig. 5.2 show a very good correlation. They confirm that the Faraday rotation angle is much higher during winter than summer and much higher at solar maximum than for solar minimum. The day/night difference can be ascribed to solar illumination, which is a dominant factor. It bears note that the Faraday rotation angle can undergo a drastic change over the course of a day. This makes the task of successfully predicting the Faraday rotation angle even more important. The question arises why the Faraday rotation is larger during winter than during summer. A possible cause could be that daytime ion production of the F_2 layer is much higher during summer, because in mid-latitudes the sun shines more directly on Earth. But due to seasonal changes the summer ion loss rate is even higher. This results in a bigger summertime loss than production, and overall the F_2 ionization is lower during summer months. This phenomenon is called the winter anomaly [111]. It only occurs during daytime and is always present in the northern hemisphere, but usually not in the southern hemisphere during periods of low solar activity. It is also interesting to note that the F_1 layer is only present during summer and absent during winter [111].

Figure 5.3 contains the second comparison with Le Vine and Kao [109] and shows the dependence of the Faraday rotation on latitude and longitude. The figure shows the same general behavior, although there are larger differences of the curve shape. Those can be traced back to the freely chosen look and azimuth angle. It can be

147
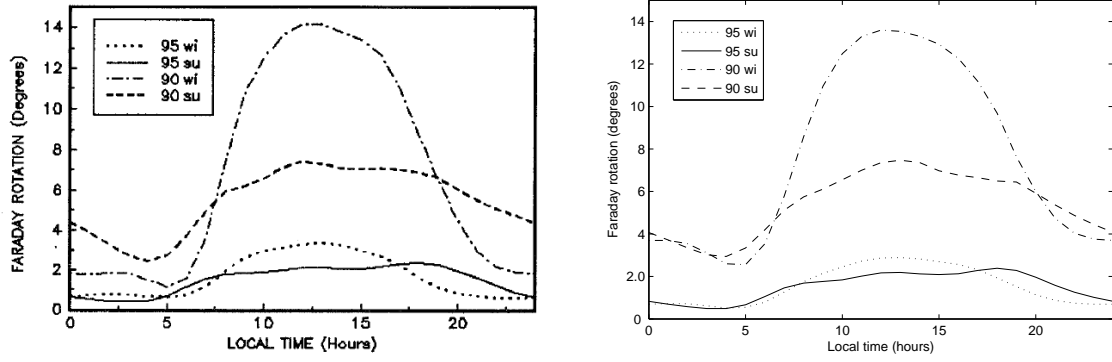
Figure 5.2: Comparison of predicted Faraday rotation as a function of local time. Figure on the left adapted from [109], page 378. Figure on the right from newly generated data. The adopted parameters are height (675 km), frequency (1.4 GHz), year (1990/1995), latitude (35° N) and longitude (75° W or 285° E). The chosen parameters are the date where 1 March was chosen as winter and 1 August as summer, the look angle (10°) and the azimuth angle (5°).

clearly seen that the Faraday rotation angle is much higher for higher latitudes.

To assess the effect of a change in the look angle, a simulation has been set up. All parameters were chosen for convenience though the year was selected as a solar maximum to get a higher Faraday rotation and the location was set to Ann Arbor, MI. The result can be seen in Fig. 5.4. It can be seen that the Faraday rotation angle could be higher for a larger look angle. But the general curve shape is maintained. This could be the reason for the difference in Fig. 5.3.

To assess the difference between solar minimum and maximum in more detail the Faraday rotation angle is calculated for the same dates as given in the paper of Le Vine and Kao [109] and as used in Figs. 5.2 and 5.3. The figures have been generated for the dates 1 March and 1 August of years 1990 and 1995 and are given in Fig. 5.6, with the data for the year 1990 in the upper two figures and the data for the year 1995 in the lower two figures. The data for 1 March appear on the left and the data for 1 August on the right. The original scaling has been kept because the maxima of the Faraday rotation angle distribution are easier to perceive. A white line has been introduced to

148
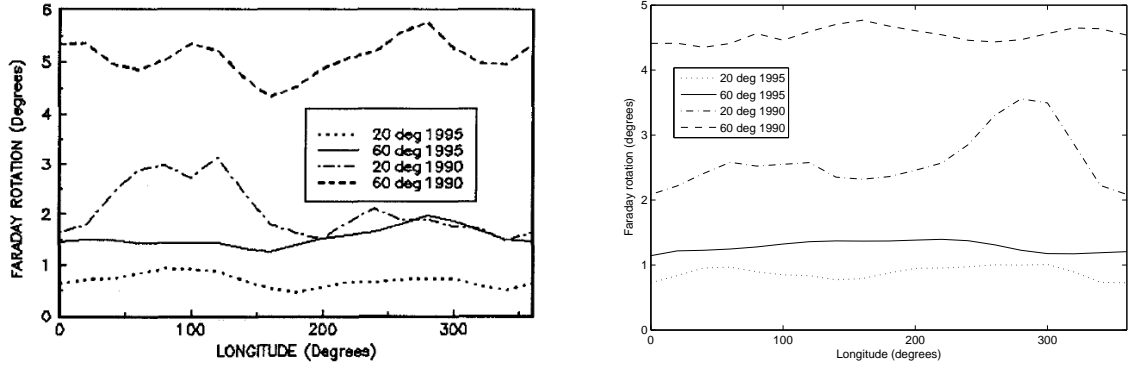
Figure 5.3: Comparison of predicted Faraday rotation as a function of longitude. Figure on the left adapted from [109], page 378. Figure on the right from newly generated data. The adopted parameters are height (675 km), frequency (1.4 GHz), year (1990/1995), time (6 am), latitude (20° N, 60° N) and longitude (75° W or 285° E). The chosen parameters are the date where 1 August was chosen as summer, the look angle (10°) and the azimuth angle (5°).
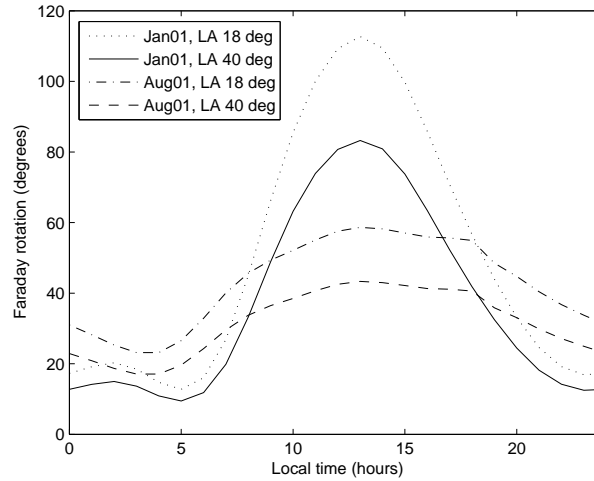
Figure 5.4: Comparison of two look angles (LA) (18°, 40°) for January and August 2001 over local time. The assumed parameters are height (1300 km), frequency (0.439 GHz), year (2001), date (1 January/1 August), look angle (18°/40°), azimuth angle (30°), latitude (43° N) and longitude (276° E).

149

make the zero-crossing of the Faraday rotation angle more clearly visible. The data in Fig. 5.6 confirm the fact that the Faraday rotation angle is significantly higher during a solar maximum (1990) than during a solar minimum (1995). Noticeable too is the difference between the March and August data sets. The Faraday rotation angle distribution peaks relatively narrow during March, but the Faraday rotation angle distribution is more widely spread for the month of August. This holds for the northern hemisphere. In the southern hemisphere the case is reversed and the Faraday rotation angle distribution is more widely spread in March. This reflects the fact that the positioning of the sun is different for March (latitude: E 3.1°, longitude: S 7.6°) and August (latitude: E 1.6°, longitude: N 18.0°). The illuminated part of the Earth also differs considerably. The positioning of the Faraday rotation angle distribution differs from 1990 to 1995. While the peak is more in the mid-latitudes during 1990, the peak in 1995 is closer to the equator. This too seems to correlate with the illumination area of the sun. The illuminated area and the sun overhead can be retrieved from [133], which provides synthetic images of the Earth's surface, each from a different perspective, that show the areas in sunlight (day) and darkness (night) at a specified date and time. Views from the sun towards the Earth for 1 March and 1 August 1990 at 12 pm can be seen in Fig. 5.5.

In Fig. 5.7 corresponding figures are generated for the years 2001 (solar maximum) and 2008 (solar minimum). The data for 2001 are given in the upper two figures and those for 2008 are given in the lower two figures. Again, the data for 1 March appear on the left and the data for 1 August on the right. The original scaling has been kept and a white line has been introduced to make the zero-crossing of the Faraday rotation angle more clearly visible. The same behavior as described above can also be recognized in Fig. 5.7, but it is also clear that the maximum Faraday rotation angle for 1990 is higher than that for 2001. Both of those years are solar maxima, but the solar maximum in 1990 was stronger (had a higher sun cycle number) than the solar
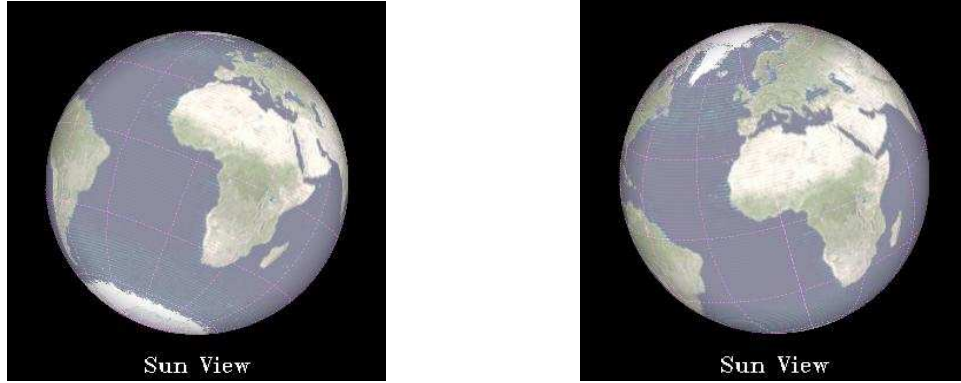
Figure 5.5: View of the Earth from the sun for 1 March (left) and 1 August (right) 1990. Figure adapted from [133]. Sun overhead at center of figure. For 1 March 1990 at (latitude: E 3.1°, longitude: S 7.6°) and for 1 August 1990 at (latitude: E 1.6°, longitude: N 18.0°).

maximum in 2001.

To highlight the impact of lower frequencies for the prediction of the Faraday rotation effect two figures in Fig. 5.8 have been generated for 1 March and 1 August 2001 (solar maximum). The frequency used is 0.439 GHz (P-band). On the left side is the plot for 1 March 2001 and on the right is the plot for 1 August 2001. It can be seen that the figures show the same general behavior as for L-band, but the magnitude of the Faraday rotation is about ten times higher. This clearly confirms the need for a mitigation strategy if P-band frequencies are to be used in the future.
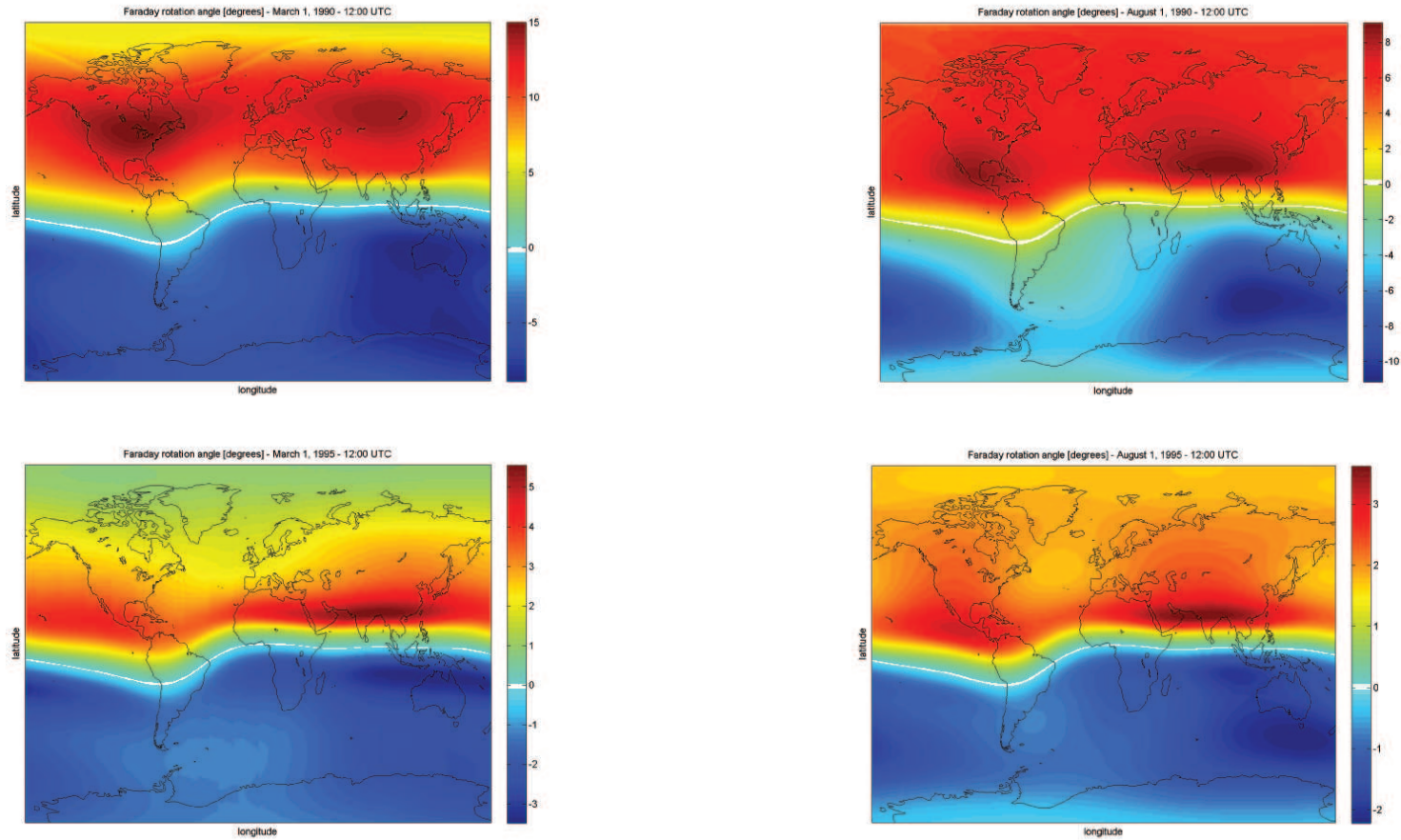
Figure 5.6: Predicted one-way Faraday rotation for 1 March and 1 August of 1990 and 1995. The parameters are height (675 km), frequency (1.4 GHz), year (1990 (upper figures)/1995 (lower figures)), date (1 March (left)/1 August (right)), time (12 pm), look angle (10°) and azimuth angle (5°). The white line was inserted to highlight the zero-crossing of the Faraday rotation.
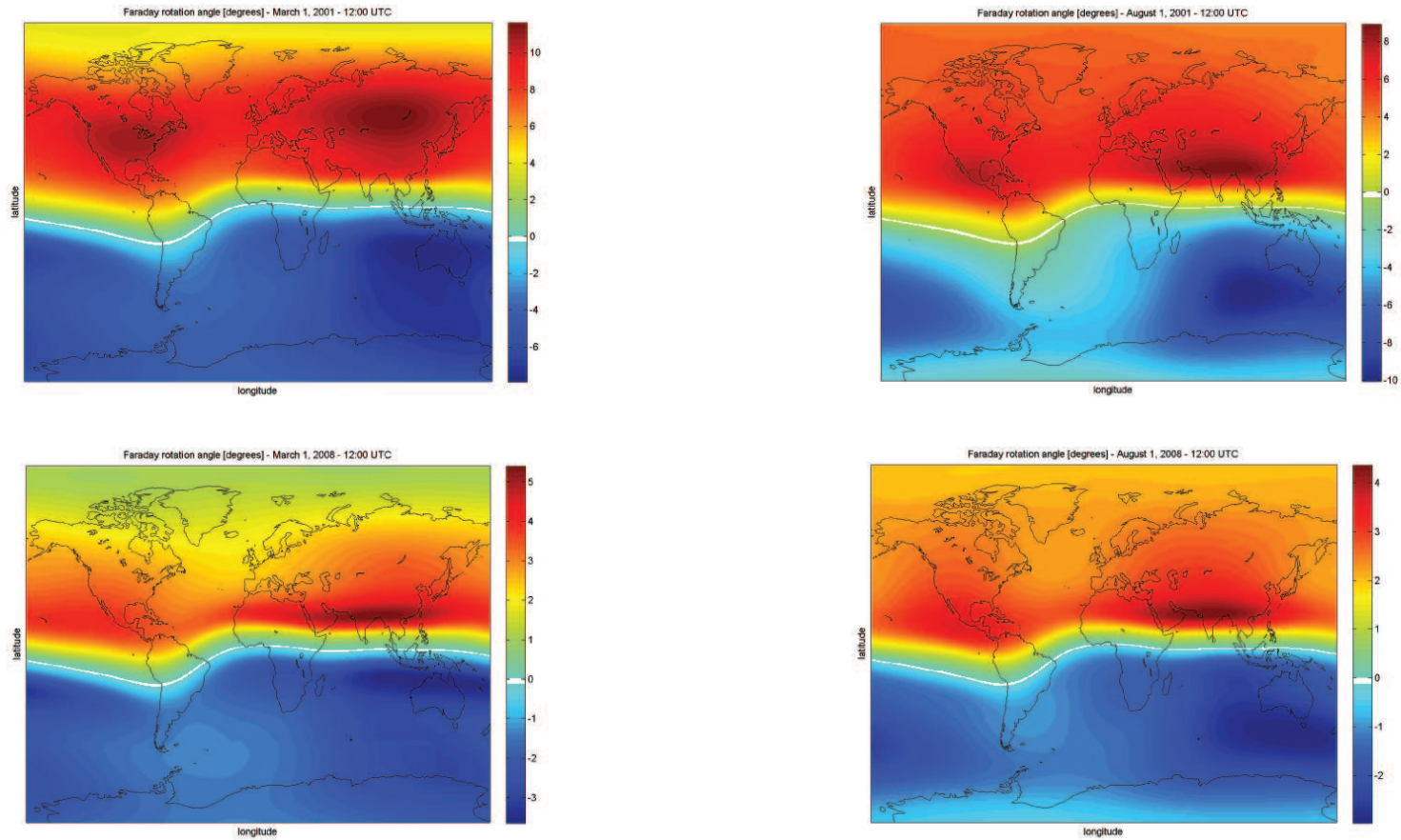
Figure 5.7: Predicted one-way Faraday rotation for 1 March and 1 August of 2001 and 2008. The parameters are height (675 km), frequency (1.4 GHz), year (2001 (upper figures)/2008 (lower figures)), date (1 March (left)/1 August (right)), time (12 pm), look angle (10°) and azimuth angle (5°). The white line was inserted to highlight the zero-crossing of the Faraday rotation.
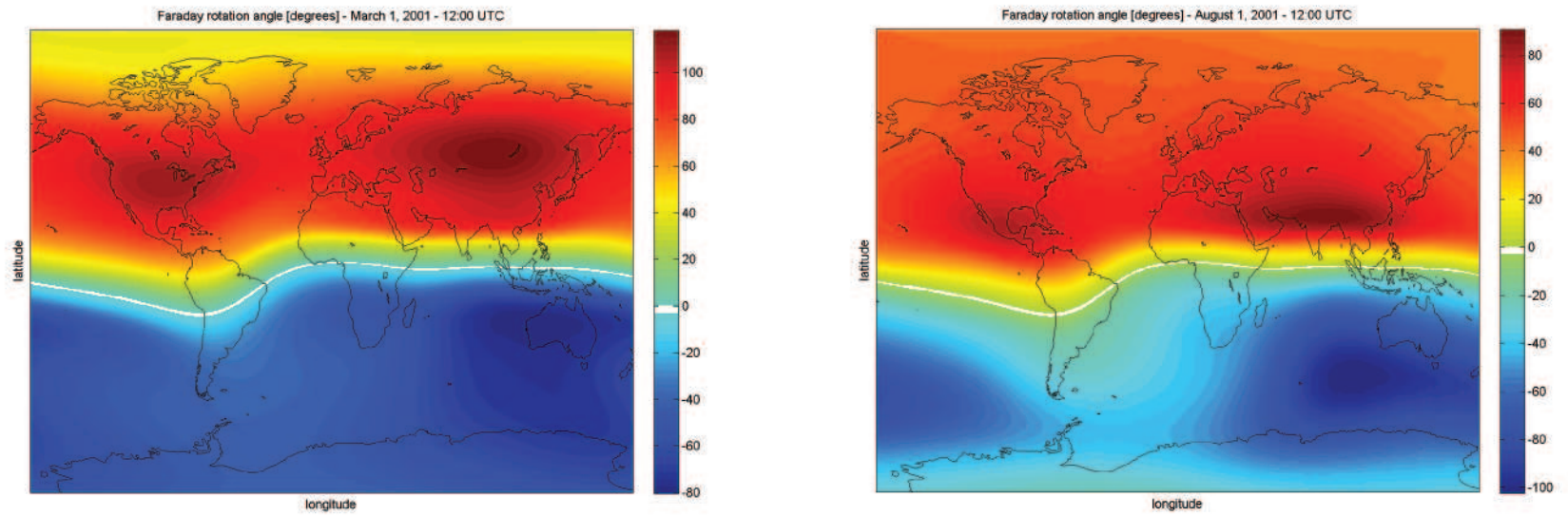
Figure 5.8: Predicted one-way Faraday rotation for 1 March and 1 August 2001 for P-band. The parameters are height (675 km), frequency (0.439 GHz), year (2001), date (1 March (left)/1 August (right)), time (12 pm), look angle (10°) and azimuth angle (5°). The white line was inserted to highlight the zero-crossing of the Faraday rotation.
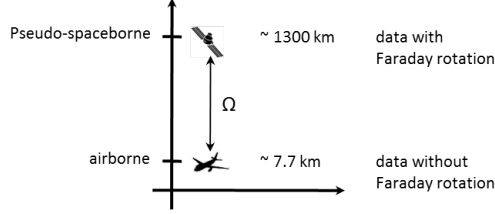
Figure 5.9: Superposition of Faraday rotation angle to airborne data leads to space-
borne data.

5.4 Generation of synthetic spaceborne data

The NASA/ JPL AIRSAR data set provides calibrated radar backscatter of the
imaged scenes for C-, L- and P-band in compressed Stokes matrix format. The Stokes
matrix can be extracted from the compressed Stokes matrix format. Then, the 16
scattering matrix cross products of the form $S_{pq}S_{pq}^*$, $(p,q) \in \{H,V\}$ are retrieved. It is
possible to retrieve the Stokes matrix from the scattering matrix, but from the Stokes
matrix it is not possible to retrieve the full scattering matrix. To bypass the need for
the scattering matrix, the scattering matrix cross products $S_{pq}S_{pq}^*$ are used throughout
this work. The synthetic spaceborne Stokes matrix is based on the AIRSAR scattering
matrix cross products $S_{pq}S_{pq}^*$ and the predicted Faraday rotation angle either assuming
no system distortion terms or including system distortion terms. This will artificially
superimpose the predicted Faraday rotation angle to the airborne radar data set, and
therefore generate synthetic spaceborne data. The concept is visualized in Fig. 5.9.
From this synthetic spaceborne Stokes matrix the 16 new scattering matrix cross
products $M_{pq}M_{pq}^*$, $(p,q) \in \{H,V\}$ can be calculated. The detailed procedure is given
in Appendix C. The synthetic spaceborne data can then be used to retrieve the
Faraday rotation angle based on the scattering matrix cross product $M_{pq}M_{pq}^*$. The
estimated Faraday rotation angle can be compared to the predicted Faraday rotation
angle, which will give a significant measure for the efficiency of the proposed approach.

An example of a real image from an AIRSAR overflight (CM5273) is given in
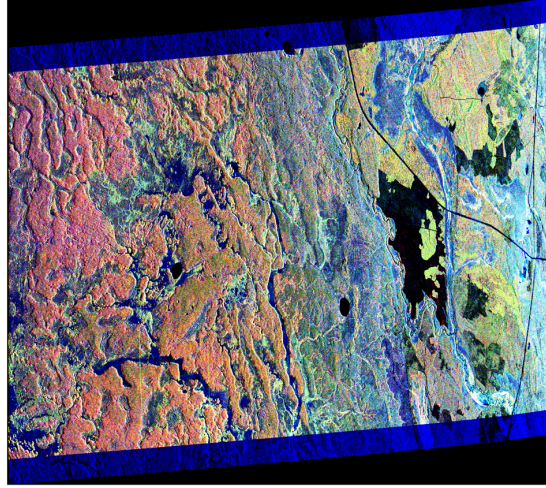
Figure 5.10: Airborne radar image CM5273 (South Fen & JP341-1) used in analysis. The along-track direction is vertical and the cross-track direction is horizontal. Line of flight on the right from bottom to top of image.

Table 5.1: Specifications of CM5273

Parameter	CM5273
flight altitude	7.6553 km
frequency	5.302 GHz (C-band), 1.250 GHz (L-band), 0.439 GHz (P-band)
year	1994
date	23. July (day of year: 204)
look angle	$22.8° - 72.4°$
azimuth angle	-19.1°
time (h)	9.30
latitude	$53.8641° \ N - 53.9605° \ N$
longitude	$255.423° \ E - 255.367° \ E$

Fig. 5.10. It shows the AIRSAR data over the South Fen & JP 341-1 site in Saskatchewan, Canada. The three colors red, green and blue are used for P-band, L-band and C-band to create the RGB image. The swath in cross-track direction covers a width of 17 km and contains 2560 samples while the swath length in the along-track direction is 10.6 km and has 1156 lines in the data. More information about the images are given in the AIRSAR header file and the relevant information for CM5273 is summarized in Table 5.1.

The Faraday rotation angle does not change over the extent of the airborne data set. The Faraday rotation angle for P-band over the Earth for the parameter given in

156
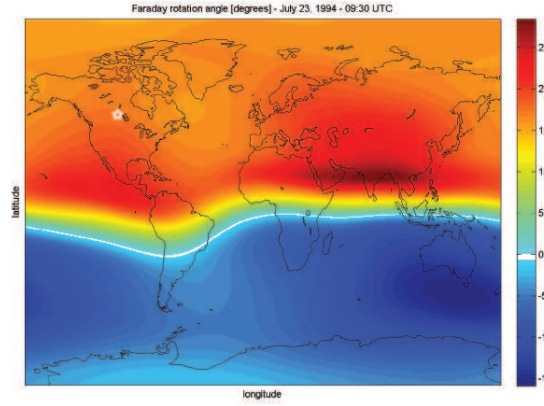
Figure 5.11: Prediction of the Faraday rotation angle for CM5273_P.DAT. The parameters for the prediction of the Faraday rotation angle are chosen as given in Table 5.1.

Table 5.1 is given in Fig. 5.11. The location of the airborne data set is marked with a white star.

The Faraday rotation angle at P-band for the location of the airborne radar image CM5273 is predicted to be around $20°$. Therefore, a fixed Faraday rotation angle of $20°$ is applied over the whole AIRSAR image assuming no other system distortion terms. The difference between radar images without Faraday rotation and images with $20°$ of Faraday rotation is shown in Fig. 5.12. A Faraday rotation angle of only $20°$ can alter the radar backscatter significantly, especially for the HH and VV channels. Another analysis is to select five pixels of different land cover types within the radar image and superimpose a Faraday rotation angle ranging from $0°$ to $360°$ assuming no other system distortion terms. This is shown in Fig. 5.13 where the respective radar backscatter coefficients of the pixels without Faraday rotation are shown as a dot. The impact of the Faraday rotation effect on the signal can be up to a 10 dB difference and shows a sinusoidal behavior. Figure 5.14 shows the error in dB (difference of signal with and without Faraday rotation angle) introduced solely by Faraday rotation angle, for a range of Faraday rotation angles from $0°$ to $360°$ assuming no other system distortion terms. The exact error propagation of this radar
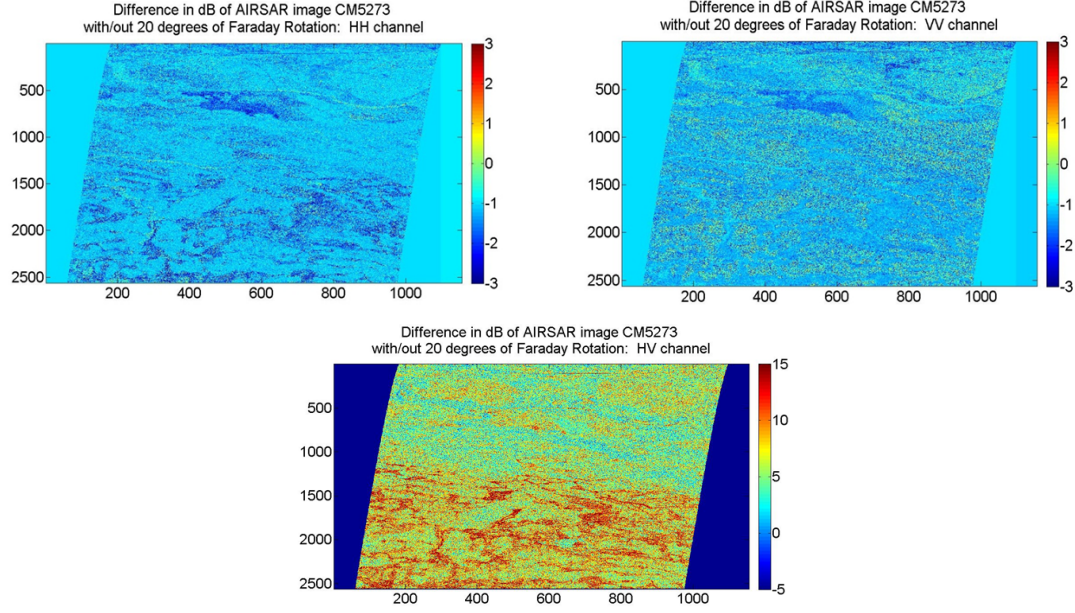
Figure 5.12: Error uncertainty analysis for P-band CM5273: Difference in dB for image with (assuming 20° over entire image) and without Faraday rotation for HH (top left), VV (top right) and HV (bottom) channels assuming no other system distortion terms.

backscatter difference due to Faraday rotation for the retrieval of soil moisture is a topic for future work.

Another AIRSAR image used in the validation is CM6367 shown in Fig. 5.15. It shows the AIRSAR data over the INJUNE 360-3 site in Queensland, Australia. The three colors red, green and blue are used for P-, L- and C-band to create the RGB image. The image contains of 2351 samples and 7334 lines. More information about this particular image is summarized in Table 5.2.

5.5 Retrieval of Faraday rotation angle assuming no other disturbances

The retrieval of the Faraday rotation angle assuming no other disturbances can be achieved by using the approach of Bickel and Bates [127]. This approach was originally introduced in 1965 [127] and has been described by Freeman in 2004 [115] as well as
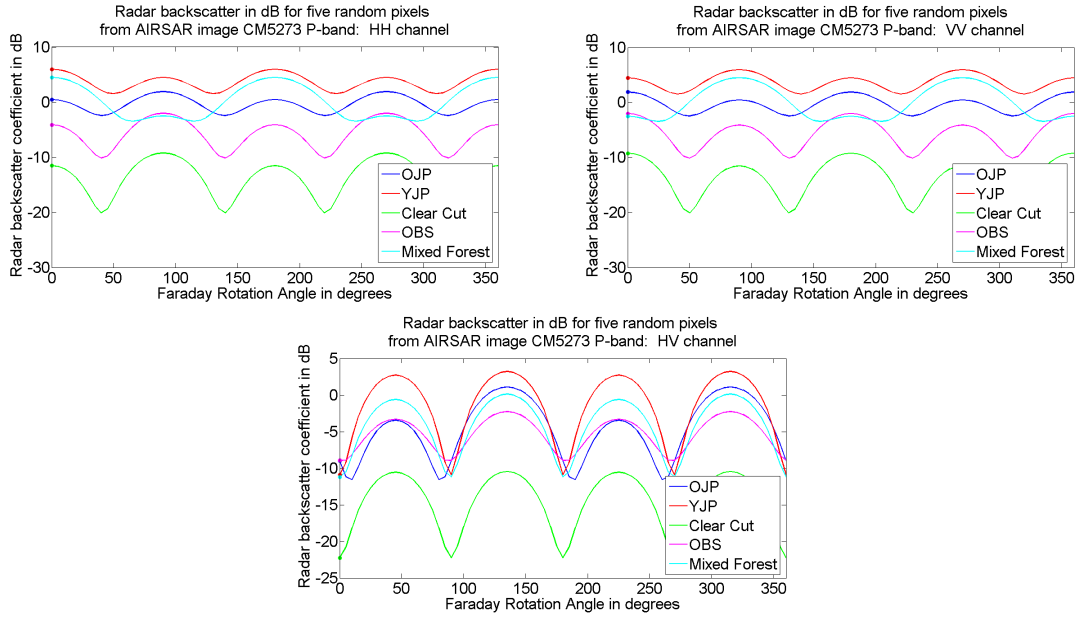
Figure 5.13: Error uncertainty analysis for P-band CM5273: Sweep of Faraday rotation angle for five pixels with different land cover types for HH (top left), VV (top right) and HV (bottom) channels assuming no other system distortion terms.
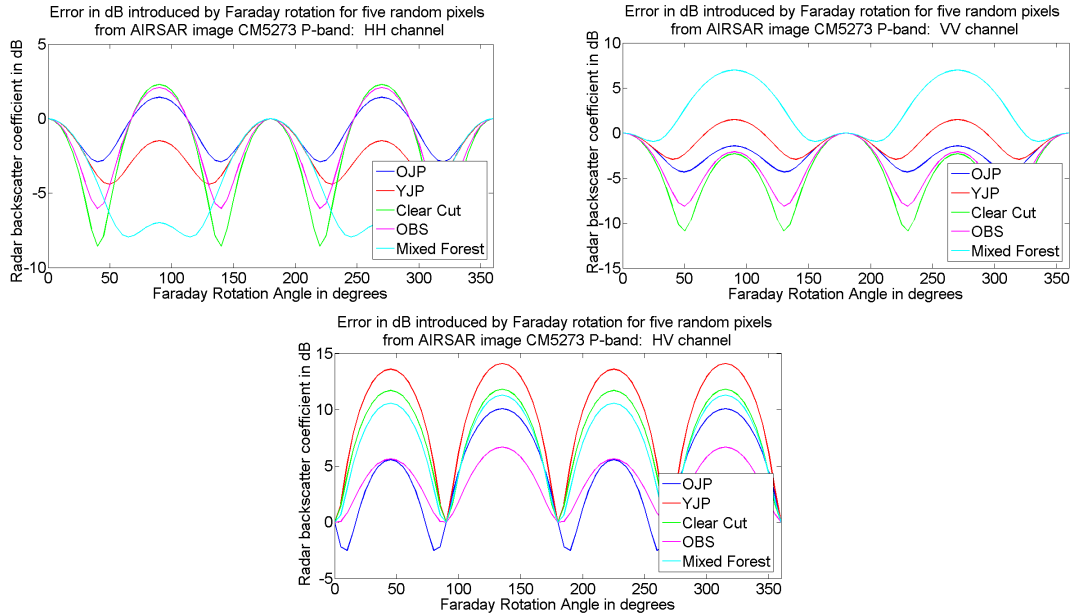
Figure 5.14: Error uncertainty analysis for P-band CM5273: Error in dB introduced by Faraday rotation for five pixels with different land cover types for HH (top left), VV (top right) and HV (bottom) channels assuming no other system distortion terms.
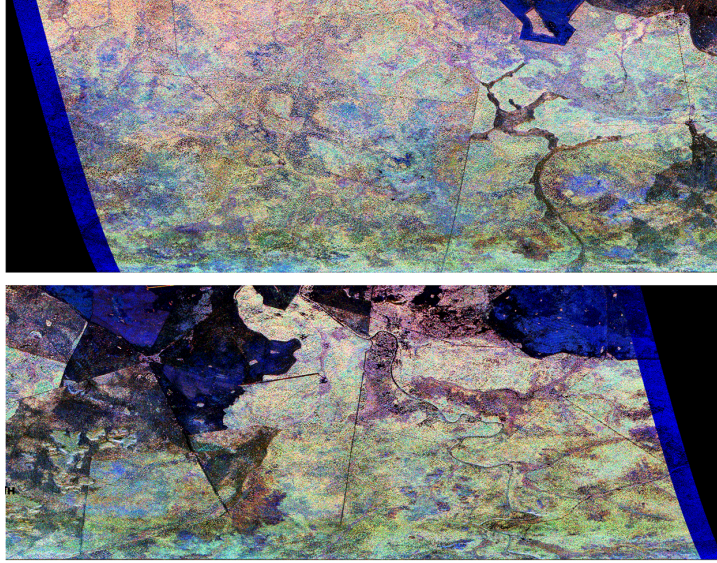
Figure 5.15: Airborne radar image CM6367 (INJUNE 360-3) used in analysis. The along-track direction is horizontal and the cross-track direction is vertical. Image has been split in flight direction. Line of flight from left to right of image (top, then bottom).

Table 5.2: Specifications of CM6367

Parameter	CM6367
flight altitude	7.7648 km
frequency	5.291 GHz (C-band), 1.239 GHz (L-band), 0.428 GHz (P-band)
year	2000
date	31. August (day of year: 244)
look angle	$26.8° - 63.2°$
azimuth angle	$0.1°$
time (h)	1.58
latitude	$-25.5835° \, N - -25.2549° \, N$
longitude	$147.4440° \, E - 147.4440° \, E$

by other authors. The availability of synthetic spaceborne data for which the Faraday rotation angle is known allows for application and validation of the Bickel and Bates approach. The Faraday rotation angle is predicted with the input parameters defined in Table 5.1 and superimposed to random pixels of the AIRSAR of image CM5273 at P-band. The comparison can be seen in Fig. 5.16. The figure on the left shows the ground truth (e.g. predicted Faraday rotation) and the estimated Faraday rotation angle. The estimated Faraday rotation reproduces the ground truth exactly for the interval from $\Omega = -45°$ to $+45°$. The figure on the right shows the tangent of the ground truth and the tangent of the estimated Faraday rotation angle. The ground truth and the estimated Faraday rotation angle show absolute consistency for the same interval. The sudden mismatch at $\Omega = -45°$ and $\Omega = +45°$ is caused by the implementation of the argument of $Z_{12}Z_{21}^*$. Due to the tangent function, the Faraday rotation effect can only be retrieved modulo $\pi/2$, which leads to a $\pi/2$ phase error. Freeman [115] suggests four ideas to mitigate this problem: (1) deploy a calibration target with a known polarization signature within the scene which should reveal the presence of this error, (2) examine the polarization signature of a flat, (slightly) rough surface for which the VV backscatter term is known to be slightly greater or equal to the HH, (3) constrain Ω itself (though this would only make sense in higher frequencies), and (4) correlate the dataset with an earlier, Faraday rotation free one. Because all of these ideas use either external information or place severe restrictions on applicability, a new approach has to be found.

A promising approach for unwrapping the phase is presented by Goldstein *et al.* [134]. It focuses on the problem of relating different individual phase measurements in a two-dimensional field by resolving the 2π-ambiguities associated with the phase of signals and is generally used for interferometric SAR applications. This approach could be adapted to mitigate the $\pi/2$ phase error. However, this approach has not been evaluated for the current work because it is based on the assumption that data
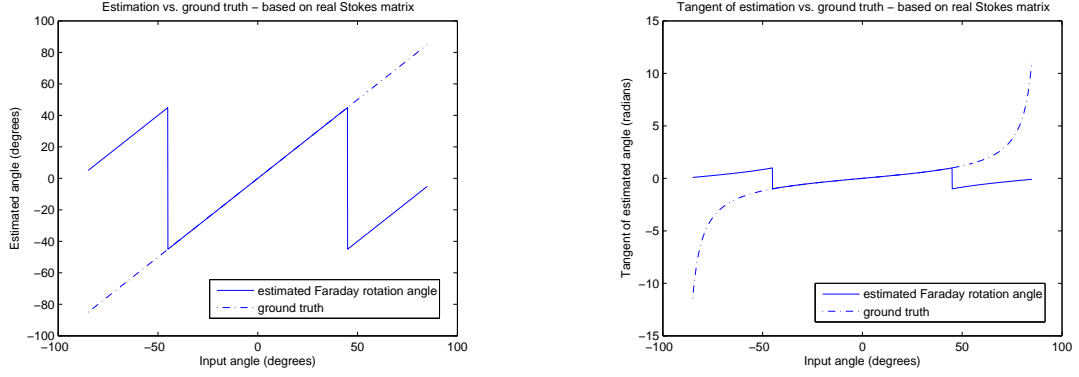
Figure 5.16: Verification of estimated Faraday rotation based on measured Stokes matrix from AIRSAR. Figure on the left shows estimated angle and ground truth over the ground truth. Figure on the right shows tangent of estimated angle and tangent of ground truth over the ground truth.

over a large area is available. If this area contained the equator, the zero-crossing of the Faraday rotation near the equator could be used as a suitable ground truth [135]. But this work uses airborne data that are only available as a thin swath of data over which the Faraday rotation tends not to change drastically.

Another convenient approach is thus developed. The predicted Faraday rotation angle is used to first mitigate the modulo $\pi/2$ uncertainty. The number of full rotations will be calculated and only the value modulo $\pi/4$ is superposed. After the retrieval of the estimated Faraday rotation angle, the full rotations are again added to the retrieved estimated angle and the complete Faraday rotation angle is available. If the proposed algorithm for the estimation of the Faraday rotation angle is used for real spaceborne data in the future, the same technique can be applied to solve the $\pi/2$ phase error. The only difference is that the Faraday rotation angle will be first predicted by the proposed simulations. This angle will then be used as a ground truth and the Faraday rotation angle can then be estimated modulo $\pi/2$.

The retrieval accuracy of the Faraday rotation angle is shown to be sufficient such that acceptable levels of backscatter distortion are not exceeded, e.g. $\Omega \leq 5°$ (or $\leq 3°$ for some applications) [136]. Freeman [115] states that acceptable levels of

backscatter distortion are not exceeded if $\Omega \leq 5°$ (or $\leq 3°$ for some applications). Wright *et al.* [137] confirm this statement by declaring that Faraday rotation angles with $\Omega > 5°$ to $8°$ (depending on land cover) are assumed to significantly affect the recovery of the signal. With the presented approach, these limits can be maintained and the Faraday rotation angle can be effectively predicted.

5.6 Retrieval of Faraday rotation angle in the presence of other system distortion terms

Ultimately, a self-contained calibration technique based on an end-to end system model including the effects of the ionosphere is needed. In this chapter a method to integrate the mitigation of the Faraday rotation effect into the calibration process is presented. This approach assumes that the Faraday rotation is known to within at least $\pm 10°$ of the true Faraday rotation angle. This can be reasonably assumed by predicting the Faraday rotation angle based on approximate distributions of the electron content in the ionosphere available from measurements and models such as the IRI and IGRF as described in chapter 5.3. Further assumptions are reciprocal crosstalk, i.e. identical crosstalk on transmit and receive ($\delta_3 = \delta_1$, $\delta_4 = \delta_2$), and backscatter reciprocity ($S_{HV} = S_{VH}$). This leads to the radar system model in Eq. (5.6). For validation, the synthetic spaceborne data assuming system distortion terms and including Faraday rotation is used allowing a near-realistic assessment of the performance. Once spaceborne radar is available with the launch of the SMAP mission, the algorithm can be applied to real data.

The specifications for the two used AIRSAR images given in Tables 5.1 and 5.2 are used to predict the Faraday rotation angles for images CM5273 and CM6367 for a SMAP flight altitude of 685 km. The predicted Faraday rotation angles are given in Table 5.3. The predicted Faraday rotation angles for these two images only reach a

total of 15 degrees, but potential Faraday rotation angles can be much higher. For the purpose of this validation, Faraday rotation angles of $\Omega = \{1°, 5°, 10°, 25°, 50°, 100°\}$ are used to generate synthetic spaceborne radar data to show successful retrieval for a wide range of Faraday rotation angles.

Table 5.3: Predicted Faraday rotation angle for AIRSAR images CM5273 and CM6367.

	CM5273	CM6367
C-band	0.10°	0.05°
L-band	1.82°	0.83°
P-band	14.77°	6.96°

Ten pixels of various land cover types are extracted from each image and synthetic spaceborne radar data are generated. The assumed ground truth for the system parameter terms is given in Table 5.4.

Table 5.4: System parameter ground truth and initial guesses.

Parameter	Ground truth	Initial guess
$\lvert f_1 \rvert$	0.89	1.00
$\angle f_1$	3°	0°
$\lvert f_2 \rvert$	1.05	1.00
$\angle f_2$	5°	0°
$\lvert \delta_1 \rvert$	0.017783 (-35 dB)	0.031623 (-30 dB)
$\angle \delta_1$	43°	0°
$\lvert \delta_2 \rvert$	0.025119 (-32 dB)	0.031623 (-30 dB)
$\angle \delta_2$	$-10°$	0°

The parameter estimation problem is formulated as a static optimization problem. The constitutive equations that contain these unknown complex parameters are, in reality, active equality constraints to the estimation problem. Such a numerical formulation is quite difficult to solve efficiently, given the presence of noise and the lack of convexity in the problem [138]. Hence, these complex equality constraints are first converted into real valued constraints by separating the real and imaginary parts of the equations. This results in 32 simultaneous non-linear equations in real variables. Then these equality constraints are relaxed by formulating the objective function as

the least square of errors in satisfying these individual equations. Consequently, this problem reduces to an unconstrained optimization problem in 24 variables, subjected to upper and lower bounds. The variables themselves are assumed to be continuous. A cost function can be solved by minimizing a cost function and balancing the unknowns to achieve optimum sensitivity. The cost function L is defined as an L2 norm relating the measured scattering matrix cross products $\boldsymbol{M}_{pq}\boldsymbol{M}_{pq}^*$ (or in this case the artificially generated synthetic spaceborne data) with the forward modeled scattering matrix cross products $M_{pq}M_{pq}^*$ as follows:

$$L = \sum_{(p,q)\in\{H,V\}} \left|\boldsymbol{M}_{pq}\boldsymbol{M}_{pq}^* - M_{pq}M_{pq}^*\right|^2 \tag{5.9}$$

The equations for each measured scattering matrix cross product $\boldsymbol{M}_{pq}\boldsymbol{M}_{pq}^*$ can be analytically expressed allowing the calculation of the forward modeled scattering matrix cross products $M_{pq}M_{pq}^*$. There are 24 unknowns: 15 complex polarimetric scattering matrix cross products $S_{pq}S_{pq}^*$, $(p,q) \in \{H,V\}$, the real and imaginary parts of δ_1 and δ_2, the Faraday rotation angle Ω as well as the real and imaginary part of f_1 and f_2, which often have substantially different orders of magnitude. Three different optimization techniques are applied. The initial guess of the system parameters are given in Table 5.4 and the polarimetric scattering matrix cross products $S_{pq}S_{pq}^*$, $(p,q) \in \{H,V\}$ are initialized with their respective measured scattering matrix cross products $\boldsymbol{M}_{pq}\boldsymbol{M}_{pq}^*$, $(p,q) \in \{H,V\}$.

The solution of this problem is explored using three different numerical optimization techniques: the Non-linear Conjugate Gradient Method (nCGM), the Quasi-Newton Method (QNM) and the Simulated Annealing method (simAnn). The nCGM and QNM are both gradient based methods that are only guaranteed to solve only for local minima in the absence of convexity. The gradient is numerically calculated using finite difference approximations. These two methods differ in the way line search is

conducted: nCGM conducts consecutive line-searches in orthogonal directions using linear approximations, whereas QNM approximates the Hessian by consecutively updating gradient information. This allows QNM to maintain a positive-definite Hessian approximation and obtain quadratic convergence, albeit, at a higher computational cost. The simAnn method is a global optimization technique for large search spaces (continuous and discrete). It is an adaptation of the Metropolis algorithm and based on principles of randomized search. This algorithm tends to be non-greedy and avoid getting stuck at local minima. However, it does require substantially more computational resources. Also due to the lack of intuitive model parameters, heuristics play a large role in its tuning. Solutions were obtained using Polak and Ribiere's numerical implementation of nCGM [139, 140], a Broyden-Fletcher-Goldfarb-Shanno (BFGS) implementation of QNM [139, 141] and a constrained simulated annealing implementation [138].

First, the retrieval accuracy of the three optimization techniques is discussed and compared on a subset of the problem. The optimization is executed on a single pixel of CM5273 for C-, L- and P-band and for Faraday rotation angles defined as $\Omega = \{1°, 5°, 10°, 25°, 50°, 100°\}$. The initial guess of the Faraday rotation angle Ω is defined to be within $\pm$ 25 degrees of the Faraday rotation ground truth. The QNM converges for the entire Faraday rotation range of $\pm$ 25 degrees from the ground truth. For each retrieval the mean and standard deviation of the absolute difference between ground truth and retrieved result for the various parameters is shown in Table 5.5. It can be seen that the QNM optimization technique performs very well, but that the phases of δ_1 and δ_2 are not reliably retrieved. This is considered acceptable since the magnitude of δ_1 and δ_2 are very small (on the order of -30 dB) such that the impact of the phase is minimal.

The nCGM converges reliably for the Faraday rotation range $\pm$ 10 degrees from the Faraday rotation ground truth. For each retrieval the mean and standard de-

Table 5.5: Retrieval accuracy with QNM for a single CM5273 pixel. Mean and standard deviation (std.) of absolute difference is reported in absolute values and absolute degrees.

Difference	C-band		L-band		P-band	
	Mean	Std.	Mean	Std.	Mean	Std.
$\angle\,\Omega$	0.0472	0.0357	0.0473	0.0441	0.2446	0.2131
$|f_1|$	0.0274	0.0208	0.0302	0.0263	0.0697	0.0315
$\angle\,f_1$	1.3852	1.5228	1.2575	1.2337	1.6376	1.6411
$|f_2|$	0.0385	0.0220	0.0416	0.0287	0.0377	0.0280
$\angle\,f_2$	1.8844	1.5516	1.3929	1.5657	1.9165	1.3043
$|\delta_1|$	0.0130	0.0113	0.0125	0.0171	0.0139	0.0124
$\angle\,\delta_1$	52.4938	39.4333	46.7628	35.2455	36.0078	23.7669
$|\delta_2|$	0.0156	0.0163	0.0198	0.0288	0.0140	0.0073
$\angle\,\delta_2$	38.5704	22.2512	42.5948	30.5893	31.2303	21.9973
$\Re\{S_{HH}S_{HH}^*\}$	0.0016	0.0011	0.0039	0.0036	0.0092	0.0161
$\Re\{S_{HH}S_{VH}^*\}$	0.0012	0.0008	0.0020	0.0020	0.0015	0.0005
$\Im\{S_{HH}S_{VH}^*\}$	0.0033	0.0018	0.0038	0.0035	0.0039	0.0033
$\Re\{S_{HH}S_{VV}^*\}$	0.0038	0.0019	0.0056	0.0042	0.0037	0.0014
$\Im\{S_{HH}S_{VV}^*\}$	0.0010	0.0005	0.0025	0.0027	0.0010	0.0007
$\Re\{S_{VH}S_{HH}^*\}$	0.0029	0.0016	0.0075	0.0049	0.0081	0.0038
$\Im\{S_{VH}S_{HH}^*\}$	0.0023	0.0011	0.0029	0.0026	0.0031	0.0019
$\Re\{S_{VH}S_{VH}^*\}$	0.0028	0.0019	0.0015	0.0013	0.0039	0.0024
$\Re\{S_{VH}S_{VV}^*\}$	0.0016	0.0009	0.0012	0.0006	0.0025	0.0025
$\Im\{S_{VH}S_{VV}^*\}$	0.0029	0.0016	0.0075	0.0049	0.0081	0.0038
$\Re\{S_{VV}S_{HH}^*\}$	0.0023	0.0011	0.0029	0.0026	0.0031	0.0019
$\Im\{S_{VV}S_{HH}^*\}$	0.0028	0.0019	0.0015	0.0013	0.0039	0.0024
$\Re\{S_{VV}S_{VH}^*\}$	0.0016	0.0009	0.0012	0.0006	0.0025	0.0025
$\Im\{S_{VV}S_{VH}^*\}$	0.0038	0.0019	0.0056	0.0042	0.0037	0.0014
$\Re\{S_{VV}S_{VV}^*\}$	0.0010	0.0005	0.0025	0.0027	0.0010	0.0007

viation of the absolute difference between ground truth and retrieved result for the various parameters is shown in Table 5.6. It can be seen that the nCGM optimization technique works well, but the phases of δ_1 and δ_2 are also not reliably retrieved. Furthermore, all other variables are retrieved less accurately than for QNM.

The simAnn technique converges for the entire Faraday rotation range of $\pm$ 25 degrees from the Faraday rotation ground truth. For each retrieval the mean and standard deviation of the absolute difference between ground truth and retrieved result for the various parameters is shown in Table 5.7. The simAnn method performs

Table 5.6: Retrieval accuracy with nCGM for a single CM5273 pixel. Mean and standard deviation (std.) of absolute difference is reported in absolute values and absolute degrees.

	C-band		L-band		P-band	
Difference	Mean	Std.	Mean	Std.	Mean	Std.
$\angle\,\Omega$	1.3868	0.7244	0.4644	0.4199	0.2414	0.0342
$\lvert f_1 \rvert$	0.0986	0.0148	0.0422	0.0140	0.1061	0.0047
$\angle\,f_1$	2.9548	0.7211	3.7219	0.4175	3.0965	0.1597
$\lvert f_2 \rvert$	0.0414	0.0147	0.0146	0.0086	0.0521	0.0051
$\angle\,f_2$	5.3413	0.5323	4.3310	0.5356	4.9667	0.1586
$\lvert \delta_1 \rvert$	0.0159	0.0059	0.0067	0.0056	0.0064	0.0026
$\angle\,\delta_1$	38.0517	3.2499	25.2773	11.6810	41.7465	1.4026
$\lvert \delta_2 \rvert$	0.0089	0.0061	0.0046	0.0028	0.0030	0.0015
$\angle\,\delta_2$	17.6966	3.4773	22.8145	14.3992	11.7284	1.2873
$\Re\{S_{HH}S_{HH}^*\}$	0.0006	0.0005	0.0017	0.0008	0.0002	0.0002
$\Re\{S_{HH}S_{VH}^*\}$	0.0014	0.0004	0.0022	0.0011	0.0002	0.0001
$\Im\{S_{HH}S_{VH}^*\}$	0.0080	0.0004	0.0047	0.0017	0.0047	0.0003
$\Re\{S_{HH}S_{VV}^*\}$	0.0032	0.0009	0.0025	0.0012	0.0007	0.0001
$\Im\{S_{HH}S_{VV}^*\}$	0.0005	0.0002	0.0015	0.0005	0.0012	0.0001
$\Re\{S_{VH}S_{HH}^*\}$	0.0014	0.0007	0.0016	0.0010	0.0010	0.0005
$\Im\{S_{VH}S_{HH}^*\}$	0.0017	0.0001	0.0012	0.0005	0.0015	0.0001
$\Re\{S_{VH}S_{VH}^*\}$	0.0056	0.0006	0.0022	0.0007	0.0037	0.0001
$\Re\{S_{VH}S_{VV}^*\}$	0.0013	0.0003	0.0024	0.0003	0.0064	0.0001
$\Im\{S_{VH}S_{VV}^*\}$	0.0014	0.0007	0.0016	0.0010	0.0010	0.0005
$\Re\{S_{VV}S_{HH}^*\}$	0.0017	0.0001	0.0012	0.0005	0.0015	0.0001
$\Im\{S_{VV}S_{HH}^*\}$	0.0056	0.0006	0.0022	0.0007	0.0037	0.0001
$\Re\{S_{VV}S_{VH}^*\}$	0.0013	0.0003	0.0024	0.0003	0.0064	0.0001
$\Im\{S_{VV}S_{VH}^*\}$	0.0032	0.0009	0.0025	0.0012	0.0007	0.0001
$\Re\{S_{VV}S_{VV}^*\}$	0.0005	0.0002	0.0015	0.0005	0.0012	0.0001

worse than the other two methods.

The retrieval sensitivity of the three optimization techniques varies over the range of initial guesses for the Faraday rotation angle. Since retrieval stability over the range of initial guess of Faraday rotation is crucial, an example for each of the three optimization techniques is discussed in Fig. 5.17. It is seen that due to the continuous nature of the variables and well-informed initial starting point, gradient based methods outperform the simAnn method for fixed computational resources. The nCGM shows greater sensitivity to the initial condition due to first order approximations in

Table 5.7: Retrieval accuracy with simAnn for a single CM5273 pixel. Mean and standard deviation (std.) of absolute difference is reported in absolute values and absolute degrees.

Difference	C-band		L-band		P-band	
	Mean	Std.	Mean	Std.	Mean	Std.
$\angle\,\Omega$	1.6124	1.1272	1.5716	7.1393	0.9414	5.2425
$\lvert f_1 \rvert$	0.0927	0.0436	0.0834	0.0474	0.0962	0.0588
$\angle\,f_1$	4.4838	3.6005	4.2943	3.4328	5.5019	4.5740
$\lvert f_2 \rvert$	0.0767	0.0530	0.0679	0.0482	0.0912	0.0663
$\angle\,f_2$	6.3151	4.5535	5.4565	3.8185	7.0450	5.2140
$\lvert \delta_1 \rvert$	0.0487	0.0368	0.0453	0.0381	0.0751	0.0558
$\angle\,\delta_1$	52.2505	37.3734	53.9736	36.9011	55.6497	39.7533
$\lvert \delta_2 \rvert$	0.0433	0.0385	0.0423	0.0383	0.0644	0.0563
$\angle\,\delta_2$	43.1759	25.5474	45.7829	26.0355	45.9672	27.9547
$\Re\{S_{HH}S_{HH}^*\}$	0.0060	0.0060	0.0102	0.0113	0.0153	0.0217
$\Re\{S_{HH}S_{VH}^*\}$	0.0033	0.0031	0.0054	0.0043	0.0032	0.0034
$\Im\{S_{HH}S_{VH}^*\}$	0.0083	0.0074	0.0078	0.0104	0.0077	0.0127
$\Re\{S_{HH}S_{VV}^*\}$	0.0050	0.0043	0.0065	0.0053	0.0055	0.0054
$\Im\{S_{HH}S_{VV}^*\}$	0.0042	0.0036	0.0061	0.0059	0.0043	0.0036
$\Re\{S_{VH}S_{HH}^*\}$	0.0044	0.0038	0.0093	0.0074	0.0115	0.0101
$\Im\{S_{VH}S_{HH}^*\}$	0.0044	0.0037	0.0085	0.0070	0.0127	0.0110
$\Re\{S_{VH}S_{VH}^*\}$	0.0058	0.0044	0.0051	0.0040	0.0065	0.0055
$\Re\{S_{VH}S_{VV}^*\}$	0.0052	0.0041	0.0052	0.0047	0.0081	0.0068
$\Im\{S_{VH}S_{VV}^*\}$	0.0044	0.0039	0.0094	0.0073	0.0114	0.0103
$\Re\{S_{VV}S_{HH}^*\}$	0.0042	0.0036	0.0084	0.0069	0.0123	0.0109
$\Im\{S_{VV}S_{HH}^*\}$	0.0057	0.0045	0.0051	0.0040	0.0064	0.0053
$\Re\{S_{VV}S_{VH}^*\}$	0.0052	0.0043	0.0051	0.0047	0.0079	0.0066
$\Im\{S_{VV}S_{VH}^*\}$	0.0047	0.0042	0.0067	0.0052	0.0055	0.0054
$\Re\{S_{VV}S_{VV}^*\}$	0.0041	0.0033	0.0062	0.0061	0.0048	0.0038

line search. It performs well for an initial guess of approximately $\pm$ 10 degrees outside which the retrieval sensitivity decreases rapidly. Points missing in the figure have been retrieved but are located outside of the 5 to 15 degrees retrieved angle range shown in the figure. The QNM proves to be most robust and efficient for problem at hand, and will be used as the solution method.

The overall performance of the QNM is further investigated by analyzing 10 pixels over various land cover types for C-, L- and P-band and $\Omega = \{1°, 5°, 25°, 50°, 100°\}$ for both CM5273 and CM6763. The retrieved mean and standard deviation of the abso-
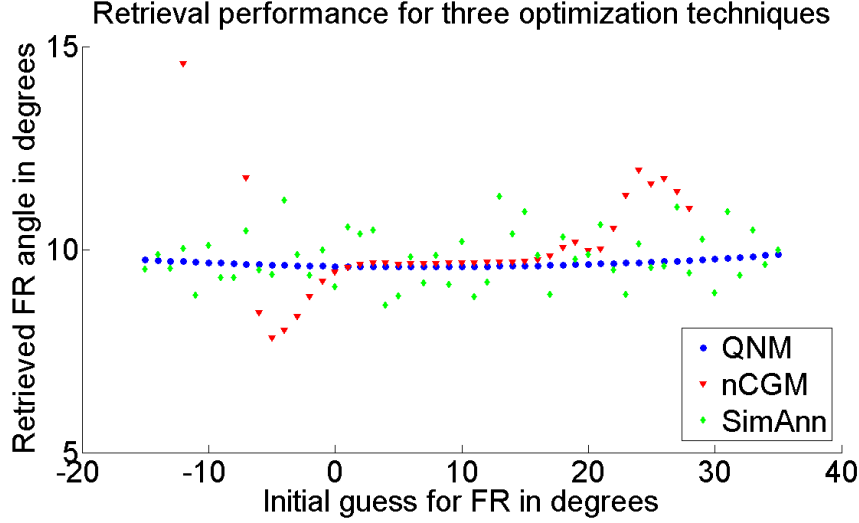
Figure 5.17: Comparison of retrieval performance for three optimization techniques: QNM, nCGM and simAnn. The Faraday rotation ground truth is 10° and the initial guess of Faraday rotation is in the range of -15° to 35°.

lute difference between ground truth and retrieved result for the various parameters is shown in Table 5.8 and 5.9. The retrieval performance with synthetic spaceborne radar data is very promising, although δ_1 and δ_2 cannot be retrieved reliably. In the future, this approach should be applied to SMAP radar data to validate its performance further. In the case that Ω is not well estimated with the IRI and IGRF models, it is possible to first use the simAnn method to find an initial guess of Ω and then subsequently use QNM to do the final retrieval. The simAnn method will find the global minimum although it requires more computational resources. A similar procedure can be applied if the initial guess of the system parameters and the scattering matrix cross products is unreliable. This two-step procedure will allow the retrieval of unknowns potentially for an even larger range of initial conditions.

5.7   Conclusion

In this chapter, a radar-only method to mitigate the Faraday rotation effect in the presence of other system distortion terms was presented. This is achieved by first

170

Table 5.8: Retrieval accuracy with QNM for a 10 pixels in CM5273. Mean and standard deviation (std.) of absolute difference is reported in absolute values and absolute degrees.

Difference	C-band		L-band		P-band	
	Mean	Std.	Mean	Std.	Mean	Std.
$\angle\,\Omega$	0.0383	0.0321	0.0631	0.0652	0.2625	1.8646
$|f_1|$	0.0350	0.0273	0.0387	0.0300	0.0548	0.0634
$\angle\,f_1$	1.5137	1.4419	1.7793	1.3143	1.9989	4.2783
$|f_2|$	0.0421	0.0284	0.0454	0.0327	0.0497	0.0647
$\angle\,f_2$	1.7845	1.4070	2.0364	1.4687	2.5824	5.7363
$|\delta_1|$	0.0114	0.0096	0.0158	0.0190	0.0232	0.0485
$\angle\,\delta_1$	39.5701	32.0028	50.4912	36.3805	46.0123	34.1199
$|\delta_2|$	0.0121	0.0132	0.0161	0.0207	0.0186	0.0263
$\angle\,\delta_2$	35.8133	27.4932	36.8417	26.9563	34.9365	26.4088
$\Re\{S_{HH}S_{HH}^*\}$	0.0014	0.0017	0.0033	0.0044	0.0152	0.1272
$\Re\{S_{HH}S_{VH}^*\}$	0.0009	0.0010	0.0019	0.0023	0.0084	0.0566
$\Im\{S_{HH}S_{VH}^*\}$	0.0026	0.0030	0.0031	0.0033	0.0119	0.0354
$\Re\{S_{HH}S_{VV}^*\}$	0.0034	0.0026	0.0038	0.0035	0.0124	0.0419
$\Im\{S_{HH}S_{VV}^*\}$	0.0011	0.0012	0.0017	0.0019	0.0056	0.0210
$\Re\{S_{VH}S_{HH}^*\}$	0.0030	0.0023	0.0057	0.0050	0.0101	0.0289
$\Im\{S_{VH}S_{HH}^*\}$	0.0008	0.0008	0.0019	0.0019	0.0061	0.0173
$\Re\{S_{VH}S_{VH}^*\}$	0.0013	0.0014	0.0022	0.0024	0.0056	0.0161
$\Re\{S_{VH}S_{VV}^*\}$	0.0014	0.0016	0.0018	0.0019	0.0042	0.0109
$\Im\{S_{VH}S_{VV}^*\}$	0.0030	0.0023	0.0057	0.0050	0.0101	0.0289
$\Re\{S_{VV}S_{HH}^*\}$	0.0008	0.0008	0.0019	0.0019	0.0061	0.0172
$\Im\{S_{VV}S_{HH}^*\}$	0.0013	0.0014	0.0022	0.0024	0.0056	0.0161
$\Re\{S_{VV}S_{VH}^*\}$	0.0014	0.0016	0.0018	0.0019	0.0042	0.0109
$\Im\{S_{VV}S_{VH}^*\}$	0.0034	0.0026	0.0038	0.0035	0.0124	0.0419
$\Re\{S_{VV}S_{VV}^*\}$	0.0011	0.0012	0.0017	0.0019	0.0056	0.0211

predicting the Faraday rotation angle at any instrument altitude, location and time on the globe based on IRI and IGRF models. With this predicted Faraday rotation angle, synthetic spaceborne radar data is generated based on AIRSAR radar data either in the presence of or assuming no system distortion terms. This artificial spaceborne data set is then used to validate the existing Bickel and Bates method to retrieve Faraday rotation angles assuming no other system distortion terms. Finally, it is used to test a novel method to retrieve Faraday rotation in the presence of other system distortion terms by defining an optimization problem. The retrieval performance is

Table 5.9: Retrieval accuracy with QNM for a 10 pixels in CM6367. Mean and standard deviation (std.) of absolute difference is reported in absolute values and absolute degrees.

Difference	C-band Mean	Std.	L-band Mean	Std.	P-band Mean	Std.
$\angle\,\Omega$	0.1846	3.6923	0.2311	0.2698	0.5369	0.8807
$|f_1|$	0.0409	0.0496	0.0490	0.0334	0.0645	0.0578
$\angle\,f_1$	1.6103	3.0102	2.3279	1.7030	2.5327	2.1181
$|f_2|$	0.0525	0.0593	0.0450	0.0326	0.0501	0.0503
$\angle\,f_2$	1.9020	3.6088	2.5983	1.7640	2.9902	2.1853
$|\delta_1|$	0.0237	0.0460	0.0183	0.0233	0.0224	0.0303
$\angle\,\delta_1$	40.2243	33.2576	54.0129	35.2390	49.0136	33.1365
$|\delta_2|$	0.0255	0.0505	0.0190	0.0230	0.0198	0.0261
$\angle\,\delta_2$	36.7686	24.4844	33.1345	24.3837	35.9994	27.1160
$\Re\{S_{HH}S_{HH}^*\}$	0.0092	0.0498	0.0042	0.0080	0.0060	0.0228
$\Re\{S_{HH}S_{VH}^*\}$	0.0053	0.0133	0.0014	0.0013	0.0029	0.0075
$\Im\{S_{HH}S_{VH}^*\}$	0.0109	0.0190	0.0021	0.0033	0.0050	0.0105
$\Re\{S_{HH}S_{VV}^*\}$	0.0187	0.0297	0.0019	0.0016	0.0033	0.0053
$\Im\{S_{HH}S_{VV}^*\}$	0.0059	0.0116	0.0010	0.0011	0.0021	0.0031
$\Re\{S_{VH}S_{HH}^*\}$	0.0186	0.0379	0.0039	0.0037	0.0048	0.0071
$\Im\{S_{VH}S_{HH}^*\}$	0.0075	0.0144	0.0021	0.0021	0.0053	0.0147
$\Re\{S_{VH}S_{VH}^*\}$	0.0068	0.0254	0.0020	0.0023	0.0042	0.0081
$\Re\{S_{VH}S_{VV}^*\}$	0.0076	0.0183	0.0017	0.0019	0.0046	0.0069
$\Im\{S_{VH}S_{VV}^*\}$	0.0186	0.0378	0.0039	0.0037	0.0048	0.0071
$\Re\{S_{VV}S_{HH}^*\}$	0.0075	0.0143	0.0021	0.0021	0.0053	0.0147
$\Im\{S_{VV}S_{HH}^*\}$	0.0068	0.0253	0.0020	0.0023	0.0042	0.0081
$\Re\{S_{VV}S_{VH}^*\}$	0.0076	0.0182	0.0017	0.0019	0.0046	0.0069
$\Im\{S_{VV}S_{VH}^*\}$	0.0187	0.0296	0.0019	0.0016	0.0033	0.0053
$\Re\{S_{VV}S_{VV}^*\}$	0.0059	0.0116	0.0010	0.0011	0.0021	0.0031

very promising for all three optimization techniques, although the QNM method was determined to be most successful. In the future, this approach should be applied to SMAP radar data to further validate its performance on real data.

CHAPTER VI

Conclusion and future work

6.1 Summary and immediate future work

In this dissertation, three important, but heretofore unaddressed, aspects in radar imaging for low frequency radars are addressed: effects of multispecies vegetation (heterogeneity at pixel level), heterogeneity at landscape level, and ionospheric effects.

In the first chapter, a generalized radar scattering model at fine scales is developed and presented. The vegetation modeling is generalized to describe multispecies multilayered vegetation allowing the modeling of any homogeneous forest with multiple species or growth stages. The below-ground modeling is generalized to an N-layered soil model capable of representing vertical soil heterogeneity in texture, moisture and roughness. The introduction of a soil moisture profile allows the modeling of a realistic hydrological behavior. Finally, a methodology to model terrain topography is developed and implemented, allowing even further generalization to include soil moisture retrieval over hilly and mountainous areas. Forward simulations of an evergreen forest over a two-dimensional slope with $\alpha \pm 3°$ and $\beta \pm 3°$ demonstrate that terrain topography modeling is crucial, especially over forested areas, as small slope variations have significant impact on radar backscatter strength. Each generalization step is validated by comparison of the simulated radar backscatter coefficients with

measured radar data. Pending issues are the VV channel imbalance for the UAVSAR radar data acquired over SMAPVEX12 and the uncalibrated tower-based radar data preventing direct comparison of the forward model accuracy at UMBS. Future work will include the acquisition of ground truth data over hilly terrain and to validate the terrain topography model with real data.

In the second chapter, the fine-scale retrieval capability is shown with two different radar data sets. L-band UAVSAR data is used to retrieve and validate surface soil moisture under a single-species boreal forest, and P-band AirMOSS data is used to retrieve and validate a RZSM profile over boreal forests. The retrieval results for the single-species boreal forest are promising, but the OBS site could not be adequately modeled due to in-scene complexity such as puddles, moss, and organic layer variations. The retrieval of RZSM is enabled with the adoption of a soil moisture profile described by a second-order polynomial. This allows the retrieval of soil moisture within a validity depth range based on the retrieval of only three coefficients, thus drastically reducing the number of unknowns. RZSM retrieval based on AirMOSS data is shown to be very promising. The forward modeling, enabling both the surface and RZSM soil moisture, has been extensively studied and improved as part of this retrieval effort. Furthermore, as part of the AirMOSS project, the framework and data handling/processing has been developed to allow soil moisture retrieval over a large area involving thousands of pixels. Future work will address the impact of constraining the soil moisture profile to hydrologically sound profiles and to utilize the radar data itself to classify land cover to be used in the retrieval.

The third chapter introduces a novel radar based technique to retrieve the coarse-scale soil moisture of a km-scale image where the homogeneity within the radar pixel can no longer be assumed. The methodology and scaling technique are developed on the basis of a sample site. A closed-loop validation depicts the impact of fine-scale heterogeneity on the coarse-scale radar backscatter coefficient. Assuming the linear

174

average of AirMOSS data over the same sample site as the measured radar backscatter coefficient, statistics can be exploited to retrieve the coarse-scale soil moisture. Two retrieval sets of the sample area are presented with promising results. The frame work is set up to allow for more validation, and future work includes collaboration with the SMAP algorithms and Cal/Val teams to test and apply this technique for core validation sites with more heterogeneity such as different land cover types, multilayered soil, different coarse-scale extents, and topography.

In the fourth chapter, a radar-only method to mitigate Faraday rotation effects in the presence of other system distortion terms is presented. Models are utilized to predict the Faraday rotation angle at any instrument altitude, location, and time on the globe. This prediction is then used to generate synthetic spaceborne data based on AIRSAR radar data - either in the presence of or assuming no other system distortion terms. This synthetic spaceborne data allows the validation of existing Faraday rotation angle retrieval methods assuming no other system distortion terms, but also the validation of the novel method. An optimization problem is formulated to retrieve the unknowns. Three different optimization techniques are compared, and the QNM method is found to be the most successful. Once spaceborne SMAP radar data becomes available, the proposed method will be applied to test its performance.

6.2   Future work

The current soil moisture retrieval technique is based on ancillary data to reduce the number of unknowns. Ideally, a high-resolution radar mission with multiple frequencies and incidence angles is envisioned to further analyze and improve the forward modeling performance and allow for more retrieval unknowns. While waiting for such a mission, there are steps that can greatly improve radar-only retrievals based on a single frequency and incidence angle. The first improvement has been partially shown in this dissertation and involves the use of radar data itself to classify land cover types

within the scene to produce higher resolution and up-to-date land cover maps. This can be extended by using not only radar data but other spaceborne or airborne data to derive up-to-date ancillary data. Finally, since the vegetation parameterization is at the core of the retrieval efforts, a technique to describe the vegetation with just a few parameters must be found. This could be achieved by leveraging allometric relations or by a different method entirely. Essentially, a few kernel parameter need to be found to successfully describe the vegetation for radar retrievals.

Currently, the soil moisture is retrieved in snapshot mode, both spatially and temporally; the soil moisture is retrieved for a single pixel at a specific time and the soil moisture retrievals of neighboring pixels are independent of each other. Setting up a retrieval procedure for a 'watershed pixel' could be the next step for even more realistic soil moisture retrievals. Watershed modeling based on ancillary data of soil texture information combined with precipitation information would allow a temporal and spatial analysis and prediction of the soil moisture. The resulting spatial and temporal correlation of soil moisture could then be used to constrain the radar-based retrieval, potentially reducing the number of unknowns from currently three at pixel level to a few at watershed level. This would also allow putting pixel level soil moisture trends into a watershed context.

APPENDICES

APPENDIX A

SMAPVEX12 Data

A.1 Introduction to SMAPVEX12

This appendix discusses the ground sampling methodology and collected vege-
tation and soil data over the forested sites during SMAPVEX12, and investigates
the available UAVSAR data. The SMAPVEX12 data set for the forested sites is
particularly interesting as it covers four very different forested sites, ranging from
homogeneous to denser, more complex forest. All sites were revisited a total of ten
times during the campaign, therefore allowing a time-series analysis. UAVSAR flew
four racetracks over the forested sites, and for each flight line, the forested sites were
included. Therefore, four different incidence angles are available for each forested site
per date. Finally, an extensive ground data set was collected during field work in-
cluding hand-held and in-situ soil moisture measurements for each flight date, precip-
itation data, forest vegetation information (both intensive and destructive sampling),
dielectric constant measurements for trunks, branches and leaves at each site, as well
as soil texture and soil roughness measurements.

A.2 Available SMAPVEX12 data for forested sites

The SMAPVEX12 campaign was conducted west of Winnipeg, Manitoba, during six weeks from 6 June to 17 July in 2012 to support SMAP pre-launch algorithm development and validation activities by providing the necessary ground truth data and measurements. Throughout the campaign, data were gathered and processed to support and assess models and algorithms used for SMAP data products, and in particular Level 2 and Level 3 retrieved surface soil moisture products. USC participated in this campaign and was responsible for sampling the forested sites. Mariko Burgin was put in charge of the design and implementation of the field work sampling strategy over the forested sites for the first three weeks, while the remaining three weeks were lead by Ruzbeh Akbar. As part of both the soil moisture and vegetation teams, ground truth data for both soil moisture and forest vegetation were collected over the six week period. These data are used to enhance and develop radar forest scattering models and to test the current radar-based soil moisture retrieval algorithms, both of which are essential to successful SMAP post-launch validation. The data collected will be used to enhance the parameterization and the radar scattering models of forest types represented within the sampled areas, and therefore to fine-tune and validate the related soil moisture retrievals over these types of forests. In this dissertation, the data is used in chapter 2.3.4 to validate the multispecies vegetation model with multilayered soil. A summary of the available data over the forested sites is given in Table A.1 and all data products are soon available for the public on the dedicated SMAPVEX12 website [142].

A.3 Field work data

The primary focus of the field work during SMAPVEX12 was (1) surface soil moisture sampling in forest regions and (2) forest vegetation sampling. The forest

Table A.1: Summary of the available SMAPVEX12 data products over the forested sites.

Data product name	Data product description
Precipitation	Precipitation and air/soil temperature at nearest weather stations measured during entire duration of campaign
UAVSAR radar data	UAVSAR radar data at four incidence angles for each observation date at approximately 0.2 arc second resolution
Forest vegetation	Intensive and destructive forest sampling measurements
Hand-held soil moisture	Calibrated hand-held soil moisture measurements on overflight days
In-situ soil moisture	Calibrated in-situ soil moisture and temperature measurements at three forested sites during entire duration of campaign
Soil texture	Soil texture (percentage sand/silt/clay and bulk density) measured at all forested sites once during campaign
Soil roughness	Soil roughness measurement at each forested site measured once during campaign

sites were chosen for optimal spatial coverage while allowing a team of four to re-visit all sites during the Passive/Active L-band Sensor (PALS) and UAVSAR flight hours. After a first site visit at the beginning of the campaign, one of the preselected sites F4 was determined to be not suitable as a forest site since larger areas consisted of marshland and deforestation was visible throughout the site. In some areas where localized/controlled tree burning had already taken place, the ground was ploughed and evidently made ready to plant crops. Four forests sites F1, F2, F3 and F5 were eventually identified for regular soil moisture and vegetation sampling. These sites can be seen in Fig. A.1.

A.3.1 Soil moisture sampling

A spatial and temporal soil moisture sampling strategy had to be implemented. Frequent revisits throughout the campaign addressed the need for better knowledge of
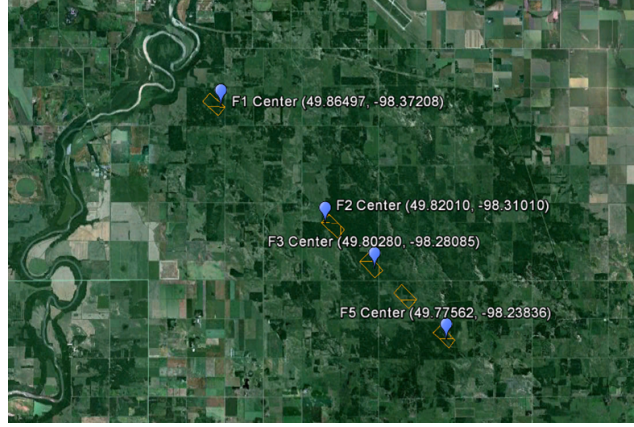
Figure A.1: Overview of five original forest sites of SMAPVEX12. Four forest sites (F1, F2, F3, F5) were selected for soil moisture and vegetation sampling. F4 was eliminated from the sampling plan since parts of it had been recently deforested.

the temporal variability of soil moisture, whereas four diverse sites allowed the spatial distribution of these dynamics. At the beginning of the campaign each site was visited and its heterogeneity investigated. The observation area for both soil moisture and vegetation sampling within each site consists of two orthogonal transects within a circle of 100 m radius. This observation area had to be carefully selected to represent the heterogeneity of the site. At four sites, F1, F2, F3 and F4, a temporary soil moisture sensor profile had previously been installed. At sites F1 and F2, this in-situ soil moisture measurement point has been included as one of the measurement points within the two transects to allow cross comparison between fixed installed soil moisture measurement and hand-held soil moisture measurement during flight days.

After determining the center point, transects were laid in north to south and east to west directions. There are nine soil moisture sampling points within each observation area: the center point and in each cardinal direction two points at 50 m and 100 m. A schematic representation of the transects can be seen in Fig. A.2. Some of the sampling points were slightly moved from their intended location if they fell into areas of standing water or marsh. For example, in F3 the southern transect had to be modified to avoid marshlands. To allow for frequent revisiting of the soil
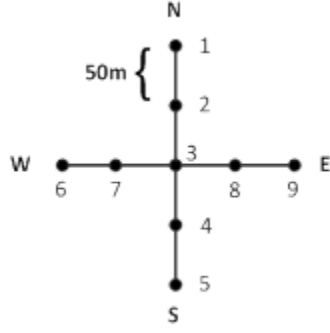
Figure A.2: Schematic representation of soil moisture transects.

moisture sampling points, the nine soil moisture sampling points per field were clearly marked at the beginning of the campaign and their respective GPS coordinates were recorded and confirmed with visualization in Google Earth. Such images can be seen in Fig. A.3.

The parameters of interest related to soil and soil moisture are:

- Soil moisture and its corresponding dielectric constant (using Steven's water probe)
- Soil organic depth
- Soil temperature at 0 cm, 5 cm and 10 cm depth
- Soil bulk density samples to characterize soil composition (i.e. percentage sand, clay, and silt)

The parameters of interest are shown in Fig. A.4. Figure A.5 shows an example soil moisture sampling location with inserted soil moisture probe.

As an example of the raw soil moisture data, Fig. A.6 shows the raw hand-held soil moisture readings at point 4 (for its location within the transect see Fig. A.2) of each transect over the entire SMAPVEX12 campaign duration. Each data point is an average of three measurements, which were taken with a Steven's water probe throughout the campaign. After conclusion of the field work campaign, the soil moisture values were first averaged for each point and then calibrated by utilizing the soil texture information that was taken at each sampling point. The calibrated soil
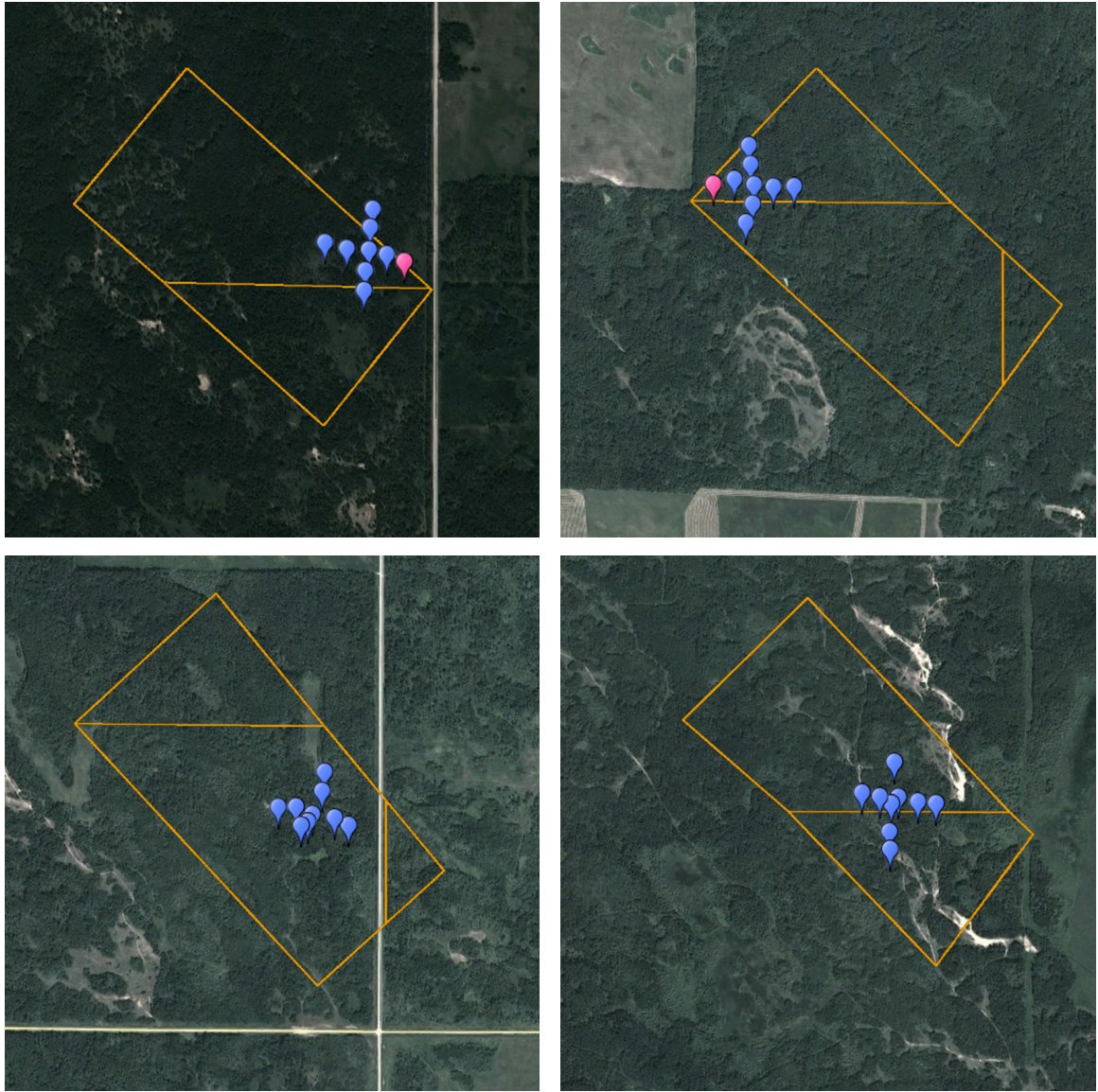
Figure A.3: Each forest site consists of 9 soil moisture sampling points oriented around a center point with two transects in approximately north/south and east/west directions. The temporary soil moisture profile location (if available) is shown with a pink marker. From top left to bottom right: F1, F2, F3 and F5.
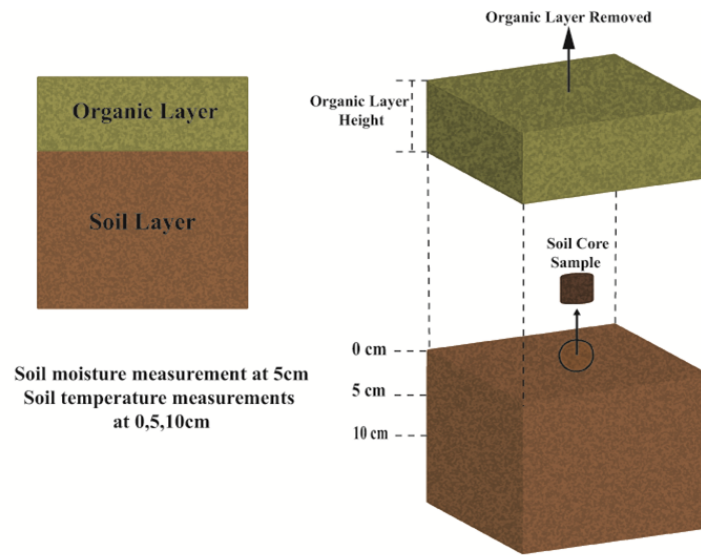
Figure A.4: Visualization of parameters of interest related to soil and soil moisture. Figure provided by Ruzbeh Akbar.

Figure A.5: Soil moisture sampling location (left) with inserted soil moisture probe (right).
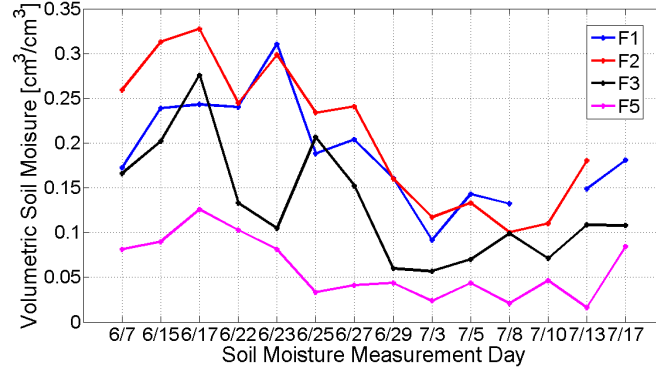
Figure A.6: Example of soil moisture dynamics. Volumetric soil moisture at point 4 for all sites over the SMAPVEX12 duration. Figure provided by Ruzbeh Akbar.

moisture data for all sites over the entire campaign can be seen in Fig. A.7. More rainfall occurred at the beginning of the campaign with drier conditions during the middle and some scattered rain events towards the end of the campaign. Figure A.6 and Fig. A.7 show this general pattern and are consistent with the observed weather conditions. Several points show non-physical soil moisture values, which can be mostly traced back to marshy conditions. The following points are therefore excluded: points 1, 5, 9 for site F2, points 2, 6, 9 for site F3, and points 2, 5, 6 and 7 for site F5. To compare the hand-held to in-situ soil moisture, all hand-held soil moisture values over the entire transect for the same date are averaged and compared to the single in-situ measurement at the respective time of the overflight. The comparison can be seen in Fig. A.8. The in-situ and hand-held soil moisture measurements generally show the same behavior, with a wet period at the beginning of the campaign, a dry down and then some rain events, but the in-situ soil moisture seems to have a lag with respect to the hand-held soil moisture measurement, which cannot be physically explained.

Figure A.9 shows the raw soil moisture readings versus the real and imaginary part of the dielectric constant of soil. The readings are from the Steven's water probe, which is capable of measuring both soil moisture and soil dielectric constant. The soil texture is set to Loam for all sites. All soil and dielectric data across all sites

(a)

(b)

(c)

(d)
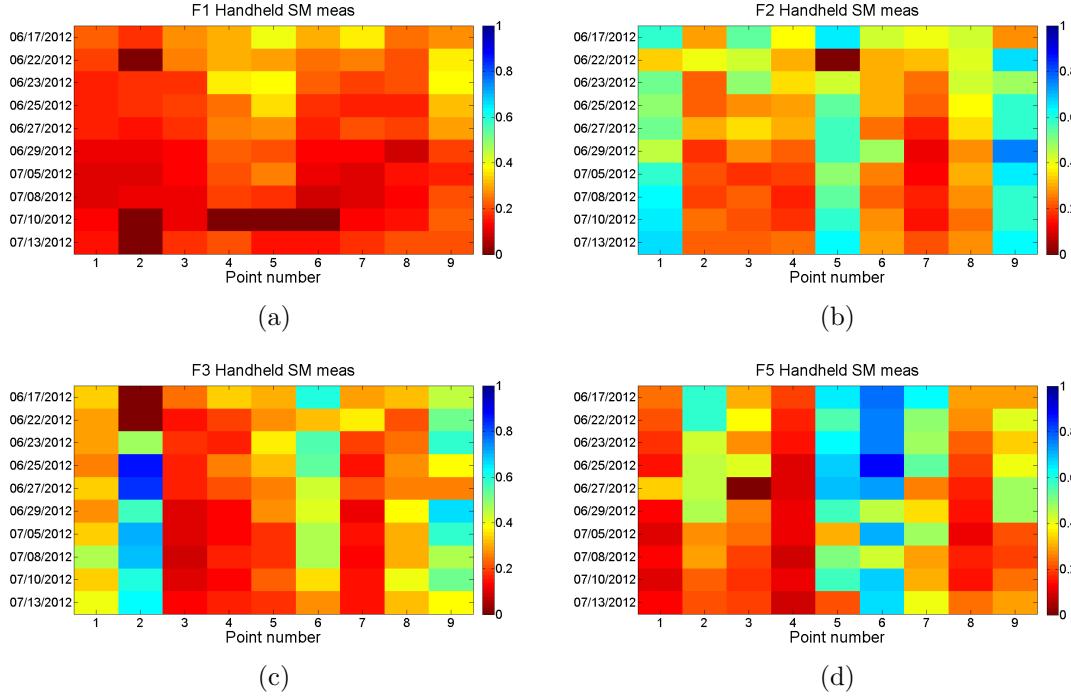
Figure A.7: Soil moisture over entire campaign (10 dates) with 9 sampling points each. From top left to bottom right: F1, F2, F3 and F5.
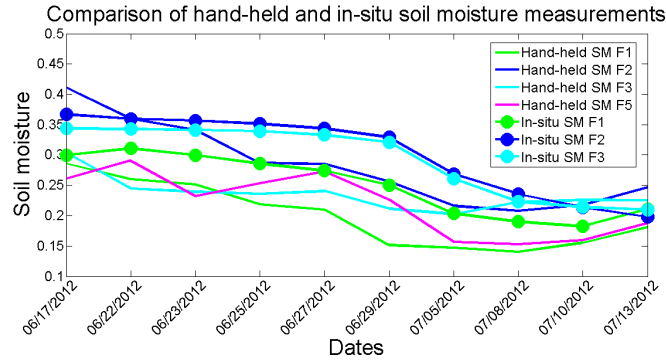
Figure A.8: Comparison of calibrated hand-held and in-situ soil moisture measurements. The calibrated hand-held soil moisture measurements have been averaged over the entire transect for each date and are compared to a single in-situ soil moisture measurement taken at the time of the hand-held soil moisture measurement and overflight.
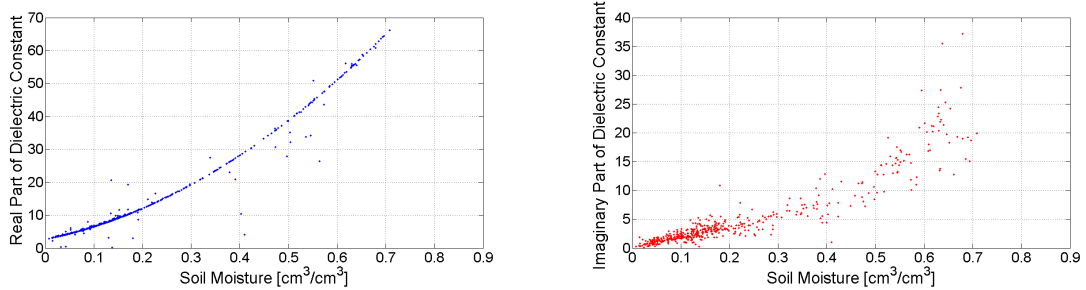
Figure A.9: Soil moisture vs. real and imaginary part of dielectric constant over all fields through the SMAPVEX12 campaign (5-17 July only). Data are from Steven's water probe readings. Figures provided by Ruzbeh Akbar.

are shown. A tight quadratic fit between soil moisture and real part of the dielectric constant can be observed. However, the plot has not been corrected for different soil textures. It is suspected that by taking the different soil textures into account, the relationship will change. With a carefully calibrated probe, this information can also be used as an additional check on soil moisture dielectric models and help with their validation and development.

A.3.2 Vegetation sampling

SMAPVEX12 forest vegetation sampling was divided into three parts: (1) spatial sampling, (2) destructive sampling and (3) dielectric constant measurements. Spatial sampling involved recording and flagging every tree with a DBH of more than 1 inch (2.54 cm) within ± 1 meter of the transect line. This was done for both transects within an observation area as shown in Fig. A.2. For each tree, the following parameters were measured:

- DBH in inches
- Height in meters
- Species

The DBH was measured with a DBH tape at breast height. The height was recorded with a hypsometer. While standing more than 10 meters away from the tree, two

187

measurements were taken with the hypsometer: distance to base of tree and distance to top of tree. The hypsometer then displayed the total height. This is a standard technique to measure tree heights, but posed a challenge in denser forests such as F2, F3 and F5 since there was a dense understory preventing line of sight measurements. The tree species was recorded by consulting a standard tree field guide [143]. The major tree species present at the sampled sites were trembling aspen, oak, and willow.

The spatial sampling measurements allowed better understanding of the denser forest sites covered in this campaign. Measurements such as forest density, tree height, DBH, tree species, as well as detailed information about branches and understory, are essential to successfully parameterize radar backscattering models. At every 10 m within the transect, the GPS coordinates and more detailed parameters in addition to the aforementioned parameters were recorded:

- Trunk height in meters
- Number of primary branches
- Angle of primary branches
- Fractional ground cover in percent
- Understory height in meters

These measurements were generally taken at the 10 m point of the tree closest to the transect line. Trunk height was recorded with the hypsometer or a yard stick. The number and angle of primary branches were recorded based on visual inspection. The fractional ground cover and understory height were measured by laying down a quadrat in a representative area close to the 10 m point and recording the values based on visual inspection or by using a yard stick for the height. Furthermore, each transect was once more independently inspected and a detailed assessment of the environment recorded. This included ground cover as well as surrounding areas of clearings or standing water. This information facilitates placing the soil moisture and tree measurements in context with the surroundings. The relationship between DBH
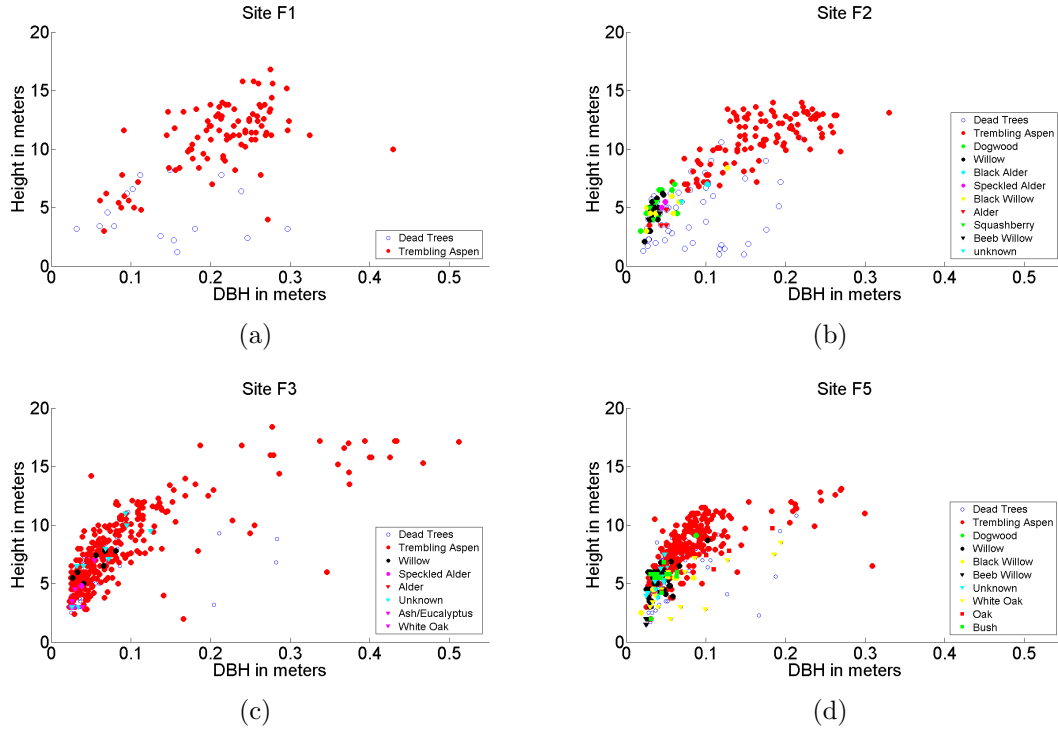
Figure A.10: Allometric relations showing Height versus DBH for all four plots.

and total tree height is interesting since it represents an allometric relation, allowing reduction of the vegetation parameters to fewer kernels and ideally enabling the representation of the forest based on one vegetation kernel only. Figure A.10 shows the allometric relations for all four sites, separated by species.

Destructive sampling involves harvesting an *average* tree for intensive destructive measurements. One average tree per field was felled and the following parameters were measured:

- Trunk diameter at each 30 cm interval
- Wafer of approximately 3 cm thickness for gravimetric measurements at each 30 cm interval
- Primary branch angles
- Number of branches (primary, secondary) and leaf count
- All branch lengths, diameters, and when possible, dielectric constant
- 3-4 samples of branches for gravimetric measurements

Figure A.11: Felled tree (left) with measurements being taken: trunk length (middle) and DBH (right).

- Note on leaf clumping

A visualization of a felled tree and the involved measurements is shown in Fig. A.11. At the time of destructive sampling, the spatial information was not processed. The average tree was selected based on visual inspection of DBH and height compared to other trees in the forest. Along with the spatial sampling information, these parameters are essential in the electromagnetic modeling of forests. Trunks and branches are modeled as cylinders with the same properties (diameters, length, dielectric, branch angle, etc.) as the average tree in the site. The measurements above provide the distributions needed to do such modeling. However, before such measurements could be done, the tree had to be felled and cut down.

Dielectric measurement of tree trunks, branches and leaves were taken using an Agilent field portable network analyzer (FieldFox N9923A). The FieldFox uses a custom made semi-rigid open-ended coaxial line to measure the reflection coefficient of the sample under test. Further analysis is then required to determine the sample's dielectric constant from the measured reflection coefficients. This sensor system was developed by Ruzbeh Akbar at USC specifically for SMAPVEX12, and due to its success, will continue to be used for future field campaigns. A laptop is used to control and automate the measurement process. The measured dielectric constant values can be directly used as input parameters in the electromagnetic forward scattering models. A typical measurement can be seen in Fig. A.12. The real and imaginary parts of the dielectric constant of the trunk of a large trembling aspen tree at different
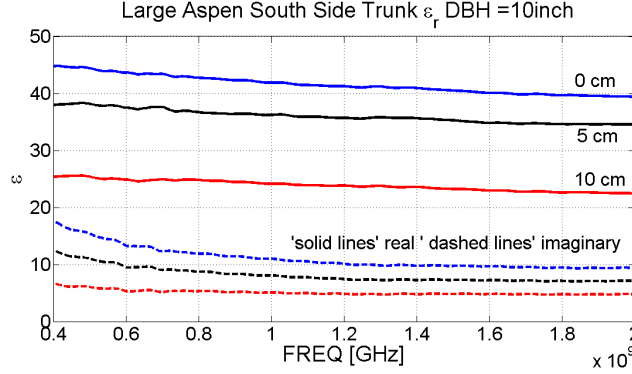
Figure A.12: Aspen trunk dielectric constant from 400 MHz to 2 GHz. Solid lines are real part and dashed lines imaginary part of dielectric constant. Figure provided by Ruzbeh Akbar.

Figure A.13: Example setup with FieldFox and laptop (on left) and drilled hole to be probed (on right).

depths can be seen. To probe deeper into the tree, a $\frac{3}{4}$" drill bit was used to drill into the tree. The coaxial probe was then placed in full contact with the trunk. The measurement frequency ranges from 400 MHz to 2 GHz, which covers both P-band and L-band and is applicable to both the SMAP and AirMOSS missions. All dielectric constant measurements will be available to the SMAP team once all post-processing and data quality checks have been performed. An example setup with FieldFox and laptop can be seen in Fig. A.13 on the left, and the drilled hole to be probed on the right.

The above discussions and presented results summarize the major activities during SMAPVEX12 by the USC forest sampling team. Many valuable experiences were

gained throughout this campaign. Most importantly, after CanEx-SM2010, where forest sampling was implemented on a smaller scale, in this campaign a well-focused and grander forest sampling technique was implemented and successfully accomplished. The sampling strategy, as mentioned, was designed to allow for both repeated visits and spatial coverage of different areas. However, the intensity of the work and the relative small team size proved to be challenging at times. The small overall team size for forest sampling, as compared to that for crop sampling, resulted in sampling of one single plot, as opposed to three plots as originally planned, at each site. Still, this effort resulted in a large volume of valuable and unique data. The large amount of ground truth collected, consisting of many different parameters applicable to many forward models, will be used to examine the existing forest forward and inverse models and help with their validations. Further improvements and changes can be drawn for future forest sampling techniques and strategies.

A.3.3 Surface roughness measurement

During the field work campaign, each forested site was visited once to conduct soil roughness measurements with a pin-board. The soil roughness measurements were led by Najib Djamai of University of Sherbrooke with assistance from the forest team. Figure A.14 shows Najib at three sites doing soil roughness measurements illustrating the different conditions. The roughness measurement overlaps with the general measurement transect. The soil roughness measurements were postprocessed by University of Sherbrooke and are also available on the dedicated SMAPVEX12 website [142].

A.4 Available radar data

The UAVSAR L-band radar data consists of slant-range and orthorectified products, incidence angle and pixel slope based on the Shuttle Radar Topography Mis-

Figure A.14: Surface roughness measurements in three sites: F5 (left), F1 (middle) and F2 (right).
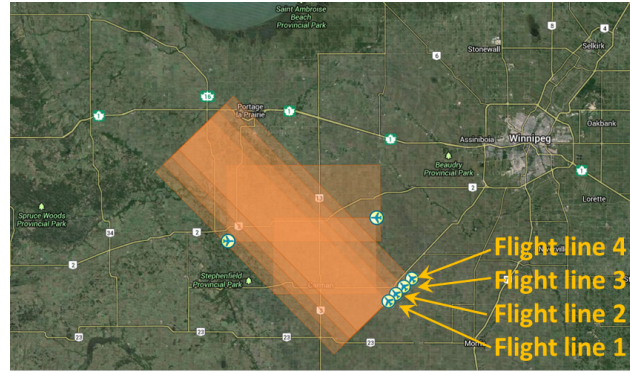
Figure A.15: Visualization of four UAVSAR flight lines available over SMAPVEX12.

sion (SRTM) Digital Elevation Model (DEM), and meta data files. The pixels are posted at an 0.2 arc second resolution, while the incidence angles range from 30 to 50 degrees. The incidence angles for the forested sites specifically are 30°, 40°, 48° and 54° for each flight date. The available UAVSAR flight lines for the forested sites are given in Table A.2. All UAVSAR data products are available on the JPL UAVSAR website [144]. In chapter 2.3.4, version 2 of the orthorectified products is used. A visualization of the four flight lines is shown in Fig. A.15. PALS data is also available over the forested sites, but has not been used for the model validation in chapter 2.3.4 of this dissertation.

Table A.2: Summary of available UAVSAR flight lines (1: westernmost, 4: eastern-most) and in-situ soil moisture data over forested sites.

Date	Available UAVSAR flight lines	Hand-held soil moisture available
06/17/2012	1 / 2 / 3 / -	✓
06/22/2012	- / 2 / 3 / 4	✓
06/23/2012	1 / 2 / 3 / 4	✓
06/25/2012	1 / 2 / - / 4	✓
06/27/2012	1 / 2 / 3 / 4	✓
06/29/2012	1 / 2 / 3 / 4	✓
07/05/2012	1 / 2 / 3 / 4	✓
07/08/2012	1 / 2 / 3 / 4	✓
07/10/2012	1 / 2 / 3 / 4	✓
07/13/2012	1 / 2 / 3 / 4	✓

A.5 Conclusion of SMAPVEX12

Many lessons were learned during SMAPVEX12. The field work technique can be further refined, for example a larger dedicated forest team would allow a repeated coverage of a larger forested area. For the destructive sampling, it is crucial to finish spatial sampling before the destructive sampling such that an average representative tree can be determined based on spatial sampling data. This would avoid a bias to larger trees. Furthermore, dielectric constant measurements should be taken on overflight days to be more representative, if the available personnel permits. Future work with the SMAPVEX12 data set includes revisiting the soil moisture calibration of the hand-held measurements to clarify the apparent bias between hand-held and in-situ profiles. The lessons learned can be utilized to improve or generate new data cubes for radar based soil moisture retrieval for SMAP. Finally, the author would like to acknowledge all SMAPVEX12 participants that braved the forest each day (rain or shine) enduring rough conditions and a plethora of ticks.

APPENDIX B

Data Processing System for Root Zone Soil Moisture Retrieval from Large-Scale P-band radar in support of Airborne Microwave Observatory of Subcanopy and Subsurface (AirMOSS)

B.1   Introduction to AirMOSS

Knowledge of the terrestrial biosphere is crucial as ecosystems are major components of the global carbon cycle, exchanging large amounts of carbon dioxide and other gases with the atmosphere. NEE quantifies these carbon fluxes, but current continental-scale estimates contain high levels of uncertainty [145]. RZSM and its spatial and temporal heterogeneity influence NEE [145–147]. The goal of the AirMOSS mission is to provide a new NEE estimate with reduced uncertainty for North America, constrained by high-resolution RZSM measurements. The AirMOSS mission, one of the five NASA EV-1 investigations selected in May 2010 [148], will accomplish this by (1) providing high-resolution radar backscatter observations used to calculate estimates of RZSM over regions representative of the major North American biomes,

(2) estimating the impact of RZSM on regional carbon fluxes, and (3) integrating the measurement-constrained estimates of regional carbon fluxes to the continental scale of North America.

The AirMOSS data products and expected science results are tailored to meet the need to reduce uncertainty in estimates of NEE through the development of methodologies to integrate remote sensing observations, in-ground soil sensors, and flux tower data into regional/continental flux models. Additionally, AirMOSS data provide a direct means for evaluating RZSM algorithms of the SMAP Decadal Survey mission and assessing the impact of fine-scale heterogeneities in its coarse-resolution products [8, 149].

AirMOSS surveys are being conducted over regions of approximately 100 km length and 25 km width centered over FLUXNET tower sites within nine biomes representative of North America, which are expected to be most influential in determining the North American NEE [150]. Table B.1 summarizes the biome types and locations within each biome type chosen for data acquisition. The surveys provide radar backscatter measurements reported at approximately 100 m spatial resolution scales and at select sub-weekly, seasonal, and annual time scales.

The AirMOSS radar and associated RZSM datasets are expected to be a major breakthrough over current point-scale RZSM measurements and will provide a critical input to carbon flux models. AirMOSS science data products include RZSM at approximately 100 m resolution (Level-2/3 RZSM), estimates of RZSM through hydrologic data assimilation and the use of land surface models (Level-4 RZSM), estimates of NEE at approximately 1 km resolution through ecosystem modeling (Level-4A NEE), and integrated North American NEE estimates at approximately 50 km resolution (Level-4B NEE). The project will conclude with a new estimate of North American NEE and a quantitative assessment of its uncertainty.

Table B.1: Summary of the AirMOSS baseline mission science study sites. The sites are selected to represent nine major biomes in North America.

Biome Number	Biome type International Geosphere-Biosphere Programme (IGBP) vegetation class	Example site name and location
1	Boreal forest/evergreen needleleaf, mixed forest, cropland mixed forest, cropland	BERMS, Saskatchewan, Canada
2	Boreal transitional/mixed forest	Howland, Maine and Harvard, Massachusetts forests
3	Temperate forest/mixed forest, cropland	Duke forest, North Carolina
4	Temperate forest/evergreen needleleaf	Metolius, Oregon
5	Temperate grasslands/crops	Marena Oklahoma In Situ Sensor Testbed (MOISST), Marena, Oklahoma
6	Mediterranean forest/woody savanna	Tonzi Ranch, California
7	Desert and shrub/open shrubland and grassland	Walnut Gulch, Arizona
8	Subtropical dry forest/broadleaf deciduous, crops, woody savanna	Chamela, Mexico
9	Tropical moist forest/evergreen broadleaf, crops	La Selva, Costa Rica

B.1.1 Instrument Characteristics

The AirMOSS P-band instrument is described in detail by Chapin *et al.* [151]. A brief summary is given here. The AirMOSS radar reuses some of the NASA/ JPL L-band UAVSAR elements, leveraging the heritage of the success of previous airborne SAR systems [152]. Like the UAVSAR system, the AirMOSS radar system fits into a pod that mounts under a NASA Gulfstream III (G-III). The NASA G-III aircraft used for AirMOSS, operated by the Johnson Space Center (JSC), is equipped with a precision autopilot that facilitates repeat-pass interferometry, although repeat-pass interferometry is not planned as part of the baseline AirMOSS project. The pod and radome are a copy of those used for UAVSAR. Both UAVSAR and AirMOSS have the same mechanical and electrical interfaces between the pod and the aircraft. The AirMOSS data are processed into synoptic imagery using synthetic aperture processing techniques. The goal for absolute calibration of AirMOSS data is 0.5 dB.

B.1.2 Measurement Approach

AirMOSS will produce estimates of RZSM with data from the P-band SAR to capture the effects of gradients of soil, topography, and vegetation heterogeneity over an area of 100 km x 25 km at each of the 9 biomes listed in Table B.1. AirMOSS will acquire these high-resolution radar data during 21 campaigns over the growing seasons in 2012-2015 with an estimated 9 science flight hours during each campaign. This encompasses three 7-14 day campaigns in each 12 month period for each of the biomes 1-5 in Table B.1, one campaign during each of the dry and wet seasons for biomes 6 and 7 in Table B.1, and one campaign for biomes 8 and 9 in Table B.1. Each 7-14 day campaign may consist of up to 3 flight days. To calibrate and verify the required science products, in-situ soil moisture profiles are installed before the first science deployment, and data will be collected through the end of the investigation in 2015. These sensors measure surface soil temperature, soil moisture content at

several different depths, and the precipitation amount at each site.

For each flight, RZSM is retrieved from radar backscatter measurements with a soil penetration depth of at least 25 centimeters in non-saturated conditions of less than 0.35 m^3/m^3 volumetric soil water content, and under less than 15 kg/m^2 of vegetation biomass. The accuracy requirement for RZSM retrieval is 0.05 m^3/m^3 root-mean squared, when averaged over all campaigns, all years and all sites. To achieve the ultimate science objective of the AirMOSS mission, namely, to deliver a new estimate of the north American NEE, these retrievals will be used in higher-level (L4) processing of RZSM and NEE via hydrologic and ecosystem modeling.

In this appendix, the data handling processor for the delivery of the RZSM at approximately 100 m resolution (Level-2/3 RZSM) is described. The strategy reported here applies to those biomes in Table B.1 that have a predominance of monospecies vegetation at most of their image pixels (even if the pixels contain different types of monospecies vegetation). The appendix includes a discussion of the properties of the radar backscattering coefficient images, the ancillary data layers, the georeferencing, stacking, and error handling of the various data layers, and our approach for processing such large and diverse volumes of data.

B.2 The L2/L3 product overview

The L2/3 RZSM products are the only set of products directly derived from the AirMOSS radar measurements (L1-S0). The higher-level products (Level 4) of the AirMOSS investigation rely on the L2/3 RZSM products and various models to generate their outputs. The L1-S0 imagery is provided at postings of 0.5 arcsecond (roughly 15 m) and 3 arcsecond (roughly 90-100 m). The AirMOSS study sites cover a wide variety of vegetation covers, such that the retrieval algorithms may vary for different sites. In general, the sites are categorized into monospecies forested sites (including bare surfaces and grasslands) and mixed species forested sites. As

such, sites 1, 4, 5, 6 and 7 in Table B.1 fall generally under the monospecies cate-
gory, and sites 2, 3, 8 and 9 fall generally under the multispecies category. The team
at USC responsible for the monospecies category, while the team at JPL is responsible
for the multispecies category. For the monospecies sites, species-specific allometric
relations can be used to render the vegetation structure from a single kernel (i.e.
from DBH) [153, 154]. The well-defined vegetation structure allows the use of the
widely accepted discrete scatterer radar vegetation models [19, 37]. Along with scat-
tering models of layered soil [45, 46], it is possible to calculate the radar measurement
corresponding to a given kernel and arbitrary soil moisture profile. The multichannel
radar data set can then be used to estimate the RZSM in an iterative scheme based
on the full scattering model. The RZSM retrievals are performed such that for each
pixel in the radar image, a smooth profile represented by a second-order polynomial
is retrieved, as detailed in chapter 2.3.6. Extensive field campaigns are ongoing to
collect ground truth data for vegetation structure throughout the AirMOSS radar
swaths. These data are being used to parameterize the scattering models and hence
making it possible to solve the retrieval problem for profiles of RZSM only. For sites
that have a predominance of mixed species vegetation, the retrievals are performed
in a slightly different fashion by the team at JPL.

B.3 Data use and data handling

In this section, first an overview of the utilized ancillary and observed data layers
used in AirMOSS is given. The data handling is then discussed by dividing the pre-
flight and post-flight tasks. An overview of the data flow and work flow is shown in
Fig. B.1. The data volume in general could be large, demanding special handling to
reduce the data in the computer memory at all times while still maintaining reasonable
execution time. Example data volume for each major data layer is given in Table B.2.
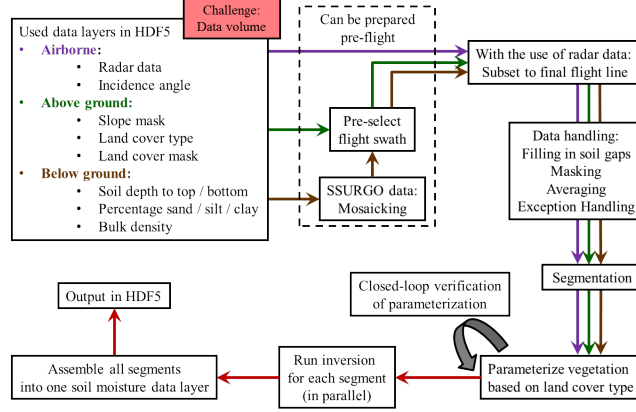
Figure B.1: Overview of data flow and work steps for AirMOSS processing algorithm.

Table B.2: Data volume for each major data layer.

Data Layer	Data Volume
Radar data (per site and date)	~15 GB
Land cover classification (per site)	~10 MB
Land cover classification mask (per site)	~50 MB
Soil texture (per site)	~40 GB

B.4 Ancillary and observed data layers

B.4.1 Observed radar data layer: L1-S0 product overview

AirMOSS delivers polarimetric P-band radar backscattering coefficients at resolutions of 0.5 and 3 arc seconds over the nine selected biomes shown in Table B.1. On overflight days, each study site is covered by flying an area approximately 25 km wide and 100 km long. This is achieved with 4 to 6 individual, parallel flight lines with regions of overlap between the adjacent lines; four to five flight lines were used for a flight altitude of 41 kft and six flight lines for an altitude of 22 kft[1]. The timing of the flights is designed to best capture the inter-seasonal and inter-annual variations of RZSM. Each flight line is delivered separately in Ground-projected gridded data (GRD) file format and Hierarchical Data Format (HDF5). Each flight line

---

[1]The reason for two different flight altitudes was a problem with the pressurized pod during the first few flight months in 2012; in later flights only high altitude flights are performed.
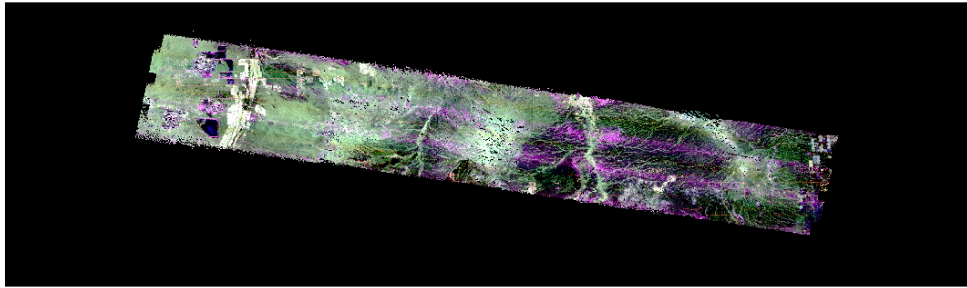
Figure B.2: RGB image of radar backscatter (R: HH, G: HV, B: VV) taken on 20 September 2012 over Walnut Gulch in Arizona with 3 arcsecond resolution, mosaicked from 6 flight lines.

covers a range of local incidence angles from approximately 25 to 65 degrees. An example for an RGB radar image of delivered radar swaths is shown in Fig. B.2. Six radar data swaths were recorded on 20 September 2012 over Walnut Gulch in Arizona and have been mosaicked to produce the shown RGB image. The L1-S0 radar data are currently being generated by the operational AirMOSS processor at JPL, and delivered to the Alaska Satellite Facility (ASF) for public access.

B.4.2 Ancillary data layers

The radar scattering model used for the L2/3 RZSM retrieval algorithm for monospecies vegetation requires the following ancillary data layers, examples of which are shown in Fig. B.3:

- Data layers delivered with the L1-S0 radar data: these include the same-resolution files (0.5 and 3 arc seconds) for incidence angle and slope. These files are described in detail in an annotation file. Additionally, KML, KMZ and PNG files are provided for each swath at each resolution to facilitate visualization.

- Land cover map from NLCD at 1 arc second resolution [94]. Currently the latest land cover classification is from 2006. For sites outside the United States,

the GlobCover data product provided by ESA at 1 arc second resolution is used as the land cover classification [95].

- SRTM at 1 arc second in the United States and SRTM 3 arc seconds outside the United States [155]. The DEM from United States Geological Survey (USGS) National Elevation Database (NED) would be available as well, but since the SRTM data are used for the generation of the L1-S0 product, the same data set is used for setting up the retrieval work flow.

- Soil texture data from SSURGO within the United States at 1 arc second resolution [96] gap-filled with STATSGO2 data, and the HWSD produced by the IIASA outside the United States at 1 arc second resolution [97].

The NLCD and SSURGO data are not available outside of the United States. Consequently, they will not be available at the BERMS, Chamela, and La Selva sites. The best available ancillary data for a given site will be used. The above list does not include any information specific to the site itself. Scientists operating flux tower sites, Long Term Ecological Research (LTER) sites, or field stations in the imaged area may have additional information which can be incorporated into the retrieval process. This data would be site specific, and while not required for the RZSM retrieval, will be used when available to enhance the retrieval quality by improving the forward modeling. The above list also does not include the data collected in the field by the project concurrent with the campaign. The following information is being collected during the field campaign activities to enhance the model parameterizations and therefore retrieval quality: vegetation geometric parameters such as height, DBH, branch lengths, branch densities, branch diameters, leaf properties, stem and branch dielectric constants. Note no meteorological data are used in the RZSM retrievals such as data from rain gauges. The RZSM retrievals will not be constrained using meteorological data (i.e. RZSM must be higher for a scene after rain than before it). However, previous day's acquisition of RZSM retrievals may be used as an initial
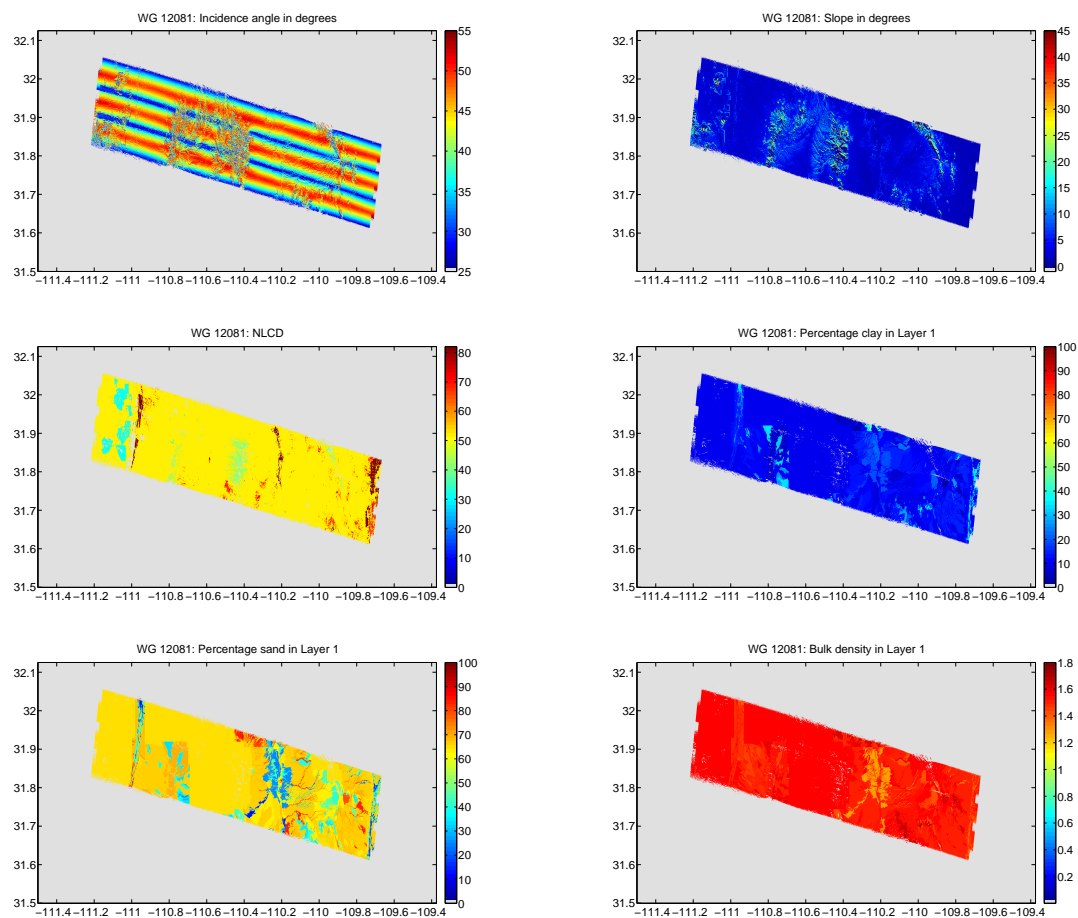
Figure B.3: Example of ancillary data layers over Walnut Gulch, Arizona: incidence angle (top left) and slope (top right) both in degrees, NLCD (middle left) and SSURGO soil texture percentage clay of layer 1 (middle right), SSURGO soil texture percentage sand (bottom left) and bulk density in $\frac{g}{cm^3}$ (bottom right) of layer 1. The incidence angle and slope are from the overflight of 20 September 2012.

guess for the RZSM to reduce the number of iterations required for a subsequent day.

B.5 Pre-flight data handling

The pre-flight data handling mainly consists of ingesting, pixel-to-pixel cross-checking, mosaicking, and performing general quality control for the SSURGO soils information, as well as laying out the grid on which all data layers are oriented and preparing the other ancillary data layers for this grid. Each pixel is characterized by the coordinates of its upper left corner; this notation is consistent for all layers. The final radar image covers an area of about 100 km x 25 km, but ancillary data are provided for a larger area (1-degree box) to allow shifts in the radar swaths due to movement during data takes.

The land cover data are delivered on a 1 arc second (∼30 m) grid, which is chosen to be the base grid for all other data layers. Based on the land cover data, a land cover mask is generated at 3 arc seconds (∼90 m), by first excluding 1 arc second pixels of specific classes, and then by averaging up to 3 x 3 arc seconds and masking the pixel out if more than half of the 1 arc second pixels are excluded. The included and excluded land cover classes for NLCD and GlobCover are shown in Table B.3 and B.4.

SSURGO data are delivered in HDF5 file format in the form of tiles. The SSURGO data contains the following parameter for each pixel: total number of soil layers, depth to top and soil texture (percentage clay, sand, silt and bulk density) for each layer. The SSURGO data has been pre-processed at Oregon State University [156] by starting from the respective shape files that fall into the 1-degree box and rasterizing the data onto a 1 arc second grid. There are substantial gaps in the SSURGO data due to non-existing data for pixels with bedrock, water features, river washes, rough broken land, rocky outcrop, or lava fields which have no soil characteristics. The soil product is therefore gap-filled with STATSGO2 data [157] to significantly reduce uncertainty

Table B.3: Land cover classes for NLCD. The classes indicated with (*) appear in Alaska only and can therefore be inherently neglected for the nine AirMOSS biomes.

NLCD value	NLCD	Included:
11	Open Water	✗
12	Perennial Ice/Snow	✗
21	Developed, Open Space	✗
22	Developed, Low Intensity	✗
23	Developed, Medium Intensity	✗
24	Developed, High Intensity	✗
31	Barren Land (Rock / Sand / Clay)	✓
41	Deciduous Forest	✓
42	Evergreen Forest	✓
43	Mixed Forest	✓
51	Dwarf Scrub	✗*
52	Shrub / Scrub	✓
71	Grassland / Herbaceous	✓
72	Sedge / Herbaceous	✗*
73	Lichens	✗*
74	Moss	✗*
81	Pasture / Hay	✓
82	Cultivated Crops	✓
90	Woody Wetlands	✗
95	Emergent Herbaceous Wetlands	✗

Table B.4: Land cover classes for GlobCover.

GlobCover value	GlobCover	Included:
11	Post-flooding or irrigated croplands	✓
14	Rainfed croplands	✓
20	Mosaic Cropland (50-70%) / Vegetation (grassland, shrubland, forest) (20-50%)	✓
30	Mosaic Vegetation (grassland, shrubland, forest) (50-70%) / Cropland (20-50%)	✓
40	Closed to open (>15%) broadleaved evergreen and/or semi-deciduous forest (>5m)	✓
50	Closed (>40%) broadleaved deciduous forest (>5m)	✓
60	Open (15-40%) broadleaved deciduous forest (>5m)	✓
70	Closed (>40%) needleleaved evergreen forest (>5m)	✓
90	Open (15-40%) needleleaved deciduous or evergreen forest (>5m)	✓
100	Closed to open (>15%) mixed broadleaved and needleleaved forest (>5m)	✓
110	Mosaic Forest/Shrubland (50-70%) / Grassland (20-50%)	✓
120	Mosaic Grassland (50-70%) / Forest/Shrubland (20-50%)	✓
130	Closed to open (>15%) shrubland (<5m)	✓
140	Closed to open (>15%) grassland	✓
150	Sparse (>15%) vegetation (woody vegetation, shrubs, grassland)	✓
160	Closed (>40%) broadleaved forest regularly flooded - Fresh water	✗
170	Closed (>40%) broadleaved semi-deciduous and/or evergreen forest regularly flooded - Saline water	✗
180	Closed to open (>15%) vegetation (grassland, shrubland, woody vegetation) on regularly flooded or waterlogged soil - Fresh, brackish or saline water	✗
190	Artificial surfaces and associated areas (urban areas >50%)	✗
200	Bare areas	✗
210	Water bodies	✗
220	Permanent snow and ice	✗

in soil texture. The pixels are recorded with their lower left coordinate notation. We ingest the different SSURGO tiles, mosaick them together while adjusting the lower left to upper right coordinate notation and re-gridding them on the land cover base 1 arc second grid. During this step the total number of subsurface layers is standardized to be the same over the whole 1-degree box. This is done by investigating the different tiles and finding a representative number of subsurface layers for the entire 1-degree box. In the next step, the data are quality controlled by checking for non-physical parameters and gap-filling with a standardized soil texture profile. The standardized soil texture profile is found by analyzing the layer properties over the whole 1-degree box. The resulting SSURGO data are then once again checked to verify that all previous steps have been successfully executed. This concludes the pre-flight preparations, which results in the land cover data at 1 arc second, the land cover mask at 3 arc seconds and the quality controlled and gap-filled SSURGO data at 1 arc seconds as can be seen in Fig. B.4.

B.5.1 Post-flight data handling

The second part of the processing starts after delivery of the calibrated L1-S0 radar data by JPL. Figure B.4 can be used to visualize the post-flight data handling. The radar data handling consists of processing the radar data and their ancillary data layers of incidence angle and slope. Based on the land cover mask, a template for the radar data and their ancillary information at 3 arc second resolution is generated. The radar backscatter coefficients for HH, VV and HV as well as the local incidence angle and slope are ingested into the base grid. The various radar data swaths for each site have to be mosaicked; as a baseline only one radar data pixel is selected for each overlap region. Therefore, flight swaths are preselected based on their local incidence angle, which range from 25 degrees to 55 degrees. For the resulting overlap area, the pixel selection is made according to prominent land cover type for each
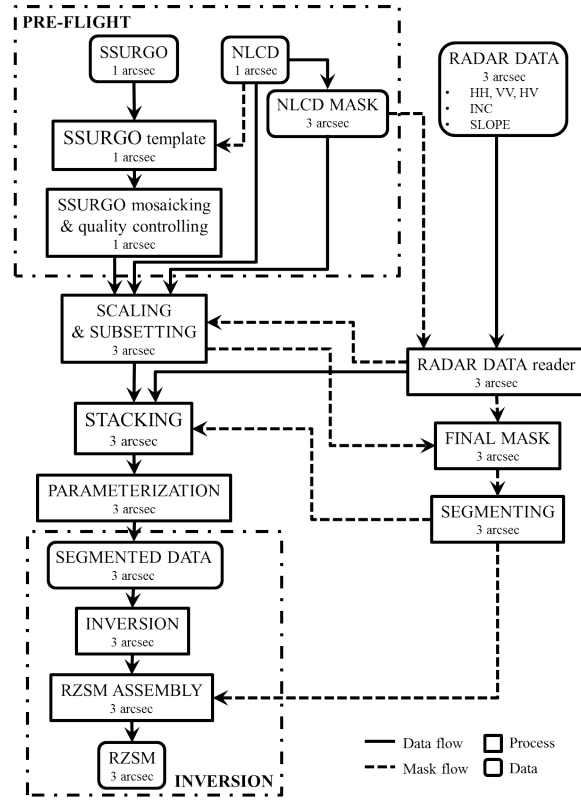
Figure B.4: Detailed flow of data and masks.
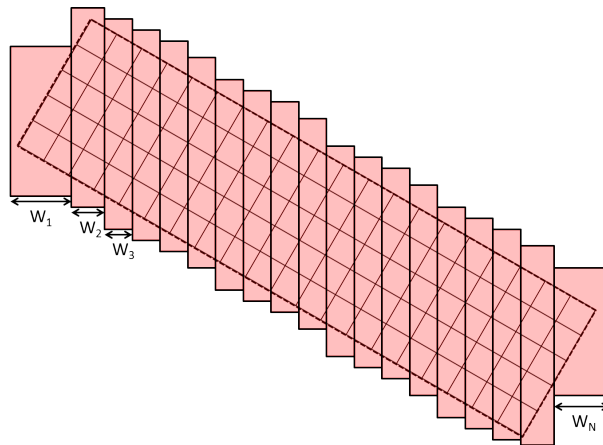
Figure B.5: Segmentation scheme for N segments.

site: the radar data with the smaller incidence angle are chosen for Walnut Gulch and MOISST where mostly grassland or bare soil is expected. For Metolius, BERMS, and Tonzi Ranch, the pixel with the larger incidence angle is chosen. An example of a mosaicked RGB image for an overflight over Walnut Gulch is shown in Fig. B.2. At a later stage both incidence angles for the overlap region will be used to further improve the soil moisture retrieval. Based on the DEM, the slope for each pixel is calculated at 3 arc second resolution by first finding the slope for each 1 arc second pixel and then averaging up to 3 arc seconds.

In the processing step of scaling and subsetting (see Fig. B.4), the land cover is scaled up to 3 arc seconds by applying a mode filter to the 1 arc second data. At the same time, the SSURGO data are scaled up to 3 arc seconds by applying a mean filter. The presence of radar data within the 1-degree box itself is used as a first mask to reduce the data volume significantly for land cover, land cover mask and SSURGO data by discarding data over pixels that do not contain any radar data. The 3 arc second land cover mask is then used in combination with the slope mask to create the final mask at 3 arc seconds, which identifies pixels enabled for inversion. Pixels are enabled for inversion if the slope of the 3 arc second pixel is smaller than 10 degrees and if the 3 arc second pixel is not masked out in the land cover mask.

To speed up inversion given by the large number of total pixels, the total number of pixels has to be divided into segments for processing. The segmenting algorithm uses the final mask and divides the total number of pixels enabled for inversion into N segments of approximately equal number of pixels. Pixels enabled for inversion are not necessarily in a block structure; the algorithm accounts for only the desired pixels in a west to east pattern. In an initial step the total number of enabled pixels is calculated to find an estimate of number of pixels per segment, the algorithm then steps line by line from the westernmost to the easternmost pixel. After each line the total number of the enabled pixels for the current segment is calculated. If the

210

pixel number is close enough to the ideal number of pixels per segment, the next segment is started. This is repeated until all pixels are associated with a segment. The segmentation algorithm provides a segmentation mask symbolically shown in Fig. B.5.

All data are brought to a 3 arc second posting and during stacking all data layers are divided according to the segmentation mask into N (to be specified) segments and temporarily saved as N MAT files. These N MAT files are then once more processed and the parameterization (such as vegetation and additional soil information) is associated with each pixel and each segment is saved as a DAT file. Stacking and associating the parameterizations are divided mainly due to two reasons: First, it is done to reduce the data volume in memory. The stacking algorithm treats each data layer separately and stores the respective segments in MAT files while the vegetation parameterization algorithm already works on the segments themselves, therefore avoiding running short on computing memory. Second, the division is done to include the parameterization at the latest stage possible to allow for easy changes in parameterization without having to revisit the whole data processing. Associating the parameterization consists of adding the vegetation parameterization and soil information. Currently, the vegetation parameterization is based on land cover type only. For each land cover type a standardized vegetation parameterization is determined based on data collected in the field. The vegetation parameterization is validated by comparing the output of the forward model against radar data over several pixels within the same scene. In addition to associating the vegetation parameterization, the soil roughness of each soil interface and the soil temperature at each layer are determined based on field measurements. All other soil information is used directly from SSURGO. At this last step of the data handling, each pixel will carry four flags consisting of one flag enabling the pixel inversion and three quality control flags for the land cover, slope, and soil. Additional to the 4 flags, each pixel carries its

Table B.5: Information contained in one DAT file.

Information	Number of parameter
Pixel number within image	2
Flags	4
General parameter (incidence angle and lambda)	2
Radar data	4
Above-ground vegetation	31
Number of soil layers	1
Soil parameter for each soil layer	8

pixel number (row and column within the segment), two general parameters (local incidence angle and lambda), four parameters as radar data (HH, VV, HV, VH), 31 parameters for the above-ground vegetation (inputs necessary for the forward model), 1 parameter specifying the number of soil layers and 8 parameters characterizing each soil layer (depth to top, layer depth, roughness, percentage clay/sand/silt, bulk density and temperature). The information contained in one DAT file is tabulated in Table B.5. These N DAT files are the segmented data ready for inversion on N processors.

B.6   Soil moisture inversion

The inversion is run on N CPUs in parallel. The computational facilities used to run the inversion algorithm are the HPCC supercomputer cluster at USC and the NASA HECC cluster. Depending on the computational facility, a different number of segments are created: either 144 segments for the HPCC supercomputer cluster or then 560, 600 or 1320 segments for the NASA HECC cluster. The inversion returns N DAT files with data at 3 arc seconds. Each DAT file reports for each pixel the pixel number (row, column), the three coefficients of the second-order polynomial (a, b, c) and the three radar backscattering coefficients (HH, VV, HV).

B.7 Post-inversion RZSM assembly

By utilizing the segmentation mask, which contains information about the location of each segment within the image, the N DAT files of results are assembled into one data layer. This data layer contains the three coefficients of the second-order polynomial (a, b, c) for each pixel from which the soil moisture at any depth within the validity range can be calculated. The validity range depends on how many soil layers and what thickness is used to discretize the moisture profile. The equation is deemed valid up to the last layer that was used for discretization; for deeper points, the calculated moisture values might become non-physical. After assembly of the retrieved values into one image, the soil moisture is visualized and validated with in-situ measurements. The in-situ measurements contain multiple permanent profiles installed near the flux tower at each of the study sites, as well as handheld soil moisture measurements from field measurement during overflight days. The internal flags for each pixel can be used to investigate any inversion problems. After careful validation, the data layer is provided to L4 in the form of an HDF5 file.

APPENDIX C

Method to generate synthetic spaceborne data based on AIRSAR data and predicted Faraday rotation angle assuming no other system distortion terms

C.1 Introduction to terminology

The scattering and Stokes matrices are widely used to relate a scattered to an incident field, but there is some confusion of the different matrices and their exact definitions, as pointed out by Guissard [158], which has been used as a reference for the following clarification of the terminology. The detailed definitions of the terminologies appear in the subsequent chapter.

The *Jones vector* is often used to represent a completely polarized electromagnetic plane by its two components in an orthogonal base. The description based on *Stokes parameters* (*Stokes vector*) is more commonly used for representing a partially polarized wave that is the result of scattering by fluctuating or random targets. The 2×2 *scattering matrix* describes the scattering phenomena and relates the scattered
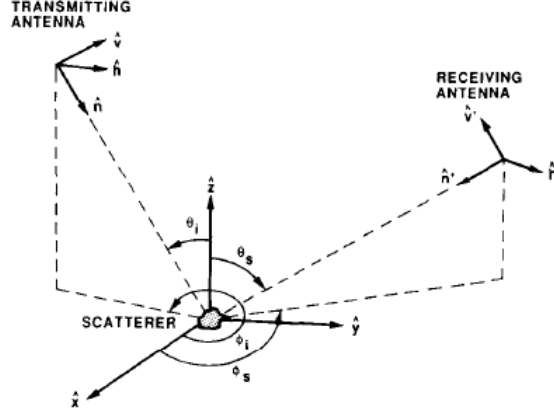
Figure C.1: Scattering geometry and local coordinate system. Figure adapted from [159], page 1584.

Jones vector to the incident Jones vector. In a similar way, the 4×4 *Muller matrix* relates the scattered Stokes vector and the incident Stokes vector. According to Guissard [158], there exists a one-to-one correspondence between the scattering matrix and the Muller matrix for a deterministic target, and the two descriptions are equivalent. For random targets, however, the scattering matrix and the Muller matrix are not the same.

Another matrix of applicable significance is the Kennaugh matrix. It is important to know how much power is available at the radar receiver given the polarization characteristics of the receiving antenna. The calculation of the received power needs another 4×4 matrix like the Muller matrix, the *Kennaugh matrix*, which in contrast to the always-asymmetric Muller matrix is always symmetric. The Muller matrix and the Kennaugh matrix in the backscatter alignment reference frame differ only in that the fourth rows have opposite signs.

Throughout this work, the Backscatter Alignment Convention (BSA) is assumed. This scattering geometry can be seen in Fig. C.1. If reciprocity is assumed in the backscattering convention the following statement holds: $S_{HV} = S_{VH}$. This is a key statement for this approach. Apart from the radar remote sensing terminology it has to be clarified that within all calculations the convention $i = -j$ for complex numbers

will be assumed.

C.2 Derivation of Stokes matrix and scattering pair-elements

The *scattering matrix S* is given as a 2×2 matrix

$$
\begin{bmatrix}
S_{HH} & S_{HV} \\
S_{VH} & S_{VV}
\end{bmatrix}
\tag{C.1}
$$

and relates the incident fields E_i to the scattered fields E_s [159]

$$
\begin{bmatrix}
E_H \\
E_V
\end{bmatrix}_s
=
\frac{e^{-jkR}}{R}
\begin{bmatrix}
S_{HH} & S_{HV} \\
S_{VH} & S_{VV}
\end{bmatrix}
\begin{bmatrix}
E_H \\
E_V
\end{bmatrix}_i
\tag{C.2}
$$

An arbitrary wave polarization is given as

$$
p =
\begin{bmatrix}
\hat{e}_h \\
\hat{e}_v
\end{bmatrix}
\tag{C.3}
$$

The incident wave can then be defined as

$$
E_i = e_h \hat{e}_h + e_v \hat{e}_v
\tag{C.4}
$$

The Stokes parameters for arbitrary wave polarizations are defined as follows with
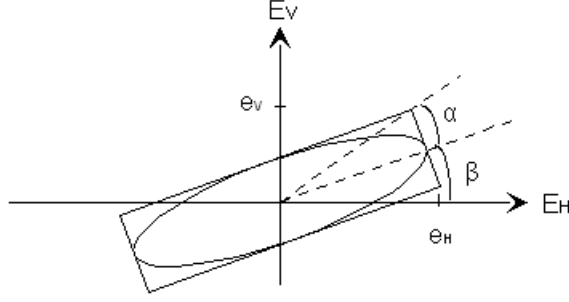
Figure C.2: Definition of the angles for the Stokes parameters.

the polarization angles defined as given in Fig. C.2:

$$
\begin{aligned}
I &= \frac{1}{\eta}(|e_h|^2 + |e_v|^2) \\
Q &= \frac{1}{\eta}(|e_h|^2 - |e_v|^2) = I\cos(2\alpha)\cos(2\beta) \\
U &= \frac{2}{\eta}\Re\{e_h e_v^*\} = I\cos(2\alpha)\sin(2\beta) \\
V &= \frac{2}{\eta}\Im\{e_h e_v^*\} = I\sin(2\alpha)
\end{aligned}
\tag{C.5}
$$

which can be written in the Stokes vector representation

$$
S = \begin{bmatrix} S_0 \\ S_1 \\ S_2 \\ S_3 \end{bmatrix} = \begin{bmatrix} I \\ Q \\ U \\ V \end{bmatrix}
\tag{C.6}
$$

With the definitions of Eq. (C.2) and (C.5) the following elements of the *Muller matrix m* can be derived:

$$
\begin{aligned}
m_{11} &= \frac{1}{4}(S_{HH}S_{HH}^* + S_{HV}S_{HV}^* + S_{VH}S_{VH}^* + S_{VV}S_{VV}^*) \\
m_{12} &= \frac{1}{4}(S_{HH}S_{HH}^* - S_{HV}S_{HV}^* + S_{VH}S_{VH}^* - S_{VV}S_{VV}^*)
\end{aligned}
$$

217

$$m_{13} = \frac{1}{2}(\Re\{S_{HH}S_{HV}^*\} + \Re\{S_{VH}S_{VV}^*\})$$

$$m_{14} = \frac{1}{2}(-\Im\{S_{HH}S_{HV}^*\} - \Im\{S_{VH}S_{VV}^*\})$$

$$m_{21} = \frac{1}{4}(S_{HH}S_{HH}^* + S_{HV}S_{HV}^* - S_{VH}S_{VH}^* - S_{VV}S_{VV}^*)$$

$$m_{22} = \frac{1}{4}(S_{HH}S_{HH}^* - S_{HV}S_{HV}^* - S_{VH}S_{VH}^* + S_{VV}S_{VV}^*)$$

$$m_{23} = \frac{1}{2}(\Re\{S_{HH}S_{HV}^*\} - \Re\{S_{VH}S_{VV}^*\})$$

$$m_{24} = \frac{1}{2}(-\Im\{S_{HH}S_{HV}^*\} + \Im\{S_{VH}S_{VV}^*\})$$

$$m_{31} = \frac{1}{2}(\Re\{S_{HH}S_{VH}^*\} + \Re\{S_{HV}S_{VV}^*\})$$

$$m_{32} = \frac{1}{2}(\Re\{S_{HH}S_{VH}^*\} - \Re\{S_{HV}S_{VV}^*\})$$

$$m_{33} = \frac{1}{2}(\Re\{S_{HH}S_{VV}^*\} + \Re\{S_{HV}S_{VH}^*\})$$

$$m_{34} = \frac{1}{2}(-\Im\{S_{HH}S_{VV}^*\} + \Im\{S_{HV}S_{VH}^*\})$$

$$m_{41} = \frac{1}{2}(\Im\{S_{HH}S_{VH}^*\} + \Im\{S_{HV}S_{VV}^*\})$$

$$m_{42} = \frac{1}{2}(\Im\{S_{HH}S_{VH}^*\} - \Im\{S_{HV}S_{VV}^*\})$$

$$m_{43} = \frac{1}{2}(\Im\{S_{HH}S_{VV}^*\} + \Im\{S_{HV}S_{VH}^*\})$$

$$m_{44} = \frac{1}{2}(\Re\{S_{HH}S_{VV}^*\} - \Re\{S_{HV}S_{VH}^*\}) \tag{C.7}$$

with the Muller matrix defined as follows:

$$m = \begin{bmatrix} m_{11} & m_{12} & m_{13} & m_{14} \\ m_{21} & m_{22} & m_{23} & m_{24} \\ m_{31} & m_{32} & m_{33} & m_{34} \\ m_{41} & m_{42} & m_{43} & m_{44} \end{bmatrix} \tag{C.8}$$

As stated in [160], the matrix should be symmetric. To achieve this, the sign of the last row of the Muller matrix is changed. This yields the symmetric Kennaugh matrix, which relates the Stokes matrix to the scattering matrix cross products $S_{pq}S_{pq}^*$, $(p,q) \in \{H,V\}$. Only the last row will be quoted:

$$m_{41} = \frac{1}{2}(-\Im\{S_{HH}S_{VH}^*\} - \Im\{S_{HV}S_{VV}^*\})$$
$$m_{42} = \frac{1}{2}(-\Im\{S_{HH}S_{VH}^*\} + \Im\{S_{HV}S_{VV}^*\})$$
$$m_{43} = \frac{1}{2}(-\Im\{S_{HH}S_{VV}^*\} - \Im\{S_{HV}S_{VH}^*\})$$
$$m_{44} = \frac{1}{2}(\Re\{S_{HV}S_{VH}^*\} - \Re\{S_{HH}S_{VV}^*\}) \tag{C.9}$$

Henceforth the Kennaugh definition will be used. But, for simplicity (and because the term is commonly used), it will still be called the Stokes matrix.

C.3 Detailed method to generate synthetic spaceborne data with Faraday rotation based on airborne data

The procedure of generating artificial spaceborne data with Faraday rotation based on airborne data can be split up in four steps. The first step is to extract the Stokes matrix from the binary data set. The used data are stored with the JPL AIRSAR data compression algorithm to reduce the data volume from 1.92 GBytes per scene to 37.5 MBytes. The compression algorithm also involves converting the scattering matrix

data into Stokes matrix data, which preserves polarimetric information. Additional compression is achieved by coding the matrix elements in a pseudo block floating point format. A total data volume reduction factor of 51.2 is typically achieved. The important assumption of the AIRSAR data compression scheme is that the measured scattering matrix has to be symmetric, i.e. $S_{VH} = S_{HV}$. This follows from reciprocity and the backscattering operation mode of AIRSAR. The resulting Stokes matrix is therefore symmetrical. With the JPL AIRSAR data compression algorithm the information of 1 pixel is stored in 10 bytes. To reconstruct the Stokes matrix from the compressed data set the following decompression operations are used [159].

$$m_{11} = M_{11} = (\frac{byte(2)}{254} + 1.5) \cdot 2^{byte(1)} \cdot gen\_scale\_factor$$

$$m_{12} = M_{12} = byte(3) \cdot \frac{M_{11}}{127}$$

$$m_{13} = M_{13} = sign(byte(4)) \cdot (\frac{byte(4)}{127})^2 \cdot M_{11}$$

$$m_{14} = M_{14} = sign(byte(5)) \cdot (\frac{byte(5)}{127})^2 \cdot M_{11}$$

$$m_{23} = M_{23} = sign(byte(6)) \cdot (\frac{byte(6)}{127})^2 \cdot M_{11}$$

$$m_{24} = M_{24} = sign(byte(7)) \cdot (\frac{byte(7)}{127})^2 \cdot M_{11}$$

$$m_{33} = M_{33} = byte(8) \cdot \frac{M_{11}}{127}$$

$$m_{34} = M_{34} = byte(9) \cdot \frac{M_{11}}{127}$$

$$m_{44} = M_{44} = byte(10) \cdot \frac{M_{11}}{127}$$

$$m_{22} = M_{11} - M_{33} - M_{44} \qquad (C.10)$$

The general scale factor gen_scale_factor is stored in the headers of the specific files and can be extracted separately. More information on the AIRSAR data format is given in chapter 4 of the AIRSAR technical manuals [161].

The second step is to retrieve the 16 scattering matrix cross products $S_{pq}S_{pq}^*$, $(p,q) \in \{H,V\}$. The following relationships are used, where 10 elements are uniquely extracted from the Stokes matrix and 6 elements are dependent.

$$S_{HH}S_{HH}^* = m_{11} + m_{12} + m_{21} + m_{22}$$

$$S_{HV}S_{HV}^* = m_{11} - m_{12} + m_{21} - m_{22}$$

$$S_{VH}S_{VH}^* = m_{11} + m_{12} - m_{21} - m_{22}$$

$$S_{VV}S_{VV}^* = m_{11} - m_{12} - m_{21} + m_{22}$$

$$S_{HH}S_{HV}^* = m_{13} + m_{23} - m_{14} - m_{24}$$

$$S_{VH}S_{VV}^* = m_{13} - m_{23} - m_{14} + m_{24}$$

$$S_{HH}S_{VH}^* = m_{31} + m_{32} - m_{41} - m_{42}$$

$$S_{HV}S_{VV}^* = m_{31} - m_{32} - m_{41} + m_{42}$$

$$S_{HH}S_{VV}^* = m_{33} - m_{44} - m_{34} - m_{43}$$

$$S_{HV}S_{VH}^* = m_{33} + m_{44} + m_{34} - m_{43}$$

$$S_{HV}S_{HH}^* = (S_{HH}S_{HV}^*)^*$$

$$S_{VV}S_{VH}^* = (S_{VH}S_{VV}^*)^*$$

$$S_{VH}S_{HH}^* = (S_{HH}S_{VH}^*)^*$$

$$S_{VV}S_{HV}^* = (S_{HV}S_{VV}^*)^*$$

$$S_{VV}S_{HH}^* = (S_{HH}S_{VV}^*)^*$$

$$S_{VH}S_{HV}^* = (S_{HV}S_{VH}^*)^* \tag{C.11}$$

The resulting scattering matrix will be symmetrical, if the assumption $S_{VH} =$

S_{HV} holds. It can then be assumed that the resulting Stokes matrix will also be symmetrical. This can only be met if reciprocity and the backscatter mode are given. Then as stated in [159]:

$$m_{11} = \frac{1}{4}[S_{HH}S_{HH}^* + 2S_{HV}S_{HV}^* + S_{VV}S_{VV}^*]$$

$$m_{12} = \frac{1}{4}[S_{HH}S_{HH}^* - S_{VV}S_{VV}^*]$$

$$m_{13} = \frac{1}{2}[\Re\{S_{HH}S_{HV}^*\} + \Re\{S_{HV}S_{VV}^*\}]$$

$$m_{14} = \frac{1}{2}[-\Im\{S_{HH}S_{HV}^*\} - \Im\{S_{HV}S_{VV}^*\}]$$

$$m_{21} = m_{12}$$

$$m_{22} = \frac{1}{4}[S_{HH}S_{HH}^* - 2S_{HV}S_{HV}^* + S_{VV}S_{VV}^*]$$

$$m_{23} = \frac{1}{2}[\Re\{S_{HH}S_{HV}^*\} - \Re\{S_{HV}S_{VV}^*\}]$$

$$m_{24} = \frac{1}{2}[-\Im\{S_{HH}S_{HV}^*\} + \Im\{S_{HV}S_{VV}^*\}]$$

$$m_{31} = m_{13}$$

$$m_{32} = m_{23}$$

$$m_{33} = \frac{1}{2}[S_{HV}S_{HV}^* + \Re\{S_{HH}S_{VV}^*\}]$$

$$m_{34} = -\frac{1}{2}\Im\{S_{HH}S_{VV}^*\}$$

$$m_{41} = m_{41}$$

$$m_{42} = m_{42}$$

$$m_{43} = m_{43}$$

$$m_{44} = \frac{1}{2}[S_{HV}S_{HV}^* - \Re\{S_{HH}S_{VV}^*\}] \tag{C.12}$$

In this case ($S_{HV} = S_{VH}$), the retrieval of the scattering matrix cross products can be either achieved similarly to the unsymmetrized Stokes matrix, or the following expressions can be applied, where 6 elements are directly extracted from the Stokes matrix and 10 elements are dependent.

$$S_{HH}S_{HH}^* = 2m_{11} + 2m_{12} - m_{33} - m_{44}$$

$$S_{HV}S_{HV}^* = m_{33} + m_{44}$$

$$S_{VV}S_{VV}^* = 2m_{11} - 2m_{12} - m_{33} - m_{44}$$

$$S_{HH}S_{HV}^* = complex(m_{13} + m_{23}, -m_{14} - m_{24})$$

$$S_{HH}S_{VV}^* = complex(m_{33} - m_{44}, -2m_{34})$$

$$S_{HV}S_{VV}^* = complex(m_{13} - m_{23}, -m_{14} + m_{24})$$

$$S_{VH}S_{VV}^* = S_{HV}S_{VV}^*$$

$$S_{HH}S_{VH}^* = S_{HH}S_{HV}^*$$

$$S_{HV}S_{VH}^* = S_{HV}S_{HV}^*$$

$$S_{VH}S_{VH}^* = S_{HV}S_{HV}^*$$

$$S_{HV}S_{HH}^* = (S_{HH}S_{HV}^*)^*$$

$$S_{VV}S_{HH}^* = (S_{HH}S_{VV}^*)^*$$

$$S_{VV}S_{HV}^* = (S_{HV}S_{VV}^*)^*$$

$$S_{VV}S_{VH}^* = (S_{VH}S_{VV}^*)^*$$

$$S_{VH}S_{HH}^* = (S_{HH}S_{VH}^*)^*$$

$$S_{VH}S_{HV}^* = (S_{HV}S_{VH}^*)^* \tag{C.13}$$

The third step is then to build the new Stokes matrix $\bar{m}$ based on the predicted Faraday rotation and the known scattering matrix cross products $S_{pq}S_{pq}^*$. The *mea-*

sured scattering matrix M is defined as a 2×2 matrix according to [115]:

$$\begin{bmatrix} M_{HH} & M_{VH} \\ M_{HV} & M_{VV} \end{bmatrix} = \begin{bmatrix} \cos\Omega & \sin\Omega \\ -\sin\Omega & \cos\Omega \end{bmatrix} \begin{bmatrix} S_{HH} & S_{VH} \\ S_{HV} & S_{VV} \end{bmatrix} \begin{bmatrix} \cos\Omega & \sin\Omega \\ -\sin\Omega & \cos\Omega \end{bmatrix}$$

$$(C.14)$$

where Ω is the Faraday rotation angle and where the elements are calculated as:

$$M_{HH} = S_{HH}\cos^2\Omega + (S_{HV} - S_{VH})\sin\Omega\cos\Omega - S_{VV}\sin^2\Omega$$

$$M_{HV} = S_{HV}\cos^2\Omega - (S_{HH} + S_{VV})\sin\Omega\cos\Omega + S_{VH}\sin^2\Omega$$

$$M_{VH} = S_{VH}\cos^2\Omega + (S_{HH} + S_{VV})\sin\Omega\cos\Omega + S_{HV}\sin^2\Omega$$

$$M_{VV} = S_{VV}\cos^2\Omega + (S_{HV} - S_{VH})\sin\Omega\cos\Omega - S_{HH}\sin^2\Omega \qquad (C.15)$$

If we assume that the calculations above are carried out for the special case $\Omega = 0°$, we can easily show that the following equations hold, which proves the consistency with Eq. (C.9):

$$m_{11} = \frac{1}{4}(M_{HH}M_{HH}^* + M_{HV}M_{HV}^* + M_{VH}M_{VH}^* + M_{VV}M_{VV}^*)$$

$$m_{12} = \frac{1}{4}(M_{HH}M_{HH}^* - M_{HV}M_{HV}^* + M_{VH}M_{VH}^* - M_{VV}M_{VV}^*)$$

$$m_{13} = \frac{1}{2}(\Re\{M_{HH}M_{HV}^*\} + \Re\{M_{VH}M_{VV}^*\})$$

$$m_{14} = \frac{1}{2}(-\Im\{M_{HH}M_{HV}^*\} - \Im\{M_{VH}M_{VV}^*\})$$

$$m_{21} = \frac{1}{4}(M_{HH}M_{HH}^* + M_{HV}M_{HV}^* - M_{VH}M_{VH}^* - M_{VV}M_{VV}^*)$$

$$m_{22} = \frac{1}{4}(M_{HH}M_{HH}^* - M_{HV}M_{HV}^* - M_{VH}M_{VH}^* + M_{VV}M_{VV}^*)$$

$$m_{23} = \frac{1}{2}(\Re\{M_{HH}M_{HV}^*\} - \Re\{M_{VH}M_{VV}^*\})$$

$$m_{24} = \frac{1}{2}(-\Im\{M_{HH}M_{HV}^*\} + \Im\{M_{VH}M_{VV}^*\})$$

224

$$m_{31} = \frac{1}{2}(\Re\{M_{HH}M_{VH}^*\} + \Re\{M_{HV}M_{VV}^*\})$$

$$m_{32} = \frac{1}{2}(\Re\{M_{HH}M_{VH}^*\} - \Re\{M_{HV}M_{VV}^*\})$$

$$m_{33} = \frac{1}{2}(\Re\{M_{HH}M_{VV}^*\} + \Re\{M_{HV}M_{VH}^*\})$$

$$m_{34} = \frac{1}{2}(-\Im\{M_{HH}M_{VV}^*\} + \Im\{M_{HV}M_{VH}^*\})$$

$$m_{41} = \frac{1}{2}(-\Im\{M_{HH}M_{VH}^*\} - \Im\{M_{HV}M_{VV}^*\})$$

$$m_{42} = \frac{1}{2}(-\Im\{M_{HH}M_{VH}^*\} + \Im\{M_{HV}M_{VV}^*\})$$

$$m_{43} = \frac{1}{2}(-\Im\{M_{HH}M_{VV}^*\} - \Im\{M_{HV}M_{VH}^*\})$$

$$m_{44} = \frac{1}{2}(\Re\{M_{HV}M_{VH}^*\} - \Re\{M_{HH}M_{VV}^*\}) \qquad \text{(C.16)}$$

It bears emphasis that M_{HV} is not equal to M_{VH}, but S_{HV} can, in certain circumstances, be assumed to be equal to S_{VH}. If Eqs. (C.16) are combined with the Eqs. (C.14) and (C.15), the following equations will result:

$$\bar{m}_{11} = \frac{1}{4}\left[S_{HH}S_{HH}^* + 2S_{HV}S_{HV}^* + S_{VV}S_{VV}^*\right]$$

$$\bar{m}_{12} = \frac{1}{4}\left[S_{HH}S_{HH}^* - S_{VV}S_{VV}^*)(\cos^4\Omega - \sin^4\Omega)\right.$$

$$\left. + 2\left(S_{HH}S_{HV}^* + (S_{HH}S_{HV}^*)^* + (S_{HV}S_{VV}^*)^* + S_{HV}S_{VV}^*\right)\cos\Omega\sin\Omega\right]$$

$$\bar{m}_{13} = \frac{1}{2}\left[(S_{VV}S_{VV}^* - S_{HH}S_{HH}^*)(\cos^3\Omega\sin\Omega - \cos\Omega\sin^3\Omega)\right.$$

$$\left. + \Re\{(S_{HH}S_{HV}^* + S_{HV}S_{VV}^*)\cos^2\Omega - ((S_{HH}S_{HV}^*)^* + (S_{HV}S_{VV}^*)^*)\sin^2\Omega\}\right]$$

$$\bar{m}_{14} = \frac{1}{2}\,\Im\{-(S_{HH}S_{HV}^* + S_{HV}S_{VV}^*)\cos^2\Omega$$

$$+ ((S_{HH}S_{HV}^*)^* + (S_{HV}S_{VV}^*)^*)\sin^2\Omega\}$$

$$\bar{m}_{21} = \frac{1}{4} \left[(S_{HH}S_{HH}^* - S_{VV}S_{VV}^*)(\cos^4 \Omega - \sin^4 \Omega) \right.$$

$$\left. - 2 \, (S_{HH}S_{HV}^* + (S_{HH}S_{HV}^*)^* + (S_{HV}S_{VV}^*)^* + S_{HV}S_{VV}^*) \cos \Omega \sin \Omega \right]$$

$$\bar{m}_{22} = \frac{1}{4} \left[(S_{HH}S_{HH}^* + S_{VV}S_{VV}^*)(\cos^4 \Omega - 2 \cos^2 \Omega \sin^2 \Omega + \sin^4 \Omega) \right.$$

$$\left. - 4 \, (S_{HH}S_{VV}^* + (S_{HH}S_{VV}^*)^*) \cos^2 \Omega \sin^2 \Omega - 2 \, S_{HV}S_{HV}^* \right]$$

$$\bar{m}_{23} = \frac{1}{2} \, \Re\{ -(S_{HH}S_{HH}^* + S_{VV}S_{VV}^*)(\cos^3 \Omega \sin \Omega - \cos \Omega \sin^3 \Omega)$$

$$+ (S_{HH}S_{HV}^* - S_{HV}S_{VV}^*) \cos^2 \Omega + ((S_{HH}S_{HV}^*)^* - (S_{HV}S_{VV}^*)^*) \sin^2 \Omega$$

$$- 2 \, S_{HH}S_{VV}^* \cos^3 \Omega \sin \Omega + 2 \, (S_{HH}S_{VV}^*)^* \cos \Omega \sin^3 \Omega \}$$

$$\bar{m}_{24} = \frac{1}{2} \, \Im\{ (S_{HV}S_{VV}^* - S_{HH}S_{HV}^*) \cos^2 \Omega + ((S_{HV}S_{VV}^*)^* - (S_{HH}S_{HV}^*)^*) \sin^2 \Omega$$

$$+ 2 \, S_{HH}S_{VV}^* \cos^3 \Omega \sin \Omega - 2 \, (S_{HH}S_{VV}^*)^* \cos \Omega \sin^3 \Omega \}$$

$$\bar{m}_{31} = \frac{1}{2} \, \Re\{ (S_{HH}S_{HV}^* + S_{HV}S_{VV}^*) \cos^2 \Omega - ((S_{HH}S_{HV}^*)^* + (S_{HV}S_{VV}^*)^*) \sin^2 \Omega$$

$$+ (S_{HH}S_{HH}^* - S_{VV}S_{VV}^*)(\cos^3 \Omega \sin \Omega + \cos \Omega \sin^3 \Omega) \}$$

$$\bar{m}_{32} = \frac{1}{2} \left[(S_{HH}S_{HH}^* + S_{VV}S_{VV}^*)(\cos^3 \Omega \sin \Omega - \cos \Omega \sin^3 \Omega) \right.$$

$$+ \Re\{ (S_{HH}S_{HV}^* - S_{HV}S_{VV}^*) \cos^2 \Omega + ((S_{HH}S_{HV}^*)^* - (S_{HV}S_{VV}^*)^*) \sin^2 \Omega$$

$$\left. + 2 \, S_{HH}S_{VV}^* \cos^3 \Omega \sin \Omega - 2 \, (S_{HH}S_{VV}^*)^* \cos \Omega \sin^3 \Omega \} \right]$$

$$\bar{m}_{33} = \frac{1}{2} \, \Re\{ S_{HV}S_{HV}^*$$

$$+ S_{HH}S_{VV}^*(\cos^4 \Omega - \cos^2 \Omega \sin^2 \Omega) + (S_{HH}S_{VV}^*)^*(\sin^4 \Omega - \cos^2 \Omega \sin^2 \Omega)$$

$$- 2 \, (S_{HH}S_{HH}^* + S_{VV}S_{VV}^*) \cos^2 \Omega \sin^2 \Omega$$

$$+ (S_{HV}S_{VV}^* - (S_{HV}S_{VV}^*)^* - S_{HH}S_{HV}^* + (S_{HH}S_{HV}^*)^*) \cos \Omega \sin \Omega \}$$

$$\bar{m}_{34} = \frac{1}{2} \, \Im\{ -S_{HH}S_{VV}^*(\cos^4 \Omega + \cos^2 \Omega \sin^2 \Omega)$$

$$- (S_{HH}S_{VV}^*)^*(\sin^4 \Omega + \cos^2 \Omega \sin^2 \Omega) + S_{HV}S_{HV}^*$$

$$+ ((S_{HH}S_{HV}^*)^* - S_{HH}S_{HV}^* + S_{HV}S_{VV}^* - (S_{HV}S_{VV}^*)^*) \cos \Omega \sin \Omega \}$$

$$\bar{m}_{41} = \frac{1}{2} \Im\{-((S_{HH}S_{HV}^* + S_{HV}S_{VV}^*)\cos^2\Omega$$

$$+ ((S_{HH}S_{HV}^*)^* + (S_{HV}S_{VV}^*)^*))\sin^2\Omega\}$$

$$\bar{m}_{42} = \frac{1}{2} \Im\{(S_{HV}S_{VV}^* - S_{HH}S_{HV}^*)\cos^2\Omega + ((S_{HV}S_{VV}^*)^* - (S_{HH}S_{HV}^*)^*)\sin^2\Omega$$

$$- 2\,S_{HH}S_{VV}^*\cos^3\Omega\sin\Omega + 2\,(S_{HH}S_{VV}^*)^*\cos\Omega\sin^3\Omega\}$$

$$\bar{m}_{43} = \frac{1}{2} \Im\{-S_{HH}S_{VV}^*(\cos^4\Omega - \cos^2\Omega\sin^2\Omega)$$

$$- (S_{HH}S_{VV}^*)^*(\sin^4\Omega - \cos^2\Omega\sin^2\Omega) - S_{HV}S_{HV}^*$$

$$+ (S_{HH}S_{HV}^* - (S_{HH}S_{HV}^*)^* + (S_{HV}S_{VV}^*)^* - S_{HV}S_{VV}^*)\cos\Omega\sin\Omega\}$$

$$\bar{m}_{44} = \frac{1}{2} \Re\{S_{HV}S_{HV}^* - S_{HH}S_{VV}^*(\cos^4\Omega + \cos^2\Omega\sin^2\Omega)$$

$$- (S_{HH}S_{VV}^*)^*(\sin^4\Omega + \cos^2\Omega\sin^2\Omega)$$

$$+ (S_{HV}S_{VV}^* - (S_{HV}S_{VV}^*)^* - S_{HH}S_{HV}^* + (S_{HH}S_{HV}^*)^*)\cos\Omega\sin\Omega\} \qquad \text{(C.17)}$$

This new Stokes matrix $\bar{m}$ is defined as follows:

$$\bar{m} = \begin{bmatrix} \bar{m}_{11} & \bar{m}_{12} & \bar{m}_{13} & \bar{m}_{14} \\ \bar{m}_{21} & \bar{m}_{22} & \bar{m}_{23} & \bar{m}_{24} \\ \bar{m}_{31} & \bar{m}_{32} & \bar{m}_{33} & \bar{m}_{34} \\ \bar{m}_{41} & \bar{m}_{42} & \bar{m}_{43} & \bar{m}_{44} \end{bmatrix} \qquad \text{(C.18)}$$

The fourth step is to retrieve the scattering matrix cross products $\bar{M}_{pq}\bar{M}_{pq}^*$, $(p,q) \in \{H,V\}$ from $\bar{m}$. To achieve this, Eq. (C.11) is reused, taking the form of Eq. (C.19). It has to be noted that $M_{pq}M_{pq}^*$ and $\bar{M}_{pq}\bar{M}_{pq}^*$ can be used interchangeably, but haven't been generated in the same way. While $M_{pq}M_{pq}^*$ has been generated with Eq. (C.14), $\bar{M}_{pq}\bar{M}_{pq}^*$ has been generated without using the scattering matrix and using the Stokes matrix instead. This means that the $\bar{M}_{pq}\bar{M}_{pq}^*$ cross products can be used in place of the $M_{pq}M_{pq}^*$ cross products.

$$\bar{M}_{HH}\bar{M}_{HH}^* = \bar{m}_{11} + \bar{m}_{12} + \bar{m}_{21} + \bar{m}_{22}$$

$$\bar{M}_{HV}\bar{M}_{HV}^* = \bar{m}_{11} - \bar{m}_{12} + \bar{m}_{21} - \bar{m}_{22}$$

$$\bar{M}_{VH}\bar{M}_{VH}^* = \bar{m}_{11} + \bar{m}_{12} - \bar{m}_{21} - \bar{m}_{22}$$

$$\bar{M}_{VV}\bar{M}_{VV}^* = \bar{m}_{11} - \bar{m}_{12} - \bar{m}_{21} + \bar{m}_{22}$$

$$\bar{M}_{HH}\bar{M}_{HV}^* = \bar{m}_{13} + \bar{m}_{23} - \bar{m}_{14} - \bar{m}_{24}$$

$$\bar{M}_{VH}\bar{M}_{VV}^* = \bar{m}_{13} - \bar{m}_{23} - \bar{m}_{14} + \bar{m}_{24}$$

$$\bar{M}_{HH}\bar{M}_{VH}^* = \bar{m}_{31} + \bar{m}_{32} - \bar{m}_{41} - \bar{m}_{42}$$

$$\bar{M}_{HV}\bar{M}_{VV}^* = \bar{m}_{31} - \bar{m}_{32} - \bar{m}_{41} + \bar{m}_{42}$$

$$\bar{M}_{HH}\bar{M}_{VV}^* = \bar{m}_{33} - \bar{m}_{44} - \bar{m}_{34} - \bar{m}_{43}$$

$$\bar{M}_{HV}\bar{M}_{VH}^* = \bar{m}_{33} + \bar{m}_{44} + \bar{m}_{34} - \bar{m}_{43}$$

$$\bar{M}_{HV}\bar{M}_{HH}^* = (\bar{M}_{HH}\bar{M}_{HV}^*)^*$$

$$\bar{M}_{VV}\bar{M}_{VH}^* = (\bar{M}_{VH}\bar{M}_{VV}^*)^*$$

$$\bar{M}_{VH}\bar{M}_{HH}^* = (\bar{M}_{HH}\bar{M}_{VH}^*)^*$$

$$\bar{M}_{VV}\bar{M}_{HV}^* = (\bar{M}_{HV}\bar{M}_{VV}^*)^*$$

$$\bar{M}_{VV}\bar{M}_{HH}^* = (\bar{M}_{HH}\bar{M}_{VV}^*)^*$$

$$\bar{M}_{VH}\bar{M}_{HV}^* = (\bar{M}_{HV}\bar{M}_{VH}^*)^* \tag{C.19}$$

The procedure for generating artificial spaceborne data with other system distur-
bance terms is very similar. The only difference is that Eq. C.14 has to be exchanged
with Eq. 5.6.

BIBLIOGRAPHY

BIBLIOGRAPHY

[1] R. M. Lucas, M. Moghaddam, and N. Cronin. Microwave scattering from mixed-species forests, Queensland, Australia. *Geoscience and Remote Sensing, IEEE Transactions on*, 42(10):2142–2159, October 2004.

[2] N. R. Peplinski, F. T. Ulaby, and M. C. Dobson. Dielectric Properties of Soils in the 0.3-1.3-GHz Range. *Geoscience and Remote Sensing, IEEE Transactions on*, 33(3):803–807, May 1995.

[3] N. R. Peplinski, F. T. Ulaby, and M. C. Dobson. Corrections to "Dielectric Properties of Soils in the 0.3-1.3-GHz Range"'. *Geoscience and Remote Sensing, IEEE Transactions on*, 33(6):1340, November 1995.

[4] X. Duan and M. Moghaddam. Low-Frequency Low-Altitude Radar System Design and Measurement for Subcanopy and Subsurface Soil Moisture Characterization. In *IEEE Aerospace Conference*, Big Sky, Montana, March 2013.

[5] S. Solomon, D. Qin, M. Manning, Z. Chen, M. Marquis, K. B. Averyt, M. Tignor, and H. L. Miller, editors. *Climate Change 2007: The Physical Science Basis. Contribution of Working Group I to the Fourth Assessment Report of the Intergovernmental Panel on Climate Change.* Cambridge University Press, Cambridge, United Kingdom and New York, NY, USA, 2007.

[6] D. Entekhabi, E.G. Njoku, P. Houser, M. Spencer, T. Doiron, Yunjin Kim, J. Smith, R. Girard, S. Belair, W. Crow, T.J. Jackson, Y.H. Kerr, J.S. Kimball, R. Koster, K.C. McDonald, P.E. O'Neill, T. Pultz, S.W. Running, Jiancheng Shi, E. Wood, and J. Van Zyl. The hydrosphere state (hydros) satellite mission: an earth system pathfinder for global mapping of soil moisture and land freeze/thaw. *Geoscience and Remote Sensing, IEEE Transactions on*, 42(10):2184–2195, 2004.

[7] M. Moghaddam, Y. Rahmat-Samii, D. Entekhabi, J. Hoffman, D. Moller, L. E. Pierce, S. Saatchi, and M. Thomason. Microwave observatory of subcanopy and subsurface (MOSS): A mission concept for global deep soil moisture observations. *Geoscience and Remote Sensing, IEEE Transactions on*, 45(8):2630–2643, August 2007.

[8] D. Entekhabi, E. G. Njoku, P. E. O'Neill, K. H. Kellogg, W. T. Crow, W. N. Edelstein, J. K. Entin, S. D. Goodman, T. J. Jackson, J. Johnson, J. Kimball,

J. R. Piepmeier, R. D. Koster, N. Martin, K. C. McDonald, M. Moghaddam, S. Moran, R. Reichle, J. C. Shi, M. W. Spencer, S. W. Thurman, L. Tsang, and J. Van Zyl. The Soil Moisture Active Passive (SMAP) Mission. *Proceedings of the IEEE*, 98(5):704–716, May 2010.

[9] A. N. Flores, V. Y. Ivanov, D. Entekhabi, and R. L. Bras. Impact of Hillslope-Scale Organization of Topography, Soil Moisture, Soil Temperature, and Vegetation on Modeling Surface Microwave Radiation Emission. *Geoscience and Remote Sensing, IEEE Transactions on*, 47(8):2557–2571, 2009.

[10] K. Lim, P. Treitz, M. Wulder, B. St.-Onge, and M. Flood. LiDAR remote sensing of forest structure. *Progress in Physical Geography*, 27(1):88–106, 2003.

[11] C. Mallet and F. Bretar. Full-waveform topographic lidar: State of the art. *ISPRS Journal of Photogrammetry and Remote Sensing*, 64(1):1–16, 2009.

[12] R. M. Lucas, J. Armston, A. C. Lee, J. Carreiras, K. Viergever, P. Bunting, D. Clewley, M. Moghaddam, P. Siqueira, and I. Woodhouse. Quantifying Carbon in Wooded Savannas: The Role of Active Sensors in Measurements of Structure and Biomass. In M.J. Hill and N.P. Hanan, editors, *Ecosystem Function in Savannas: Measurement and Modelling at Landscape to Global Scales*. Taylor & Francis, New York, 2010.

[13] M. A. Karam, A. K. Fung, R. H. Lang, and N. S. Chauhan. A Microwave Scattering Model for Layered Vegetation. *Geoscience and Remote Sensing, IEEE Transactions on*, 30(4):767–784, July 1992.

[14] P. Liang, L. E. Pierce, and M. Moghaddam. Radiative Transfer Model for Microwave Bistatic Scattering from Forest Canopies. *Geoscience and Remote Sensing, IEEE Transactions on*, 43(11):2470–2483, November 2005.

[15] I. H. Woodhouse and D. H. Hoekman. Radar modeling of coniferous forest using a tree growth model. *International Journal of Remote Sensing*, 21(8):1725–1737, May 2000.

[16] K. C. McDonald, M. C. Dobson, and F. T. Ulaby. Using Mimics To Model L-band Multiangle and Multitemporal Backscatter from A Walnut Orchard. *Geoscience and Remote Sensing, IEEE Transactions on*, 28(4):447–491, July 1990.

[17] G. Sun and K. J. Ranson. A Three-Dimensional Radar Backscatter Model of Forest Canopies. *Geoscience and Remote Sensing, IEEE Transactions on*, 33(2):372–382, March 1995.

[18] P. Liang, M. Moghaddam, L. E. Pierce, and R. M. Lucas. Radar backscattering model for multilayer mixed-species forests. *Geoscience and Remote Sensing, IEEE Transactions on*, 43(11):2612–2626, November 2005.

[19] S. L. Durden, J. J. van Zyl, and H. A. Zebker. Modeling and observation of the radar polarization signature of forested areas. *Geoscience and Remote Sensing, IEEE Transactions on*, 27(3):290–301, May 1989.

[20] G. Sun, D. S. Simonett, and A. H. Strahler. A radar backscatter model for discontinuous coniferous forests. *Geoscience and Remote Sensing, IEEE Transactions on*, 29(4):639–650, July 1991.

[21] Y. Wang, J. Day, and G. Sun. Santa Barbara microwave backscattering model for woodlands. *International Journal of Remote Sensing*, 14(8):1477–1493, May 1993.

[22] D. Liu, G. Sun, Z. Guo, K. J. Ranson, and Y. Du. Three-dimensional coherent radar backscatter model and simulations of scattering phase center of forest canopies. *Geoscience and Remote Sensing, IEEE Transactions on*, 48(1):349–357, January 2010.

[23] Y. C. Lin and K. Sarabandi. A Monte Carlo coherent scattering model for forest canopies using fractal-generated trees. *Geoscience and Remote Sensing, IEEE Transactions on*, 37(1):440–451, January 1999.

[24] N. S. Chauhan, R. L. Lang, and K. J. Ranson. Radar modeling of a boreal forest. *Geoscience and Remote Sensing, IEEE Transactions on*, 29(4):627–638, July 1991.

[25] J. A. Richards, G. Sun, and D. S. Simonett. L-band radar backscatter modeling of forest stands. *Geoscience and Remote Sensing, IEEE Transactions on*, 25(4):487–498, July 1987.

[26] M. Moghaddam and S. Saatchi. Analysis of Scattering Mechanisms in SAR imagery over Boreal Forest: Results from BOREAS '93. *Geoscience and Remote Sensing, IEEE Transactions on*, 33(5):1290–1296, September 1995.

[27] C. F. Bohren and D. R. Huffman. *Absorption and Scattering of Light by Small Particles*. Weinheim: Wiley-VCH Verlag GmbH & Co., 2004.

[28] H. C. Van de Hulst. *Light Scattering by Small Particles*. New York: Dover Publications, 1981.

[29] A. Ishimaru. *Wave Propagation and Scattering in Random Media: Vol. 2*. New York: Academic, 1987.

[30] L. Tsang and J. A. Kong. *Scattering of Electromagnetic Waves: Advanced Topics*. New York: Wiley-Interscience, 2001.

[31] G. Valenzuela. Depolarization of EM Waves by Slightly Rough Surfaces. *Antennas and Propagation, IEEE Transactions on*, 15(4):552–557, July 1967.

[32] J. A. Kong. *Electromagnetic Wave Theory*. EMW Publishing, Cambridge, Massachusetts, USA, 2008.

[33] Jet Propulsion Laboratory. Ancillary Data Report: Vegetation Water Content. URL: `http://smap.jpl.nasa.gov/science/dataproducts/ATBD/`. [Online; accessed 10-December-2013].

[34] J. A. Richards. Radar backscatter modelling of forests: a review of current trends. *International Journal of Remote Sensing*, 11(7):1922–1312, July 1990.

[35] M. Burgin, M. Moghaddam, and R. M. Lucas. Multilayered multiple-species forest scattering model based on a wave theory approach (invited). In *Geoscience and Remote Sensing Symposium (IGARSS), 2010 IEEE International*, Oahu, Hawaii, July 2010.

[36] M. Burgin, M. Moghaddam, and R. M. Lucas. Radar backscattering model for multispecies forests based on wave theory. In *National Radio Science Meeting*, Boulder, CO, January 2010.

[37] M. Burgin, D. Clewley, R. M. Lucas, and M. Moghaddam. A generalized radar backscattering model based on wave theory for multilayer multispecies vegetation. *Geoscience and Remote Sensing, IEEE Transactions on*, 49(12):4832–4845, December 2011.

[38] M. E. Bowen, C. A. McAlpine, A. P. N. House, and G. C. Smith. Agricultural landscape modification increases the abundance of an important food resource: Mistletoes, birds and brigalow. *Biological Conservation*, 142(1):122–133, January 2009.

[39] P. K. Tickle, A. Lee, R. M. Lucas, J. Austin, and C. Witte. Quantifying Australian forest floristics and structure using small footprint LiDAR and large scale aerial photography. *Forest Ecology and Management*, 223(1-3):379–394, March 2006.

[40] J. M. Dwyer. *Tree growth and mortality and implications for restoration and carbon sequestration in Australian subtropical semi-arid forests and woodlands*. PhD thesis, University of Queensland, 2010.

[41] R. J. Scholes and S. R. Archer. Tree-grass interactions in savannas. *Annual Review of Ecology and Systematics*, 28(1):517–544, 1997.

[42] J. C. Scalan. Woody overstory and herbaceous understory in Acacia harpophylla (brigalow) woodlands. *Australian Journal of Botany*, 16:521–529, 1991.

[43] R. M. Lucas, J. D. Armson, R. Fairfax, R. Fensham, A. Accad, J. Carreiras, J. Kelley, P. Bunting, D. Clewley, S. Bray, D. Metcalfe, M. Dwyer, M. Bowen, T. Eyre, and M. Laidlaw. An evaluation of the ALOS PALSAR L-Band Backscatter - Above ground biomass relationship Queensland, Australia: Impacts of surface moisture condition and vegetation structure. *Selected Topics in*

Applied Earth Observations and Remote Sensing, IEEE Journal of, 3(4):576–593, December 2010.

[44] E. S. Ksischke, M. A. Tanase, L. L. Bourgeau-Chavez, and M. Borr. Soil moisture limitations on monitoring boreal forest regrowth using spaceborne L-band SAR data. *Remote Sensing of Environment*, 115:227–232, December 2011.

[45] A. Tabatabaeenejad and M. Moghaddam. Bistatic scattering from three-dimensional layered rough surfaces. *Geoscience and Remote Sensing, IEEE Transactions on*, 44(8):2102–2114, August 2006.

[46] A. Tabatabaeenejad, X. Duan, and M. Moghaddam. Coherent Scattering of Electromagnetic Waves from Two-Layer Rough Surfaces Within the Kirchhoff Regime. *Geoscience and Remote Sensing, IEEE Transactions on*, 51(7):3943–3953, July 2013.

[47] R. Magagi, A. Berg, K. Goita, S. Belair, T. Jackson, B. Toth, A. Walker, H. McNairn, P. O'Neill, M. Moghaddam, I. Gherboudj, A. Colliander, M. Cosh, J. Belanger, M. Burgin, J. Fisher, S. Kim, JP Rousseau, N. Djamai, J. Shang, and A. Merzouki. Canadian Experiment for soil moisture in 2010 (CanEx-SM10): Overview and preliminary results. *Geoscience and Remote Sensing, IEEE Transactions on*, 51(1):347–363, January 2013.

[48] D. Stangel and S. Kelly. BOREAS HYD-01 Volumetric Soil Moisture Data, 1999. URL: `http://daac.ornl.gov/cgi-bin/dsviewer.pl?ds_id=255`, retrieved 7 November 2013.

[49] D. W. Anderson. BOREAS TE-01 SSA Soil Lab Data, 2000. URL: `http://daac.ornl.gov/cgi-bin/dsviewer.pl?ds_id=530`, retrieved 7 November 2013.

[50] Prof. Valeriy Ivanov. Personal communication. University of Michigan, 2013.

[51] V. L. Mironov, L. G. Kasolapova, and S. V. Fomin. Physically and Mineralogically Based Spectroscopic Dielectric Model for Moist Soils. *Geoscience and Remote Sensing, IEEE Transactions on*, 47(7):2059 – 2070, Jul. 2009.

[52] V. L. Mironov, L. G. Kasolapova, and S. V. Fomin. Correction to Physically and Mineralogically Based Spectroscopic Dielectric Model for Moist Soils. *Geoscience and Remote Sensing, IEEE Transactions on*, 47(7):2085, Jul. 2009.

[53] Jet Propulsion Laboratory. SMAP Level 2 & 3 Soil Moisture (Passive). URL: `http://smap.jpl.nasa.gov/science/dataproducts/ATBD/`. [Online; accessed 10-December-2013].

[54] A. Tabatabaeenejad, M. Burgin, and M. Moghaddam. Impact of subsurface layers on subcanopy soil moisture retrieval from radar. In *Geoscience and Remote Sensing Symposium (IGARSS), 2012 IEEE International*, Munich, Germany, July 2012.

[55] A. Tabatabaeenejad, M. Burgin, X. Duan, and M. Moghaddam. P-band radar retrieval of subcanopy and subsurface soil moisture profile as a second-order polynomial: First AirMOSS Results. *IEEE Transactions on Geoscience and Remote Sensing*, in revision.

[56] A. J. Luckman. The effects of topography on mechanisms of radar backscatter from coniferous forest and upland pasture. *Geoscience and Remote Sensing, IEEE Transactions on*, 36(5):1830–1834, 1998.

[57] Y.-C. Lin and K. Sarabandi. Electromagnetic scattering model for a tree trunk above a tilted ground plane. *Geoscience and Remote Sensing, IEEE Transactions on*, 33(4):1063–1070, 1995.

[58] J.M. Lopez-Sanchez, H. Esteban-Gonzalez, M. Baquero-Escudero, and J. Fortuny-Guasch. An electromagnetic scattering model for multiple tree trunks above a tilted rough ground plane. *Geoscience and Remote Sensing, IEEE Transactions on*, 37(2):659–667, 1999.

[59] L. Tsang, K. H. Ding, G. Zhang, C.C. Hsu, and J.-A. Kong. Backscattering enhancement and clustering effects of randomly distributed dielectric cylinders overlying a dielectric half space based on Monte-Carlo simulations. *Antennas and Propagation, IEEE Transactions on*, 43(5):488–499, 1995.

[60] G. Smith-Jonforsen, L. M. H Ulander, and X. Luo. Low VHF-band backscatter from coniferous forests on sloping terrain. *Geoscience and Remote Sensing, IEEE Transactions on*, 43(10):2246–2260, 2005.

[61] J. J. Van Zyl. The Effect of Topography on Radar Scattering from Vegetated Areas. *Geoscience and Remote Sensing, IEEE Transactions on*, 31(1):153–160, January 1993.

[62] X. Duan and M. Moghaddam. 3-D Vector Electromagnetic Scattering From Arbitrary Random Rough Surfaces Using Stabilized Extended Boundary Condition Method for Remote Sensing of Soil Moisture. *Geoscience and Remote Sensing, IEEE Transactions on*, 50(1):87–103, January 2012.

[63] M. A. El-Rayes and F. T. Ulaby. Microwave Dielectric Spectrum of Vegetation-Part I: Experimental Observations. *Geoscience and Remote Sensing, IEEE Transactions on*, GE-25(5):541–549, 1987.

[64] S. O. Nelson. Dielectric properties of agricultural products-measurements and applications. *Electrical Insulation, IEEE Transactions on*, 26(5):845–869, 1991.

[65] F. T. Ulaby and R. P. Jedlicka. Microwave Dielectric Properties of Plant Materials. *Geoscience and Remote Sensing, IEEE Transactions on*, GE-22(4):406–415, 1984.

[66] M. T. Hallikainen, F. T. Ulaby, M. C. Dobson, M. A. El-Rayes, and Lil-Kun Wu. Microwave Dielectric Behavior of Wet Soil-Part 1: Empirical Models and Experimental Observations. *Geoscience and Remote Sensing, IEEE Transactions on*, GE-23(1):25–34, 1985.

[67] F. T. Ulaby and M. A. El-Rayes. Microwave Dielectric Spectrum of Vegetation - Part II: Dual-Dispersion Model. *Geoscience and Remote Sensing, IEEE Transactions on*, GE-25(5):550–557, 1987.

[68] C. Matzler. Microwave (1-100 GHz) dielectric model of leaves. *Geoscience and Remote Sensing, IEEE Transactions on*, 32(4):947–949, 1994.

[69] M. C. Dobson, F. T. Ulaby, M. T. Hallikainen, and M. A. El-Rayes. Microwave Dielectric Behavior of Wet Soil-Part II: Dielectric Mixing Models. *Geoscience and Remote Sensing, IEEE Transactions on*, GE-23(1):35–46, 1985.

[70] L. L. Hess, J. M. Melack, S. Filoso, and Y. Wang. Delineation of inundated area and vegetation along the Amazon floodplain with the SIR-C synthetic aperture radar. *Geoscience and Remote Sensing, IEEE Transactions on*, 33(4):896–904, 1995.

[71] L. L. Hess, J. M. Melack, E. M. L. M Novo, C. C. F. Barbosa, and M. Gastil. Dual-season mapping of wetland inundation and vegetation for the central Amazon basin. *Remote Sensing of Environment*, 87(4):404 – 428, 2003.

[72] J. J. Van Zyl. Unsupervised classification of scattering behavior using radar polarimetry data. *Geoscience and Remote Sensing, IEEE Transactions on*, 27(1):36–45, 1989.

[73] J.-S. Lee, M. R. Grunes, E. Pottier, and L. Ferro-Famil. Unsupervised terrain classification preserving polarimetric scattering characteristics. *Geoscience and Remote Sensing, IEEE Transactions on*, 42(4):722–731, 2004.

[74] A. Freeman and S. L. Durden. A three-component scattering model for polarimetric SAR data. *Geoscience and Remote Sensing, IEEE Transactions on*, 36(3):963–973, 1998.

[75] S. R. Cloude and E. Pottier. A review of target decomposition theorems in radar polarimetry. *Geoscience and Remote Sensing, IEEE Transactions on*, 34(2):498–518, 1996.

[76] S. R. Cloude and E. Pottier. An entropy based classification scheme for land applications of polarimetric SAR. *Geoscience and Remote Sensing, IEEE Transactions on*, 35(1):68–78, 1997.

[77] M. C. Dobson, F. T. Ulaby, T. LeToan, A. Beaudoin, E. S. Kasischke, and N. Christensen. Dependence of radar backscatter on coniferous forest biomass. *Geoscience and Remote Sensing, IEEE Transactions on*, 30(2):412–415, 1992.

[78] T. Le Toan, A. Beaudoin, J. Riom, and D. Guyon. Relating forest biomass to SAR data. *Geoscience and Remote Sensing, IEEE Transactions on*, 30(2):403–411, 1992.

[79] K. J. Ranson and G. Sun. Mapping biomass of a northern forest using multi-frequency SAR data. *Geoscience and Remote Sensing, IEEE Transactions on*, 32(2):388–396, 1994.

[80] M. C. Dobson, F. T. Ulaby, L. E. Pierce, T. L. Sharik, K. M. Bergen, J. Kellndorfer, J. R. Kendra, E. Li, Y.-C. Lin, A. Nashashibi, K. Sarabandi, and P. Siqueira. Estimation of forest biophysical characteristics in Northern Michigan with SIR-C/X-SAR. *Geoscience and Remote Sensing, IEEE Transactions on*, 33(4):877–895, 1995.

[81] S. S. Saatchi and M. Moghaddam. Estimation of crown and stem water content and biomass of boreal forest using polarimetric SAR imagery. *Geoscience and Remote Sensing, IEEE Transactions on*, 38(2):697–709, 2000.

[82] L. E. Pierce, K. Sarabandi, and F. T. Ulaby. Application of an artificial neural network in canopy scattering inversion. *International Journal of Remote Sensing*, 15(16):3263–3270, 1994.

[83] Y. Wang and D. Dong. Retrieving forest stand parameters from SAR backscatter data using a neural network trained by a canopy backscatter model. *International Journal of Remote Sensing*, 18(4):981–989, 1997.

[84] Z. S. Haddad, P. Dubois, and J. J. Van Zyl. Bayesian estimation of soil parameters from radar backscatter data. *Geoscience and Remote Sensing, IEEE Transactions on*, 34(1):76–82, 1996.

[85] S.-B. Kim, M. Moghaddam, L. Tsang, M. Burgin, X. Xu, and E. G. Njoku. Models of L-Band Radar Backscattering Coefficients Over Global Terrain for Soil Moisture Retrieval. *Geoscience and Remote Sensing, IEEE Transactions on*, PP(99):1–1, 2013. *in press.*

[86] M. Moghaddam and S.S. Saatchi. Monitoring tree moisture using an estimation algorithm applied to SAR data from BOREAS. *Geoscience and Remote Sensing, IEEE Transactions on*, 37(2):901–916, 1999.

[87] M. Moghaddam, S. Saatchi, and R. H. Cuenca. Estimating subcanopy soil moisture with radar. *Journal of Geophysical Research: Atmospheres*, 105(D11):14899–14911, 2000.

[88] T. A. Warner, M. D. Nellis, and G. M. Foody. *The SAGE Handbook of Remote Sensing*. SAGE Publications Ltd, 2009.

[89] A. Corana, M. Marchesi, C. Martini, and S. Ridella. Minimizing multimodal functions of continuous variables with the simulated annealing algorithm. *ACM Transactions on Mathematical Software (TOMS)*, 13(3):262–280, 1987.

[90] A. Corana, M. Martini, C. Martini, and S. Ridella. Corrigenda: Minimizing Multimodal Functions of Continuous Variables with the Simulated Annealing Algorithm. *ACM Transactions on Mathematical Software (TOMS)*, 15(3):287, 1989.

[91] N. Metropolis, A. W. Rosenbluth, M. N. Rosenbluth, A. H. Teller, and E. Teller. Equation of State Calculations by Fast Computing Machines. *The Journal of Chemical Physics*, 21(6), 1953.

[92] A. Tabatabaeenejad and M. Moghaddam. Inversion of Subsurface Properties of Layered Dielectric Structures With Random Slightly Rough Interfaces Using the Method of Simulated Annealing. *Geoscience and Remote Sensing, IEEE Transactions on*, 47(7):2035–2046, July 2009.

[93] A. Tabatabaeenejad, M. Burgin, and M. Moghaddam. Potential of L-band Radar for Retrieval of Canopy and Subcanopy Parameters of Boreal Forests. *Geoscience and Remote Sensing, IEEE Transactions on*, 50(6):2150–2160, June 2012.

[94] Multi-Resolution Land Characteristics Consortium (MRLC). National Land Cover Database (NLCD) 2006. `http://www.mrlc.gov/nlcd2006.php`. [Online; accessed 22-May-2013].

[95] European Space Agency (ESA). European Space Agency GlobCover Portal. `http://due.esrin.esa.int/globcover/`. [Online; accessed 22-May-2013].

[96] Natural Resources and Conservation Service (NRCS). Soil Survey Geographic (SSURGO). `http://soils.usda.gov/survey/geography/ssurgo/`. [Online; accessed 22-May-2013].

[97] International Institute for Applied Systems Analysis (IIASA). Harmonized World Soil Database. `http://webarchive.iiasa.ac.at/Research/LUC/External-World-soil-database/HTML/`. [Online; accessed 22-May-2013].

[98] M. Moghaddam, D. Entekhabi, Y. Goykhman, Ke Li, Mingyan Liu, A. Mahajan, A. Nayyar, D. Shuman, and D. Teneketzis. A Wireless Soil Moisture Smart Sensor Web Using Physics-Based Optimal Control: Concept and Initial Demonstrations. *Selected Topics in Applied Earth Observations and Remote Sensing, IEEE Journal of*, 3(4):522–535, 2010.

[99] M. Moghaddam, D. Entekhabi, M. Liu, D. Teneketzis, R. Cook, G. Palanisamy, S. S. Vannan, and R. Devarakonda. SoilSCAPE: Soil moisture Sensing Controller And oPtimal Estimator. URL: `http://soilscape.usc.edu/`, retrieved 10 November 2013.

[100] W. T. Crow, A. A. Berg, M. H. Cosh, A. Loew, B. P. Mohanty, R. Panciera, P. de Rosnay, D. Ryu, and J. P. Walker. Upscaling sparse ground-based soil moisture observations for the validation of coarse-resolution satellite soil moisture products. *Reviews of Geophysics*, 50(2), 2012.

[101] M. Drusch, E. F. Wood, and C. Simmer. Up-scaling effects in passive microwave remote sensing: ESTAR 1.4 GHz measurements during SGP '97. *Geophysical Research Letters*, 26(7):879–882, 1999.

[102] J. F. Galantowicz, D. Entekhabi, and E. G. Njoku. Estimation of soil-type heterogeneity effects in the retrieval of soil moisture from radiobrightness. *Geoscience and Remote Sensing, IEEE Transactions on*, 38(1):312–315, 2000.

[103] X. Zhan, W. T. Crow, T. J. Jackson, and P. E. O'Neill. Improving Spaceborne Radiometer Soil Moisture Retrievals With Alternative Aggregation Rules for Ancillary Parameters in Highly Heterogeneous Vegetated Areas. *Geoscience and Remote Sensing Letters, IEEE*, 5(2):261–265, 2008.

[104] W. L. Crosson, A. S. Limaye, and C.A. Laymon. Impacts of Spatial Scaling Errors on Soil Moisture Retrieval Accuracy at L-Band. *Selected Topics in Applied Earth Observations and Remote Sensing, IEEE Journal of*, 3(1):67–80, 2010.

[105] U. K. Khankhoje, M. Burgin, and M. Moghaddam. On the accuracy of averaging radar backscattering coefficients for bare soils using the finite element method. *Geoscience and Remote Sensing Letters*, accepted for publication.

[106] K. J. Ranson, R. Lang, and G. Sun. BOREAS RSS-15 SIR-C and TM Biomass and Landcover Maps of the NSA and SSA, 1999. URL: `http://daac.ornl.gov/BOREAS/guides/RSS15_SIRC_Biomass.html`, retrieved 2 November 2013.

[107] A. Freeman and S. Saatchi. On the Detection of Faraday Rotation in Linearly Polarized L-band SAR Backscatter Signatures. *Geoscience and Remote Sensing, IEEE Transactions on*, 42(8):1–10, August 2004.

[108] R. A. Thompson, J. M. Moran, and G. W. Swenson. *Interferometry and Synthesis in Radio Astronomy*. John Wiley and Sohns, New York, 1986.

[109] D. M. Le Vine and M. Kao. Effects of Faraday Rotation on microwave remote sensing from space at L-band. *Geoscience and Remote Sensing, IEEE Transactions on*, 1:377–379, August 1997.

[110] E. J. M. Rignot. Effect of Faraday rotation on L-band interferometric and polarimetric synthetic-aperture radar data. *Geoscience and Remote Sensing, IEEE Transactions on*, 38(1):383–390, 2000.

[111] K. Davies. *Ionospheric Radio*. Peter Peregrinus Ltd, London, United Kingdom, 1990.

[112] E. Chapin, S. F. Chan, B. D. Chapman, C. W. Chen, J. M. Martin, T. R. Michel, R. J. Muellerschoen, Xiaoqing Pi, and P. A. Rosen. Impact of the ionosphere on an L-band space based radar. In *Radar, 2006 IEEE Conference on*, pages 8 pp.–, 2006.

[113] European Space Agency. Future biomass mission. URL: `http://www.esa.int/Our_Activities/Observing_the_Earth/The_Living_Planet_Programme/Earth_Explorers/Future_missions/About_future_missions`. [Online; accessed 22-October-2013].

[114] Jet Propulsion Laboratory. L1B&C_S0: Level 1B and Level 1C Radar Data Products. URL: `http://smap.jpl.nasa.gov/science/dataproducts/ATBD/`. [Online; accessed 22-October-2013].

[115] A. Freeman. Calibration of linearly polarized polarimetric SAR data subject to Faraday Rotation. *Geoscience and Remote Sensing, IEEE Transactions on*, 42(8):1617–1624, August 2004.

[116] A. Freeman. SAR calibration: An overview. *Geoscience and Remote Sensing, IEEE Transactions on*, 30(6):1107–1121, November 1992.

[117] M. W. Whitt, F. T. Ulaby, P. Polatin, and V. V. Liepa. A general polarimetric radar calibration technique. *Antennas and Propagation, IEEE Transactions on*, 39(1):62–67, January 1991.

[118] A. Freeman, Y. Shen, and C. W. Werner. Polarimetric SAR calibration experiment using active radar calibrators. *Geoscience and Remote Sensing, IEEE Transactions on*, 28(2):224–240, March 1990.

[119] J. D. Klein. Polarimetric SAR Calibration Using Two Targets And Reciprocity. In *Geoscience and Remote Sensing Symposium, 1990. IGARSS '90. 'Remote Sensing Science for the Nineties'., 10th Annual International*, pages 1105–1108, 1990.

[120] A. Freeman. A new system model for radar polarimeters. *Geoscience and Remote Sensing, IEEE Transactions on*, 29(5):761–767, September 1991.

[121] K. Sarabandi and F. T. Ulaby. A convenient technique for polarimetric calibration of single-antenna radar systems. *Geoscience and Remote Sensing, IEEE Transactions on*, 28(6):1022–1033, 1990.

[122] J. J. Van Zyl. Calibration of polarimetric radar images using only image parameters and trihedral corner reflector responses. *Geoscience and Remote Sensing, IEEE Transactions on*, 28(3):337–348, May 1990.

[123] J. D. Klein. Calibration of complex polarimetric SAR imagery using backscatter correlations. *Aerospace and Electronic Systems, IEEE Transactions on*, 28(1):183–194, 1992.

[124] A. Quegan. A unified algorithm for phase and cross-talk calibration of polarimetric data - theory and observations. *Geoscience and Remote Sensing, IEEE Transactions on*, 32:89–99, January 1994.

[125] K. Sarabandi, L. E. Pierce, and F. T. Ulaby. Calibration of a polarimetric imaging SAR. *Geoscience and Remote Sensing, IEEE Transactions on*, 30(3):540–549, May 1992.

[126] A. Freeman. An "exact" Solution To The Problem Of Calibrating Stokes Matrix Polarimetric SAR Data. In *Geoscience and Remote Sensing Symposium, 1990. IGARSS '90. 'Remote Sensing Science for the Nineties'., 10th Annual International*, pages 773–777, 1990.

[127] S. H. Bickel and R. H. T. Bates. Effects of magneto-ionic propagation on the polarization scattering matrix. *Proceedings of the IEEE*, 53(8):1089–1091, 1965.

[128] J. Nicoll, F. Meyer, and M. Jehle. Prediction and detection of Faraday rotation in ALOS PALSAR data. *Geoscience and Remote Sensing, IEEE Transactions on*, pages 5210–5213, July 2007.

[129] D. Bilitza. International Reference Ionosphere (IRI), 2012. URL: `http://iri.gsfc.nasa.gov/`, retrieved 22 April 2012.

[130] C. Finlay. International Geomagnetic Reference Field (IGRF), 2012. URL: `http://www.ngdc.noaa.gov/IAGA/vmod/igrf.html`, retrieved 22 April 2012.

[131] British Geological Survey. International Geomagnetic Reference Field (IGRF) synthesis form, 2008. URL: `http://www.geomag.bgs.ac.uk/gifs/igrf_form.shtml`, retrieved 13 July 2008.

[132] National Space Science Data Center distributed through NASA. Models of IRI and IGRF. URL: `http://nssdcftp.gsfc.nasa.gov/`, Retrieved 13 July 2008. path: models/ionospheric/iri/iri2007/.

[133] Astronomical Applications Department. Day and Night across the Earth. URL: `http://aa.usno.navy.mil/data/docs/earthview.php`. [Online; accessed 25 July 2013].

[134] R. M. Goldstein, H. A. Zebker, and C. L. Werner. Satellite radar interferometry: Two-dimensional phase unwrapping. *Radio Science*, 23(4):713–720, Jul-Aug 1988.

[135] R.-Y. Qi and Y.-Q. Jin. Analysis of the Effects of Faraday Rotation on Spaceborne Polarimetric SAR Observations at P-Band. *Geoscience and Remote Sensing, IEEE Transactions on*, 45(5):1115–1120, May 2007.

[136] M. Burgin, M. Moghaddam, and A. Freeman. Direct estimation of Faraday Rotation and other system distortion parameters from polarimetric SAR data. In *Geoscience and Remote Sensing Symposium (IGARSS), 2010 IEEE International*, Oahu, Hawaii, July 2010.

[137] P. Wright, S. Quegan, N. Wheadon, and D. Hall. Faraday rotation effects on L-band spaceborne SAR data. *Geoscience and Remote Sensing, IEEE Transactions on*, 41(12):2735–2744, December 2003.

[138] P. Y. Papalambros and D. J. Wilde. *Principles of Optimal Design: Modeling and Computation*. Cambridge University Press, second edition edition, 2000. ODE Laboratory, ODE Toolkit.

[139] W. H. Press, B. P. Flannery, S. A. Teukolsky, and W. T. Vetterling. *Numerical Recipes in Fortran 77: The Art of Scientific Computing*. Cambridge University Press, 1992.

[140] J. R. Shewchuk. An Introduction to the Conjugate Gradient Method Without the Agonizing Pain, Edition 1 $\frac{1}{4}$. URL: `http://www.cs.berkeley.edu/~jrs/jrspapers.html#cg`. [Online; accessed 28-October-2013].

[141] Mathworks Documentation Center. fminunc quasi-newton Algorithm. URL: `http://www.mathworks.com/help/optim/ug/unconstrained-nonlinear-optimization-algorithms.html#brnpcye`. [Online; accessed 13 November 2013].

[142] University of Sherbrooke. Smapvex (smap validation experiment 2012). URL: `http://pages.usherbrooke.ca/smapvex12/`. [Online; accessed 28-June-2013].

[143] J. L. Farrar. *Trees in Canada*. Fitzhenry and Whiteside, 1995.

[144] Jet Propulsion Laboratory. Uavsar (uninhabited aerial vehicle synthetic aperture radar). URL: `http://uavsar.jpl.nasa.gov/`. [Online; accessed 28-June-2013].

[145] C. Beer, M. Reichstein, E. Tomelleri, P. Ciais, M. Jung, N. Carvalhais, C. Rdenbeck, M. A. Arain, D. Baldocchi, G. B. Bonan, A. Bondeau, A. Cescatti, G. Lasslop, A. Lindroth, M. Lomas, S. Luyssaert, H. Margolis, K. W. Oleson, O. Roupsard, E. Veenendaal, N. Viovy, C. Williams, F. I. Woodward, and D. Papale. Terrestrial gross carbon dioxide uptake: Global distribution and covariance with climate. *Science*, 329(5993):834–838, Aug. 2010.

[146] J. Xiao, Q. Zhuang, B. E. Law, D. D. Baldocchi, J. Chen, A. D. Richardson, J. M. Melillo, K. J. Davis, D. Y. Hollinger, S. Wharton, R. Oren, A. Noormets, M. L. Fischer, S. B. Verma, D. R. Cook, G. Sun, S. McNulty, S. C. Wofsy, P. V. Bolstad, S. P. Burns, P. S. Curtis, B. G. Drake, M. Falk, D. R. Foster, L. Gu, J. L. Hadley, G. G. Katul, M. Litvak, S. Ma, T. A. Martin, R. Matamala, T. P. Meyers, R. K. Monson, J. W. Munger, W. C. Oechel, U. Kyaw Tha Paw, H. P. Schmid, R. L. Scott, G. Starr, A. E. Suyker, and M. S. Torn. Assessing net ecosystem carbon exchange of U. S. terrestrial ecosystems by integrating eddy covariance flux measurements and satellite observations. *Agricultural and Forest Meteorology*, 151(1):60–69, Jan. 2011.

[147] C. Yi et. al. Climate control of terrestrial carbon exchange across biomes and continents. *Environmental Research Letters*, 5(3), 2010.

[148] B. D. Allen, S. A. Braun, J. H. Crawford, E. J. Jensen, C. E. Miller, M. Moghaddam, and H. Maring. Proposed investigations from NASA's Earth Venture-1 (EV-1) airborne science selections. In *Geoscience and Remote Sensing Symposium (IGARSS), 2010 IEEE International*, pages 2575–2578, 2010.

[149] Committee on Earth Science, Applications from Space: A Community Assessment, and National Research Council Strategy for the Future. *Earth Science and Applications from Space: National Imperatives for the Next Decade and Beyond.* The National Academies Press, 2007.

[150] W. Peters, A. R. Jacobson, C. Sweeney, A. E. Andrews, T. J. Conway, K. Masarie, J. B. Miller, L. M. P. Bruhwiler, G. Petron, A. I. Hirsch, D. E. J. Worthy, G. R. van der Werf, J. T. Randerson, P. O. Wennberg, M. C. Krol, and P. P. Tans. An atmospheric perspective on North American carbon dioxide exchange: CarbonTracker. *Proc. National Academy of Sciences of the United States of America (PNAS)*, 104(48):18925–18930, Nov. 2007.

[151] E. Chapin, A. Chau, J. Chen, B. Heavey, S. Hensley, Y. Lou, R. Machuzak, and M. Moghaddam. AirMOSS: An Airborne P-band SAR to measure root-zone soil moisture. In *Radar Conference (RADAR), 2012 IEEE*, pages 693–698, 2012.

[152] S. Hensley, K. Wheeler, G. Sadowy, C. Jones, S. Shaffer, H. Zebker, T. Miller, B. Heavey, E. Chuang, R. Chao, K. Vines, K. Nishimoto, J. Prater, B. Carrico, N. Chamberlain, J. Shimada, M. Simard, B. Chapman, R. Muellerschoen, C. Le, T. Michel, G. Hamilton, D. Robison, G. Neumann, R. Meyer, P. Smith, J. Granger, P. Rosen, D. Flower, and R. Smith. The UAVSAR instrument: Description and first results. In *Radar Conference, 2008. RADAR '08. IEEE*, pages 1–6, 2008.

[153] D. A. King. Allometry and Life History of Tropical Trees. *Journal of Tropical Ecology*, 12(1):25–44, Jan. 1996.

[154] L. A. McDade, K. S. Bawa, H. A. Hespenheide, and G. S. Hartshorn. *La Selva: Ecology and Natural History of a Neotropical Rain Forest.* University Of Chicago Press, 1994.

[155] Jet Propulsion Laboratory. The Shuttle Radar Topography Mission (SRTM). `http://www2.jpl.nasa.gov/srtm/`. [Online; accessed 22-May-2013].

[156] R. Cuenca and C. Kunkel. Private communication. Oregon State University, 2012.

[157] Natural Resources and Conservation Service (NRCS). U.S. General Soil Map (STATSGO2). `http://soildatamart.nrcs.usda.gov`. [Online; accessed 22-May-2013].

[158] A. Guissard. Mueller and Kennaugh Matrices in Radar Polarimetry. *Geoscience and Remote Sensing, IEEE Transactions on*, 32(3):590–597, May 1994.

[159] H. A. Zebker and J. J. Van Zyl. Imaging Radar Polarimetry: A Review. *Proceedings of the IEEE*, 79(11):1583–1606, November 1991.

[160] J. J. Van Zyl, H. A. Zebker, and C. Elachi. Imaging radar polarization signatures: Theory and observation. *Radio Science*, 22(4):529–543, Jul-Aug 1987.

[161] Jet Propulsion Laboratory. AIRSAR General Reference Manual (PDF format). URL: `http://airsar.jpl.nasa.gov/documents/instrument.htm`. [Online; accessed 30-October-2013].